A new parameterization of aircraft icing accounting for microphysical properties of clouds

Zur Erlangung des akademischen Grades eines
DOKTORS DER NATURWISSENSCHAFTEN (Dr. rer. nat.)
von der KIT-Fakultät für Physik des
Karlsruher Instituts für Technologie (KIT)

genehmigte

DISSERTATION

von

M.Sc. (Meteorology) Sven Werchner
aus Waghäusel

Tag der mündlichen Prüfung:	02.12.2022
Referent:	Prof. Dr. Christoph Kottmeier
Korreferentin:	Prof. Dr. Corinna Hoose

This document is licensed under a Creative Commons
Attribution-ShareAlike 4.0 International License (CC BY-SA 4.0):
https://creativecommons.org/licenses/by-sa/4.0/deed.en

Abstract

The effects of aircraft icing comprise of (i) simple inconveniences, like flight delays, (ii) increased fuel consumption and (iii) severe performance degradations, potentially resulting in the loss of control over the aircraft. The accretion of ice onto the aircraft is considered the reason for several documented fatal crashes. Because of this safety hazard for aviation, weather services around the world use aircraft icing prediction schemes to forecast the location and intensity of icing environments, based on the output of numerical weather prediction models.

Although aircraft icing occurs by the freezing of supercooled liquid droplets impinging onto the aircraft's surface, current icing prediction schemes do not consider microphysical quantities, like the droplets' size or their spectrum, in their design. Analytical icing related algorithms tend to respect the droplets' size, but in a simplified, heuristic way.

The present work develops a new physically based aircraft icing parameterization employing the two main physical processes involved in aircraft icing, namely the droplet impingement and the freezing of the impinged droplets. The former is represented by the droplets' impingement efficiency, which is computed by evaluating droplet trajectories in the vicinity of the object. The freezing model used in this new parameterization allows for the differentiation of different icing phases, a dry icing phase solely accreting rime ice and a wet icing phase accreting glaze ice and a liquid water film due to the release of latent heat whilst freezing, allowing for a more detailed forecast and analysis. This new aircraft icing parameterization is implemented in a numerical weather forecast model to simulate icing conditions for two former case studies and an additional icing incident. The simulations reproduce the results of the case studies properly and enhance them with additional icing related quantities. Contrary to currently used heuristic approaches to the impingement efficiency, this new physically based approach gives a greater differentiation of high impingement efficiency values. Using this new parameterization, the present work further investigates the role of microphysical quantities by conducting sensitivity studies focused on the explicit consideration of the droplet spectrum and the aerosol load, which is represented by the cloud droplet number density for one experiment and by the number density of aerosols acting as cloud condensation nuclei for the droplet nucleation parameterization for the other. Since the new aircraft icing parameterization introduces further influencing quantities, a further sensitivity investigation focusing on the relative airspeed is conducted.

The present work shows that the explicit consideration of the cloud droplet spectrum affects the impingement and icing related quantities only minorly. The alteration of the cloud droplet number density, as a proxy for the effect of the aerosol load, has large implications for the impingement, accretion rates and amounts as well as composition of the accreted material. Altering the number density of cloud condensation nuclei instead affects the impingement mainly in low impinging environments and the composition of the accreted material due to impacts on the accretion of rime ice. Glaze ice and liquid water accretion are largely unaffected. The relative airspeed also affects the droplet impingement, but its largest effect is on the accretion rates caused by the impinging water and the composition of the accreted material.

The newly developed physically based parameterization of aircraft icing also gives the possibility to design a new online icing prediction scheme, as it is implemented into an operatively used numerical weather forecast model. This requires additional efforts in designing an appropriate icing intensity scale as well as in testing, validating and tuning.

Contents

1 Introduction **1**

2 Theory and fundamentals **5**

2.1 Aircraft icing as a safety hazard 5

2.2 Formation of liquid droplets in the atmosphere 6

2.3 Water's efficiency in impinging aircrafts 11

2.4 Freezing behaviour of impinged water 15

2.5 Operational aircraft icing prediction schemes 18

3 Model description and new aircraft icing parameterization **25**

3.1 The model system ICON-ART 25

3.2 Droplet activation parameterization 27

3.3 Development and implementation of a new aircraft icing parameterization 29

3.4 Adaptation of model setup configurations 35

4 Simulations of icing environments with the new parameterization **39**

4.1 Case study: Cold Lake in Alberta, Canada 39

4.1.1 24th of October 2016 (CAN24) 40

4.1.2 26th of October 2016 (CAN26) 48

4.2 Case study: Guadarrama Mountains, Spain (SPN) 56

4.3 Reported icing incident: Baden-Wuerttemberg, Germany (BWF) 63

5 Sensitivity to the explicit consideration of the droplet spectrum **73**

5.1 Expectations 73

5.2 Results 73

6 Sensitivity to aerosol load **81**

6.1 Modification of cloud droplet numbers 81

6.1.1 Expectations 81

6.1.2 Results 81

6.2 Modification of CCN numbers 90

6.2.1 Expectations 90

6.2.2 Results 90

7 Sensitivity to the relative airspeed **101**

7.1 Expectations 101

7.2 Results 101

8 Application in a future improved icing prediction scheme **111**

9 Conclusions **113**

Bibliography **120**

Acknowledgements **131**

Danksagung **133**

1 Introduction

The weather is a significant contributor to hazards for aviation. In most cases of delays occuring in air traffic the weather situation is the underlying reason. However, next to such inconveniences, also a non-negligible number of fatal accidents is caused by the atmospheric state. A study by the Federal Aviation Administration's National Aviation Safety Data Analysis Center revealed that 21.3 % of the investigated accidents were contributed or caused by the weather (Mecikalski et al. 2007). Mecikalski et al. (2007) further state that in-flight icing is a critical factor in the weather's contribution to aviation hazards for all sizes of planes not only regarding travel delay, but also more significant concerns like the crashing of an ATR-72 commuter airline on 31st of October 1994, killing 68 people.

Due to the additional mass and especially the alteration of the airflow around the airfoil, the performance of the aircraft deteriorates once ice accretes on it. This can cause effects from inconveniences like increased fuel usage up to complete losses of control leading to crashes (Boudala et al. 2019), putting high importance on analyzing aircraft icing conditions (Fernández-González et al. 2014) and diagnosing and forecasting its occurrences, which remains a challenge (Mecikalski et al. 2007). Weather services around the world offer icing prediction schemes, tackling this challenge with their models. Examples for this are the Current Icing Potential (Bernstein et al. 2005) in North America or the ADWICE system (Kalinka et al. 2017) of the German Weather Service (DWD).

Additional efforts are made to better understand the exact implications aircraft icing conditions have on the aircrafts' performance. The Institute of Flight Systems of the German Aerospace Center (DLR-FT) develops aircraft simulation models with the intent to investigate the effects of ice accretion exerted onto an aircraft, e.g. in the scope of the SuLaDI project (Deiler 2013a; Deiler 2013b). The works of Cao et al. (2016), Jung et al. (2011) and Papadakis et al. (2004) are examples that employ further methods, techniques and measurements focused on the shape in which ice accretes onto an aircraft's wing and aid in the design and engineering of airfoils and safety measures.

While there are instances of aircraft icing caused by ice crystals in the atmosphere at high altitudes, so called ice crystal icing (ICI), which is the subject of the EU project MUSIC-haic (Villedieu et al. 2019), most aircraft icing incidents occur when supercooled cloud droplets hit the surface of the aircraft causing them to spontaneously freeze upon it. Current research efforts for improving the prediction of these icing environments is therefore based upon a more accurate forecasting of the atmosphere's supercooled liquid water content (SLWC). A time-lag-ensemble method employed by Xu et al. (2019) on the High-Resolution Rapid Refresh model results in an improved SLWC forecast raising the capture rate of icing reports compared to its deterministic variant, also introducing, however, an increased false alarm rate as trade-off. Kringlebotn Nygaard et al. (2011) evaluated the Weather Research and Forecasting (WRF) model's ability in predicting SLWC at ground level using different grid spacings and microphysics schemes, resulting in heavy reductions of absolute errors with increasing horizontal resolution. Thompson et al. (2017) shows that this forecasting skill extends to further characteristics of icing environments.

The present work also focuses on aircraft icing caused by supercooled cloud droplets and its representation in weather models. Contrary to the aforementioned research, however, its emphasis is on the representation of the actual physical processes involved in aircraft icing in icing environments.

The atmosphere is able to hold water vapour to an extent that is exponentially dependent on the temperature. This thermodynamic limit is responsible for the creation of liquid water. An initially subsaturated air parcel that cools down by rising and expanding while maintaining its water vapour concentration, can become saturated and supersaturated in this process. The excess water vapour needs to change phase as it cannot be held by the atmosphere anymore. For this, aerosol particles come into play as cloud condensation nuclei (CCN) to aid in the condensation process, forming a cloud with a water content that corresponds to the excess water vapour concentration. Although this is a highly simplified description it still imparts the main thermodynamic processes (Seinfeld and Pandis 2016). Supercooling describes the phenomenon that water can remain in a liquid state at temperatures below its triple point of 0.01 °C, which marks the temperature at which all three water phases coexist as well as the highest temperature for ice to prevail. Water molecules need to arrange in an ice-like structure for freezing to occur. These ice crystal embryos require a critical size for stable development. Due to their generation being random via molecular motion that depends on its temperature, combined with the limited amount of water lowers the temperature at which ice nucleates within a droplet significantly. This holds for ice nucleation without a participating particle, so called homogeneous ice nucleation (Lohmann et al. 2016). According to Gent et al. (2000) homogeneous nucleation may require temperatures down to $-40\,°\mathrm{C}$, depending on the water's purity and the droplets' size. Contrary, heterogeneous ice nucleation takes place at higher temperatures since another substance is participating as an ice nucleating particle (INP). An INP has an ice-like structure, which leads the water coming into contact with it to be aligned accordingly. This reduces both the randomness of the embryo formation and the required amount of water molecule to reach the critical size, which enables nucleation at higher temperatures (Lohmann et al. 2016). The atmosphere enables supercooling frequently down to $-20\,°\mathrm{C}$, only seldomly going beyond $-30\,°\mathrm{C}$ (Gent et al. 2000). Supercooled droplets remain liquid until they get in contact with either an ice nucleating particle forming ice crystals or a suitable surface, on which they freeze spontaneously, like an aircraft. How efficiently incoming supercooled liquid water impinges onto the aircraft depends greatly on the sizes of the incoming droplets. This is a consequence of the fact that the aircraft (or other objects) disturb the ambient airflow. Due to their high inertia, large droplets are less affected by the disturbance, leading to a trajectory that is more likely to impinge onto the object, than smaller droplets that are more easily diverted around the object following the streamlines (Gent et al. 2000). However, current icing prediction schemes do not consider the cloud droplet spectrum nor any representation of the droplet size to forecast icing conditions and icing intensities.

The present work investigates the possibilities of using microphysical quantities of clouds for identifying icing conditions and quantifying icing intensity, as well as the role of the aerosol load. The idea behind the latter is that the size of liquid water droplets is mainly determined by the amound of available cloud condensation nuclei provided as aerosols. Hence, the present work answers the following questions:

- Is the explicit consideration of the cloud droplet spectrum beneficial to only using the mean droplet size?
- How sensitive is the identification of icing conditions and the quantification of their intensity to the aerosol load acting as cloud condensation nuclei?

Both of these questions require an aircraft icing parameterization that explicitly considers microphysical quantities like the liquid water content and especially the cloud droplet spectrum. In the scope of the present work such a parameterization is newly developed relying, contrary to current parameterizations and prediction schemes, on the representation of the main physical processes in aircraft icing, which are the impingement of supercooled liquid water and the actual freezing process, instead of heuristic approaches. The impingement process is quantified by computing the droplets' trajectories in the disturbed airflow around the object. The freezing process is based on the freezing model introduced by Zhang et al. (2016). One of its features is the separation between a dry icing phase, in which the impinging water freezes entirely, and a wet icing phase, where due to the latent heat released during freezing and the heat capacity of the already accreted ice parts of the impinging water remain in a liquid state. As the new parameterization relies on the actual droplet sizes and spectra, it is fit to answer the questions above. The second question, however, is divided into two parts: Since the new parameterization has no direct dependency on the aerosol load and the main influence of the aerosol load is the alteration of the cloud droplet number density, the first approach to the question is to investigate the sensitivity to this cloud droplet number density. This gives a maximum estimate that is mostly independent on the specific cloud droplet nucleation parameterization in use. The second part investigates the sensitivity to the aerosol load by varying the amount of aerosols provided to the cloud droplet nucleation parameterization as CCN. In addition, the development of this new aircraft icing parameterization begs the question of the way it represents icing environments. Additionally, it requires further parameters, like the relative airspeed, which is also not considered in current icing prediction schemes, raising an additional question:

- How sensitive are icing conditions and intensities to the relative airspeed?

To answer these research questions, the ICON-ART model (ICOsahedral Non-hydrostatic model framework - Aerosols and Reactive Trace gases, (Zängl et al. 2015; Rieger et al. 2015)) is extended by the newly developed aircraft icing parameterization and used to simulate four icing scenarios originating off of case studies and a local report of icing.

The following chapter 2 provides the theoretical background and fundamentals as well as the current state of research required to understand the work presented. It gives an overview of the intricacies regarding aircraft icing, an explanation of the forming of liquid water in the atmosphere, the definition and computation of the impingement efficiency and a description of the freezing model by Zhang et al. (2016) that are both used for the newly developed aircraft icing parameterization. The chapter closes with an overview of current icing prediction schemes' functionalities. Chapter 3 introduces the model and parameterizations used, starting with a description of ICON-ART, followed by that of its representation of the cloud droplet nucleation. The newly developed physical based aircraft icing parameterization is then presented with its two main parts of droplet impingement and the actual freezing model, as well as its implementation extending the ICON-ART code. The chapter closes with the description of the general and individual model configurations used for the simulations conducted in the scope of the present work. With the theoretical and technical setup provided, chapter 4 presents the functionality and features of the newly developed icing parameterization by simulating four different cases, based on two aircraft icing related case studies, located in Canada and Spain, enabling a basic validation of the implementation, and an additional reported icing incident in Baden-Wuerttemberg, Germany. These form the basis for the upcoming sensitivity investigations. Chapter 5 deals with the potential benefits of the explicit consideration of the cloud droplet spectrum. Chapter 6 investigates the sensitivity of the identification of icing environments and their intensity to the aerosol load. Its first part looks into the effect of varying cloud droplet number density as a proxy for the aerosol load to give a maximum estimate of the effect, and the second part applies the variation of the aerosol load as cloud condensation nuclei to the cloud droplet nucleation parameterization. Chapter 7 answers the question that originated from the development of the new aircraft icing parameterization, how sensitive icing environments are to the relative airspeed of the passing aircraft. Chapter 8 describes further possibilities of the new aircraft icing parameterization for new online icing prediction schemes. The work is concluded with chapter 9 summarizing and discussing the results achieved.

2 Theory and fundamentals

The following part introduces the phenomenon of aircraft icing, its potential effects and influencing factors. It shows that icing occurs due to supercooled droplets, so this part also introduces nucleation of liquid water, its properties and the role of aerosols. As the supercooled droplets need to impact the aircraft to freeze upon it, the concept of collection or impingement efficiency and the freezing process itself is introduced, which form the two main parts of the new aircraft icing parameterization developed in the present work. This chapter closes with an overview on operational aircraft icing prediction schemes.

2.1 Aircraft icing as a safety hazard

An aircraft passing through a supercooled cloud provides a suitable surface for the droplets to freeze upon, leading to an accretion of ice on the aircraft. Figure 2.1 shows such a case of ice accretion on the leading edge of an aircraft's airfoil with an ice thickness of a few centimetres. Additionally, a few spots of ice beyond the leading edge are indicated that may originate from temporarily melted ice flowing downstream and refreezing there, so-called runback icing. Gent et al. (2000) name a selection of parameters that affect the amplitude of the ice accretion: the ambient air temperature, the liquid water content (LWC), the size of the droplets, the airspeed and the altitude. The first three parameters are independent of the aircraft itself and therefore describe the role of the atmosphere regarding aircraft icing. The latter two describe the aircraft's role. As the ambient air temperature influences the availability of convective cooling, it affects the dissipation of latent heat that is released when the supercooled droplets freeze upon the aircraft. Lower temperature values enhance convective cooling and hence provide a greater tendency for freezing to occur. A secondary effect, the ambient air temperature has, is the connection between droplet size and supercooling itself. Reduced ambient air temperature enables only the smaller droplets to remain in the liquid state, which leads to a reduction of the probability to encounter high amounts of supercooled liquid water. Therefore, the ambient air temperature is the most critical influencing parameter towards ice accretion (Gent et al. 2000). Further according to Gent et al. (2000) the LWC affects the ice accretion in multiple ways. As it provides the water to potentially be frozen upon the aircraft, the LWC needs to be greater than 0 for icing to occur. However, the specific amount is not further indicative to whether icing occurs, but to the actual ice growth rate and total ice amount expected, if it does. It also affects whether rime or also glaze ice is accreted. Larger values result in more latent heat released to be removed, which tends towards the formation of glaze ice. Low values, especially in combination with low ambient air temperature lead more towards rime ice formation. Gent et al. (2000) also states the importance of the droplets' size, as it determines how much of the LWC is impinging onto the body's surface. Large droplets have large inertia and are therefore less affected by the disturbed airflow around the body and so are more likely to impinge onto it. The inertia of very large droplets, so-called supercooled large droplets (SLD), „leads to near-ballistic trajectories, hardly, if at all, affected by the local flow conditions" (Gent et al. 2000, p. 2882), raising the importance of the SLD regarding flight safety. Smaller droplets, on the other hand, tend to miss the body and therefore their contribution to the amount of impacting water is rather insignificant. Although the sizes of droplets within a cloud vary, the median volumetric diameter (MVD) is often used to characterize the droplet spectrum. It is further elaborated that with reductions in ambient air temperature, the sizes of supercooled liquid droplets are also reduced, as larger droplets tend to not remain in the supercooled state (Gent et al. 2000). Although not being an icing condition in itself, Gent et al. (2000) does not understate the role the airspeed and altitude have for aircraft icing. The airspeed determines the intercepted air volume, hence water mass, in a given

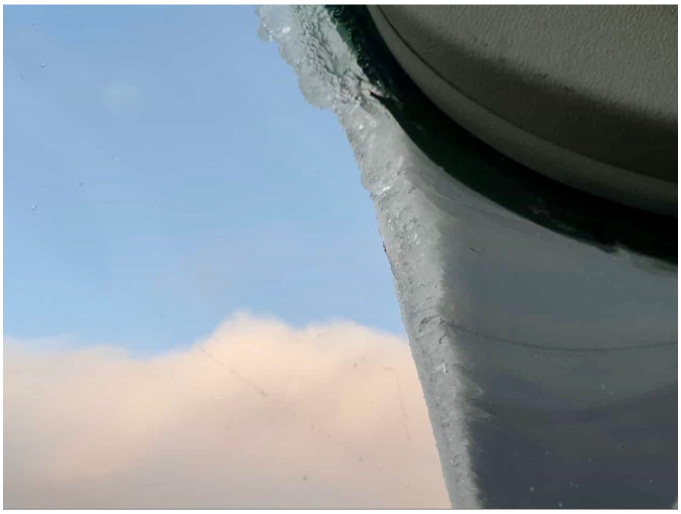

Figure 2.1: Ice accretion on the leading edge of a lightweight aircraft's airfoil. Minor incidents of runback icing are also indicated (Photo taken during private flight by a hobby pilot).

time and therefore the accreted amount of water. The altitude has more indirect influences as it describes the likelihood of icing conditions to occur. However, with the other parameters fixed, the altitude would not influence the ice accretion considerably. It is an important consideration when regarding the necessity of bleed air for anti-icing measures, as it is reduced with increasing altitude.

Aircraft icing poses a serious safety hazard for aviation as it not only adds additional mass to the aircraft, but it also impacts its aerodynamic properties, overall deteriorating its flight performance. While this can properly be prepared for with anti- and de-icing measures, preventing of ice accretion by applying chemicals onto the airfoil pre-flight and removing accreted ice with inflatable boots in-flight, the latent heat released upon freezing can remelt the ice partially. The flight wind then pushes this semi-liquid water further downstream the airfoil, away from the original point of impact, causing it to freeze upon yet uniced parts, also referred to as runback icing, which lay beyond safety measures installed. In general, the smaller the aircraft the more sensitive it is to the effects of icing (Gent et al. 2000). Gent et al. (2000) further elaborates that during take-off, icing results in an „increased ground roll, decreased stall margins and climb rate“ (Gent et al. 2000, p. 2885) and additionally states that iced wings and tails „can cause serious stability and control“ (Gent et al. 2000, p. 2885) issues, which can lead to the loss of control over the aircraft. While in cruise, icing reduces the maximum speed as well as the ceiling height. Due to the additional mass and adverse effect on aerodynamic properties, an iced aircraft experiences higher fuel consumptions. This can, especially for smaller aircrafts, cause the loss of maintaining level flight. The approach or landing of an iced aircraft can result in „uncommanded ‘pitch-overs’“ (Gent et al. 2000, p. 2885) due to stalling tailplanes. Additionally Gent et al. (2000) points out that iced probes and sensors on the aircraft cause problems due to inaccurate data being processed.

2.2 Formation of liquid droplets in the atmosphere

As supercooled liquid water is the main driver for aircraft icing, the following part introduces how droplets are formed in the atmosphere.

The amount of water vapour the atmosphere can hold is given by the saturation vapour pressure of water e_s. The Clausius-Clapeyron equation describes the dependency of e_s on temperature T,

$$\frac{\mathrm{d}e_\mathrm{s}}{\mathrm{d}T} = \frac{1}{T}\frac{l_\mathrm{v}}{\alpha_\mathrm{v} - \alpha_\mathrm{l}}. \tag{2.1}$$

Here l_v is the latent heat of vapourization in $\mathrm{J\,kg^{-1}}$ and α_vll is the specific volume of water vapour and liquid water, respectively, in $\mathrm{m^3\,kg^{-1}}$ (Seinfeld and Pandis 2016). Equation 2.1 is applicable for the saturation vapour pressure above a flat surface. However, droplets offer a curved interface only. The curvature affects the saturation vapour pressure due to the Gibbs free energy that is associated with the forming of a curved interface (Seinfeld and Pandis 2016). The Gibbs free energy G is a highly useful thermodynamic variable for atmospheric applications and is defined as

$$G = U + pV - TS, \tag{2.2}$$

with the internal energy U in J, describing the energy of atoms and molecules in a system (e.g. an air parcel), the pressure p in Pa, volume V in $\mathrm{m^3}$, temperature T in K and entropy S in $\mathrm{J\,K^{-1}}$. Seinfeld and Pandis (2016) states, referring to Denbigh and Denbigh (1981) that a system's Gibbs free energy tends to decrease,

$$\mathrm{d}G \leq 0, \tag{2.3}$$

which basically stems from the second law of thermodynamics,

$$\mathrm{d}S \geq 0, \tag{2.4}$$

applied to a system at constant pressure and temperature. So, for a droplet to form the Gibbs free energy of the droplet (G_droplet) has to be lower than the Gibbs free energy of the supersaturated pure water vapour (G_vapour). Further following Seinfeld and Pandis (2016), the change in Gibbs free energy

$$\Delta G = G_\mathrm{droplet} - G_\mathrm{vapour}, \tag{2.5}$$

can be evaluated using the Gibbs free energies for a single molecule in the vapour, g_v, and the liquid, g_l, phase, as well as the number of molecules that change phase n and the free energy for forming a curved interface:

$$\Delta G = n\,(g_\mathrm{l} - g_\mathrm{v}) + 4\pi R_\mathrm{p}^2 \sigma. \tag{2.6}$$

R_p in m and σ in $\mathrm{N\,m^{-1}}$ in equation 2.6 are the curvature's radius and the surface tension, respectively. The latter describes the energy required to increase the surface area by 1 unit (Seinfeld and Pandis 2016). R_p can be used in conjunction with the „volume occupied by a molecule in the liquid phase“ (Seinfeld and Pandis 2016, p. 420), v_l in $\mathrm{m^3}$, to calculate n with

$$n = \frac{4\pi R_\mathrm{p}^3}{3 v_\mathrm{l}}. \tag{2.7}$$

Seinfeld and Pandis (2016) also states that at constant temperature and due to no changes in overall water molecule count, $\mathrm{d}g = v\mathrm{d}p$ and therefore

$$g_\mathrm{l} - g_\mathrm{v} = (v_\mathrm{l} - v_\mathrm{v})\,\mathrm{d}p. \tag{2.8}$$

As a water vapour molecule occupies significantly more volume than a liquid water molecule considering the conditions of interest, $v_\mathrm{l} - v_\mathrm{v} \approx -v_\mathrm{v}$. Assuming the vapour phase as an ideal gas, this leads to

$$g_\mathrm{l} - g_\mathrm{v} = -kT \int_{e_\mathrm{s,0}}^{e_\mathrm{s}} \frac{\mathrm{d}p}{p} = -kT \ln \frac{e_\mathrm{s}}{e_\mathrm{s,0}} = -kT \ln S, \tag{2.9}$$

with the Boltzmann constant $k = 1.381 \times 10^{-23}\,\mathrm{J\,K^{-1}}$, the water vapour pressure over a flat surface, $e_{\mathrm{s,0}}$, the actual partial pressure over the liquid, e_{s}, both in Pa and the saturation ratio S ($= \frac{e_{\mathrm{s}}}{e_{\mathrm{s,0}}}$) (Seinfeld and Pandis 2016). Substituting equations 2.9 and 2.7 into equation 2.6 yields

$$\Delta G = -\frac{4}{3}\pi R_{\mathrm{p}}^{3}\frac{kT}{v_{\mathrm{l}}}\ln S + 4\pi R_{\mathrm{p}}^{2}\sigma. \tag{2.10}$$

Equation 2.10 shows that for $S < 1$ both terms are positive and the change in the Gibbs free energy increases monotonically with R_{p}. However, if supersaturation is considered ($S > 1$), the first term is negative while the second remains positive. Since the first term scales with the cube of R_{p}, while the second one only with its square, the second term dominates for small values of R_{p} yielding positive changes in Gibbs free energy, and the first one for larger values of R_{p}, ultimately yielding negative changes. To determine a critical radius R_{p}^{*} at which the maximum value for ΔG is reached, $\frac{\partial \Delta G}{\partial R_{\mathrm{p}}} = 0$ needs to be solved for the particle radius (Seinfeld and Pandis 2016):

$$R_{\mathrm{p}}^{*} = \frac{2\sigma v_{\mathrm{l}}}{kT\ln S}. \tag{2.11}$$

This equation 2.11 creates are relationship between the critical radius of the droplet to the saturation ratio S. Rearranging and applying the definition of S, the so called Kelvin equation is achieved:

$$e_{\mathrm{s}} = e_{\mathrm{s,0}}\exp\left(\frac{2\sigma v_{\mathrm{l}}}{kTR_{\mathrm{p}}}\right). \tag{2.12}$$

„The Kelvin equation tells us that the vapo[u]r pressure over a curved interface always exceeds that of the same substance over a flat surface.“ (Seinfeld and Pandis 2016, p. 421)

The previous part only considers a pure substance (namely, water). However, pure water droplets virtually do not occur in the atmosphere. There are always some soluble compounds dissolved in the droplets, e.g. sea-salt. The following part introduces the effect those compounds have on the vapour pressure based on a flat water solution. To achieve water equilibrium between the gas and liquid phases the corresponding water chemical potentials need to be equal in both phases (Seinfeld and Pandis 2016):

$$\mu_{\mathrm{w,g}} = \mu_{\mathrm{w,aq}}. \tag{2.13}$$

Seinfeld and Pandis (2016) further derive this to calculate the partial pressure for water vapour over the solution, $e_{\mathrm{s,sol}}$ in Pa, via

$$e_{\mathrm{s,sol}} = \gamma_{\mathrm{w}} x_{\mathrm{w}} e_{\mathrm{s,0}}. \tag{2.14}$$

with γ_{w} the water activity coefficient and x_{w} the water's mole fraction in the solution (Seinfeld and Pandis 2016). This equation 2.14 allows accounting for nonideality by γ_{w}. However, as atmospheric water solutions are highly dilute, the water activity coefficient approaches 1. Applying this to equation 2.14 turns it into Raoult's law:

$$e_{\mathrm{s,sol}} = x_{\mathrm{w}} e_{\mathrm{s,0}}. \tag{2.15}$$

Since $x_{\mathrm{w}} < 1$, the water vapour pressure over the solution is always lower than the water vapour pressure over pure water (Seinfeld and Pandis 2016).

As stated earlier, the Kelvin equation 2.12 shows that the water vapour pressure over a curved surface is increased compared to a flat surface. Raoult's law, on the other hand, describes a reduction in water vapour pressure over a solution compared to pure water. To see, how these two effects interact with one another, as liquid water in the atmosphere comes in the form of aqueous solution droplets, the Kelvin equation 2.12 is applied to a solution:

$$\frac{e_{\mathrm{s}}\left(D_{\mathrm{p}}\right)}{e_{\mathrm{s,sol}}} = \exp\left(\frac{4\bar{v}_{\mathrm{w}}\sigma_{\mathrm{w}}}{RTD_{\mathrm{p}}}\right). \tag{2.16}$$

In equation 2.16 the droplet's radius is replaced with its diameter D_{p} in m. Furthermore the argument of the exponential function is now presented in its mole based form, while equation 2.12 is molecule based. This requires the usage of the universal gas constant $R = kN_{\mathrm{A}} = 8.314\,\mathrm{J\,mol^{-1}\,K^{-1}}$ and the partial molar volume for water in the solution $\bar{v}_{\mathrm{w}}$ in $\mathrm{m^3\,mol^{-1}}$. This and the partial molar volume for the soluble substance in the solution, $\bar{v}_{\mathrm{s}}$ in $\mathrm{m^3\,mol^{-1}}$, satisfy

$$\frac{\pi}{6}D_{\mathrm{p}}^3 = n_{\mathrm{w}}\bar{v}_{\mathrm{w}} + n_{\mathrm{s}}\bar{v}_{\mathrm{s}}, \tag{2.17}$$

with the amount of water and soluble material n_{w} and n_{s} both in mol. Substituting equation 2.15 into 2.16 yields

$$\frac{e_{\mathrm{s}}\left(D_{\mathrm{p}}\right)}{x_{\mathrm{w}}e_{\mathrm{s,0}}} = \exp\left(\frac{4\bar{v}_{\mathrm{w}}\sigma_{\mathrm{w}}}{RTD_{\mathrm{p}}}\right). \tag{2.18}$$

The water's mole fraction x_{w} can be substituted by using equation 2.17 and approximated by assuming a dilute solution:

$$\frac{1}{x_{\mathrm{w}}} = 1 + \frac{n_{\mathrm{s}}}{n_{\mathrm{w}}} = 1 + \frac{n_{\mathrm{s}}\bar{v}_{\mathrm{w}}}{\frac{\pi}{6}D_{\mathrm{p}}^3 - n_{\mathrm{s}}\bar{v}_{\mathrm{s}}} \approx 1 + \frac{n_{\mathrm{s}}\bar{v}_{\mathrm{w}}}{\frac{\pi}{6}D_{\mathrm{p}}^3}. \tag{2.19}$$

With equation 2.19 equation 2.18 can be evaluated to

$$\ln\left(\frac{e_{\mathrm{s}}\left(D_{\mathrm{p}}\right)}{e_{\mathrm{s,0}}}\right) = \frac{4\bar{v}_{\mathrm{w}}\sigma_{\mathrm{w}}}{RTD_{\mathrm{p}}} - \ln\left(1 + \frac{6n_{\mathrm{s}}\bar{v}_{\mathrm{w}}}{\pi D_{\mathrm{p}}^3}\right). \tag{2.20}$$

As $\frac{6n_{\mathrm{s}}\bar{v}_{\mathrm{w}}}{\pi D_{\mathrm{p}}^3} \to 0$ for dilute solutions, $\ln(1+x) \approx x$ for $x \to 0$ can be used to further simplify equation 2.20, yielding

$$\ln\left(\frac{e_{\mathrm{s}}\left(D_{\mathrm{p}}\right)}{e_{\mathrm{s,0}}}\right) = \frac{4\bar{v}_{\mathrm{w}}\sigma_{\mathrm{w}}}{RTD_{\mathrm{p}}} - \frac{6n_{\mathrm{s}}\bar{v}_{\mathrm{w}}}{\pi D_{\mathrm{p}}^3}. \tag{2.21}$$

Defining two constants $A = \frac{4\bar{v}_{\mathrm{w}}\sigma_{\mathrm{w}}}{RT}$ and $B = \frac{6n_{\mathrm{s}}\bar{v}_{\mathrm{w}}}{\pi}$ equation 2.21 can be written as

$$\ln\left(\frac{e_{\mathrm{s}}\left(D_{\mathrm{p}}\right)}{e_{\mathrm{s,0}}}\right) = \frac{A}{D_{\mathrm{p}}} - \frac{B}{D_{\mathrm{p}}^3}. \tag{2.22}$$

This is one form of the Köhler equation, which combines the effects in play over an aqueous solution droplet: the Kelvin effect ($\frac{A}{D_{\mathrm{p}}}$) increasing the vapour pressure and the solute effect ($-\frac{B}{D_{\mathrm{p}}^3}$) decreasing the vapour pressure. Due to the differing powers for the droplet's diameters used, the Kelvin effect tends to dominate for larger droplets, while smaller droplets favour the solute effect (Seinfeld and Pandis 2016).

One can define a critical droplet diameter $D_{\mathrm{p,c}}$ at which the saturation relative to a flat surface of pure water reaches its maximum value,

$$D_{\mathrm{p,c}} = \sqrt{\frac{3B}{A}}. \tag{2.23}$$

The corresponding critical saturation $S_{\mathrm{c}} = \frac{e_{\mathrm{s}}\left(D_{\mathrm{p,c}}\right)}{e_{\mathrm{s,0}}}$ then evaluates to (Seinfeld and Pandis 2016)

$$\ln S_{\mathrm{c}} = \sqrt{\frac{4A^3}{27B}}. \tag{2.24}$$

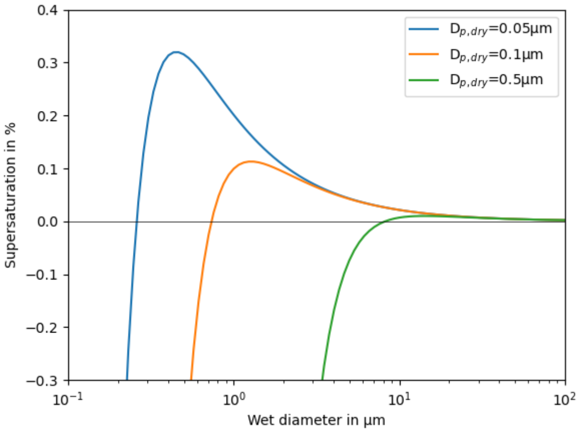

Figure 2.2: Koehler curves for the dependency of the supersaturation on the droplet diameter for NaCl solution droplets with dry diameters 0.05,0.1 and 0.5 µm at 293 K. Dry NaCl particles are assumed to be spherical (Seinfeld and Pandis 2016).

Figure 2.2 shows a size-saturation plot of the Koehler equation. As one can see, there are saturation values that correspond to two particle sizes. The one left of $D_{\mathrm{p,c}}$ is in a stable equilibrium: If the droplet gains or loses water by small perturbations, the vapour pressure increases or decreases slightly. Since the ambient vapour pressure stays constant, the droplet then loses or gains water again, respectively, returning to its original state. The particle sizes on the right of $D_{\mathrm{p,c}}$, however, are in an unstable equilibrium: Small gains and loses result in decreased and increased vapour pressures, leading to further gains and loses, respectively. A growing droplet then grows until the supersaturation is consumed and a diminishing droplets shrinks until the stable equilibrium value is reached. So a particle can only reach a stable equilibrium at the state that corresponds to the smaller diameter (Seinfeld and Pandis 2016).

Since the critical saturation S_{c} describes the maximum vapour pressure the droplet can exert, an environment with a saturation exceeding S_{c} causes any droplet to grow indefinitely. At this point the particle is activated and is considered a cloud droplet (Seinfeld and Pandis 2016). In the scope of the present work, the model simulations parameterize this process as presented by Fountoukis and Nenes (2005). Chapter 3.2 introduces the details of this parameterization.

This process can also occur in subfreezing conditions or alternatively the activated cloud droplets become supercooled while growing to significant sizes. In the early stages of this droplet growth, this happens by condensation of additional water molecules onto the droplet. Seinfeld and Pandis (2016) introduce the corresponding mass transfer equation as

$$\frac{\mathrm{d}m_{\mathrm{d}}}{\mathrm{d}t} = 2\pi D_{\mathrm{p}} D_v' \left(c_{\mathrm{w},\infty} - c_{\mathrm{w}}^{\mathrm{eq}}\right). \tag{2.25}$$

In equation 2.25 m_{d} is the droplet mass in kg and D_v' the water vapour diffusivity in $\mathrm{m^2\,s^{-1}}$, corrected for noncontinuum effects. Once the droplet diameter significantly exceeds 1 µm these effects diminish and D_v can be used instead. $c_{\mathrm{w},\infty}$ is the ambient concentration of water vapour, while $c_{\mathrm{w}}^{\mathrm{eq}}$ is the droplet's equilibrium water vapour concentration in $\mathrm{kg\,m^{-3}}$ (Seinfeld and Pandis 2016). With

$$\frac{\mathrm{d}m_{\mathrm{d}}}{\mathrm{d}t} = \frac{1}{2}\pi \rho_{\mathrm{w}} D_{\mathrm{p}}^2 \frac{\mathrm{d}D_{\mathrm{p}}}{\mathrm{d}t}, \tag{2.26}$$

using ρ_{w} as the water density in $\mathrm{kg\,m^{-3}}$, and applying the ideal gas law for the partial water pressure

$$e_{\mathrm{s}} = \frac{n_{\mathrm{w}}}{V_{\mathrm{air}}} RT = \frac{m_{\mathrm{w}}}{M_{\mathrm{w}} V_{\mathrm{air}}} RT = \frac{c_{\mathrm{w}}}{M_{\mathrm{w}}} RT \tag{2.27}$$

to equation 2.25 gives an equation for the growth of the droplet's diameter as

$$D_\mathrm{p}\frac{\mathrm{d}D_\mathrm{p}}{\mathrm{d}t} = \frac{4D_v' M_\mathrm{w}}{\rho_\mathrm{w} RT}\left(e_{\mathrm{s},\infty} - e_\mathrm{s}\left(D_\mathrm{p}\right)\right). \tag{2.28}$$

In these equations n_w represents the amount of water in mol, V_air the considered air volume in m^3, M_w is the molar mass of water in $\mathrm{kg\,mol^{-1}}$, $e_{\mathrm{s},\infty}$ describes the ambient partial water pressure, while $e_\mathrm{s}\left(D_\mathrm{p}\right)$ is the partial water pressure around a cloud droplet with a diameter of D_p. The partial water pressure is given in Pa (Seinfeld and Pandis 2016).

Equation 2.28 shows that the droplet growth depends on the size of the droplet itself. Small droplets experience a quick build-up in diameter. The larger the droplet becomes, the slower it grows. This effectively limits the size to which droplets can grow by condensation alone. For droplets to grow to precipitable sizes, they need to coalesce by colliding with one another (collision-coalescence process). This happens due to updrafts or settling, as drops of differing sizes have different corresponding velocities, enabling collisions to occur (Seinfeld and Pandis 2016). Seinfeld and Pandis (2016) describes the growth rate of a large drop falling by accretion of smaller drops, as those fall slower, with

$$\frac{\mathrm{d}m}{\mathrm{d}t} = \frac{\pi}{4}E_\mathrm{coll}E_\mathrm{coal}\left(D_\mathrm{p}+d_\mathrm{p}\right)^2 w_\mathrm{L}\left(v_\mathrm{D}-v_\mathrm{d}\right). \tag{2.29}$$

In equation 2.30 m is the mass of the large drop in kg, E_coll and E_coal are the collision and coalescence efficiency, which are separated as colliding drops can bounce off instead of coalescing, D_p and d_p are the diameters of the large and the smaller drop in m, w_L is the small drops' liquid water content and v_D and v_d denote their respective fall speeds (Seinfeld and Pandis 2016). The idea behind E_coll is that the large drop collides with smaller drops below it, if they are in the confines of a cylinder of diameter y (in m). Drops outside of it are diverted around the large drop. With y given for smaller drops of a diameter d_p, E_coll is defined as (Seinfeld and Pandis 2016)

$$E_\mathrm{coll} = \frac{y^2}{\left(D_\mathrm{p}+d_\mathrm{p}\right)^2}. \tag{2.30}$$

Gent et al. (2000) state that the atmosphere enables supercooling down to about $-20\,^\circ\mathrm{C}$ frequently, which is a significantly higher temperature than the required temperature for liquid water droplets to freeze due to the required size of an ice crystal embryo, for it develop stably. This is due to the involvement of ice nucleating particles (INP), as these help aligning the water molecules in an ice-like structure and reduce the require amount of water molecules to reach the critical embryo size, ultimately enabling ice nucleation at higher temperatures than for the homogeneous process (Lohmann et al. 2016).

So, for aircraft icing to occur, cloud droplets need to form in the atmosphere, for which CCN are required, grow to significant size (as the following section will highlight) and be in a supercooled state, which requires the absence of INPs that would glaciate the supercooled cloud.

2.3 Water's efficiency in impinging aircrafts

One major aspect of the newly developed parameterization is the impingement of supercooled liquid water.

The knowledge of the impinging amount of liquid water onto an object is required for different meteorological studies, mainly to determine the accretion of ice the object experiences (McComber and Touzot 1981). This can be used not only to aid in deciding where to install protective systems (Papadakis et al. 1991) for icing or warn for icing environments, but also to measure the supercooled liquid water content by its freezing upon a cylinder (McComber and Touzot 1981). The impingement determination is the first stage for analysing icing events and generally consists of both the location of the impact and the rate with which the cloud droplets deposit on the object (Gent et al. 2000). The relevant quantity is called impingement efficiency, however, it is also referred to as „water-

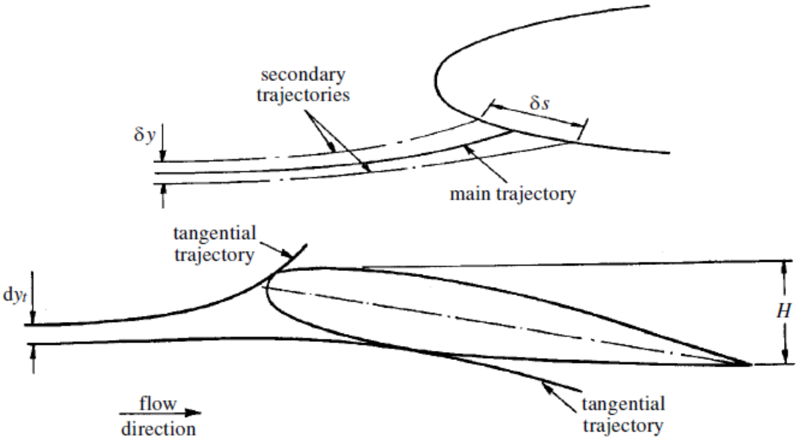

Figure 2.3: Illustration of the local impingement efficiency (top) and the overall impingement efficiency (bottom) (Source: (Gent et al. 2000)).

collection or catch-efficiency distribution“ (Gent et al. 2000, p. 2885-2886) or „collection efficiency“ (McComber and Touzot 1981, p. 1032). It describes the proportion of the liquid water content (LWC) that impinges onto a given surface location (local impingement efficiency) or onto the entire object (overall impingement efficiency) (Gent et al. 2000). The difference between these two forms of impingement efficiency is illustrated in figure 2.3. The former is crucial for modelling the shape in which ice will accrete on the investigated object. With it Papadakis et al. (2004) show that ice accretion on a NACA 23012 airfoil develops a double horn structure. Cao et al. (2016) require the local impingement efficiency to investigate the effects meteorological quantities have on both the amount and the shape of ice accretion. Knowing the shape of the accreted ice aids in better understanding the hazards posed to an aircraft by the icing process, especially regarding its aerodynamic properties and flight capabilities (Dai et al. 2021; Cao et al. 2018).

While the local impingement efficiency is needed in the more engineering and design aspects of aircraft icing, the overall impingement efficiency is more suited for application in icing prediction schemes. Consequently, this is the relevant quantity for the present work as well. Although operational icing prediction schemes do not actively rely on the impingement efficiency, there are ice accretion algorithms, mostly in use for analytical purposes that do. However, the calculation of the impingement efficiency is based on empirical formulars applying the Reynolds number and an inertia parameter. With this, they show a dependency on the mean droplet size in a simplified way. Chapter 4 introduces such ice accretion algorithms. In contrast, the new aircraft icing parameterization that is developed in the scope of the present work (detailed in chapter 3.3), determines the overall impingement efficiency by analysing trajectories of droplets respecting their size.

Multiplying the impingement efficiency with the LWC and the ambient wind velocity gives the mass flux of water onto the object's surface (McComber and Touzot 1981).

The reason not every water droplet impacts with an object that intercepts its pathway is that the object itself disturbs the airflow to pass around it. The reason not all water droplets miss the object is their inertia. According to Gent et al. (2000), the inertia is proportional to the droplet's mass, which is proportional to its diameter cubed. The airflow's influence on the droplet, however, is proportional to its diameter squared. Consequently, larger droplets tend to stay in their original, undisturbed trajectory, rather than being affected by the disturbance the object poses, and are therefore likely to impact. Smaller droplets, on the other hand, are more susceptible to being deflected by the disturbed windfield around the object. Hence, the ratio of the droplet's inertia and the aerodynamic forces acting on it determines whether it impinges or not (Gent et al. 2000).

To determine the impingement efficiency of an amount of droplets with a certain diameter their trajectories need to be calculated. There are in general two types of such calculations, a Lagrangian formulation and an Eulerian one. The former tracks the trajectory of individual droplets from a starting position in the undisturbed wind field upstream the object. Gent et al. (2000) state that „five to seven chord lengths ahead of the body" (Gent et al. 2000, p. 2886) is generally sufficient. The Eulerian approach computes the water's volume fraction at every resolved position and is therefore a direct measure of the impingement efficiency (Gent et al. 2000). The present work uses the Lagrangian approach whose governing equations are derived in the following.

This derivation in large parts follows the work of Gent et al. (2000), who focus exemplatory on the x-direction and state important assumptions: The droplets are considered spherical, do not deform and do not collide or coalesce with other droplets. The droplets' effect on the aerodynamic flow is negligible for the concentration of water droplets is sufficiently small, which allows an independent treatment of droplets and airflow. Furthermore, droplets only experience aerodynamic drag, gravity and buoyancy. Other forces are neglected, like turbulent effects. The negligence of turbulence is due to the fact that this only plays a significant role for the smallest of droplets that could be diverted towards and onto the object's surface by it. However, as these droplets also carry only little mass, the overall impact on the impingement efficiency is expected to be negligible.

The coordinate system used is such that the chord of the object is aligned with the x-axis. The x- and z-axis span the plane on which the object lies. However, the z-axis is not further considered. The y-axis is therefore aligned with the height of the object. Since the object's chord need not be horizontal, the angle between it and the horizon is required and denoted with α. Applying this and the assumptions stated earlier, the aerodynamic force acting on a single droplet is (Gent et al. 2000)

$$F_\mathrm{a} = \frac{1}{2} C_\mathrm{D} \rho_\mathrm{a} A_\mathrm{d} V_\mathrm{res}^2, \tag{2.31}$$

with C_D the droplet's drag coefficient, ρ_a the air density in $\mathrm{kg\,m^{-3}}$ and A_d the droplet's frontal area in m^2. V_res is the resultant of the relative velocity between droplet and the wind field:

$$V_\mathrm{res}^2 = u_\mathrm{rel}^2 + v_\mathrm{rel}^2 = (u_\mathrm{a} - u_\mathrm{d})^2 + (v_\mathrm{a} - v_\mathrm{d})^2. \tag{2.32}$$

In equation 2.32 and henceforth u denotes the velocity component in x-direction and v its y-component. The subscripts „a" , „d" and „rel" for the velocity components stand for air, droplet and the relative value between air and droplet, respectively. Focusing on the x-component of the aerodynamic force yields

$$F_\mathrm{a,x} = \frac{1}{2} C_\mathrm{D} \rho_\mathrm{a} A_\mathrm{d} V_\mathrm{res} u_\mathrm{rel}. \tag{2.33}$$

Additionally, the x-component of the gravitational force acting on the droplets is

$$F_\mathrm{g,x} = m_\mathrm{d} g \left(1 - \frac{\rho_\mathrm{a}}{\rho_\mathrm{d}}\right) \sin\alpha, \tag{2.34}$$

with the droplet mass m_d in kg and the gravitational constant $g = 9.81\,\mathrm{m\,s^{-2}}$. With the acting forces described the acceleration in x-direction can be derived with

$$\frac{\mathrm{d}u_\mathrm{d}}{\mathrm{d}t} = \frac{F_\mathrm{a,x} + F_\mathrm{g,x}}{m_\mathrm{d}}. \tag{2.35}$$

Substituting equations 2.33 and 2.34 into 2.35 and applying $m_\mathrm{d} = \frac{\pi}{6} D^3 \rho_\mathrm{d}$ as well as $A_\mathrm{d} = \frac{\pi}{4} D^2$ yields

$$\frac{\mathrm{d}u_\mathrm{d}}{\mathrm{d}t} = \frac{18 C_\mathrm{D} \rho_\mathrm{a} V_\mathrm{res} u_\mathrm{rel}}{24 \rho_\mathrm{d} D} + \left(1 - \frac{\rho_\mathrm{a}}{\rho_\mathrm{d}}\right) g \sin\alpha. \tag{2.36}$$

Using the droplet's Reynolds number

$$R = \frac{\rho_\mathrm{a} V_\mathrm{res} D}{\mu} \tag{2.37}$$

equation 2.36 can be further simplified to

$$\frac{\mathrm{d}u_\mathrm{d}}{\mathrm{d}t} = \frac{18 C_\mathrm{D} R \mu u_\mathrm{rel}}{24 \rho_\mathrm{d} D^2} + \left(1 - \frac{\rho_\mathrm{a}}{\rho_\mathrm{d}}\right) g \sin\alpha. \tag{2.38}$$

This uses the atmosphere's dynamic viscosity μ in $\mathrm{kg\,m^{-1}\,s^{-1}}$. Introducing a modified inertia parameter

$$K = \frac{\rho_\mathrm{d} D^2}{18\mu} \tag{2.39}$$

results in

$$\frac{\mathrm{d}u_\mathrm{d}}{\mathrm{d}t} = \frac{C_\mathrm{D} R u_\mathrm{rel}}{24K} + \left(1 - \frac{\rho_\mathrm{a}}{\rho_\mathrm{d}}\right) g \sin\alpha. \tag{2.40}$$

The acceleration in y-direction can be determined likewise resulting in

$$\frac{\mathrm{d}v_\mathrm{d}}{\mathrm{d}t} = \frac{C_\mathrm{D} R v_\mathrm{rel}}{24K} - \left(1 - \frac{\rho_\mathrm{a}}{\rho_\mathrm{d}}\right) g \cos\alpha. \tag{2.41}$$

This set of equations can be solved numerically. The initial droplet velocity at the starting point of the trajectory, which is several chord lengths ahead, is assumed to be same as the aerodynamic flow (Gent et al. 2000). Depending on the size of the droplet and the starting y-value (relative to the object) it can therefore be determined, whether the droplet impinges. Hence, for a given droplet size there is an initial Δy, in which the droplets impinge. The overall impingement efficiency E is defined as the ratio between this initial Δy and the y-extent of the object H (Gent et al. 2000), see also figure 2.3:

$$E = \frac{\Delta y}{H}. \tag{2.42}$$

In order to solve the equation set 2.40 and 2.41, the velocity field around the object must be known, so the wind velocity can be calculated at every location the droplet trajectory passes through. The structure of the velocity field depends on the object disturbing the ambient airflow, while the ambient airflow mostly determines the amplitude of the disturbed velocity field. For most objects such a velocity field needs to be derived numerically, however, there are a few for which an analytical solution exists, e.g. a cylinder.

The drag coefficient C_D depends on the Reynolds number in a complex manner. For $0.2 < R < 2.0$ McComber and Touzot (1981) (referring to Beard and Pruppacher 1969) state

$$\frac{C_\mathrm{D} R}{24} = 1 + 0.102 \cdot R^{0.955}, \tag{2.43}$$

for $2 < R < 21$

$$\frac{C_\mathrm{D} R}{24} = 1 + 0.115 \cdot R^{0.802} \tag{2.44}$$

and for $21 < R < 200$

$$\frac{C_\mathrm{D} R}{24} = 1 + 0.189 \cdot R^{0.632}. \tag{2.45}$$

Gent et al. (2000) as well as McComber and Touzot (1981) also provide a value for $200 < R < 3500$ (referring to Goldstein 1965)

$$\frac{C_\mathrm{D} R}{24} = 1 + 0.197 \cdot R^{0.63} + 2.6 \times 10^{-4} \cdot R^{1.38}. \tag{2.46}$$

For Reynolds numbers larger than 3500 Gent et al. (2000) refers to Hansman (1984)

$$\frac{C_\mathrm{D} R}{24} = 1.699 \times 10^{-5} \cdot R^{1.92}. \tag{2.47}$$

This applies especially to supercooled large drops (SLD).

2.4 Freezing behaviour of impinged water

Supercooled liquid water impinging onto an object starts to freeze for the object providing a suitable surface for ice formation. Messinger (1953) describes an approach to the prediction of ice-accretion by assuming that the process is governed by balancing of a number of heat flows (Gent et al. 2000). The process of ice and water accretion loses heat to the air, while the actual freezing produces latent heat (Myers 2001). However, Messinger (1953) also considers mechanisms that influence this heat balance: Heat is lost due to „convective heat transfer at the water surface, Q_c“ (Myers 2001, p. 212), evaporation, Q_e and cooling by the impinging droplets, Q_d (Myers 2001). The system also gains heat by the impinging droplets' kinetic energy, Q_k, the latent heat release upon freezing Q_l and aerodynamic heating Q_a (Myers 2001). Respecting these terms for heat loss and gain, the balance takes the following form, with all Q-terms in $\mathrm{W\,m^{-2}}$:

$$Q_\mathrm{c}+Q_\mathrm{e}+Q_\mathrm{d}=Q_\mathrm{k}+Q_\mathrm{l}+Q_\mathrm{a}. \tag{2.48}$$

Equation 2.48 is used by Messinger (1953) to calculate a freezing fraction F. F describes the mass fraction of water turning into ice upon impinging the object's surface (Myers 2001). This leads to the development of an ice and water layer. Liquid water is furthermore assumed to flow downstream (hence termed runback water), potentially freezing upon other parts of the object.

The Messinger model forms the base for every freezing model in use, however, in its original stage it has some limitations and draw-backs: Although it differentiates between rime and glaze icing, which is based upon the freezing fraction, the transition switches the value of the freezing fraction instantaneously from a value of 1 (rime icing) to a value below 1 for glaze icing, retaining this value for the remainder of the freezing procedure (Myers 2001). Furthermore the ice and water layers are considered isothermal in the Messinger model, hence neglecting heat conduction through these layers. This is a valid assumption for the water layer, assuming the water being well mixed. However, this no longer holds in the ice layer (Myers 2001). Both limitations cause the Messinger model to generally underestimate the ice accretion. Myers (2001) shows that especially the conduction aspect is crucial in the ice accretion process. He solves the heat equations in both layers to improve heat transfer estimations. It also allows the determination of an ice thickness at which the rime icing transitions to glaze icing, which is further developed on by Zhang et al. (2016).

The base to determine the temperature profiles in the ice and water layer is a Stefan problem („standard method of specifying a phase change“ (Myers 2001, p. 213)). For this, Myers (2001) declares the thickness of the ice layer upon the object as $B(t)$. When rime ice is accreted, there is no accretion of liquid water yet, hence why it is also referred to as dry icing. During wet icing glaze ice and liquid water accrete and the water thickness is denoted with $h(t)$. $T_\mathrm{i}(z,t)$ and $T_\mathrm{w}(z,t)$ stand for the temperature in the ice and water, respectively. Four equations are needed to govern a Stefan problem: „heat equations in the ice and water, a mass balance, and a phase change or Stefan condition at the ice/water interface“ (Myers 2001, p. 213):

$$\frac{\partial T_\mathrm{i}}{\partial t}=\frac{\kappa_\mathrm{i}}{\rho_\mathrm{i}c_\mathrm{i}}\frac{\partial^2 T_\mathrm{i}}{\partial z^2} \tag{2.49}$$

$$\frac{\partial T_\mathrm{w}}{\partial t}=\frac{\kappa_\mathrm{w}}{\rho_\mathrm{w}c_\mathrm{w}}\frac{\partial^2 T_\mathrm{w}}{\partial z^2} \tag{2.50}$$

$$\rho_\mathrm{i}\frac{\partial B}{\partial t}+\rho_\mathrm{w}\frac{\partial h}{\partial t}=EV\cdot\mathrm{LWC} \tag{2.51}$$

$$\rho_\mathrm{i}L_\mathrm{f}\frac{\partial B}{\partial t}=\kappa_\mathrm{i}\frac{\partial T_\mathrm{i}}{\partial z}-\kappa_\mathrm{w}\frac{\partial T_\mathrm{w}}{\partial z}. \tag{2.52}$$

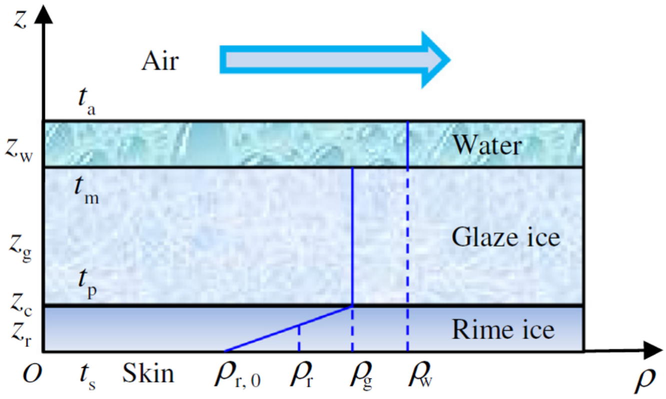

Figure 2.4: Representation of the icing model by Zhang et al. (2016), illustrating the thicknesses of the different accreted substances z_r, z_g and z_w as well as the critical ice thickness z_c. It also highlights the development of the rime ice density, reaching the value of glaze ice once z_c is reached (Source: (Zhang et al. 2016)).

In equations 2.49 to 2.52, $\kappa_{\mathrm{i|w}}$ is the thermal conductivity in $\mathrm{W\,m^{-1}\,K^{-1}}$, $c_{\mathrm{i|w}}$ is the specific heat in $\mathrm{J\,kg^{-1}\,K^{-1}}$ and $\rho_{\mathrm{i|w}}$ is the density in $\mathrm{kg\,m^{-3}}$ for ice and water, respectively. It is further noted that ρ_{i} takes different values for rime and glaze ice. Myers (2001) uses two distinct values and assumes an instantaneous transition between the two. Zhang et al. (2016), however, introduces a time dependency for the density of rime ice, letting it approach the value for glaze ice over time. E is the impingement efficiency, V the freestream velocity in $\mathrm{m\,s^{-1}}$ and LWC is the liquid water content in $\mathrm{kg\,m^{-3}}$. Solving this equation set, especially the heat equations 2.49 and 2.50, requires boundary and initial conditions. Myers (2001) formulates those as: (1) The object has high conductivity and a much greater mass than the ice to accrete, so the temperature of the ice directly at the surface of the object equals the surfaces temperature (T_{s}):

$$T_{\mathrm{i}}(0,t) = T_{\mathrm{s}}. \tag{2.53}$$

(2) At the phase change boundary the temperature is steady and equals the freezing temperature ($T_{\mathrm{f}} = 273.15\,\mathrm{K}$):

$$T_{\mathrm{i}}(B,t) = T_{\mathrm{w}}(B,t) = T_{\mathrm{f}}. \tag{2.54}$$

During rime icing, there is no phase change boundary and therefore this condition is not imposed.
(3) The heat flux at the air/water interface is determined based on the heat balance (equation 2.48) „by convection, heat from incoming droplets, evaporation, aerodynamic heating, and kinetic energy“ (Myers 2001, p.213)

$$-\kappa_{\mathrm{w}} \frac{\partial T_{\mathrm{w}}}{\partial z} = Q_{\mathrm{c}} + Q_{\mathrm{e}} + Q_{\mathrm{d}} - Q_{\mathrm{a}} - Q_{\mathrm{k}}. \tag{2.55}$$

This can also be applied in the dry icing phase. However, some terms need to be adjusted, as it is an air/ice interface, namely the convective heat transfer for a water surface is replaced with its equivalent for an ice surface (Q_{ci}) and the sublimative (Q_{s}) replaces the evaporative heat loss:

$$-\kappa_{\mathrm{i}} \frac{\partial T_{\mathrm{i}}}{\partial z} = Q_{\mathrm{ci}} + Q_{\mathrm{s}} + Q_{\mathrm{d}} - Q_{\mathrm{a}} - Q_{\mathrm{k}}. \tag{2.56}$$

(4) The object is initially clean from ice and water (Myers 2001):

$$B = h = 0 \qquad \text{for} \qquad t = 0. \tag{2.57}$$

Zhang et al. (2016) tackle one of the drawbacks in the model by Myers (2001), the constant properties of rime ice. Contrary to the constant properties for liquid water and glaze ice, Zhang et al. (2016) consider rime ice as a porous medium, whose initial properties depend on airflow parameters and show significant difference to those of glaze ice. The rime ice's physical properties also change with the current ice thickness reaching those of glaze ice at the transition from the dry to the wet icing phase (Zhang et al. 2016), as illustrated in figure 2.4.

Zhang et al. (2016) assume the heat conduction to be quasi-stable and therefore express it regarding the z-dimension, so along the layer thickness, for the different layers:

$$\text{Rime ice:} \qquad \frac{\partial}{\partial z}\left(k_{\mathrm{r}}\frac{\partial T_{\mathrm{r}}}{\partial z}\right)=0, \tag{2.58}$$

$$\text{glaze ice:} \qquad \frac{\partial^2 T_{\mathrm{g}}}{\partial z^2}=0, \tag{2.59}$$

$$\text{water film:} \qquad \frac{\partial^2 T_{\mathrm{w}}}{\partial z^2}=0. \tag{2.60}$$

$T_{\mathrm{r|g}}$ in K is the temperature of rime and glaze ice, respectively, and k_{r} is the thermal conductivity of rime ice in $\mathrm{W\,m^{-1}\,K^{-1}}$. The relevant physical properties of rime ice are its density, its volume fraction and its thermal conductivity. According to Zhang et al. (2016) the rime density (in Pa) at the surface can be empirically determined with

$$\begin{aligned}\rho_{\mathrm{r,0}} &= 1000\exp\left(-0.15\cdot\left(1+\frac{6043}{S^{2.65}}\right)\right)\\ S &= \frac{\mathrm{MVD}^{0.82}V^{0.59}\left(1000\mathrm{LWC}\right)^{0.21}}{\left(10D\right)^{0.48}\left(273.15\,\mathrm{K}-T_{\mathrm{a}}\right)^{0.23}}.\end{aligned} \tag{2.61}$$

MVD is the median volume diameter of the droplet spectrum in µm and D is the object's leading edge diameter in m. As stated above, the rime density is equal to the glaze density at the transition from dry to wet icing. This transitions occurs at a specific value for the ice thickness, called critical ice thickness z_{c}. Assuming a linear variation with the rime ice thickness from $z=0$ to $z=z_{\mathrm{c}}$, the rime density at a specific rime ice thickness can be calculated by

$$\rho_{\mathrm{r}}=\frac{\rho_{\mathrm{g}}-\rho_{\mathrm{r,0}}}{z_{\mathrm{c}}}z+\rho_{\mathrm{r,0}}. \tag{2.62}$$

The volume fraction of rime ice is given by

$$f_{\mathrm{r}}=\frac{\rho_{\mathrm{r}}-\rho_{\mathrm{a}}}{\rho_{\mathrm{g}}-\rho_{\mathrm{a}}} \tag{2.63}$$

and the thermal conductivity by (Zhang et al. 2016)

$$k_{\mathrm{r}}=k_{\mathrm{g}}\frac{k_{\mathrm{g}}+2k_{\mathrm{a}}-2\left(1-f_{\mathrm{r}}\right)\left(k_{\mathrm{g}}-k_{\mathrm{a}}\right)}{k_{\mathrm{g}}+2k_{\mathrm{a}}+\left(1-f_{\mathrm{r}}\right)\left(k_{\mathrm{g}}-k_{\mathrm{a}}\right)}. \tag{2.64}$$

With these physical properties the temperature distributions in the different layers can be derived from equations 2.58 to 2.60, using the introduced boundary conditions (Zhang et al. 2016):

$$T_{\mathrm{r}}=\left(T_{\mathrm{p}}-T_{\mathrm{s}}\right)\frac{\ln\left(\frac{B_{\mathrm{k}}}{k_{\mathrm{r,0}}}z+1\right)}{\ln\left(\frac{B_{\mathrm{k}}}{k_{\mathrm{r,0}}}z_{\mathrm{c}}+1\right)}+T_{\mathrm{s}}, \tag{2.65}$$

$$T_{\mathrm{g}}=\frac{T_{\mathrm{f}}-T_{\mathrm{p}}}{z_{\mathrm{g}}}\left(z-z_{\mathrm{c}}\right)+T_{\mathrm{p}}, \tag{2.66}$$

$$T_{\mathrm{w}}=T_{\mathrm{m}}+\frac{Q_{\mathrm{a}}+Q_{\mathrm{k}}-h_{\mathrm{e}}\left(T_{\mathrm{f}}-T_{\mathrm{a}}\right)}{h_{\mathrm{e}}z_{\mathrm{w}}+k_{\mathrm{w}}}\left(z-z_{\mathrm{i}}\right). \tag{2.67}$$

T_p is the temperature at the rime/glaze-transition in K, $B_\mathrm{k} = \frac{k_\mathrm{g} - k_\mathrm{r,0}}{z_\mathrm{c}}$ is the mean change of the rime's thermal conductivity in $\mathrm{W\,m^{-2}\,K^{-1}}$. h_e is the equivalent heat transfer coefficient in $\mathrm{W\,m^{-2}\,K^{-1}}$. Zhang et al. (2016) define it as

$$h_\mathrm{e} = h_\mathrm{con} + \chi e_0 + \mathrm{LWC} \cdot VEc_\mathrm{w}, \tag{2.68}$$

with the convective heat transfer coefficient, h_con, in $\mathrm{W\,m^{-2}\,K^{-1}}$, the evaporation coefficient χ in $\mathrm{m\,s^{-1}}$, the vapour pressure constant, $e_0 = 27.03\,\mathrm{Pa\,K^{-1}}$ and the water's specific heat, c_w in $\mathrm{J\,kg^{-1}\,K^{-1}}$.

This freezing model by Zhang et al. (2016) forms the freezing part of the new aircraft icing parameterization developed in the scope of the present work. Further details on how it is incorporated are provided in chapter 3.3.

2.5 Operational aircraft icing prediction schemes

Since aircraft icing is a serious safety hazard for aviation, weather services around the world offer prediction schemes to operationally forecast icing conditions. Contrary to the new parameterization developed in the scope of the present work, these do not describe the underlying physical processes of impingement and freezing directly and have a limited set of input parameters provided by model simulations. Additionally, proxy information are used to estimate microphysical quantities like the droplet size. This reduced complexity allows their operational use in a post-processing step of the numerical weather forecast. A selection of these prediction schemes is introduced in the following.

The „current icing potential" (CIP) is a result of the United States' Federal Aviation Administration's (FAA) Aviation Weather Research Program (Bernstein et al. 2005). It creates a „three-dimensional diagnosis of the potential for icing and SLD" (Bernstein et al. 2005, p. 970) by combining the output of a numerical model with pilot-reports (PIREP), satellite and radar data and surface and lightning observations (Bernstein et al. 2005). The determination requires a set of six steps: (1) Placing the datasets on a common grid, (2) finding locations of clouds and precipitation with satellite, surface and radar data, (3) applying membership functions to fields of icing-related quantities, (4) determination of the physical icing situation based on a decision tree, (5) calculation of the initial icing and SLD potentials and (6) adjusting the initial values using pilot reports, vertical velocity and supercooled liquid water (SLW) (Bernstein et al. 2005).

PIREPs are only placed onto the grid, if they „occured within the last hour" (Bernstein et al. 2005, p. 973). The cloudiness is determined extending upon the techniques of Lee et al. (1997) and Thompson et al. (1997). Since Bernstein et al. (1997) state that „icing rarely occurs with less than broken cloud cover" (Bernstein et al. 2005, p. 973), a grid box is only considered an icing candidate, if 40 % or more of the corresponding satellite pixels are cloudy. Due to contamination of several fields in the solar terminator, the cloudiness of a grid box cannot be derived from satellite data alone. So, additional factors are considered, like surface observations and modelled temperature values (Bernstein et al. 2005). Additionally, the cloud-top height is determined by comparing the infrared temperature, measured from the satellite, with the modelled temperature profile. Strong inversions close to the cloud-top temperature the satellite measures, may therefore lead to overestimations of the actual cloud-top height. Determination of cloud-base height and precipitation type, if present, takes place by considering observation data (Bernstein et al. 2005). Instead of using thresholds, CIP attempts „to mimic the gradual transition from icing to nonicing environments associated with [certain] field[s]" (Bernstein et al. 2005, p. 974). These fields are the temperature, relative humidity, the cloud-top temperature, vertical velocity, SLW and PIREP. For this fuzzy-logic membership function are used (Bernstein et al. 2005). The temperature field serves mostly as a proxy for indicating the likelihood of SLW. Korolev et al. (2003) came to the understanding that temperatures close to freezing favor SLW, while SLW become rare at temperature values below −25 °C. However, deep convection seems to be an exception, as Cober et al. (2001) states, so an additional fuzzy-logic for temperature is applied when in a convective environment (Bernstein et al. 2005). Several field campaigns' data indicate a temperature range between $-15\,^{\circ}\mathrm{C}$ and $-3\,^{\circ}\mathrm{C}$ having the most occurrances of icing (Sand et al. 1984; Schultz and Politovich 1992; Cober et al. 1995). Bernstein et al. (2005) compare the fuzzy-logic for the temperature field with PIREPs and state that icing occurs most for a forecasted temperature between $-8\,^{\circ}\mathrm{C}$ and $-6\,^{\circ}\mathrm{C}$. However, this temperature range does not always lead to icing conditions. The cloud-top temperature serves a similar purpose as the modelled temperature, estimating the cloud's likelihood to contain liquid water (Bernstein et al. 2005). Rauber et al. (2000) found warm cloud tops implying the cloud to be dominated by liquid water. Cloud tops that are cold enough to nucleate ice particles, can conversely lead to those particles growing and ultimately falling through the cloud, glaciating it in the process (Hill 1980; Politovich and Bernstein 1995). The transition from a liquid to ice dominated state happens gradually with decreasing cloud-top temperature, according to Geresdi et al. (2005). The modelled relative humidity is used in CIP to assess the likelihood of clouds existing between the cloud top and base values observed. Meeting the expectations, icing events were reported most frequently in environments with high relative humidity (Bernstein et al. 2005). Vertical velocity acts as an amplifier or dampener of the initial icing potential (up to 25 %). With a cloud present, upward velocity eases the production of liquid water, while downward motion may indicate its waning (Bernstein et al. 2005). The previous quantities all act as proxy for an estimation of the amount of SLW for CIP, however, also explicitly predicted SLW by the numerical model is taken into account. As CIP is designed to diagnose the presence rather than the actual amount of SLW, the corresponding membership function only gives the values 1, if SLW is predicted, and 0 otherwise. The modelled SLW has shown to work as a good positive indicator for icing, but is „not proven to work well as a negative" (Bernstein et al. 2005, p. 977) one. Therefore this quantity aids only in boosting the initial icing potential (Bernstein et al. 2005). A PIREP's influence decreases with range from a grid point and only extends to 150 km horizontally and 300 m vertically. PIREPs reporting „no icing" are not used (Bernstein et al. 2005).

Physical icing situations taken into account in CIP are single-layer clouds, multiple cloud layers, a cloud-top temperature gradient in a single cell, classical freezing rain and deep convection (Bernstein et al. 2005): A nonprecipitating single-layer cloud poses the simplest icing situation. Here the initial icing potential is determined with the cloud-top temperature information and adjusted using the temperature and relative humidity fields. Precipitation adds some complexity. Liquid precipitation combined with high cloud-top temperatures imply the presence of large droplets due to an active collision-coalescence (Cober et al. 1996; Rauber et al. 2000) and therefore a high icing potential beneath the cloud base reaching up to at least the lowest cloud layer. If snow is precipitating, ice particles are present in the lowest cloud layer, scavenging the SLW, which majorly or even completely glaciates the cloud according to Geresdi et al. (2005), reducing the maximum icing potential (Bernstein et al. 2005). Multiple cloud layers are treated separately, if no precipitation falls from the upper layer. Precipitation reaching the surface lead to adjustments to the lowest cloud layer solely (Bernstein et al. 2005). A gradient in the cloud-top temperature within a single grid box indicates a possible transition to take place. In this case the cloud-top temperature chosen to determine the maximum icing potential depends on the altitude of the grid-box considered (Bernstein et al. 2005). The classical structure for freezing-rain is a layer with subfreezing temperatures above a layer with above-freezing above a layer with again subfreezing temperatures. Snow falls from the upper cold layer through the warm layer, where it melts forming rain, falling further through the cold layer below getting supercooled, forming freezing rain (Bernstein et al. 2005). The upper layer cloud is treated like a single-layer cloud. The warm layer is too warm for icing to occur, resulting in an icing potential of 0. The lower layer cloud beneath the warm layer needs to consider the melting process taken place in the warm layer. Surface observations of liquid precipitation or ice pellets imply a high likelihood that icing (and SLD) are present in the lower cold layer (Bernstein et al. 2005). Regarding the role of deep convection Squires and Knight (1982) already found that strong upward motion leads to the production of large amounts of SLW and also SLD. The CIP accounts for this by applying a special temperature membership function for deep convective situation. The cloud-top temperature loses significance in these situations since the strong lift can lead to SLW productions exceeding depletion commonly expected with colder cloud-tops (Bernstein et al. 2005).

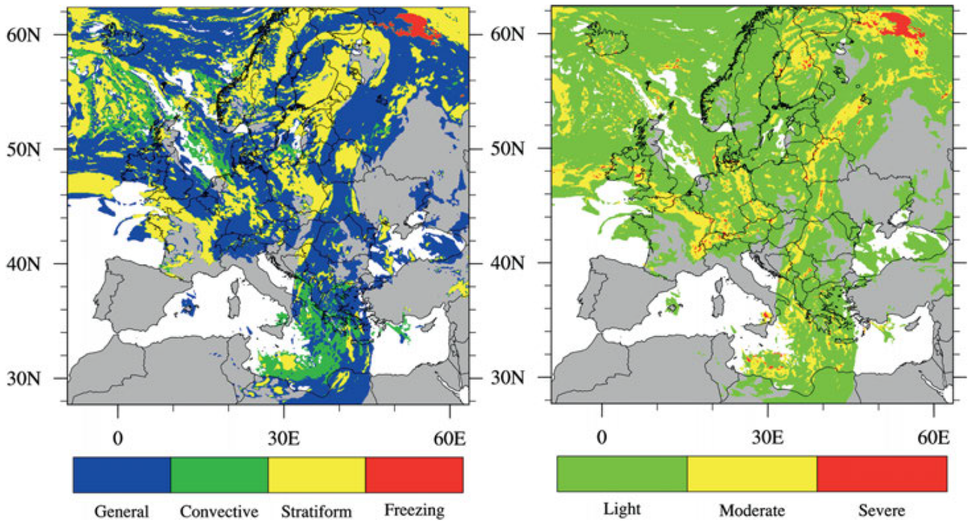

Figure 2.5: ADWICE's PIP output. Horizontal distribution of the icing scenarios identified (left) and of the associated icing intensity levels (right) (Source: (Kalinka et al. 2017)).

With all these information provided the CIP calculates an initial icing potential, which ranges from 0.0 to 1.0, and adjusts it by using recent PIREPs, modeled vertical velocity and SLW forecasts. Those are also these quantities that are commonly used in manual icing forecast to adjust the confidence of icing to be present. While all of these factors can increase the initial icing potential with a recent report of icing (by up to 35 %), a forecast of upward vertical velocity (by up to 25 %) and SLW (by up to 40 %), only the forcast of downward motion decreases it (by up to 25 %) (Bernstein et al. 2005).

Another icing prediction scheme, used for the European airspace, is the Advanced Diagnosis and Warning System for Aircraft Icing Environments (ADWICE), which is operated by the German Weather Service (DWD) (Kalinka et al. 2017). While CIP is purely diagnostic, combining multiple data sources to estimate the presence of icing environments, ADWICE also includes a prognostic part forecasting areas with icing hazards based on numerical weather prediction model data alone (Kalinka et al. 2017). This Prognostic Icing Algorithm (PIA) is an indispensable extension for its operational use at DWD (Leifeld 2004; Kalinka et al. 2017). It outputs a three-dimensional icing product called Prognostic Icing Product (PIP) providing the spatial distribution of four distinct icing scenarios and the expected levels of the associated icing intensity encountered (Kalinka et al. 2017). Figure 2.5 illustrates PIP's output. As Thompson et al. (1997) suggest, the PIP is used as a first guess and improved with additional data in the Diagnostic Icing Algorithm (DIA). The resulting Diagnostic Icing Product (DIP) is the final product of the ADWICE system (Kalinka et al. 2017).

As stated above, ADWICE differentiates between four icing scenarios, namely „Freezing“, „Stratiform“, „Convective“ and „General“ . An assigned scenario gives an idea of the droplet size that is to be expected within the icing area (Kalinka et al. 2017). The PIA identifies the assignment of each grid cell to one of these scenarios, which the DIA in a subsequent step then confirms, extends or rejects. To determine the expected icing severity, membership functions for selected meteorological quantities provided by or derived from the numerical forecast model are applied, whose weights depend on the assigned icing scenario for each grid cell (Kalinka et al. 2017).

The identification of the icing scenarios by the PIA is based on the forecasted profiles of temperature and specific humidity. Examples are displayed in figure 2.6. The threshold values originate from the development of the Integrated Icing Diagnostic Algorithm (IIDA) by McDonough and Bernstein (1999) that Leifeld (2004) adapted for Europe. Supercooled drizzle and rain is expected in the „Freezing“-scenario. These pose a major hazard amongst icing conditions and generate solely „by a subfreezing air mass below a melting layer“ (Kalinka et al. 2017, p. 444). The assumption is that solid precipitation falls through the melting layer. If this layer has a

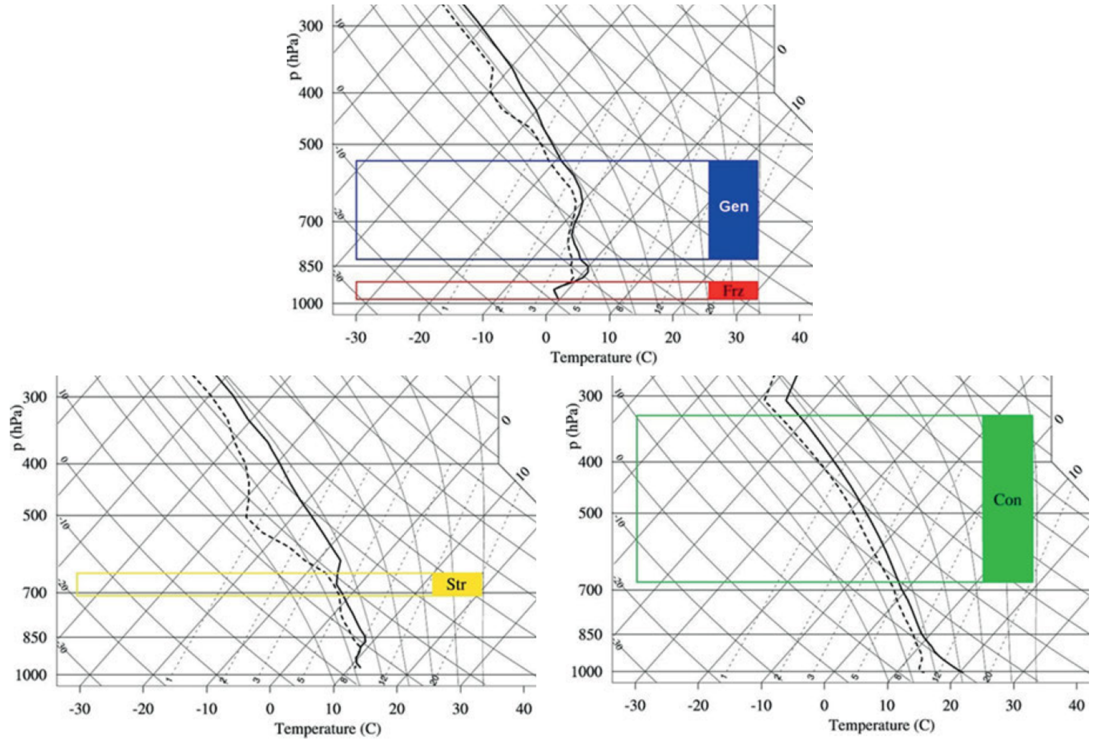

Figure 2.6: ADWICE's PIA scenario identification. Temperature and dewpoint profiles highlighting the scenarios „General“ (blue), „Freezing“ (red), „Stratiform“ (yellow) and „Convective“ (green) (Source: (Kalinka et al. 2017) - modified).

sufficient vertical extent, the solid particles fully melt. The now liquid precipitation falls into the subfreezing air below becoming supercooled. The PIA scans the given profiles from the surface to the top, first searching for a layer with $T < 0\,^\circ\mathrm{C}$. If found, the vertical boundaries of the melting layer are determined, if present. It is also required that a precipitating cloud, identified solely with the temperature and humidity profile, with a minimal vertical extent of 3000 m is present above the melting layer, as well as a potential layer of dry air not exceeding 3000 m vertical extent between the precipitating cloud and the melting layer. If such conditions are found, the PIA assigns every layer below the melting layer with $-20\,^\circ\mathrm{C} < T < 0\,^\circ\mathrm{C}$ the „Freezing“-scenario (Kalinka et al. 2017). In the „Stratiform“-scenario, there is a stratiform cloud with subfreezing temperatures capped by an inversion. Here droplet growth is mainly due to collision-coalescence processes, resulting in the formation of freezing drizzle. Identifying this scenario, PIA searches for a cloud layer with $-12\,^\circ\mathrm{C} < T < 0\,^\circ\mathrm{C}$ (Cober and Isaac 2012) and relative humidities of at least 80 % throughout. The top of the stratiform cloud is determined when a characteristic gradient in relative humidity of 2.5 % per 100 m is met or exceeded. Since the stratiform cloud can glaciate and therefore deplete the supercooled liquid water by ice particles falling in, it is required that no precipitating cloud is found within 3000 m above. Meeting these conditions, the layer is assigned the scenario „Stratiform“ (Kalinka et al. 2017). Due to the strong updrafts and condensation processes related to the „adiabatic cooling of lifted air masses“ (Kalinka et al. 2017, p. 445), convective cloud system call for a specific scenario „Convective“. The spatial resolution of the underlying numerical model is about 7 km, so convective cells are not resolved. Hence, a parameterization for convective processes is needed (e.g. the mass flux scheme by Tiedtke (1989)) that provides a value for the convective cloud base, z_{base}, and cloud top, z_{top} (Kalinka et al. 2017). PIA evaluates the convective clouds' vertical extent

$$\Delta z_{\mathrm{conv}} = z_{\mathrm{top}} - z_{\mathrm{base}}. \tag{2.69}$$

Since shallow convection is generally not a significantly hazardous icing situation, a minimum vertical extent of 3000 m is required. Additionally the convective layer must satisfy $-40\,^\circ\mathrm{C} < T < 0\,^\circ\mathrm{C}$ for all convective layers

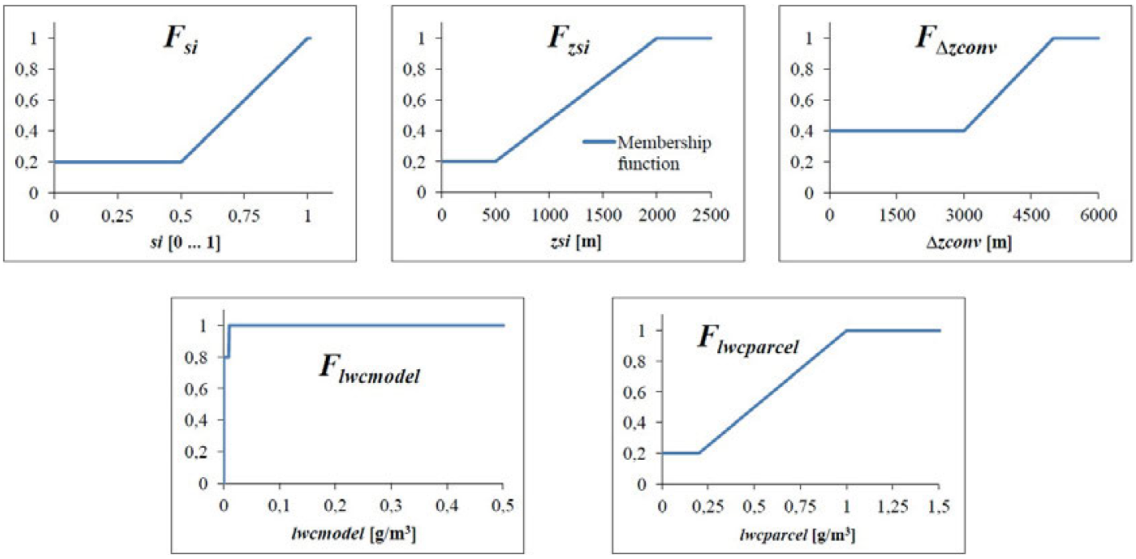

Figure 2.7: ADWICE's membership functions for the supersaturation over ice (top left), its vertical extent (top center), convective clouds' vertical extent (top right) and the two LWC alternatives, as the model result (bottom left) and computed via a parcel method (bottom right) (Source: (Kalinka et al. 2017)).

being assigned the scenario „Convective“ (Kalinka et al. 2017). The icing scenarios „Freezing“, „Stratiform“ and „Convective“ are assigned to clouds or cloud layers that potentially carry SLD. However, non-SLD clouds may also cause aircraft icing to occur. These are represented with the „General“-scenario. So if there are clouds that are not assigned to one of the former scenarios, but have a temperature between $-20\,^{\circ}\mathrm{C}$ and $0\,^{\circ}\mathrm{C}$ combined with an appropriate humidity that is temperature-dependent, it is assigned the scenario „General“. The threshold values for the relative humidity are 63 % at $-20\,^{\circ}\mathrm{C}$, 82 % at $0\,^{\circ}\mathrm{C}$ and linearly interpolated in between (Kalinka et al. 2017), derived from radiosonde observations in the vicinity of PIREPs report icing conditions by Forbes et al. (1993). According to Tafferner et al. (2003) a high false alarm rate is generally produced when forecasting icing conditions based solely on modelled humidity and temperature fields. To reduce the false alarm rate observational data „from SYNOP stations, METeorological Aerodrome Reports (METAR)“ (Kalinka et al. 2017, p. 446) as well as remote sensing data is combined with the PIP in the DIA. PIA and DIA ultimately detect icing environments assigning appropriate icing scenarios. The expected intensity of the icing encountered in these environments and scenarios is then determined. This value is proportional to the supercooled liquid water content (SLWC) as it should correlate with the rate the ice accretes onto the aircraft's structures. The underlying numerical model provides a LWC field ($\mathrm{LWC}_{\mathrm{model}}$). However, as some design aspects prevent a satisfactory description of both amount and distribution of liquid water (Köhler and Görsdorf 2014), an additional set of atmospheric quantities are derived from the model's output to act as a proxy for the SLWC. Leifeld (2004) introduced both the supersaturation over ice (s_{i}) and its vertical extent (zs_{i}) to this set of parameters, as it indicates the presence of droplets feeding the supersaturation whilst evaporating. Tafferner et al. (2003) provide an alternative value for the LWC, next to the one from the model itself, which is calculated based on a parcel method ($\mathrm{LWC}_{\mathrm{parcel}}$), providing an adiabatic estimate of the available liquid water through vertical transport. The already mentioned vertical extent of convective systems Δz_{conv} finds another use in this parameter set, as the probability of SLW correlates with it (Kalinka et al. 2017). These five parameters are organized in membership functions that map their actual value to a factor F_x between 0 and 1. Figure 2.7 shows a representation of those membership functions. Additionally, each parameters is assigned a weighting factor w_x, which depends on the specific icing scenario. The icing intensity value is then calculated by

$$I = \sum_x w_x F_x. \tag{2.70}$$

This icing intensity value is then mapped to one of four icing intensity levels: No icing ($I = 0$), light icing ($0 < I < 0.4$), moderate icing ($0.4 \leq I < 0.7$) and severe icing ($0.7 \leq I \leq 1.0$). The icing scenario „Freezing" is always assigned the severe icing intensity level, as it is almost certain to encounter SLD. Scenarios „General" and „Stratiform" weigh all five parameters equally, while the „Convective" only considers $\mathrm{LWC}_{\mathrm{parcel}}$ (75 %) and Δz_{conv} (25 %) (Kalinka et al. 2017).

These examples of operationally used aircraft icing prediction schemes show that the physical processes of aircraft icing are not described, but their effect estimated by sets of empirically chosen proxy variables and membership functions. Interestingly, these sets do not contain microphysical quantities beyond the LWC, like the cloud droplet number density or cloud droplet diameters, ultimately determining the impingement efficiency. Contrary to these, the aircraft icing parameterization developed in the scope of the present work describes the physical processes of impingement efficiency and freezing behaviour of the impinging water, explicitly requiring information on microphysical quantities. Additionally, while current aircraft icing prediction schemes are executed during the post-processing, this new parameterization is executed online during the numerical weather prediction simulation.

3 Model description and new aircraft icing parameterization

While current icing prediction schemes forecast icing areas and give an estimate on the expected severity, the more qualitative categorization lacks an actual value for the expected ice accretion rate. Furthermore aircraft specific aspects like heated surfaces or especially relative windspeed are and can not be considered, as well as crucial aspects for droplet impingement like the droplets' size and their size distribution. Experimental and research methods for improving these prediction schemes focus on improving the forecasting of supercooled liquid water, not on the actual icing process. Ice accretion algorithms actively using an empirically determined impingement efficiency and relative windspeed exist, however those are not in use in operational icing forecasts and mostly do not differentiate between rime icing, glaze icing and liquid water accretion when quantifying the icing intensity. One of those is introduced in chapter 4. Although the prognostic parts of icing prediction schemes (e.g. the PIA from ADWICE) use model data, the selected fields are limited, so that a correction effort with observation data is required to reduce false alarms.

Tackling these drawbacks, the present work aims for a more quantitative approach on forecasting aircraft icing intensity. This is achieved by the development of an online physically based aircraft icing parameterization and its implementation into the numerical weather model ICON-ART. The parameterization consists of two parts: calculating the overall impingement efficiency and simulating the actual freezing process. The following parts introduce the underlying model ICON-ART and the parameterization for droplet nucleation used. The latter is due to the sensitivity investigations conducted in the present work, one of which focuses on the load of aerosols acting as CCN. This chapter also describes the newly developed icing parameterization and concludes with informations regarding the model configuration for the analyses to be conducted.

3.1 The model system ICON-ART

ICON-ART is the extension of the „ICOsahedral Non-hydrostatic (ICON) modelling framework“ (Zängl et al. 2015) by the ART module, which stands for „Aerosols and Reactive Trace gases“ (Rieger et al. 2015).

The initial development of ICON was „a joint project between the German Weather Service (DWD) and the Max Planck Institute for Meteorology (MPI-M)“ (Zängl et al. 2015). Throughout the years further institutions joined this effort for developing a system that unifies global numerical weather forecast and climate modelling capabilites: The German Climate Computing Center (DKRZ) and the Karlsruhe Institute of Technologie (KIT).

The rise of high-performance computing systems in the early- to mid-2000s called for the drop of both hydrostatic dynamical cores and spectral and regular latitude-longitude grids (Zängl et al. 2015). The new grids commonly used are icosahedral grids (Tomita and Satoh 2004), centroidal Voronoi grids (Skamarock et al. 2012) and cubed-sphere grids (Ullrich and Jablonowski 2012). ICONs development aimed to achieve improvements regarding conservational properties compared to the global models GME (Majewski et al. 2002) and ECHAM (Stevens et al. 2013). It was also obligatory to achieve „exact local mass conservation and mass-consistent tracer transport“ (Zängl et al. 2015). Further goals were enabling improved scalability for future computing architectures and the capability to mix both one-way and two-way nesting as well as vertical nesting (Zängl et al. 2015). Although Gassmann (2011) points out some conceptual disadvantages, which also necessitated the removal of the desired goal to exactly conserve energy, it was decided that ICON, as its name suggests, employs an icosahedral-triangular

C grid structure instead of a hexagonal one (Zängl et al. 2015). The base for the unstructured grid is a spherical icosahedron consisting of 20 equally sized equilateral triangles that is successively refined. The refinement takes place in two parts: The first one is the root division, where the basic triangles' edges are equally divided into n parts. The nomenclature used describing the process is Rn. This yields n^2 spherical triangles in each of the original ones. The second part of refinement is the execution of k bisection steps, which further divides the triangles into 4 smaller triangles per step, which is termed Bk, ultimately ending in a RnBk-grid (Zängl et al. 2015). Tomita et al. (2001) describe spring dynamics to be used for further optimization of icosahedral grids, which are applied for intermediate and final grids in ICON. The number of cells (n_c), of edges (n_e) and of vertices (n_v) for a RnBk-grid is given by

$$n_\mathrm{c} = 20n^2 4^k; \qquad n_\mathrm{e} = 30n^2 4^k; \qquad n_\mathrm{v} = 10n^2 4^k + 2 \tag{3.1}$$

and the effective gridsize ($\overline{\Delta x}$) by

$$\overline{\Delta x} = \sqrt{\frac{\pi}{5}} \frac{r_\mathrm{E}}{n 2^k} \tag{3.2}$$

with the Earth's radius r_E in m (Zängl et al. 2015).

Gassmann and Herzog (2008) suggested the prognostic variables the ICON model's non-hydrostatic equation system is based upon, which takes the following form:

$$\frac{\partial \widehat{v_\mathrm{n}}}{\partial t} + \frac{\partial \widehat{K_\mathrm{h}}}{\partial n} + \left(\widehat{\zeta} + f\right) \widehat{v_\mathrm{t}} + \widehat{w} \frac{\partial \widehat{v_\mathrm{n}}}{\partial z} = -c_\mathrm{pd} \widehat{\Theta_\mathrm{v}} \frac{\partial \overline{\pi}}{\partial n} - F\left(v_\mathrm{n}\right), \tag{3.3}$$

$$\frac{\partial \widehat{w}}{\partial t} + \widehat{\boldsymbol{v}_\mathrm{h}} \cdot \nabla \widehat{w} + \widehat{w} \frac{\partial \widehat{w}}{\partial z} = -c_\mathrm{pd} \widehat{\Theta_\mathrm{v}} \frac{\partial \overline{\pi}}{\partial z} - g, \tag{3.4}$$

$$\frac{\partial \overline{\rho} \widehat{\Theta_\mathrm{v}}}{\partial t} + \nabla \cdot \left(\overline{\rho \widehat{\boldsymbol{v}} \widehat{\Theta_\mathrm{v}}}\right) = \overline{Q}, \tag{3.5}$$

$$\frac{\partial \overline{\rho}}{\partial t} + \nabla \cdot \left(\overline{\rho} \widehat{\boldsymbol{v}}\right) = 0, \tag{3.6}$$

$$\frac{\partial \overline{\rho} \widehat{q_k}}{\partial t} + \nabla \cdot \left(\overline{\rho} \widehat{q_k} \widehat{\boldsymbol{v}}\right) = -\nabla \cdot \left(\overline{\boldsymbol{J}_k} + \overline{\rho q_k'' \boldsymbol{v}''}\right) + \overline{\sigma_k}. \tag{3.7}$$

In this set of equations 3.3 to 3.7 v_n and v_t are the horizontal wind components in $\mathrm{m\,s^{-1}}$ perpendicular and tangential to the triangle's edge respectively, w is the vertical wind component in $\mathrm{m\,s^{-1}}$, ρ is the air density in $\mathrm{kg\,m^{-3}}$ and Θ_v is the virtual potential temperature in K. $\boldsymbol{v}$ and $\boldsymbol{v}_\mathrm{h}$ refer to the three dimensional and horizontal wind vectors respectively and are given in $\mathrm{m\,s^{-1}}$. Additionally in use are the vertical vorticity component ζ, the coriolis parameter f (both in $\mathrm{s^{-1}}$), the horizontal part of the kinetic energy $\widehat{K_\mathrm{h}} = \frac{1}{2}\left(\widehat{v_\mathrm{n}}^2 + \widehat{v_\mathrm{t}}^2\right)$ in $\mathrm{m^2\,s^{-2}}$ and the Exner function π. c_pd is the specific heat capacity for dry air at constant pressure in $\mathrm{J\,kg^{-1}\,K^{-1}}$, $g = 9.81\,\mathrm{m\,s^{-2}}$ is the gravitational acceleration and $F\left(v_\mathrm{n}\right)$ and Q are source terms for horizontal movement in $\mathrm{m\,s^{-2}}$ and diabatic heating in $\mathrm{kg\,K\,m^{-3}\,s^{-1}}$ respectively. Both the classic Reynold's mean $\phi = \overline{\phi} + \phi'$ and the barycentric mean $\phi = \widehat{\phi} + \phi''$ ($\widehat{\phi} = \frac{\overline{\rho\phi}}{\overline{\rho}}$) are in use. According to Rieger et al. (2015) local mass conservation is easily achieved by using ρ and Θ_v in flux form.

The computation of advection in ICON is separated into horizontal and vertical advection enabling both a more efficient and exact determination than computing the three dimensional advection. This is mainly due to the fact that this separation allows the application of different methods (Rieger et al. 2015).

The development of the ART extension is mainly conducted at the Institute for Meteorology and Climate Research (IMK) of the Karlsruhe Institute of Technology. It was also used in ICON-ART's predecessor COSMO-ART studying „the feedback between aerosol, trace gases and the atmosphere" (Rieger et al. 2015) (Vogel et al. 2009; Bangert et al. 2012; Lundgren et al. 2013). This is extended upon for the ICON-ART model system, including chemistry descriptions for the stratosphere and troposphere as well as aerosol chemistry and dynamics.

Additionally, for it being a fully online-coupled model system, the impact of aerosols and gases on radiation and clouds can be accounted for (Rieger et al. 2015). An important aspect of ICON-ART is the spatiotemporal development of trace gases and aerosols, respecting mass conservation. For a gaseous tracer l, the ratio of its partial density and the total air density (or its mass mixing ratio) is treated in flux form according to (Rieger et al. 2015)

$$\frac{\partial \overline{\rho}\widehat{\Psi_{g,l}}}{\partial t} = -\nabla \cdot \left(\widehat{\boldsymbol{v}}\overline{\rho}\widehat{\Psi_{g,l}}\right) - \nabla \cdot \left(\overline{\rho \boldsymbol{v}'' \Psi''_{g,l}}\right) + P_l - L_l + E_l. \tag{3.8}$$

In equation 3.8 $\Psi_{g,l}$ is the mass mixing ratio of the gas l in $\mathrm{kg\,kg^{-1}}$, P_l, L_l and E_l are its chemical production rate and its loss and emission rate in $\mathrm{kg\,m^{-3}\,s^{-1}}$. $\nabla \cdot \left(\widehat{\boldsymbol{v}}\overline{\rho}\widehat{\Psi_{g,l}}\right)$ describes the flux divergence and includes both horizontal and vertical advection. $\nabla \cdot \left(\overline{\rho \boldsymbol{v}'' \Psi''_{g,l}}\right)$ describes the induced change due to turbulent fluxes (Rieger et al. 2015). In ICON, these turbulent fluxes are computed using a one-dimensional prognostic TKE (Turbulent Kinetic Energy) scheme by Raschendorfer (2001).

An aerosol l's mass mixing ratio, its mass concentration divided by total air density, is treated in a similar way according to the flux form equation (Rieger et al. 2015)

$$\frac{\partial \overline{\rho}\widehat{\Psi_l}}{\partial t} = -\nabla \cdot \left(\widehat{\boldsymbol{v}}\overline{\rho}\widehat{\Psi_l}\right) - \nabla \cdot \left(\overline{\rho \boldsymbol{v}'' \Psi''_l}\right) - \frac{\partial}{\partial z}\left(v_{\mathrm{sed},l}\overline{\rho}\widehat{\Psi_l}\right) - \lambda_l \overline{\rho}\widehat{\Psi_l} + E_l. \tag{3.9}$$

Equation 3.9 shows that there is no chemical production for aerosols (like sea-salt or mineral dust), and the loss rate for aerosols comprises sedimentation with the sedimentation velocity $v_{\mathrm{sed},l}$ in $\mathrm{m\,s^{-1}}$ and washout with the washout coefficient λ_l in $\mathrm{s^{-1}}$ for an aerosol l. For monodisperse aerosols this describes the spatiotemporal evolution sufficiently. ICON-ART also represents polydisperse aerosols by a set of lognormal distributions. The standard deviation is held constant for each distribution and both their mass mixing ratio and the number mixing ratio are prognostic. Hence, equation 3.9 is not only applied to the mass mixing ratios of each distribution but also to their respective number mixing ratio (Rieger et al. 2015).

3.2 Droplet activation parameterization

To accurately represent water in the atmosphere, all phases need to be accounted for. In the scope of this work, liquid water plays a crucial role, as it is required for aircraft icing to occur. Since the impact the aerosol load exerts as CCN onto aircraft icing is a point of investigation in this present work, the droplet formation, as the CCN's point of impact, is of particular interest here. Hence, the following introduces the parameterization used to compute the droplet nucleation process.

ICON-ART implements the parameterization presented by Fountoukis and Nenes (2005), which is a continued development of the work by Nenes and Seinfeld (2003), combined with some corrections by Barahona and Nenes (2007) and Barahona et al. (2010). The parameterization is based on a number of modes of lognormally distributed aerosol concentrations that can be activated into droplets according to the Koehler law. While aerosol distributions are described most of the time based on the particle diameter

$$n^{\mathrm{d}}\left(D_{\mathrm{p}}\right) = \frac{\mathrm{d}N}{\mathrm{d}\ln D_{\mathrm{p}}} = \sum_{i=1}^{n_{\mathrm{m}}} \frac{N_i}{\sqrt{2\pi}\ln\sigma_i} \exp\left[-\frac{\ln^2 \frac{D_{\mathrm{p}}}{D_{\mathrm{g},i}}}{2\ln^2\sigma_i}\right], \tag{3.10}$$

Nenes and Seinfeld (2003) transform it into a critical supersaturation base, assuming that the chemical composition of one aerosol mode is indifferent toward size (Fountoukis and Nenes 2005)

$$n^{\mathrm{s}}(s) = \frac{\mathrm{d}N}{\mathrm{d}s} = -\frac{\mathrm{d}N}{\mathrm{d}\ln D_{\mathrm{p}}}\frac{\mathrm{d}\ln D_{\mathrm{p}}}{\mathrm{d}s} = -n^{\mathrm{d}}\left(D_{\mathrm{p}}\right)\frac{\mathrm{d}\ln D_{\mathrm{p}}}{\mathrm{d}s}. \tag{3.11}$$

D_p is the particle diameter in m, N_i is the aerosol's number concentration in mode i in m^{-3}, $D_\mathrm{g,i}$ and σ_i are the geometric mean diameter in m and geometric standard deviation of mode i, respectively, n_m is the number of modes and s is the critical supersaturation. The connection between critical supersaturation and particle size can be derived from equation 2.24. Its constant B depends on the amount of soluble material n_s, which is given by (Seinfeld and Pandis 2016)

$$n_\mathrm{s} = \frac{\nu \pi D_\mathrm{p}^3 \rho_\mathrm{p}}{6 M_\mathrm{p}}, \tag{3.12}$$

assuming a spherical particle with diameter D_p in m, density ρ_p in $\mathrm{kg\,m^{-3}}$ and a molecular weight M_p in $\mathrm{kg\,mol^{-1}}$. ν is the number of ions produced by the dissociation of one particle's molecule. Additionally, since (critical) supersaturation (s) is generally low $\ln S_\mathrm{c} = \ln(1+s)$ can be approximated to $\ln S_\mathrm{c} \approx s$. Hence, equation 2.24 can be derived to (Seinfeld and Pandis 2016)

$$s = \left(\frac{4A^3 \rho_\mathrm{w} M_\mathrm{p}}{27 \nu \rho_\mathrm{p} M_\mathrm{w} D_\mathrm{p}^3} \right)^{\frac{1}{2}}. \tag{3.13}$$

which Fountoukis and Nenes (2005) further develop to

$$\frac{\mathrm{d} \ln D_\mathrm{p}}{\mathrm{d}s} = -\frac{2}{3s}. \tag{3.14}$$

Substituting equations 3.10 and 3.14 into equation 3.11 yields

$$n^\mathrm{s}(s) = \sum_{i=1}^{n_\mathrm{m}} \frac{2N_i}{3s\sqrt{2\pi}\ln\sigma_i} \exp\left[-\frac{\ln^2\left(\frac{s_{\mathrm{g},i}}{s}\right)^{\frac{2}{3}}}{2\ln^2\sigma_i} \right]. \tag{3.15}$$

with $s_{\mathrm{g},i}$ as the critical supersaturation of a particle with diameter $D_{\mathrm{g},i}$. Fountoukis and Nenes (2005) further introduces the total number of activated droplets based on the maximum supersaturation, s_max, a parcel reaches with

$$N_\mathrm{d} = \int_0^{s_\mathrm{max}} n^\mathrm{s}(s)\,ds = \sum_{i=1}^{n_\mathrm{m}} \frac{N_i}{2} \mathrm{erfc}\left[-\frac{2\ln\frac{s_{\mathrm{g},i}}{s_\mathrm{max}}}{3\sqrt{2}\ln\sigma_i} \right]. \tag{3.16}$$

In equation 3.16 $\mathrm{erfc}(x) = 1 - \mathrm{erf}(x)$ uses the error function erf.

To determine the maximum supersaturation of an adiabatic parcel, the temporal development of its supersaturation is needed. According to Pruppacher and Klett (2012) and Seinfeld and Pandis (2016), this can be described for a cloud parcel ascending with a constant velocity V in $\mathrm{m\,s^{-1}}$, as

$$\frac{\mathrm{d}s}{\mathrm{d}t} = \alpha V - \gamma \frac{\mathrm{d}W}{\mathrm{d}t} \tag{3.17}$$

with

$$\alpha = \frac{g M_\mathrm{w} L}{c_\mathrm{p} R T^2} - \frac{g M_\mathrm{a}}{RT} \qquad \text{and} \qquad \gamma = \frac{p M_\mathrm{a}}{p^\mathrm{s} M_\mathrm{w}} + \frac{M_\mathrm{w} L^2}{c_\mathrm{p} R T^2}. \tag{3.18}$$

The definitions for α and γ as well as some of the nomenclature is taken from Fountoukis and Nenes (2005), since the γ in Nenes and Seinfeld (2003) is erroneous. In equations 3.17 and 3.18 $\frac{\mathrm{d}W}{\mathrm{d}t}$ denotes the condensation rate of liquid water onto the droplets in $\mathrm{kg\,kg^{-1}\,s^{-1}}$, $g = 9.81\,\mathrm{m\,s^{-2}}$ is the gravitational acceleration, $M_\mathrm{w} = 18.01528\,\mathrm{g\,mol^{-1}}$ and M_a in $\mathrm{g\,mol^{-1}}$ are the molecular weights of water and air, respectively. L is the latent heat released by condensation of water in $\mathrm{J\,kg^{-1}}$, c_p is the heat capacity of air at constant pressure in $\mathrm{J\,kg^{-1}\,K^{-1}}$ and $R = 8.314\,\mathrm{J\,mol^{-1}\,K^{-1}}$ is the universal gas constant. The air temperature T is given in K and p^s is the saturation vapour pressure of water in Pa.

Setting equation 3.17 to 0 enables the computation of s_max. Fountoukis and Nenes (2005) use the definition of the condensation rate presented by Nenes and Seinfeld (2003) as well as the droplet growth rate presented by Seinfeld and Pandis (2016) to get

$$\frac{2\alpha V \rho_\mathrm{a}}{\pi \gamma \rho_\mathrm{w}} - G s_\mathrm{max} I\left(0, s_\mathrm{max}\right) = 0 \tag{3.19}$$

with

$$G = \frac{4}{\frac{\rho_\mathrm{w} R T}{p^\mathrm{s} D_\mathrm{v} M_\mathrm{w}} + \frac{L \rho_\mathrm{w}}{k_\mathrm{a} T}\left(\frac{L M_\mathrm{w}}{R T} - 1\right)}, \tag{3.20}$$

as Barahona and Nenes (2007), refering to Seinfeld and Pandis (2016) corrected the version of Fountoukis and Nenes (2005), with the thermal conductivity of air k_a in $\mathrm{J\,m^{-1}\,K^{-1}\,s^{-1}}$ and the water vapour diffusivity in air D_v in $\mathrm{m^2\,s^{-1}}$, and

$$I\left(0, s_\mathrm{max}\right) = \int_0^{s_\mathrm{max}} \left[D_\mathrm{p}^2\left(\tau\right) + \frac{G}{\alpha V}\left(s_\mathrm{max}^2 - s\left(\tau\right)^2\right)\right]^{\frac{1}{2}} n^\mathrm{s}\left(s\right) ds. \tag{3.21}$$

The implementation determines s_max by a bisection scheme, starting with $s_\mathrm{max,low} = 1 \times 10^{-5}$, $s_\mathrm{max,high} = 1$ and $s_\mathrm{max,mean} = \frac{s_\mathrm{max,low} + s_\mathrm{max,high}}{2}$. These values are applied to an implementation of equation 3.21 (extended with a correction term for kinetically limited large particles (Barahona et al. 2010)) and 3.19. $s_\mathrm{max,mean}$ is then assigned to either $s_\mathrm{max,low}$ or $s_\mathrm{max,high}$ depending on which of those share the same sign in the evaluation of 3.19, given that $s_\mathrm{max,mean}$ does not evaluate to 0 well enough on its own. The process is repeated until the $s_\mathrm{max,mean}$ fits equation 3.19 good enough and is then assigned to s_max. The total number of activated droplets is then calculated by applying equation 3.16.

3.3 Development and implementation of a new aircraft icing parameterization

The idea behind this work is to extend ICON-ART itself with a new aircraft icing parameterization that is more thoroughly based on the physical aspects of impingement and the actual freezing. This part describes the implementation and development of this new parameterization, which is a purely diagnostic procedure having no influence on the atmospheric state.

As chapter 2.3 states, the impingement efficiency describes the proportion of the ambient liquid water content that lands upon the object, either on a specific location or overall. While the local impingement efficiency in the former case is important for designing and engineering of airfoils, the overall impingement efficiency in the latter case is the relevant quantity for analysing icing environments and hence for this newly developed aircraft icing parameterization.

In this new aircraft icing parameterization, the overall impingement efficiency is computed for every grid point containing liquid water using equation 2.42 in a Lagrangian approach. The object on which the supercooled liquid droplets are to impinge and freeze upon is a cylinder, aligned horizontally and in a way that impinging droplets hit its mantle (see figure 3.1 for reference). It acts as a proxy for more complex shapes to quantify the freezing behaviour and icing potential, and offers a standardized view on the subject. According to Boudala et al. (2019) the Federal Aviation Administration (FAA) bases its ruling for flightworthiness in icing conditions on the ice accretion on a cylinder. But also scientific work regarding the analyses of the atmosphere concerning icing environments uses the cylinder as accretion object, both in measuring (Hauf and Schröder 2006) and modelling (McComber and Touzot 1981).

One of the benefits of using a cylinder is that the airflow around this object is simple and analytically computable, if turbulent effects are neglected. This is reasonable, since here turbulence predominantly affects the smallest droplets by potentially increasing their impingement efficiency. The overall potential additional mass, however, is small compared to the impinging masses of larger droplets and therefore not expected to relevantly alter the computed

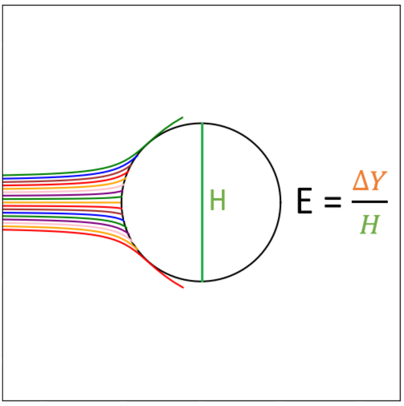

Figure 3.1: Schematic of the computation of the overall impingement efficiency for a cylinder. The colorful lines on the left side of the circle, as a projection of the cylinder, represent the different droplet trajectories of which only the top and bottom most manage to avoid the cylinder.

impingement efficiency. With an ambient wind velocity given, the wind field around a cylinder is computed by (McComber and Touzot 1981)

$$U_{\mathrm{cyl}} = 1 + \frac{Y^2 - X^2}{\left(X^2 + Y^2\right)^2} \tag{3.22}$$

$$V_{\mathrm{cyl}} = \frac{-2XY}{\left(X^2 + Y^2\right)^2} \tag{3.23}$$

Equations 3.22 and 3.23 are written in dimensionless form. $U_{\mathrm{cyl}} = \frac{u_{\mathrm{cyl}}}{V_\infty}$ and $V_{\mathrm{cyl}} = \frac{v_{\mathrm{cyl}}}{V_\infty}$ are the x- and y-components of the airflow around the cylinder, respectively, normalized with the ambient wind velocity V_∞ (in $\mathrm{m\,s^{-1}}$), which in the case of an aircraft is the relative airspeed it experiences. The coordinate system used is described in section 2.3. The coordinates X and Y are given relative to the center of the cylinder and are normalized with the cylinder's radius r_{cyl} (in m), so $X = \frac{x}{r_{\mathrm{cyl}}}$ and $Y = \frac{y}{r_{\mathrm{cyl}}}$ (McComber and Touzot 1981).
As stated by Gent et al. (2000) choosing a droplet's starting position 5 chord lengths ahead of the cylinder, which is its diameter, is appropriate to ensure the wind field being yet undisturbed. Hence, the x-component of the starting positions is chosen to be $x_{\mathrm{start}} = -10 r_{\mathrm{cyl}}$, relative to the cylinder's center. At such starting positions an assumption can be made that the droplet's velocity is equal to the ambient wind velocity. However, for larger droplets (SLDs, having diameters exceeding 40 µm (Gent et al. 2000)) an adjustment to this initial droplet velocity is required to account for the droplets' terminal velocity. To determine the overall impingement efficiency, according to equation 2.42 a Δy needs to be computed. H is straight forward when regarding a cylinder, as it is its diameter $H = 2r_{\mathrm{cyl}}$. Δy is the difference between the top-most and bottom-most starting positions that result in an impact of the droplet,

$$\Delta y = y_{\mathrm{top}} - y_{\mathrm{bot}}. \tag{3.24}$$

Figure 3.1 illustrates the computation of the overall impingement efficiency for a cylinder as used in this parameterization. In general there are two ways to determine y_{top} and y_{bot}: using pre-assigned, fixed positions or choosing a new position based on the result of the previous one. The former results ultimately in a lot of unnecessary trajectory computations and the computational cost scale linearly with the aimed accuracy. Hence, this parameterization utilizes a binary search approach to choose a new starting position. The downside of this approach is that two searches need to be done, while a fixed position approach determines y_{top} and y_{bot} simultaneously. However, the second search still benefits from the results of the first one, reducing its impact on the overall computational costs. The binary search nature of the method reflects in the fact that the absolute change in the y-direction for the next trajectory computation is halved with every consecutive step and the sign of the change is determined by whether the current trajectory impacts the cylinder. The search is considered completed when a certain threshold of the absolute change for the upcoming step is undercut.

The algorithm first determines y_{bot} and starts with $y = 0$ and an absolute value for the change of $\mathrm{d}y = r_{\mathrm{cyl}}$. This initial value for $\mathrm{d}y$ is due to the fact that the theoretical maximum value of the overall impingement efficiency is 1. Analysing equation 2.42 in this regard, yields $\Delta y \leq H = 2r_{\mathrm{cyl}}$. Actual unity of the overall impingement efficiency, however, is not realistic, so shifting the starting position by H upon impacting will result in a missing trajectory in the next step, leading to a shifting of $\frac{H}{2} = r_{\mathrm{cyl}}$ in the opposing direction in the subsequent one. By choosing $\mathrm{d}y = r_{\mathrm{cyl}}$, this extra step is already accounted for. If the current droplet trajectory impacts with the cylinder, the next y-component is determined by subtracting $\mathrm{d}y$ from it, otherwise it is added. Then $\mathrm{d}y$ is halved for the next step. With the y_{bot} value computed, the algorithm determines y_{top}. The initial y-component used is not greater than $y_{\mathrm{bot}} + r_{\mathrm{cyl}}$, with the same reasoning as the initial $\mathrm{d}y$ when searching for y_{bot}. However, it can be lower, if during the search for y_{bot} one of the trajectories went above the cylinder and its starting y-component is less than $y_{\mathrm{bot}} + r_{\mathrm{cyl}}$. In either case the initial $\mathrm{d}y$ is the difference between the initial y-component and y_{bot}. The same strategy applies as before, except that an impacting trajectory causes an increase of the initial y-component and a missing trajectory a corresponding decrease. With both y_{bot} and y_{top} computed, the algorithm calculates the overall impingement efficiency applying equations 3.24 and 2.42. Although the algorithm for determining the overall impingement efficiency consists of a multitude of computations, it requires only the droplet size, the ambient windspeed (which is the relative airspeed experienced by the aircraft) and the size of the cylinder as input.

The introduced part of the parameterization determines the overall impingement efficiency for droplets of one size. Hence, to compute the overall impingement efficiency of a droplet spectrum, this part is executed for every considered droplet size in the spectrum and the individual overall impingement efficiency values are linearly combined weighted with the respective mass fractions the droplet sizes represent in the overall spectrum. The cloud droplet spectrum in ICON-ART is based on the two-moment scheme by Seifert and Beheng (2006). They describe the size distribution for the number density of cloud droplets with the generalized Γ-distribution, which is often used to describe hydrometeors' size distributions,

$$f(m) = A m^{\nu} \exp\left(-\lambda m^{\mu}\right). \tag{3.25}$$

with the hydrometeor's mass m in kg, the parameters ν and μ that depend on the kind of hydrometeor investigated and the coefficients A and λ which are defined as (Seifert and Beheng 2006)

$$A = \frac{\mu N}{\Gamma\left(\frac{\nu+1}{\mu}\right)} \lambda^{\frac{\nu+1}{\mu}} \qquad \text{and} \tag{3.26}$$

$$\lambda = \left[\frac{\Gamma\left(\frac{\nu+1}{\mu}\right)}{\Gamma\left(\frac{\nu+2}{\mu}\right)} \overline{m}\right]^{-\mu}. \tag{3.27}$$

Equations 3.26 and 3.27 use the hydrometeor's number concentration N in m^{-3} and its mean mass $\overline{m} = \frac{M}{N}$ in kg, also using the hydrometeor's mass concentration M in $\mathrm{kg\,m}^{-3}$ and the Gamma function Γ.

While freezing precipitation (like drizzle or rain) also causes aircraft icing incidents to occur, the hydrometeors of interest for the present work are cloud droplets, as these are the ones to which the design of the new parameterization applies. According to Seifert and Beheng (2006) cloud droplets are represented with $\nu = \mu = 1$, hence

$$f_{\mathrm{c}}(m) = \frac{4N_{\mathrm{c}}}{\overline{m}^2} m \cdot \exp\left(-\frac{2m}{\overline{m}}\right). \tag{3.28}$$

The mass concentration of cloud droplets can then be described with

$$M_\mathrm{c} = \int_0^\infty m \cdot f_\mathrm{c}(m)\,\mathrm{d}m. \tag{3.29}$$

To respect the cloud droplet spectrum in computing the overall impingement efficiency, the spectrum needs to be appropriately discretized. For this a minimum m_min and maximum cloud droplet mass m_max is required, which are to be chosen, such that only negligible parts of the mass concentration are truncated. The values chosen in this parameterization are $m_\mathrm{min} = \frac{\overline{m}}{40}$ and $m_\mathrm{max} = 5\overline{m}$. This leads to a truncated mass concentration of

$$M_\mathrm{c,trunc} = \int_{m_\mathrm{min}}^{m_\mathrm{max}} m \cdot f_\mathrm{c}(m)\,\mathrm{d}m = 0.997211 \cdot M_\mathrm{c}. \tag{3.30}$$

Additionally, an appropriate step width is needed. In the default configuration of this parameterization, this is set to $\Delta m = \frac{\overline{m}}{20}$, which divides the range in 100 parts that are evaluated. This leads to a total discretized mass concentration of

$$M_\mathrm{c,disc} = \sum_{i=0}^{99} m_i \cdot f_\mathrm{c}(m_i)\,\Delta m \approx 0.9972317 \cdot M_\mathrm{c} \tag{3.31}$$

$$m_i = m_\mathrm{min} + i \cdot \Delta m. \tag{3.32}$$

Using this discretization leads to only about 0.3 % of the mass concentration to remain unconsidered for the computation of the total overall impingement efficiency. With this, for every droplet mass m_i the previously described algorithm determines an overall impingement efficiency E_i. The total overall impingement efficiency is then computed with

$$E_\mathrm{total} = \frac{\sum_{i=0}^{99} m_i \cdot f_\mathrm{c}(m_i)\,\Delta m E_i}{M_\mathrm{c,disc}}. \tag{3.33}$$

Since this way of calculating the total overall impingement efficiency comes with additional computational costs, the parameterization is designed in such a way that the treatment of the spectrum can be switched off, so that the total overall impingement efficiency is solely determined by the overall impingement efficiency of the mean droplet mass, and that when explicitly treating the spectrum the accuracy can be adjusted by changing the number of parts into which the range is divided. Furthermore, the computation is omitted if there is no liquid water.

With the total overall impingement efficiency that will be denoted in the following with E (omitting the „total“ subscript), determined, the freezing part of the parameterization is executed. To avoid unnecessary computational efforts, the calculating of the various icing quantities is only conducted, if $E > 0$ and the temperature is subfreezing. This part of the parameterization applies the model developed by Zhang et al. (2016), the governing equations of which were introduced previously in chapter 2.4. As it differentiates the freezing process into a dry and wet icing phase, the point at which that shift happens needs to be determined. It can be expressed by both a critical ice thickness, z_c in m, and the time it takes to reach it, t_c in s. According to Zhang et al. (2016), the following conditions are met when z_c is reached:

$$T_\mathrm{p} = T_\mathrm{f}, \qquad \left.\frac{\mathrm{d}z_\mathrm{g}}{\mathrm{d}t}\right|_{z=z_\mathrm{c}} = \left.\frac{\mathrm{d}z_\mathrm{r}}{\mathrm{d}t}\right|_{z=z_\mathrm{c}}, \qquad \left.\frac{\mathrm{d}z_\mathrm{w}}{\mathrm{d}t}\right|_{z=z_\mathrm{c}} = 0, \tag{3.34}$$

with temperature at the rime/glaze interface T_p in K, the freezing temperature $T_\mathrm{f} = 273.15\,\mathrm{K}$ and the thicknesses of glaze ice z_g, rime ice z_r and of the liquid water film z_w in m. These conditions are applied to equation 2.52, which takes the following form, since from this point on glaze ice is accreted,

$$\rho_\mathrm{g} L_\mathrm{f} \frac{\mathrm{d}z_\mathrm{g}}{\mathrm{d}t} = k_\mathrm{g} \frac{\mathrm{d}T_\mathrm{g}}{\mathrm{d}z} - k_\mathrm{w} \frac{\mathrm{d}T_\mathrm{w}}{\mathrm{d}z}. \tag{3.35}$$

Equation 3.35 defines the interface between the solid and the liquid phase (Zhang et al. 2016) and can be further developed using the temperature equations 2.66 and 2.67 to

$$\rho_\mathrm{g} L_\mathrm{f} \frac{\mathrm{d}z_\mathrm{g}}{\mathrm{d}t} = k_\mathrm{g} \frac{T_\mathrm{f} - T_\mathrm{p}}{z_\mathrm{g}} - \rho_\mathrm{w} k_\mathrm{w} \frac{Q_\mathrm{a} + Q_\mathrm{k} - h_\mathrm{e}\left(T_\mathrm{f} - T_\mathrm{a}\right)}{h_\mathrm{e}\left[\mathrm{LWC} \cdot VE\left(t - t_\mathrm{c}\right) - \rho_\mathrm{g} z_\mathrm{g}\right] + \rho_\mathrm{w} k_\mathrm{w}}. \tag{3.36}$$

Additionally the relationship between the thickness of the glaze ice layer, z_g in m, and the liquid water film, $z_\mathrm{w} (= h)$ in m, is used that Zhang et al. (2016) describe with

$$z_\mathrm{w} = \frac{\mathrm{LWC} \cdot VE\left(t - t_\mathrm{c}\right) - \rho_\mathrm{g} z_\mathrm{g}}{\rho_\mathrm{w}}. \tag{3.37}$$

Ultimately, Zhang et al. (2016) derive the critical ice thickness as

$$z_\mathrm{c} = \frac{k_\mathrm{g}\left(T_\mathrm{f} - T_\mathrm{s}\right)}{\mathrm{LWC} \cdot VEL_\mathrm{f} + Q_\mathrm{a} + Q_\mathrm{k} - h_\mathrm{e}\left(T_\mathrm{f} - T_\mathrm{a}\right)} \frac{k_\mathrm{g} - k_\mathrm{r,0}}{k_\mathrm{g} \ln \frac{k_\mathrm{g}}{k_\mathrm{r,0}}}, \tag{3.38}$$

which is computed in the newly developed aircraft icing parameterization, along with t_c that Zhang et al. (2016) derive to be

$$t_\mathrm{c} = \frac{\rho_\mathrm{g} + \rho_\mathrm{r,0}}{2\mathrm{LWC} \cdot VE} z_\mathrm{c}. \tag{3.39}$$

Until this point in time in the grid cell is reached, the impinging water droplets freeze entirely to rime ice. The temporal development of the rime ice thickness is determined by the mass balance for dry mode icing (equation 2.51 with $\frac{\partial B}{\partial t} = \frac{\partial z_\mathrm{r}}{\partial t}$ and $\frac{\partial h}{\partial t} = \frac{\partial z_\mathrm{w}}{\partial t} = 0$), which results in (Zhang et al. 2016)

$$z_\mathrm{r} = \frac{\sqrt{2\mathrm{LWC} \cdot VE \frac{\rho_\mathrm{g} - \rho_\mathrm{r,0}}{z_\mathrm{c}} t + \rho_\mathrm{r,0}^2} - \rho_\mathrm{r,0}}{\rho_\mathrm{g} - \rho_\mathrm{r,0}} z_\mathrm{c}. \tag{3.40}$$

If the object stays longer than t_c, it enters the wet icing phase. The rime ice thickness has reached its maximum value ($z_\mathrm{r} = z_\mathrm{c}$) and the additional impinging water is now accreting as glaze ice and liquid water. These accretions are described by equations 3.36 and 3.37.

The new aircraft icing parameterization integrates equation 3.36 numerically, using an internal time step of $\Delta t = 1 \times 10^{-2}\,\mathrm{s}$ (or the remaining time the object stays in the grid cell, if it is lower). This low value for the internal time step is chosen to achieve an accurate distribution of the impinging water during the wet icing phase between glaze ice and liquid water accretion, as one of the main unique features of this parameterization, even if the transition into it happens close to the end of the stay in the icing environment. With z_g determined, the parameterization applies equation 3.37 to compute z_w.

Additionally, the freezing part of the icing parameterization also determines the mean accretion rates the object experienced of rime, glaze ice and liquid water by dividing the thickness values with the corresponding time it took to reach it.

It is imminent that the period of time the object stays in the grid cell is crucial for this new aircraft icing parameterization, as it determines the scope of rime ice accretion, whether glaze ice and liquid water are accreted and if so, how much of it, and also the ice and liquid water accretion rates. To get a representative value for the icing state of a grid cell, figure 3.2 shows the representative path the object takes traversing a triangular grid cell. Its travelling speed corresponds to the relative airspeed that was also previously used to determine the overall impingement efficiency. This leads to a traversing time of

$$t_\mathrm{max} = \frac{\delta s}{V_\infty} = \frac{\sqrt{\sqrt{3} \cdot A_\mathrm{cell}}}{V_\infty}, \tag{3.41}$$

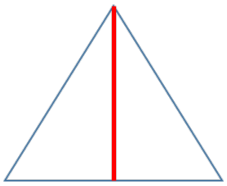

Figure 3.2: Representative path (red) an aircraft takes traversing a triangular grid cell. This information is used to compute its traversing time to determine the different phases of aircraft icing.

with the length of the path traversed δs in m and the grid cell's area A_{cell} in m^2. Using t_{max} the mean accretion rates are computed with

$$\text{IAR}_\text{r} = \frac{z_\text{r}}{t_\text{r}}; \qquad t_\text{r} = \min\left(t_\text{c}, t_{\text{max}}\right), \tag{3.42}$$

$$\text{IAR}_\text{g} = \frac{z_\text{g}}{t_{\text{max}} - t_\text{c}}, \tag{3.43}$$

$$\text{WAR} = \frac{z_\text{w}}{t_{\text{max}} - t_\text{c}}. \tag{3.44}$$

In equations 3.42 to 3.44, $\text{IAR}_{\text{r|g}}$ is the mean ice accretion rate for rime and glaze ice, respectively, in m s^{-1} and WAR is the mean water accretion rate also in m s^{-1}.

To convey an idea of how certain input variables affect this newly developed, physically based aircraft icing parameterization figure 3.3 highlights how the droplet diameter in the top left, the ambient wind speed in the top right, the radius of the cylinder in the central left, the LWC in the central right and the ambient air temperature in the bottom panel alter two crucial quantities for the aircraft icing process, the overall impingement efficiency and the critical ice thickness, which are represented by the black and the blue curves, respectively. For each plot the respective other variables are held constant at 30 µm for the droplet diameter, 89.4 m s^{-1} for the ambient wind speed, 3.5 cm for the cylinder radius, 0.1 g m^{-3} for the LWC and -10 °C for the ambient air temperature. As the top plots and the central left one show, the corresponding variables affect both the overall impingement efficiency and the critical ice thickness. For the droplet diameter, the changes are stark for low values, with an increase in droplet diameter increasing the overall impingement efficiency and decreasing the critical ice thickness. Varying the ambient air speed induces changes to a lesser scale in the shown range. However, the changes are also stronger for lower wind speed values and an increasing wind speed yields increased overall impingement efficiency and reduced critical ice thickness. Changes in the cylinder radius are significantly less impactful regarding the critical ice thickness (note the corresponding ordinate is linearly scaled for this variable, contrary to the logarithmic scales for the other). Additionally contrary to the previous variables an increase in cylinder radius in the shown range results in a reduced overall impingement efficiency, while the critical ice thickness increases. The remaining plots show that effects on the overall impingement efficiency are not required to impact the critical ice thickness, as both the LWC and the ambient air temperature show no effect on the overall impingement efficiency, yet still influence the critical ice thickness. Increasing the LWC reduces the critical ice thickness. This is especially strong for low LWC values. While increasing ambient air temperature also decreases the critical ice thickness, the highest impact is experienced at the highest temperature values.

Contrary to current operational prediction schemes and analytical ice accretion algorithms, this new aircraft icing parameterization is used online in ICON-ART, explicitly considers further microphysical quantities, uses a more thorough physical description of the relevant processes and gives a more detailed quantification of the intensity of aircraft icing conditions.

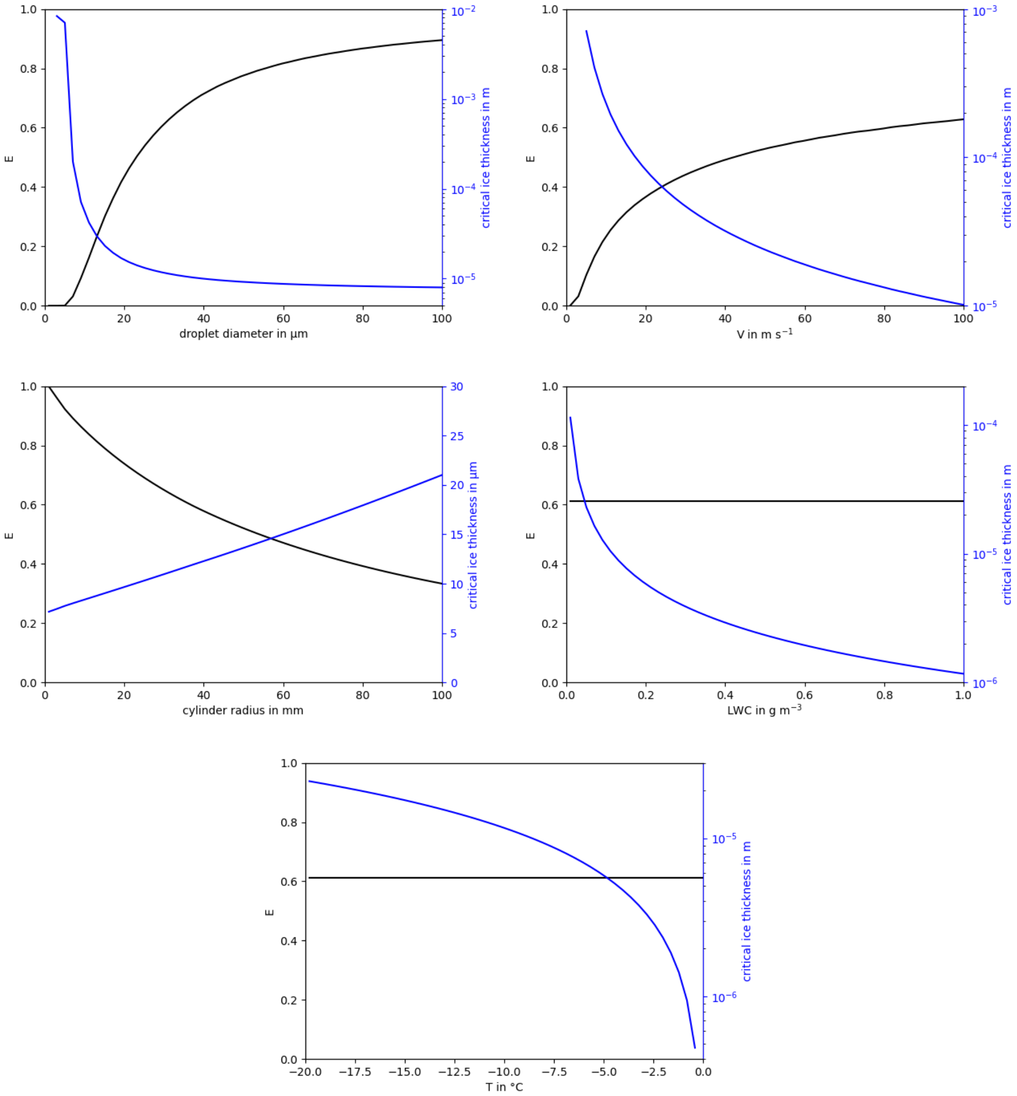

Figure 3.3: Sensitivity of the overall impingement efficiency (black) and the critical ice thickness (blue), as computed by the newly developed aircraft icing parameterization, on the droplet diameter (top left), the ambient wind speed (top right), the cylinder radius (center left), the LWC (center right) and the ambient air temperature (bottom).

3.4 Adaptation of model setup configurations

As the present work is a modelling study using the ICON-ART model, the following part details the general and specific configurations used for the different simulations conducted. All simulations are performed using the so-called „limited area mode“ (LAM) of the ICON-ART model, restricting the computations to a limited area instead of the whole globe. Hence, additionally to the information about the initial conditions, the model needs information about meteorological data at the boundaries, which are updated in hourly intervals. Both the initial and the boundary conditions originate from preparatory global, nested ICON-ART simulations performed at a lower horizontal resolution, namely on a R3B09 grid with an effective gridsize of about 3.3 km. The actual LAM simulations also use a nested setup, ultimately performing the computations on a R3B11 (and in one case on a R3B12) grid, which has an effective gridsize of about 800 m (and 400 m). The timestep chosen for the inner most nest is 5 s (and 2.5 s). The simulation period covers a span of 24 h, during which the data is output in 10 min-intervals. It is additionally noted that due to the high horizontal resolution convection is explicitly computed instead of being parameterized and the two-moment microphysics scheme of Seifert and Beheng (2006) is employed. Regarding cloud droplet nucleation, prognostic aerosols are used as cloud condensation nuclei.

The domains of the simulations conducted differentiate between four cases, three of which originate from two case studies. The fourth one is motivated by a local report of icing by a hobby pilot. The first case study is conducted around Cold Lake, Canada on the 24th and the 26th of October 2016 and is labelled CAN24 and CAN26, respectively. The second case, labelled SPN, is located at the Guadarrama Mountains in Spain, while the case around the local report of icing is labelled BWF, as the icing incident occured in Baden-Wuerttemberg, Germany. These cases are further detailed in the upcoming chapter 4. The limited area grids employed for the different cases span from 52°N 112°W to 56°N 108°W for the CAN24 and CAN26 case, from 39°N 5.5°W to 43°N 2°W for the SPN case and from 46°N 6°E to 52°N 11°E for the BWF case. The simulation periods start at 0 UTC on the 24th of October 2016, 26th of October 2016, 1st of February 2012 and 7th of December 2019 for the CAN24, CAN26, SPN and BWF case, respectively. The BWF case is the aforementioned case, where the simulations nest down to R3B12.

The specific simulations that are performed onto the aforementioned cases orient on the research questions introduced: The main simulation represents a reference scenario, which gives an unaltered representation of the icing situation based on the newly developed physically based aircraft icing parameterization, to which the other simulations compare against. This reference scenario is labelled REF, performs the overall impingement computation by explicitly considering the cloud droplet spectrum, as described in chapter 3.3, and employs a relative airspeed of $89.4\,\mathrm{m\,s^{-1}}$. The cylinder to which the ice and water accretion is simulated has a diameter of 7 cm, a value regularly used in aircraft icing research enabling comparison possibilities, and no heating of the exposed surface is regarded, so it is considered to have the surrounding's air temperature. Additionally, the initial aerosol load acting as CCN, which is sea-salt in these simulations, is set to $5 \times 10^{8}\,\mathrm{m^{-3}}$ and no further emission of the material is considered. The number density of the ice nucleating particles (INP), which are mineral dust particles in these simulations, is set to $3 \times 10^{6}\,\mathrm{m^{-3}}$. Although the INP are not part of the sensitivity analyses conducted in the present work, the model atmosphere should not be void of it. This is due to heterogeneous ice nucleation, for which the parameterization by Phillips et al. (2013) is used in the model, limiting the frequencies of supercooled environments by glaciation of the supercooled cloud.

To investigate the question, whether the explicit consideration of the droplet spectrum is beneficial, the BULK simulations are performed. These compute the overall impingement efficiency only regarding the mean droplet size and therefore not considering the actual droplet spectrum.

The NC01 and NC10 simulations deal with the aircraft icing's sensitivity to the cloud droplet number concentration. They apply a factor of 0.1 and 10.0, respectively, to it before its use inside the aircraft icing parameterization. The remainder of the configuration matches REF.

ACI01 and ACI10 simulations apply the same set of sensitivity factors. However, the point of application differs, as

Table 3.1: Overview of the simulations conducted in the present work. The bold font highlights the change in setup compared to the REF simulation.

Simulation	Explicit treatment of droplet spectrum	Factor applied to droplet number density	Factor applied to CCN number density	Relative airspeed in $\mathrm{m\,s^{-1}}$
REF (or V89)	yes	1	1	89.4
BULK	**no**	1	1	89.4
NC01	yes	**0.1**	1	89.4
NC10	yes	**10**	1	89.4
ACI01	yes	1	**0.1**	89.4
ACI10	yes	1	**10**	89.4
V60	yes	1	1	**60.0**
V30	yes	1	1	**30.0**

they alter the aerosol load passed as CCN to the cloud droplet nucleation parameterization. Its result is the number density of nucleated water droplets, a quantity used by the new aircraft icing parameterization, hence enabling the investigation of the aircraft icing's sensitivity towards the aerosol load acting as CCN. The other configuration settings are equal to those of REF.

The final research question arises directly out of the newly developed aircraft icing parameterization and focuses on the role of the relative airspeed. Answering this question, the simulations V60 and V30 are used. They differ from the REF simulation by employing a relative airspeed of $60\,\mathrm{m\,s^{-1}}$ and $30\,\mathrm{m\,s^{-1}}$, respectively. Additionally, it is noted that the REF simulation is also labelled V89 (as it employs a relative airspeed of $89.4\,\mathrm{m\,s^{-1}}$) in that part of the sensitivity analysis.

Table 3.1 gives an overview of the conducted simulations and highlights which parts of the experiment simulations are altered compared to the reference simulation.

4 Simulations of icing environments with the new parameterization

The previous parts of the present work explain the bases and backgrounds used to develop the new aircraft icing parameterization and how it is configured for its further usage. The upcoming part is dedicated to the application of the parameterization. For this, two icing related case studies are simulated: The first one was conducted by Boudala et al. (2019) at Cold Lake, Canada at the end of October 2016. It is chosen due to the setup of an extensive observational network, enabling comparisons of multiple quantities. The second one chosen was conducted by Fernández-González et al. (2014) flying over the Guadarrama Mountains in Spain at the start of February 2012, as it highlights shortcomings of current operational icing prediction schemes. An additional simulation is presented, motivated as a local application by a private report of icing of a light aircraft by a hobby pilot in Baden-Wuerttemberg, Germany in December 2019.

4.1 Case study: Cold Lake in Alberta, Canada

Aircraft icing reports are common at Cold Lake in Alberta, Canada. However, as forecasting aircraft icing poses a challenge, Boudala et al. (2019) set up an observational network around the Cold Lake Regional Airport, 54°N and 110°W, to investigate weather conditions associated with such icing events (Boudala et al. 2019). The study area is 541 m above sea level. The aircraft icing observations are provided by a number of pilot reports (PIREPs), which determine the observational data to be examined. Most icing events were reported during takeoff and landing (Boudala et al. 2019). Figure 4.1 shows the location of Cold Lake Regional Airport. Boudala et al. (2019) focus their analyses on two dates, the 24th and 26th of October 2016, during which they also evaluate two empirical ice accretion algorithms, whose results are based on the ice accretion onto a nonrotating cylinder, experiencing a

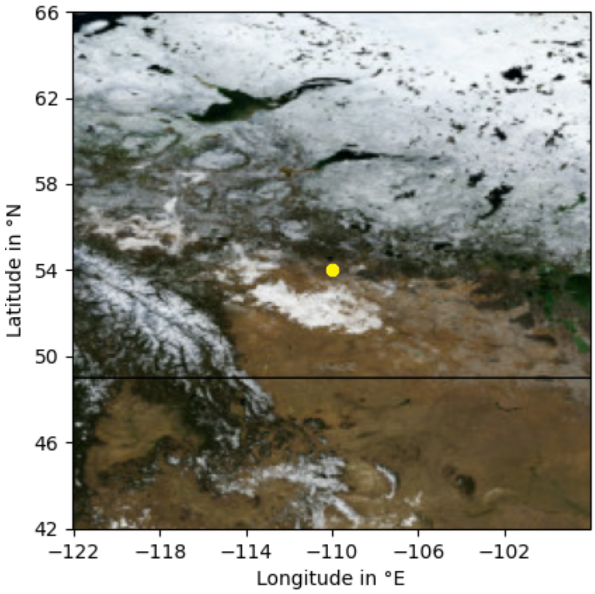

Figure 4.1: Location of Cold Lake Regional Airport in Alberta, Canada (marked with a yellow dot).

relative airspeed of 89.4 $\mathrm{m\,s^{-1}}$ and 60.0 $\mathrm{m\,s^{-1}}$. Those relative airspeeds are linked to cruise travel and take-off or landing, respectively. Boudala et al. (2019) describe these ice accretion algorithms as

$$\mathrm{IAR1} = \frac{E \cdot \mathrm{LWC} \cdot V}{\rho_\mathrm{i}} \tag{4.1}$$

$$\mathrm{IAR2} = E \cdot \mathrm{LWC} \cdot V. \tag{4.2}$$

IAR is short for ice accretion rate, IAR1 is given in $\mathrm{m\,s^{-1}}$ and IAR2 in $\mathrm{kg\,m^{-2}\,s^{-1}}$. E is the dimensionless overall impingement efficiency and V is the relative airspeed the cylinder experiences. The overall impingement efficiency is calculated empirically by Boudala et al. (2019), following the formulation by Finstad et al. (1988),

$$E_\mathrm{emp} = A - 0.028 - C\,(B - 0.0454)\,. \tag{4.3}$$

A, *B* and *C* are coefficients obeying

$$A = 1.066K^{-0.0616}\exp\left(-1.103K^{-0.688}\right), \tag{4.4}$$

$$B = 3.64K^{-0.498}\exp\left(-1.497K^{-0.694}\right) \qquad \text{and} \tag{4.5}$$

$$C = 0.00637\,(\Phi - 100)^{0.381}\,. \tag{4.6}$$

„using the dimensionless Stokes number K and Langmuir's parameter Φ" (Boudala et al. 2019, p. 491). Additionally a „High Resolution Deterministic Prediction System (HRDPS)" (Boudala et al. 2019, p. 488) with a horizontal grid size of 2.5 km is used aiding in the analysis process. For further details about the observational instruments and model system in use, the author refers to Boudala et al. (2019) and Milbrandt et al. (2016).

4.1.1 24th of October 2016 (CAN24)

On the 24th of October 2016, Cold Lake lied beneath a large scale ridge of the 500 hPa geopotential, in which a small trough formed in the early hours approaching Cold Lake over the course of the day, as is shown in the top plots in Figure 4.2. The bottom plots in Figure 4.2 further indicate a low pressure system at the North American west coast, which leads to predominantly eastern winds of about 20 $\mathrm{km\,h^{-1}}$ throughout the day. According to the station data at Cold Lake (Environment and Climate Change Canada 2022a) the atmosphere was very humid with relative humidity above 90 % throughout the day, leading to fog, with temperatures around freezing reaching a maximum value of 1.2 °C.

At 18:49 UTC a transport aircraft reported light icing that day, which it encountered at 217 m above ground level (Boudala et al. 2019).

The top left plot in figure 4.3 shows the three dimensional distribution of the simulated LWC using ICON-ART encountered in the investigation area around the time the icing was reported. With non-zero values near the ground level, this matches well with the reported foggy conditions mentioned above. Overall the situation presents itself as predominantly stratiform with most of the LWC being found towards the North and East of the simulated area. The top right plot displays the corresponding distribution of the mean droplet diameter, indicating droplet sizes being around 20 to 30 µm in the majority of instances. There are only a few instances with droplets smaller than 10 µm or with SLDs (larger than 40 µm). The bottom left plot highlights the supercooled nature of the clouds by showing the cloud temperatures simulated, while the bottom right plot presents an idea of the icing intensity by showing the three dimensional distribution of the simulated thickness of the entire ice layer (rime and glaze ice) expected to accrete when traversing the grid cell. This is a result of the newly developed aircraft icing parameterization. The plot shows a high spatial heterogeneity in the icing intensity, especially in the vertical dimension. The highest

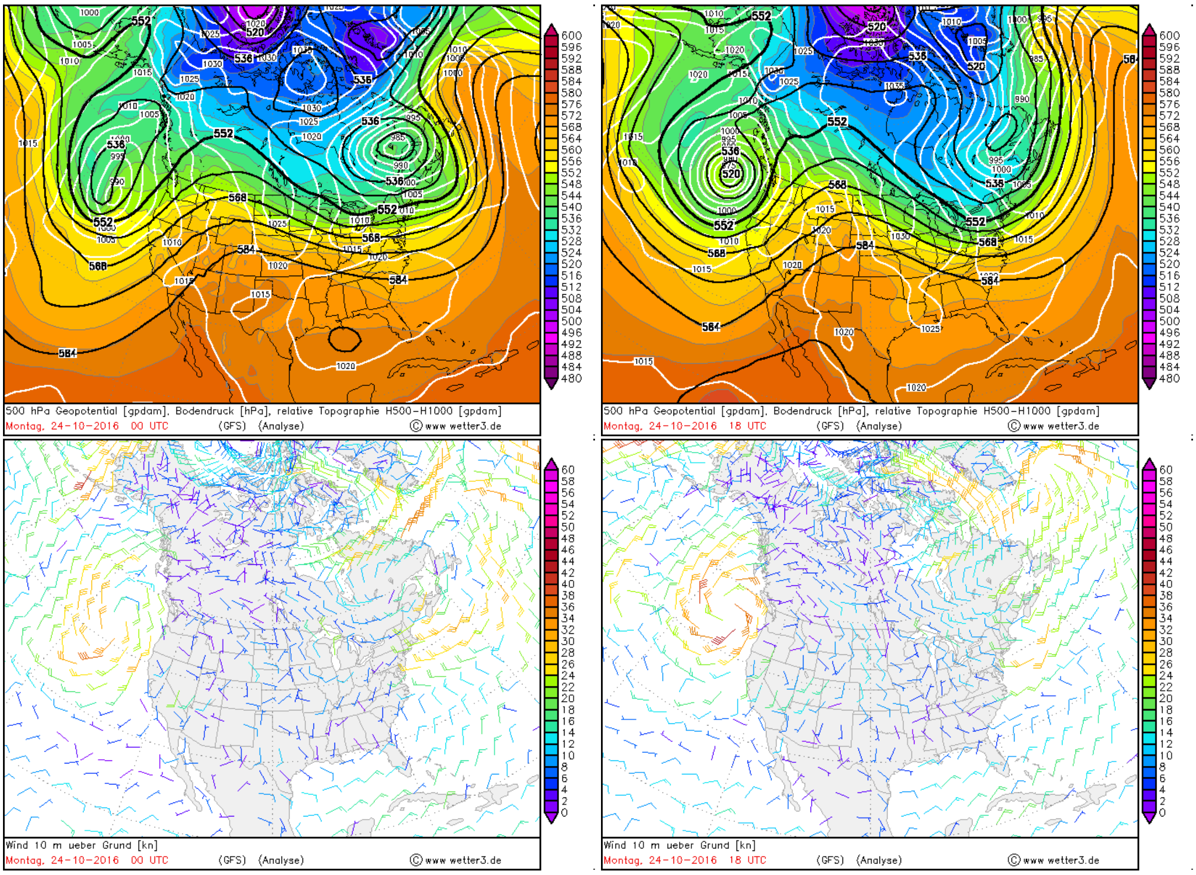
500 hPa Geopotential [gpdam], Bodendruck [hPa], relative Topographie H500–H1000 [gpdam]
Montag, 24–10–2016 00 UTC (GFS) (Analyse) © www.wetter3.de
500 hPa Geopotential [gpdam], Bodendruck [hPa], relative Topographie H500–H1000 [gpdam]
Montag, 24–10–2016 18 UTC (GFS) (Analyse) © www.wetter3.de
Wind 10 m ueber Grund [kn]
Montag, 24–10–2016 00 UTC (GFS) (Analyse) © www.wetter3.de
Wind 10 m ueber Grund [kn]
Montag, 24–10–2016 18 UTC (GFS) (Analyse) © www.wetter3.de

Figure 4.2: Synoptic weather situation for North America on 24th of October 2016: (top) 500hPa Geopotential height and (bottom) 10 m wind speed at 00 UTC (left) and 18 UTC (right), [Source: (Behrendt and Mahlke 2003)]

icing intensity values can be found in the northern parts of the simulation area in the higher altitudes.
Boudala et al. (2019) analyse the icing conditions by investigating time series of vertical profiles for several quantities. The results of the present work are compared against those in the following: Figure 4.4 shows the temporal development of the vertical profiles for temperature in the left and specific humidity in the right panel for the investigated date at the three grid cells surrounding 110°W and 54°N. The time and altitude of the reported icing are marked with a yellow dot and show that it occured in a humid and supercooled environment. Although the simulation (REF as described in chapter 3.4) is basic, it reproduces the results in Boudala et al. (2019) well. However, at around 22 UTC and an altitude of 2000 m, Boudala et al. (2019) simulated a more humid environment with respect to the specific humidity. As liquid, not gaseous, water is required for aircraft icing, the specific humidity may only act as an indicator for such environments. More relevant quantities are the LWC and the cloud droplet number density, determining the droplet size, which is a crucial quantity for the droplet impingement. Figure 4.5 presents those two cloud related quantities. The yellow dots in both plots indicate that liquid water is simulated at the time and altitude the icing was reported. In general the structure of the LWC again fits Boudala et al. (2019) well. However, this basic setup seems to underestimate the quantitative value. The cloud droplet number density, however, tends to be overestimated in some instances, but reproduce the overall distribution presented by Boudala et al. (2019) well. This suggests that the chosen value for the aerosol load of $5 \times 10^8\,\mathrm{m}^{-3}$ is a fitting representation. Moving towards analysing actual icing quantities, figure 4.6 shows the overall impingement efficiency calculated based on the empirical algorithm used in Boudala et al. (2019) (E_{emp}) in its left panel and as a result of the newly developed parameterization used in the present work (E) in its right. As the yellow dots indicate, the reported aircraft icing event occured in an environment, in which both variants for the overall impingement efficiency show positive values, so parts of the LWC is expected to impinge onto the

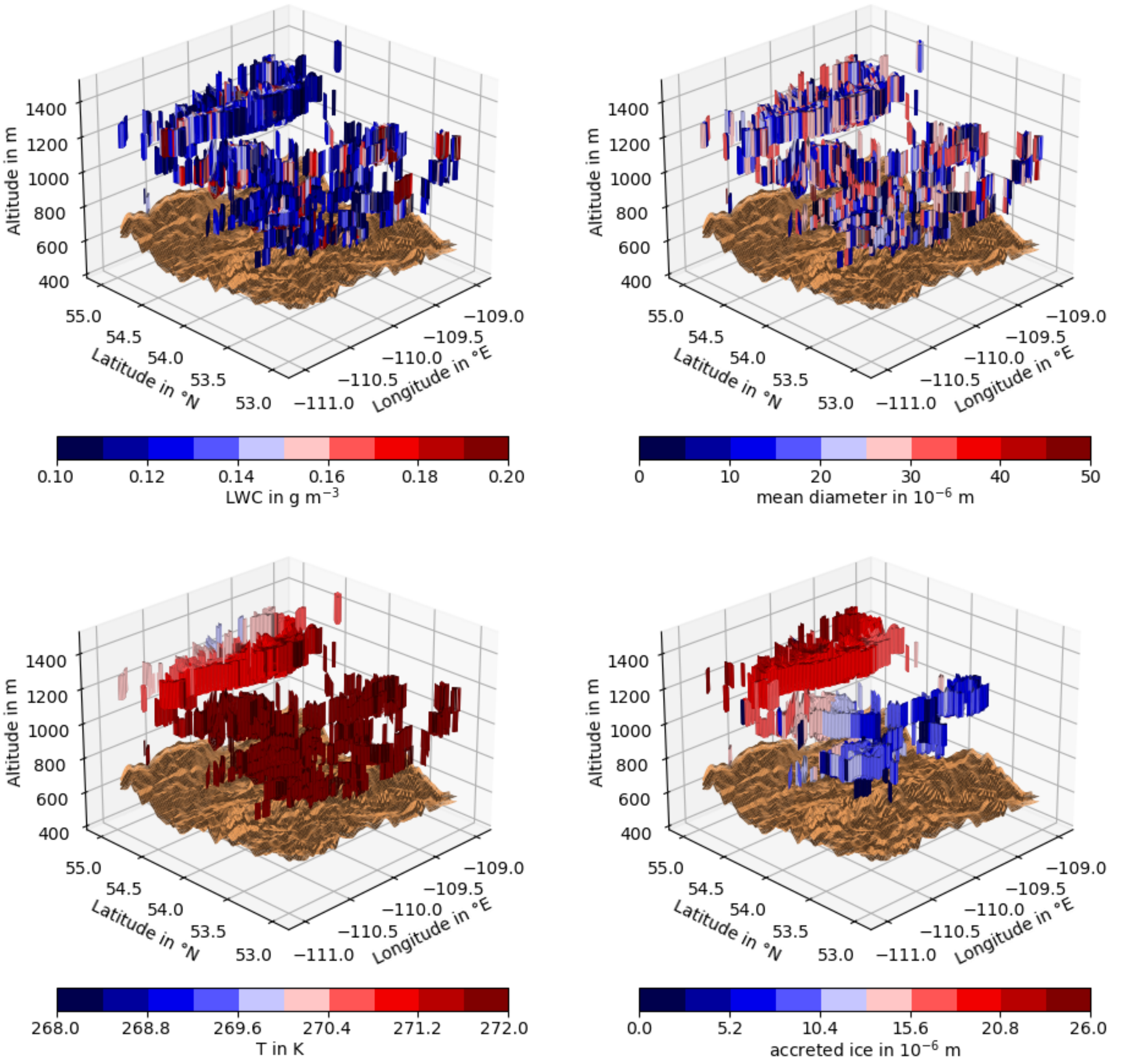

Figure 4.3: 3D distribution of simulated LWC (top left), mean droplet diameter (top right), cloud temperature (bottom left) and accreted ice (bottom right) around Cold Lake on 24th October 2016 at 18:50 UTC, matching the icing report. Only environments with a LWC of at least $0.1\,\mathrm{g\,m^{-3}}$ are displayed.

aircraft. However, the newly developed parameterization returns a lower impingement efficiency value than the empirical formulation in this environment. Overall, the two plots point towards two main differences between the impingement efficiency variants: First of all, the E_{emp} values cap out at around 0.7, while the more physically based approach of the newly developed parameterization gives E values of up to 0.9. Additionally, the lower end of the range is more represented in the new parameterization, which leads to the second point. Compared to the empirical formulation, the new parameterization offers a greater differentiation of the impingement efficiency values. To further investigate the validity of these points, this local analysis hints at, figure 4.7 shows the distribution of the overall impingement efficiency over the entire simulation domain and period for the empirical formulation in the left and the new parameterization in the right panel. These histograms support the statements above, as the empirical formulation does range to about 0.7 while the new parameterization also gives values above 0.8. Furthermore, the primary peak shown in the distribution of the empirical formulation reaches higher values as the one for the new parameterization and the secondary maximum for the latter peaks at lower values than for the former. This indicates a greater differentiation of this quantity in the new parameterization, which is confirmed, as the standard deviation of the right distribution of 0.256 is higher than the 0.197 of the left one. The overall

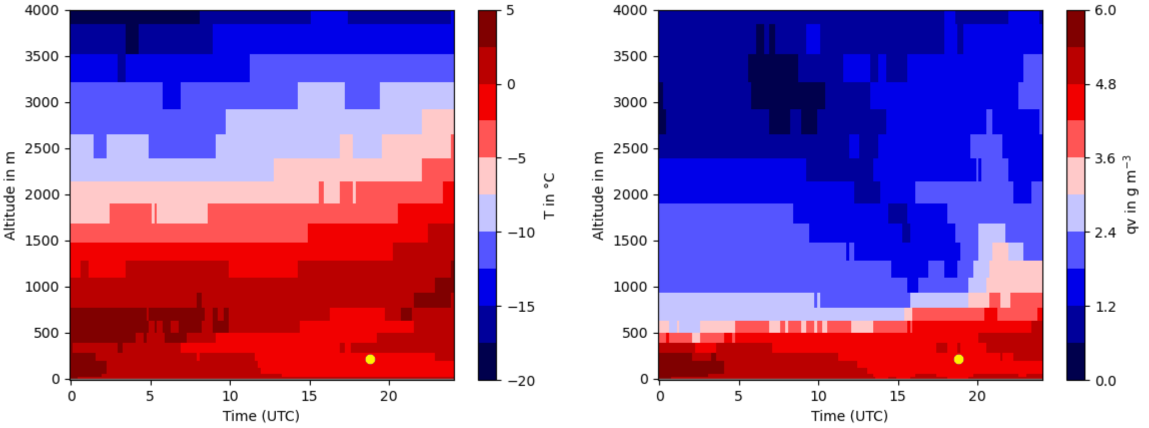

Figure 4.4: Time series of vertical profiles for temperature (left) and specific humidity (right) at Cold Lake on 24th October 2016 as simulated by the model, the icing report (18:49 UTC at 217 m of altitude) is marked as a yellow dot.

impingement efficiency is a driving factor for aircraft icing, since it is one of the quantities determining how much of the ambient LWC gets in contact with the aircraft, however, on its own it is not sufficient to characterize the icing environment. For this Boudala et al. (2019) use ice accretion rates, calculated by the above mentioned ice accretion algorithms. Figure 4.8 shows what separates the newly developed parameterization from those simple algorithms. The latter only consider ice (with one density) and neglect water that may remain liquid and therefore freeze upon different parts of the aircraft. The left plot shows the so called critical ice thickness and the right one the critical time, after which the critical ice thickness is reached. Until the critical ice thickness is reached, icing occurs only by the accretion of rime ice, after the critical time has past, glaze ice and liquid water are accreted. The plots show that for this case, the critical ice thickness is mostly around a few micrometers and is reached in the first second staying in the icing environments. However, there are, if rare, also cases where the critical ice thickness is several meters and the critical time surpasses several hours. In such cases it is safe to assume that the entirety of the icing event stays dry with no liquid water remaining behind. But for the most part, an icing event has both a dry and a wet phase, which can easily be understood considering that the passing time through the grid cell for an aircraft in this simulation is about 12.5 s. Figure 4.9 presents the results the new icing parameterization provides for this given situation as it shows the temporal development of the vertical profiles for the accreted thickness in its left and the accretion rate in its right column for rime ice in the top row, glaze ice in the middle row and liquid water in the bottom row according to the new icing parameterization. The thickness of the rime ice layer

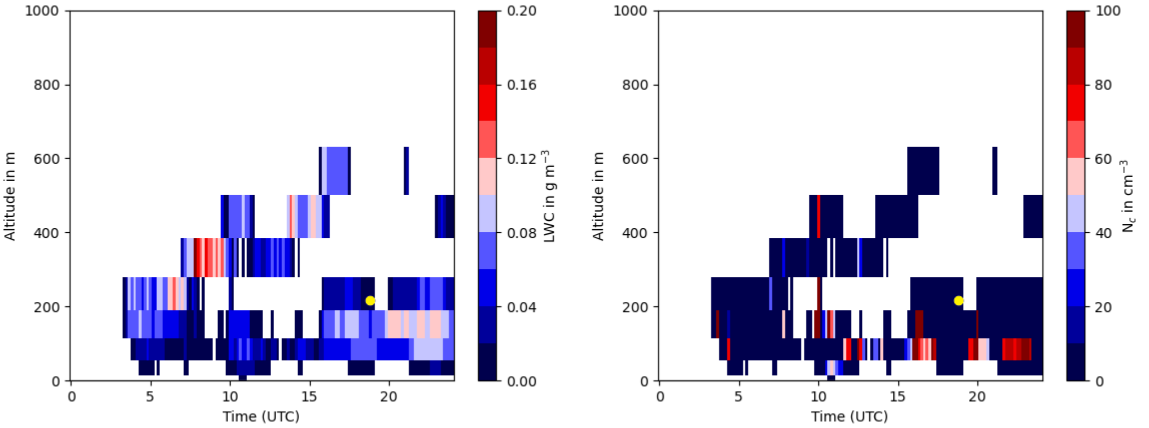

Figure 4.5: Time series of vertical profiles for LWC (left) and cloud droplet number density (right) at Cold Lake on 24th October 2016 as simulated by the model, the icing report (18:49 UTC at 217 m of altitude) is marked as a yellow dot.

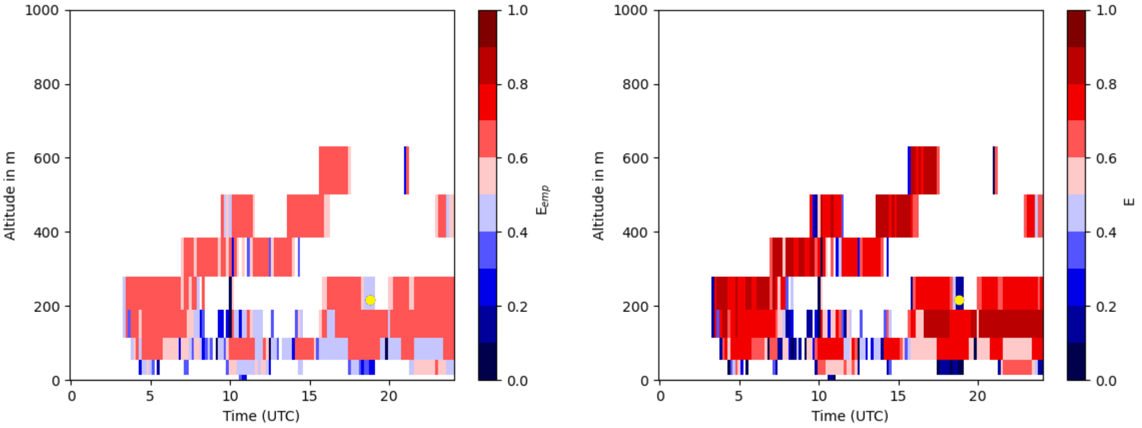

Figure 4.6: Time series of vertical profiles for overall impingement efficiency, calculated with an empirical formulation (left) and as the result of the new parameterization (right) at Cold Lake on 24th October 2016, the icing report (18:49 UTC at 217 m of altitude) is marked as a yellow dot.

in the top left plot resembles the plot for the critical ice thickness of figure 4.8 in most instances, which meets expectations as both represent the dry icing phase. While the critical ice thickness gives the maximum extent of it, the rime ice thickness shows the actual achieved value. The high resemblance of the two plots shows that in most instances the wet icing phase is initiated by surpassing the critical value. However, there are also instances, where the actually achieved rime ice thickness is below the critical value, indicating only the dry icing phase being in effect. One of these is, interestingly, around the point of the icing report, others are, e.g. in the lowest layer at around 17 UTC to 19 UTC. The rime accretion rates in the top right plot indicate that in most instances the accretion is around $1\,\mathrm{cm\,h^{-1}}$ to $2\,\mathrm{cm\,h^{-1}}$ which relates to a trace to light icing environment. Nevertheless, from around 8 UTC to 10 UTC the rime icing rates are higher, indicating more moderate (rime) icing intensities. It is noted that high rime accretion rates do not need to coincide with high rime thickness values. The plot for the glaze ice thickness in the left center shows that not only is rime ice not the sole contributor to the ice accretion but also that its contribution can be significantly less than that of glaze ice. Additionally, the plot confirms the previously identified sections, where the rime ice accretion is less than the critical ice thickness, as those sections show no glaze ice accretion and therefore do not initiate the wet icing phase. While the final thickness of the accreted glaze ice tends to exceed that of rime ice, its accretion rate is heavily reduced compared to the rime accretion rate. The explanation for this lies in the fact that the overall accretion rate is for the most part determined by the impinging water flux, which remains undisturbed when changing from the dry to the wet icing phase in this new aircraft icing

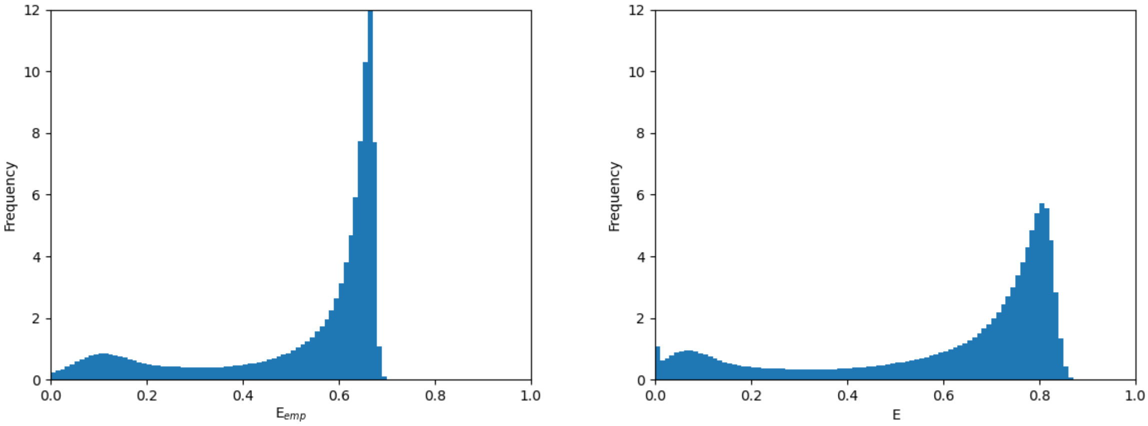

Figure 4.7: Histograms (relative frequency) of the overall impingement efficiency, calculated with an empirical formulation (left) and as the result of the new parameterization (right) for the entire simulation domain and period (24th October 2016).

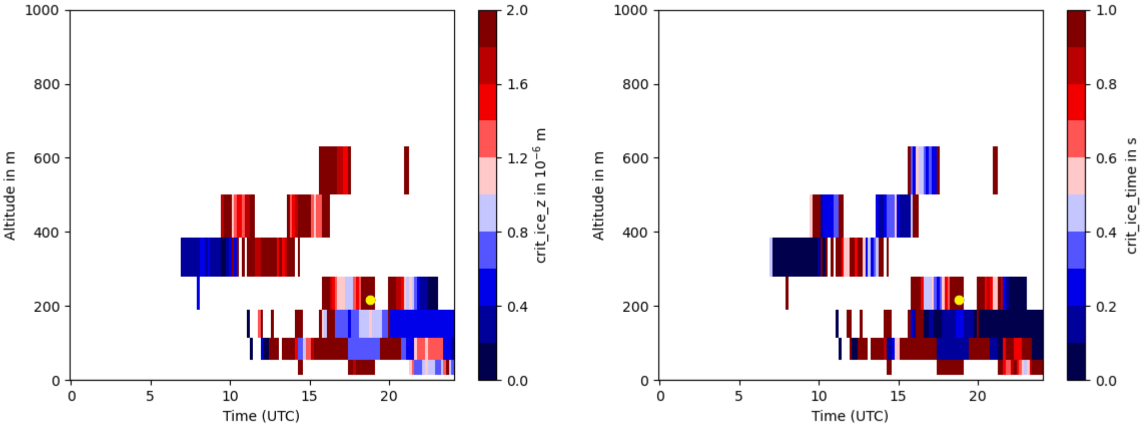

Figure 4.8: Time series of vertical profiles for the critical ice thickness (left) and the critical time (right) at Cold Lake on 24th October 2016, the icing report (18:49 UTC at 217 m of altitude) is marked as a yellow dot.

parameterization. However, the impinging water is now only partially frozen, so only parts of the incoming flux lead to ice accretion while the remainder feeds the liquid water film. In addition, but only to a minor extent, the higher density of glaze ice compared to rime ice further reduces the glaze accretion rate. The simultaneously to glaze ice accreted liquid water exceeds its accretion partner in most cases as the bottom plots indicate. In those cases the vast majority of the impinging water does not freeze immediately at around the impinging zone. This, however, does not mean that this part of the water is not freezing at all and does not contribute to the dangers of aircraft icing. This liquid water flows downstream the aircraft's airfoil, ultimately encountering surfaces on which it can freeze. So beyond the mass it adds, it also impacts parts of the aircraft that may not be as well protected from icing to occur as the impinging zones. These local analyses give an idea on the different scopes and relations between the individual parts of the icing process. Figure 4.10 completes those by presenting the distribution of the rime fraction, i.e. the fraction of rime ice thickness to the total thickness of the accreted water (solid and liquid) in its left plot and of the ratio between the liquid water and glaze ice accretion once the wet icing phase is initiated in its right plot. It represents the data generated during the entire simulation period over the entire domain. The rime fraction histogram supports what is hinted at in the profile plots of figure 4.9, namely that only a small part of icing incidents solely experiences the dry icing phase (rime fraction of 1). In most cases rime accretion is only a small part, seldomly surpassing 20 % of the total accretion. The isolated column at unity indicates that those cases with exclusively dry icing behave as such due to an inflated value of the critical ice thickness. Supporting the liquid water's role described above, the histogram of the ratio between its and the glaze ice's accretion shows that while cases with more glaze ice than liquid water exist (indicated by the first two columns), in most cases the liquid exceeds the solid phase. In rare cases water accretion surpasses glaze accretion by factors greater than 30, yet factors up to 10 are quite common. To further investigate these three contributors of aircraft icing, figure 4.11 presents the role the ambient air temperature exerts on these. The plot shows the thickness of the total accreted ice on the abscissa, of the water film on the ordinate and the temperature color coded. With a plethora of points of relatively high temperature compared to those of lower temperature, it can be stated that this form of aircraft icing is predominantly a phenomenon in lower and therefore warmer altitudes. Additionally, the plot indicates a limit for the total ice thickness for a given temperature, which decreases with increasing temperature, as is intuitively expected. Once water and ice thickness are about equal, the limit of the ice thickness at that temperature seems to be closely reached, emphasizing that any additional water would nearly exclusively contribute to the liquid water film.

Combining the different contributions into a mean total water accretion rate for passing through a grid cell provides a comparable value with simpler algorithms and a simplified way to evaluate the hazard imposed by aircraft icing.

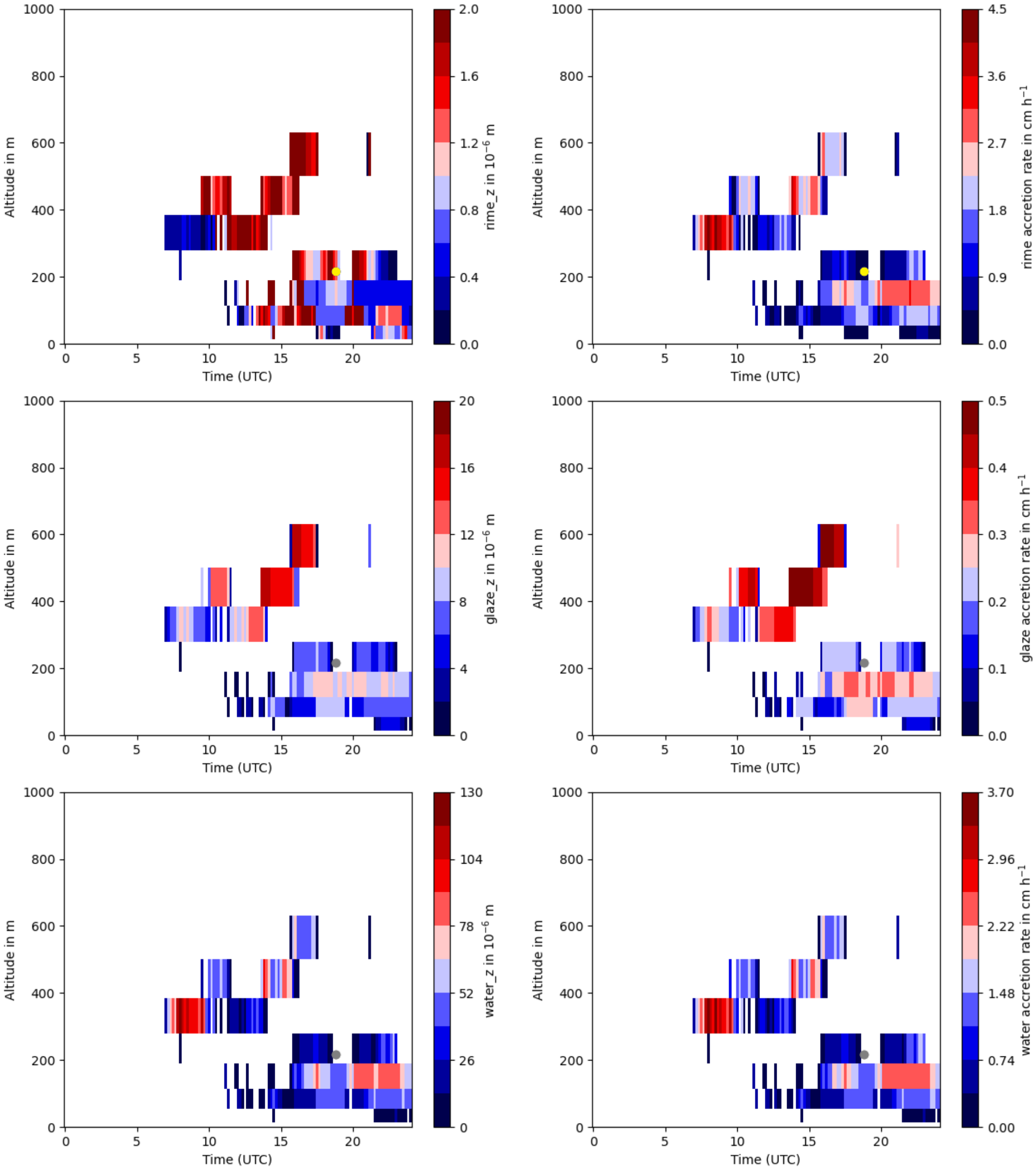

Figure 4.9: Time series of vertical profiles for the accreted thickness (left) and the accretion rate (right) for rime (top), glaze (center) and liquid water (bottom) accretion at Cold Lake on 24th October 2016, the icing report (18:49 UTC at 217 m of altitude) is marked as a yellow or gray dot.

Figure 4.12 presents this total water accretion rate as the time series of the profile at the specific location in the left plot and in the right plot as a histogram for the entire simulation domain and period. Boudala et al. (2019) give threshold values for the icing intensity scale to categorize the icing environment into trace (below 0.6 cm h^{-1}), light (0.6 cm h^{-1} to 2.5 cm h^{-1}), moderate (2.5 cm h^{-1} to 7.5 cm h^{-1}) or severe icing (above 7.5 cm h^{-1}). Those values correspond to the IAR1-algorithm used in their work and described above. When applying these same threshold values to the total water accretion rate presented in figure 4.12, the reported icing event would be considered as a trace icing scenario. However, it is imminent that the accretion rates vary spatially, especially vertically. Just below the marked spot the icing intensity would be classified as light, borderlining moderate. The histogram shows that the vast majority of icing environments around Cold Lake (for that investigated date) experience trace and light

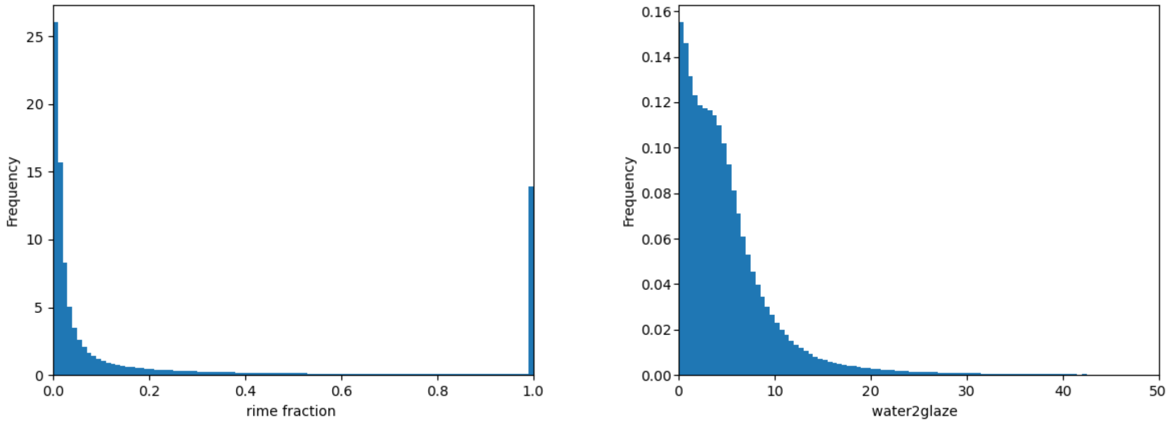

Figure 4.10: Histograms (relative frequency) of the fraction of rime accretion to the total accretion (left) and ratio between the simultaneously accreted liquid water and glaze ice (right) for the entire simulation domain and period of the 24th of October.

icing. Moderate icing intensity occurs rather seldomly and only in rare cases severe conditions are met. This is in line with reports stated by Boudala et al. (2019).

Summarizing, the newly developed aircraft icing parameterization is able to reproduce the icing conditions reported well. The physically based approach for the computation of the overall impingement efficiency used in this parameterization differs significantly from the empirical computation used by Boudala et al. (2019), both in range and variability. Especially for high impinging environments, the empirical formulation seems to hit its limits. The aircraft icing parameterization highlights a vast majority of instances with wet icing conditions, where the accreted water film often surpasses the ice thickness. Once the water accretion equals the ice accretion additional incoming water nearly exclusively remains liquid indicating a maximum ice thickness that depends on the ambient air temperature.

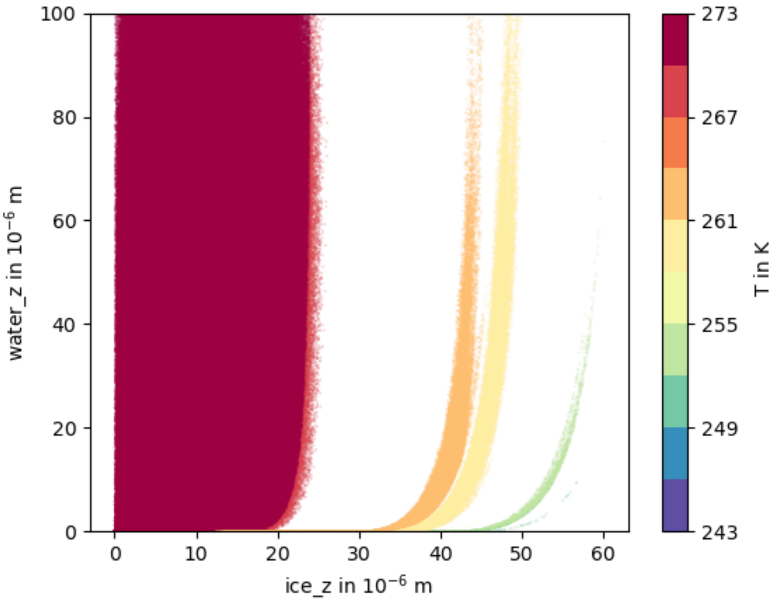

Figure 4.11: Relation between ice and liquid water accretion and temperature, the abscissa shows the accreted ice thickness, the ordinate gives the thickness of the liquid water film and the temperature of the grid cell is color coded. Data for the entire simulation domain and period is used.

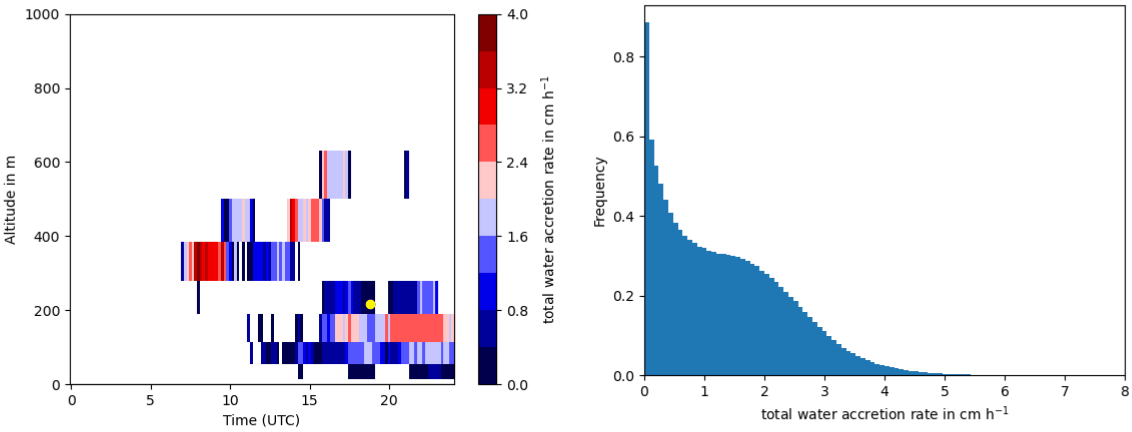

Figure 4.12: Time series of vertical profile for the total water accretion rate - rime, glaze ice and liquid water (left) and its histogram (right). The reported icing event is marked with a yellow dot in the former and the latter incorporates data for the entire simulation domain and period.

4.1.2 26th of October 2016 (CAN26)

The synoptic weather situation above Cold Lake on the 26th of October 2016 is defined by the passing of a small trough in the 500 hPa geopotential, indicated by the top plots in Figure 4.13. As the bottom plots in Figure 4.13 show, the low pressure system over the North American west coast was still present, initially determining the wind field above Cold Lake, which is described by easterly winds of around 10 km h^{-1}. However the system's influence weakens throughout the day leading to a shift to westerly winds of around 20 km h^{-1} in the second half of the day. The station data (Environment and Climate Change Canada 2022b) further indicate that the initially saturated air experiences slow drying to about 80 % relative humidity throughout the day. The air temperature is in the range of 1 to 2 °C, with the occasional rain showers.

For this day, Boudala et al. (2019) state two icing reports: At 14:42 UTC a cargo aircraft experienced light rime icing in an altitude of 2500 to 3300 m above ground level and at 19:22 UTC a fighter jet encountered icing approaching the airport in an altitude of 186 m above ground level (Boudala et al. 2019). To give an idea of the weather situation at the first icing report, the 3D-plots in figure 4.14 give an impression of the LWC in the top left, the mean droplet diameter in the top right, the cloud temperature in the bottom left and the simulated thickness of the accreted ice in the bottom right panel at 14:42 UTC. The LWC is shown in multiple layers indicating rather stratiform conditions. The clouds are located more to the North of the simulated area, where the surface is more mountaineous. The top right plot highlights that the mean droplet size is between 10 and 30 µm in most shown environments. The cloud temperatures show the supercooled nature of the clouds presented, but also indicate significant horizontal variability caused by considerably warmer air in the Northeast of the domain. The total accreted ice thickness, as shown in the bottom right plot, increases strongly with altitude, but gives also considerable values near ground level, which additionally show horizontal heterogeneity.

Similar to the previous date, Boudala et al. (2019) analysed the environment with both measurements and model data. The results of the present work are compared against those analyses in the following: The profile of the temporal development of the temperature in the left plot of figure 4.15 fits well with the model results of Boudala et al. (2019) overall, but differs in one key structural aspect. In the early hours Boudala et al. (2019) does not have a supercooled layer between 500 m and 1000 m. Both models, however, seem to underestimate the temperature measurements in the lower layers. The yellow dots indicating the time and altitude of the reported icing events show that the events all occured in sub-freezing temperatures. The specific humidity in the right plot of figure 4.15 also agrees well with Boudala et al. (2019). The elevated values at around 4:00 UTC tend to be more in line with the measurements than the model. Although these continuous quantities reveal the validity of the given model setup, they do not act as more than basic proxy information for aircraft icing conditions. Figure 4.16 adds to

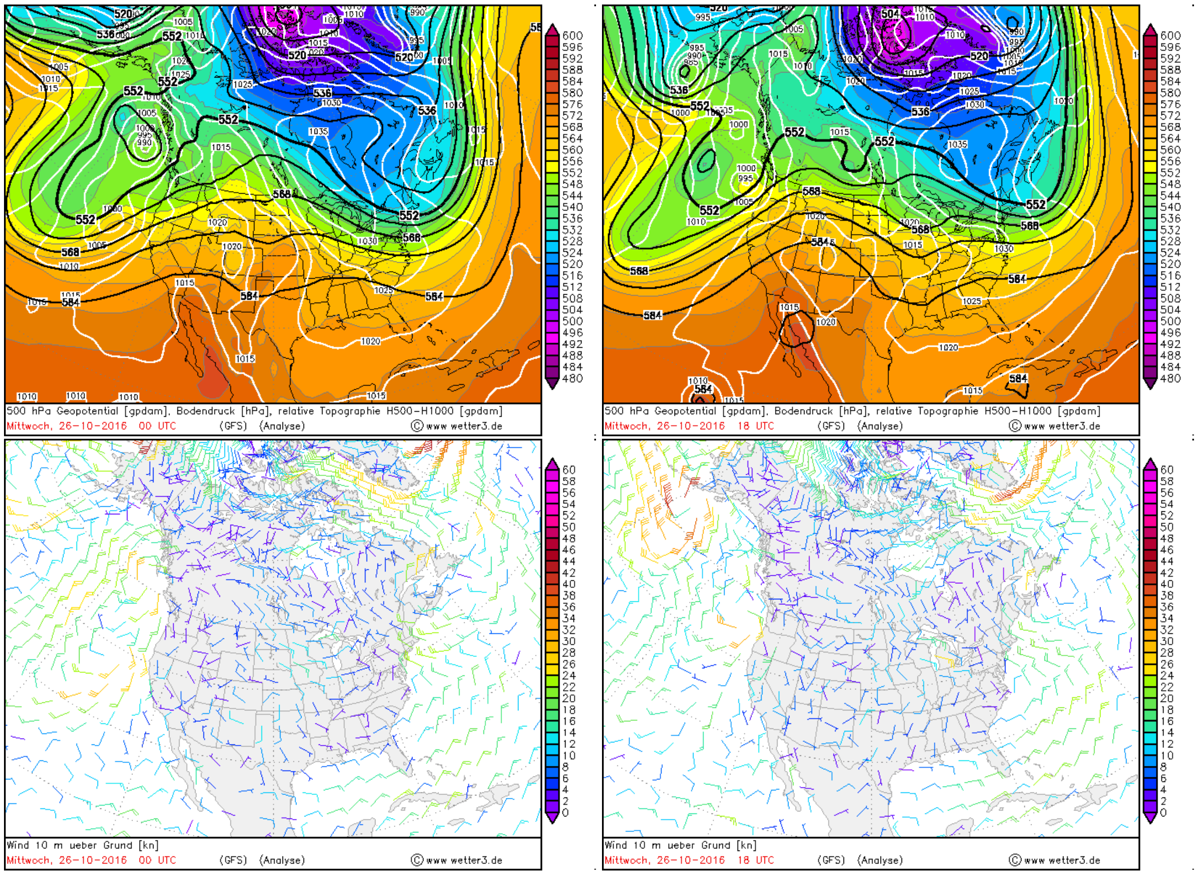
500 hPa Geopotential [gpdam], Bodendruck [hPa], relative Topographie H500-H1000 [gpdam]
Mittwoch, 26-10-2016 00 UTC (GFS) (Analyse) © www.wetter3.de
500 hPa Geopotential [gpdam], Bodendruck [hPa], relative Topographie H500-H1000 [gpdam]
Mittwoch, 26-10-2016 18 UTC (GFS) (Analyse) © www.wetter3.de
Wind 10 m ueber Grund [kn]
Mittwoch, 26-10-2016 00 UTC (GFS) (Analyse) © www.wetter3.de
Wind 10 m ueber Grund [kn]
Mittwoch, 26-10-2016 18 UTC (GFS) (Analyse) © www.wetter3.de

Figure 4.13: Synoptic weather situation for North America on 26th of October 2016: (top) 500hPa Geopotential height and (bottom) 10 m wind speed at 00 UTC (left) and 18 UTC (right), [Source: (Behrendt and Mahlke 2003)]

those by providing profiles of the temporal development for the LWC in its left panel and the cloud droplet number density in its right, which give a more thorough idea for the icing intensity, especially in combination with the temperature information. The left plot shows no LWC in the region of interest for the first icing report, 14:42 UTC between 2500 m and 3300 m of altitude and also for the second one positive LWC is modelled in slightly higher altitudes. Additionally, a comparison with the results of Boudala et al. (2019) shows differences in amplitude and structure. The descending branch between 4 and 8 UTC agrees quite well, however this plot shows a more pronounced structure between 0 and 5 UTC below 1000 m, a less pronounced one between 5 and 10 UTC around 1500 m and less LWC after 10 UTC. The data underlying these profile plots is taken from the grid cells surrounding the previously specified location of the airport (54°N 110°W), which is probably not the location the icing events were reported from, explaining the absence of icing conditions at the gray dots. As one can see in the top left 3D plot in figure 4.14, the positive LWC values in the altitudes of the first report are to the North of the domain. Also, Boudala et al. (2019) do not specify, if their presented model results are of a certain location or a spatially averaged value, so differences especially in discontinuous quantities may originate therein. The structural differences of the LWC, especially regarding the location of the larger structures, are probably due to the one key difference in the temperature field, where ICON-ART (contrary to the model used by Boudala et al. (2019)) modelled a sub-freezing layer just below 1000 m beginning at 0 UTC, see left panel of figure 4.15. This probably initiated cloud nucleation processes, which only occured later in Boudala et al. (2019), coinciding with sub-freezing air in their model. Interestingly, the ICON-ART data seems to agree better with the measurements conducted by Boudala et al. (2019) as these also show a similar structure. Supporting the claim of the non-agreement regarding the icing reports (gray dots) being a location issue, figure 4.17 shows the LWC at two different locations to the North and Northeast in the left and right plot, respectively. Lacking further information, these locations are as likely as the

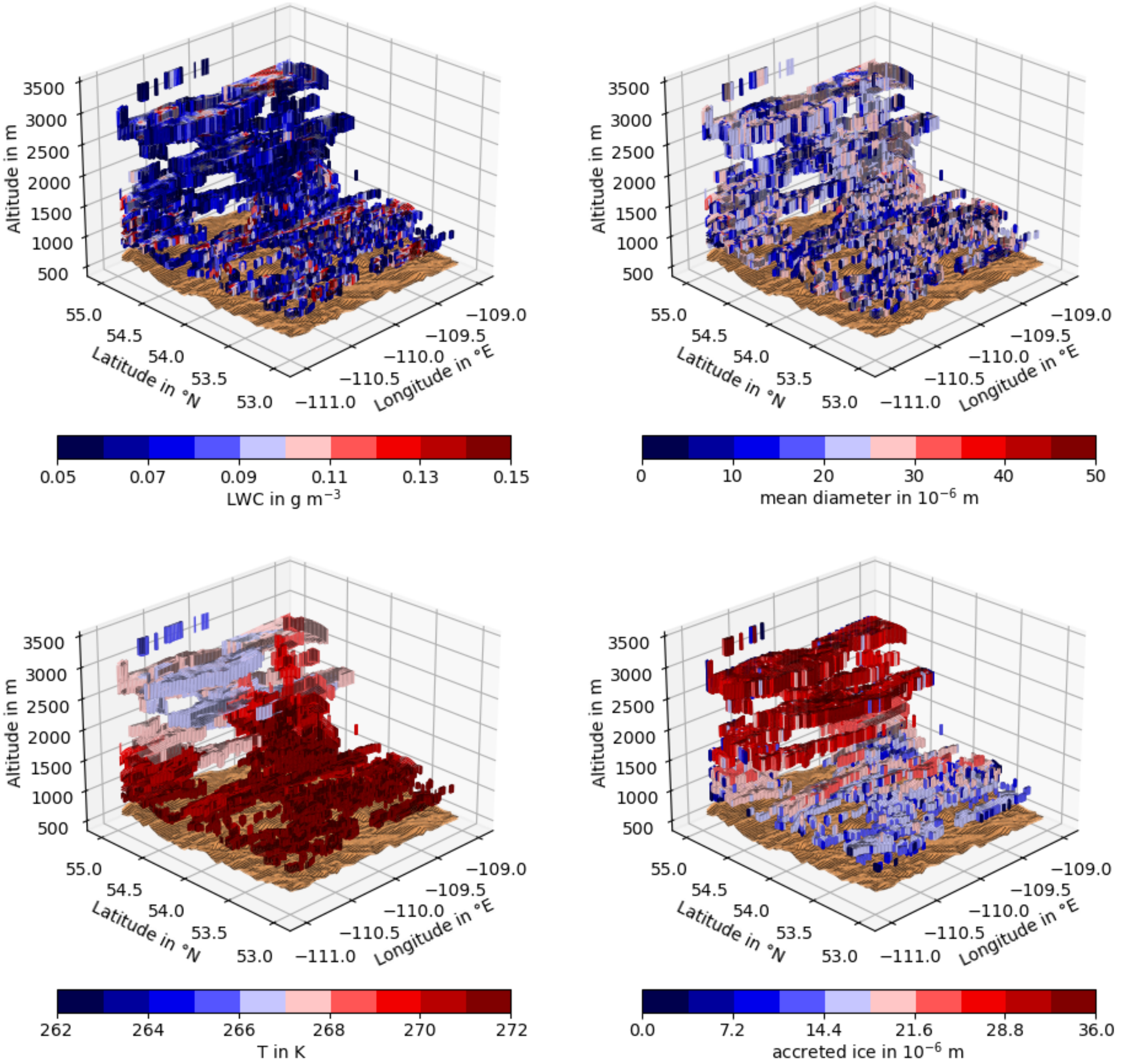

Figure 4.14: 3D distribution of simulated LWC (top left), mean droplet diameter (top right), cloud temperature (bottom left) and accreted ice (bottom right) around Cold Lake on 26th October 2016 at 14:40 UTC, matching the first icing report. Only environments with a LWC of at least 0.05 $\mathrm{g\,m^{-3}}$ are displayed.

previous one to be where the reported icing incidents occured. These plots show non-zero values for the LWC at both the times and altitudes, where the corresponding icing was reported. The cloud droplet number density in the right plots of figure 4.16 is naturally strongly linked to the LWC. Comparable to the previous case, the cloud droplet number density fits the results of Boudala et al. (2019) qualitatively well, but tends to overestimate the actual amount in some instances. The LWC and the cloud droplet number density determine the cloud droplet size and therefore the impingement efficiency, which is presented in figure 4.18. It shows the temporal development of the overall impingement efficiency's profile, calculated with the empirical algorithm used by Boudala et al. (2019) in the left (E_{emp}) and with the newly developed, physically based parameterization in the right plot (E). Comparable to the findings for the 24th of October, the achieved span of the new parameterization is greater than with the empirical formulation and it shows a larger differentiation, especially in environments with greater overall impingement efficiency. Although there are some parts, where the new parameterization yields lower values, a greater differentiation for low impingement efficiency environments is not as apparent as in the previous case. For further investigations, figure 4.19 shows the corresponding histograms of overall impingement efficiencies. The left plot shows the result of the empirical formulation, while the right plot represents the new parameterization.

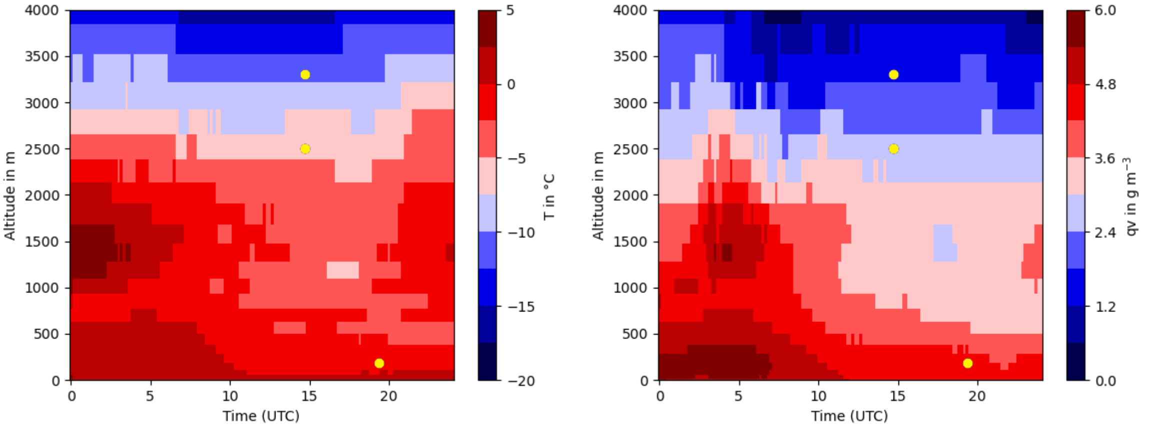

Figure 4.15: Time series of vertical profiles for temperature (left) and specific humidity (right) at Cold Lake on 26th October 2016 as simulated by the model, the icing reports (14:42 UTC at 2500 m to 3300 m of altitude and 19:22 UTC at 186 m of altitude) are marked as yellow dots.

The differences in these two histograms support the findings for the 24th of October: E_{emp} caps out at around 0.7, while the physical formulation in the new parameterization reaches E-values up to 0.9. Additionally, the latter's distribution shows more differentiation between the values on the upper end and also, to a lesser extent, on the lower end. The secondary maximum in the distribution for the physical formulation is again shifted to lesser values than for the empirical formulation. The greater differentiation between the values is confirmed by the standard deviation of the shown distributions: While the empirical formulation's standard deviation is 0.207, the physically based formulation's is higher at 0.267. Overall, the similarity between these two histograms and those for the 24th of October indicates the intrinsic nature of the differences between the represented formulations. After this investigation of the drivers and proxies of aircraft icing, further investigations focus on the actual icing quantities computed by the new parameterization. Figure 4.20 presents both the critical ice thickness in the left plot and the time until that thickness is accreted in the right plot. The critical ice thickness marks the point in the icing process, in which the dry transitions into the wet icing phase, where some of the impinging water stays liquid. Comparable to the results for the 24th of October, these plots show that the critical ice thickness only seldomly reaches values greater 10 µm and is reached in the first few seconds of entering the icing environments. With a typical time of stay in a cell of about 12.5 s, this suggests that also on this date the wet icing phase is initiated in most instances. In addition, the plots also show the vertical and temporal inhomogeneity of the critical ice thickness. In cases, this is also reflected in the critical time, especially at around 15 to 16 UTC, where the

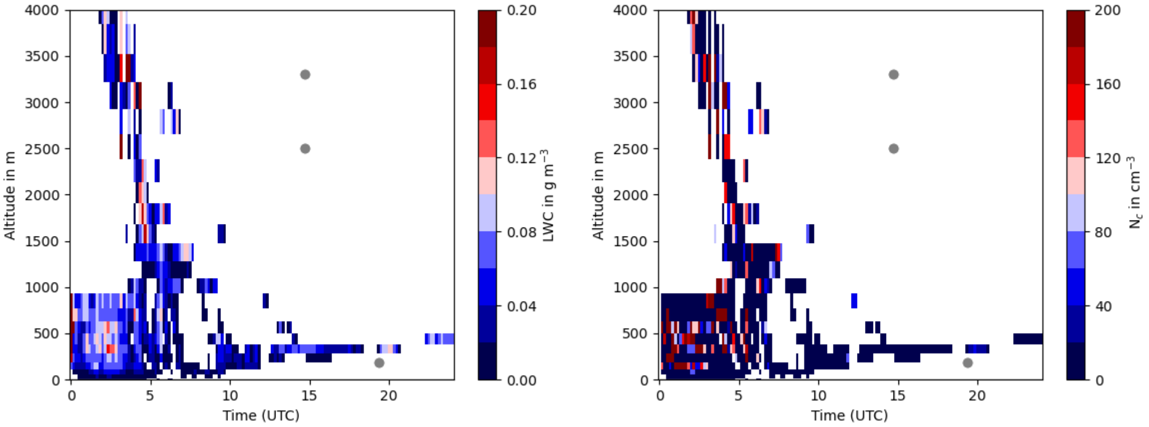

Figure 4.16: Time series of vertical profiles for LWC (left) and cloud droplet number density (right) at Cold Lake on 26th October 2016 as simulated by the model, the icing reports (14:42 UTC at 2500 m to 3300 m of altitude and 19:22 UTC at 186 m of altitude) are marked as gray dots.

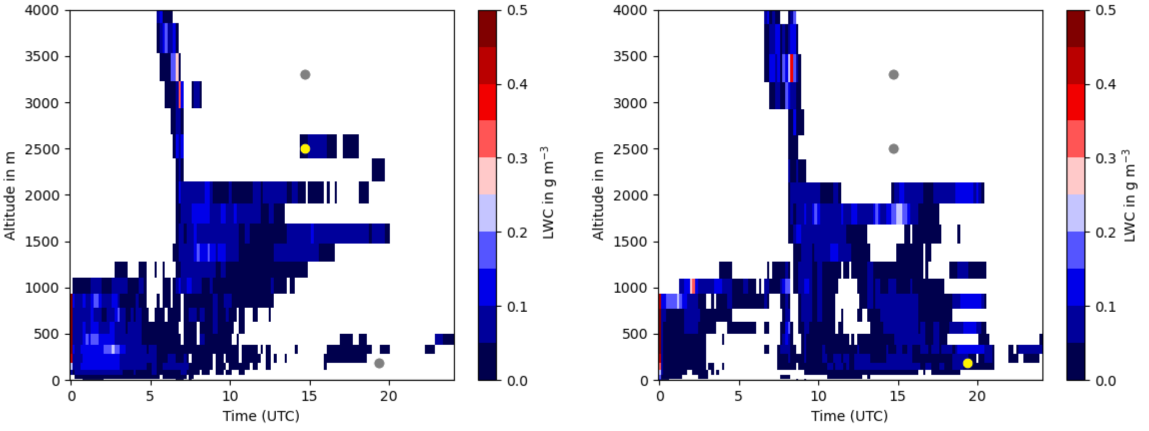

Figure 4.17: Time series of vertical profiles for LWC at potential locations for the first (left) and the second (right) icing report on 26th October 2016 as simulated by the model. the icing reports (14:42 UTC at 2500 m to 3300 m of altitude and 19:22 UTC at 186 m of altitude) are marked as gray and yellow dots.

lowest icing layer shows values that may hint to pure dry icing and one layer above wet icing is quickly initiated. For the actual ice accretion, figure 4.21 presents the temporal development of the profiles for the thickness in the left column and accretion rate in the right column of rime and glaze ice in the top and middle row as well as of the water film in the bottom row. Comparable to the 24th of October the rime ice thickness (top left) resembles the previously shown critical ice thickness for the most part, indicating that not only dry, but also wet icing takes place. However, there are instances, where the rime does not accrete up to its critical value, for example the previously mentioned lowest icing layer at around 15 to 16 UTC. In those cases, only rime ice is accreted. The top right plot of the mean rime ice accretion rate shows that in the majority of cases the rate does not go beyond 3 cm h^{-1} and the variations in both time and altitude are small. However, for this date at around 4 UTC at an altitude of 3500 m above ground, there seems to be an icing environment that reaches substantially higher rime accretion rates of around 8 cm h^{-1}. Interestingly, the accreted rime ice thickness at this point is lower than in its surrounding points, which have lower accretion rates and higher thickness values. Confirming the initiation of wet icing in the vast majority of cases, the plot for the glaze ice thickness (center left) shows positive values mostly everywhere, where also rime icing occured. Additionally it confirms, the previously assumed pure dry icing happening in the lowest layer at around 15 to 16 UTC, as only for a brief period at 15 UTC glaze ice is accreted. In most of the shown instances the glaze ice thickness surpasses the rime ice thickness substantially. Contrary,

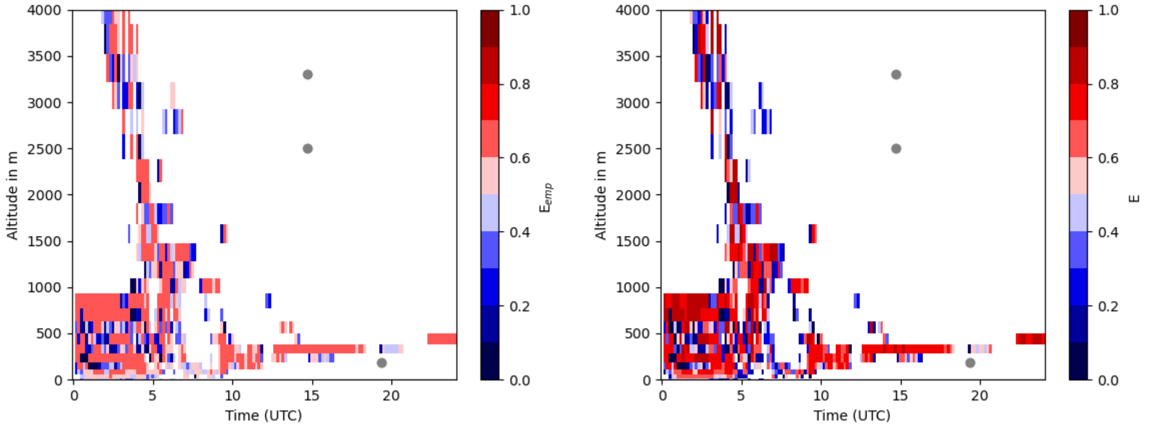

Figure 4.18: Time series of vertical profiles for overall impingement efficiency, calculated with an empirical formulation (left) and as the result of the new parameterization (right) at Cold Lake on 26th October 2016, the icing reports (14:42 UTC at 2500 m to 3300 m of altitude and 19:22 UTC at 186 m of altitude) are marked as gray dots.

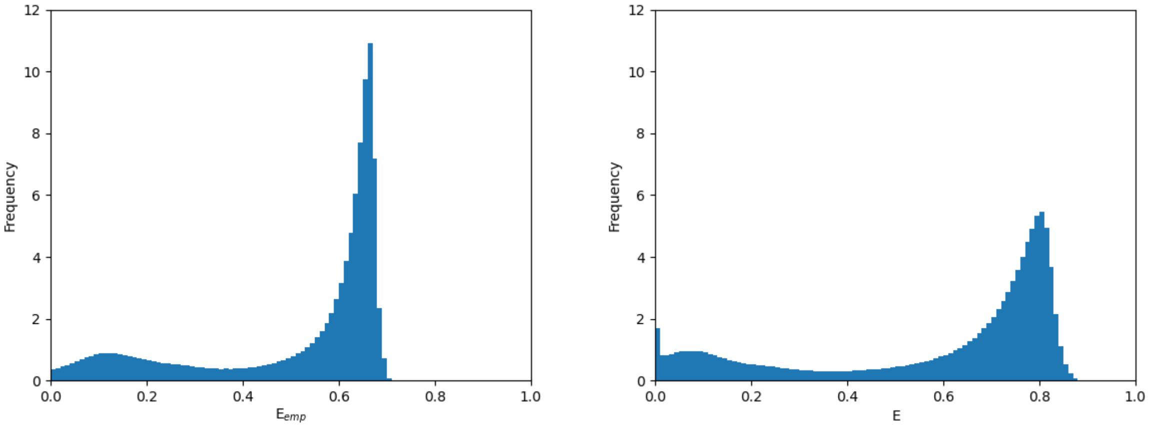

Figure 4.19: Histograms (relative frequency) of the overall impingement efficiency, calculated with an empirical formulation (left) and as the result of the new parameterization (right) for the entire simulation domain and period (26th October 2016).

comparable to the findings for the 24th of October, the mean glaze accretion rate (center right) is substantially lower than the rime accretion rate, only seldomly surpassing $1.0\,\mathrm{cm\,h^{-1}}$. This shows again that not only is the wet icing phase triggered in most cases, but also that most of the time of stay in the corresponding grid cell is spent in this phase. Since liquid water accretion happens simultaneously with glaze ice accretion, the water film thickness (bottom left) shows positive values, where the glaze ice thickness also does. The amount of liquid water and, consequently, its mean accretion rate (bottom right), however, surpass those of glaze ice in most instances, indicating the importance of this differentiation. This is in line with the findings for the previous case on 24th of October. For a more statistical analysis, figure 4.22 shows the distribution of the fraction of rime ice to the total accreted mass in the left and the relation between water film and glaze ice thickness in the right plot for the entire simulation domain and period. This distribution of the rime fraction looks qualitatively similar to the one for the 24th of October, with a peak at value 1.0, indicating solely dry icing phase being effective, and a second maximum at very low fraction values, decreasing rapidly in frequency for higher rime fractions. Contrary to the distribution on 24th of October the peak at 1.0 has a higher value than the one at 0.0. Nevertheless, there are still overall more icing cases entering the wet icing phase than those staying in the dry icing phase. However, this is less pronounced than for the 24th of October. The ratio between water and glaze ice accretion also shows a distribution resembling the previous one. Overall there are more cases where the accreted water amount surpasses the amount of glaze ice, although not as much as for the 24th of October. This lesser extent of the liquid water surplus is further indicated

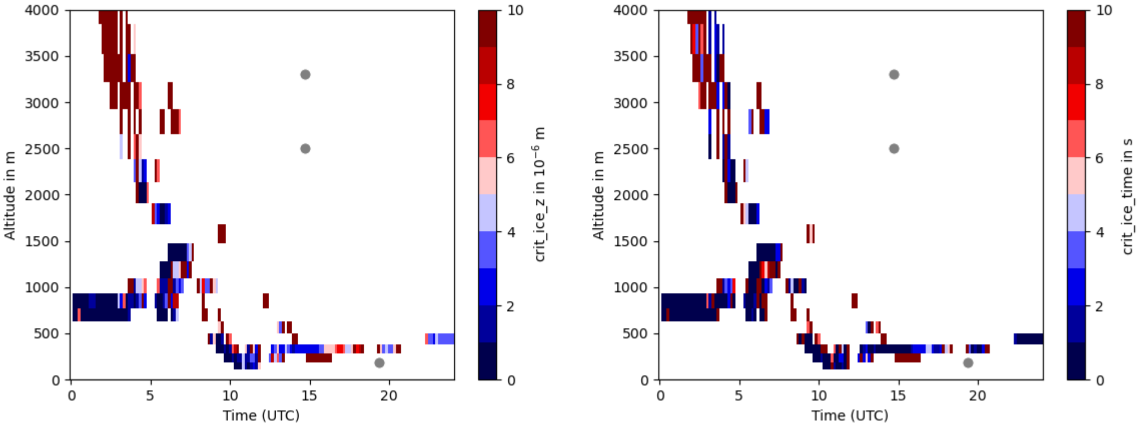

Figure 4.20: Time series of vertical profiles for the critical ice thickness (left) and the critical time (right) at Cold Lake on 26th October 2016, the icing reports (14:42 UTC at 2500 m to 3300 m of altitude and 19:22 UTC at 186 m of altitude) are marked as gray dots.

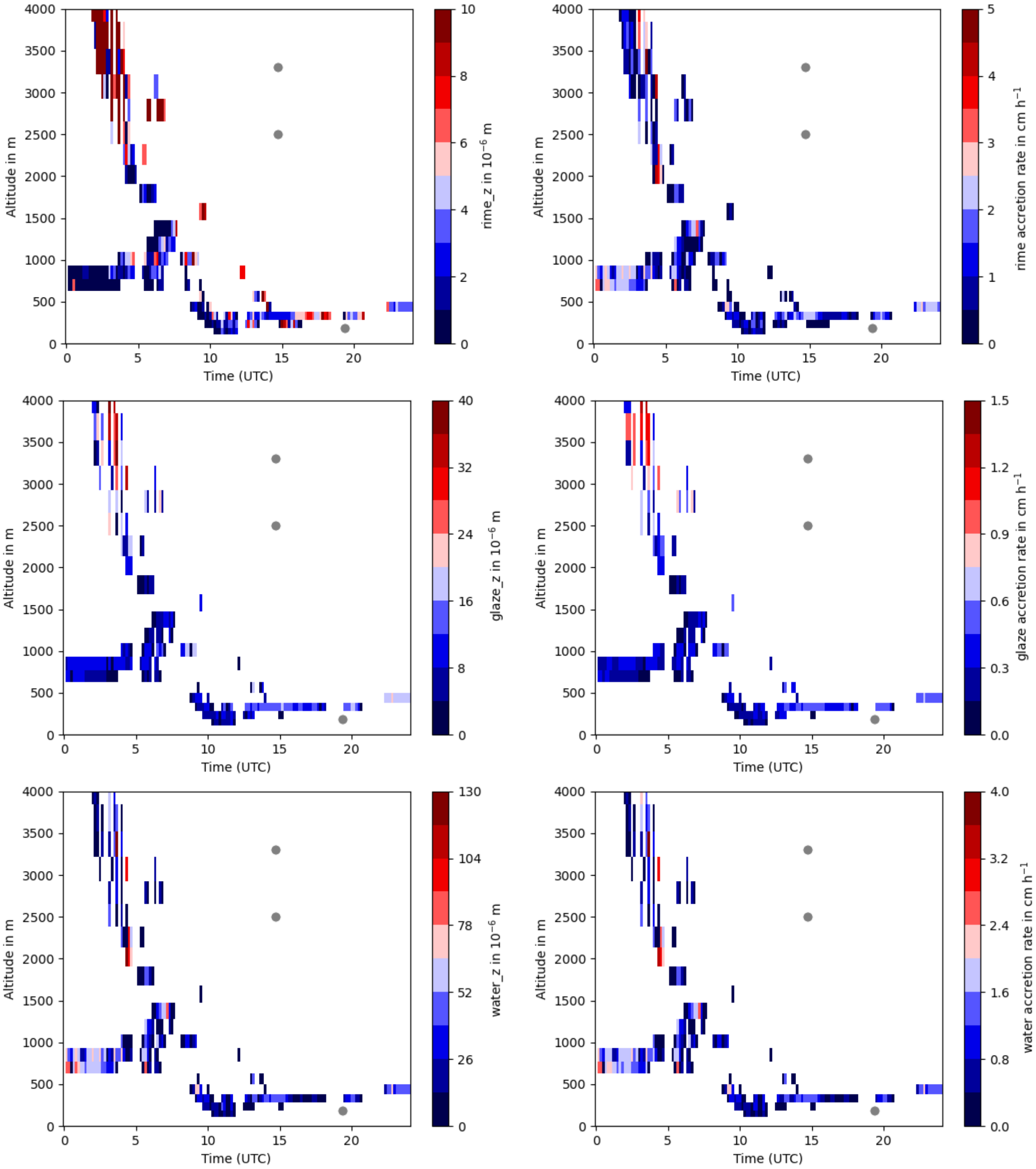

Figure 4.21: Time series of vertical profiles for the accreted thickness (left) and the accretion rate (right) for rime (top), glaze (center) and liquid water (bottom) accretion at Cold Lake on 26th October 2016, the icing reports (14:42 UTC at 2500 m to 3300 m of altitude and 19:22 UTC at 186 m of altitude) are marked as gray dots.

by the fact that the highest ratios between liquid water and glaze ice accretions are significantly lower than for the 24th of October. As both the maximum amount of rime ice accretion and the water to glaze ice accretion ratio depend on the ambient temperature, these differences in the distributions shown in figure 4.22 indicate icing conditions occuring in colder environments. Figure 4.23 confirms this indication. It shows the relation between the accreted total ice and water film thickness as a function of the ambient air temperature. Comparable to the previous plots, this also resembles its counterpart for the 24th of October. However, it shows additional curves as additional temperature environments are affected by icing conditions. These fit nicely into the empty spaces in figure 4.11 and also extend the effective temperature range to lower values. The temperature values occuring in both situations show the same characteristica between figure 4.11 and 4.23, supporting the statement in the case of

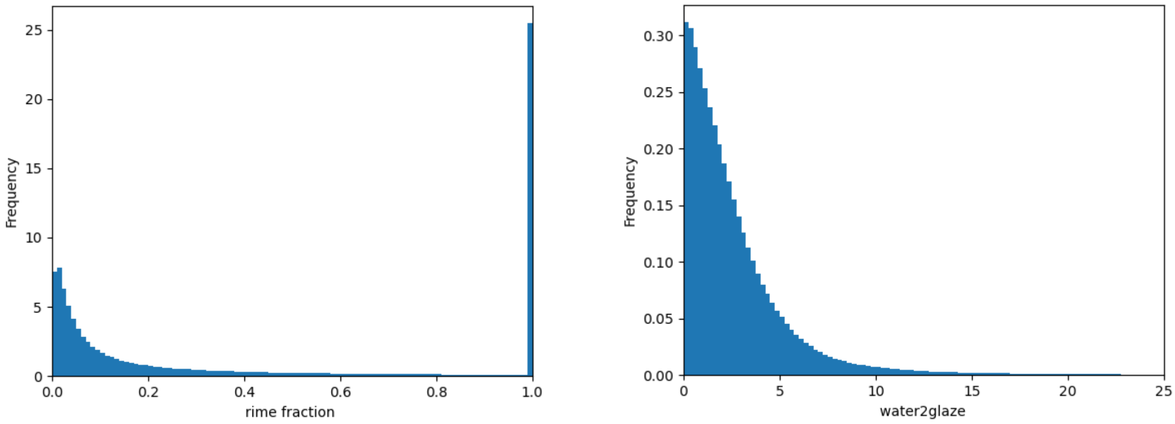

Figure 4.22: Histograms (relative frequency) of the fraction of rime accretion to the total accretion (left) and ratio between the simultaneously accreted liquid water and glaze ice (right) for the entire simulation domain and period of the 26th of October.

the 24th of October that the temperature dependency for the relation between total ice and liquid water accretion is an intrinsic feature of the freezing parameterization independent of the actual meteorological situation. Although the liquid water accretion does not contribute to ice accretion on the point of droplet impingement, it must not be ignored, as the flight wind makes it flow downstream, ultimately reaching parts of the airfoil with less or no ice accretion, to freeze there. This is especially hazardous as those parts are most likely less protected against icing. Figure 4.24 shows the mean combined accretion rate caused by the impinging water, so considering rime and glaze ice as well as liquid water. This indiscrimination between the icing types gives a first estimate on the overall icing intensity that is comparable to simpler algorithms like the ones presented in Boudala et al. (2019). The left panel shows the temporal development of the vertical profile of the quantity and the right panel its overall distribution throughout the simulation. The left plot indicates a comparable temporal and vertical inhomogeneity to the previous profiles. The strongest inhomogeneity is found at around 4 to 5 UTC in an altitude of about 3500 m above ground level, where there seems to be an environment with accretion rates surpassing the scale, while the environments around show low total water accretion rates. The histogram on the right panel presents

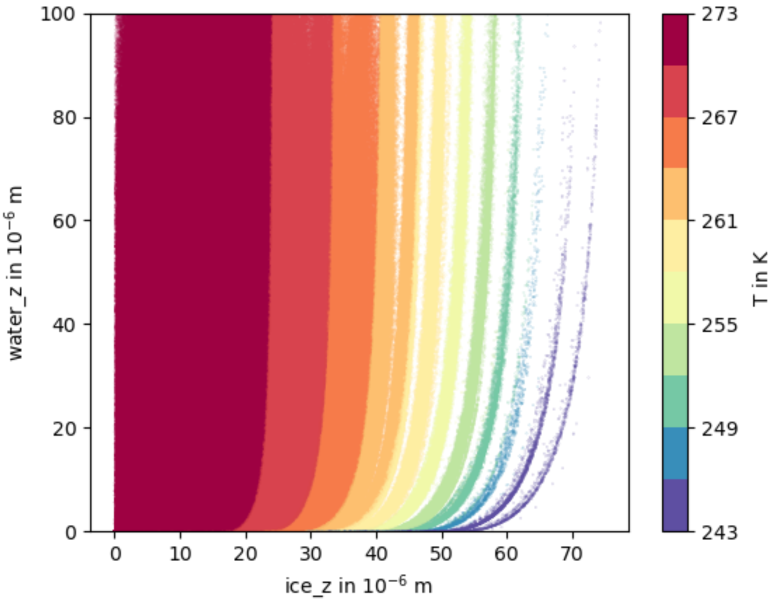

Figure 4.23: Relation between ice and liquid water accretion and temperature, the abscissa shows the accreted ice thickness, the ordinate gives the thickness of the liquid water film and the temperature of the grid cell is color coded. Data for the entire simulation domain and period is used.

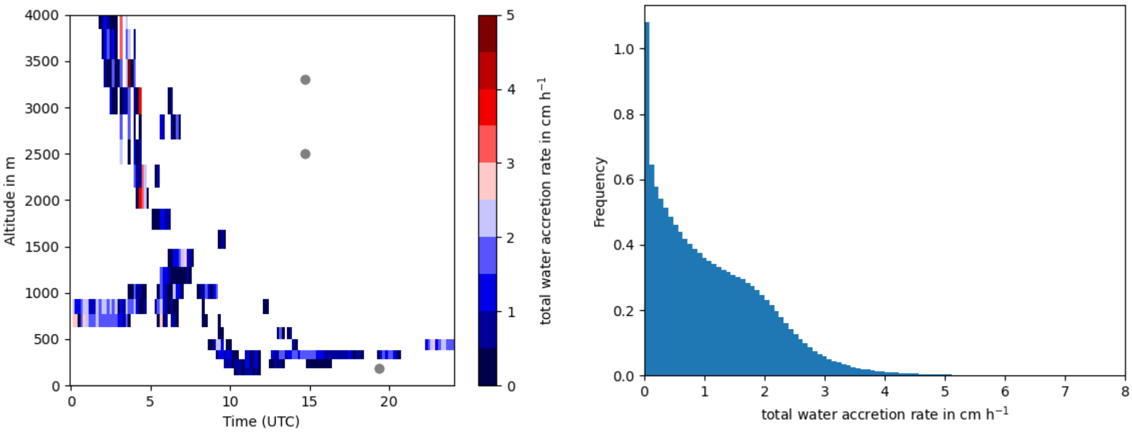

Figure 4.24: Time series of vertical profile for the total water accretion rate - rime, glaze ice and liquid water (left) and its histogram (right). The reported icing events are marked with a gray dot in the former and the latter incorporates data for the entire simulation domain and period.

similar characteristics to its counterpart in figure 4.12. However, the decrease in frequency with increasing rates is stronger already at lower values and the peak at 0.0 is more pronounced. The previous statement regarding the seldomly occuring moderate and severe icing events (2.5 cm h^{-1} and higher) in Cold Lake, Canada, motivated by figure 4.12, is further supported with this distribution.

Summarizing, the simulated meteorological quantities agree well with the results of Boudala et al. (2019) overall. However, one crucial difference is the simulation of a supercooled layer in the early hours. This results in additionally identified icing environments compared to Boudala et al. (2019). The simulations seem to fail in identifying the reported icing environments, especially the one in higher altitudes. This is most likely due to the chosen location the profiles are evaluated of. The physically based approach for computing the overall impingement efficiency differs from the empirical formulation in both range and variability, which is comparable to the previous case. As is the commonness of wet icing to occur. Contrary to the previous case, icing conditions are met in different altitudes with different ambient air temperatures, extending the previously mentioned intrinsic relationship between this quantity and the maximum accreted ice thickness.

4.2 Case study: Guadarrama Mountains, Spain (SPN)

With the aim of improving the forecast of SLD concentration, which have a crucial role in detecting and quantifying icing environments, Fernández-González et al. (2014) set out „to collect scientific data from in-cloud systems capable of producing rainfall during winter“ (Fernández-González et al. 2014, p. 2). The C-212-200 aircraft used in this research project was planned „to fly in an icing environment“ on the 1st of February 2012. On the way to its destination, leaving „the Torrejón de Ardoz military base (Madrid)“ (Fernández-González et al. 2014, p. 2), it encountered unexpected heavy icing over the Lozoya Valley in the Guadarrama Mountains, which forced the flight to be terminated prematurely. As the flight was already collecting valid data, Fernández-González et al. (2014) analysed those investigating the discrepancy between the synoptic forecast and the locally encountered icing conditions.

As indicated in figure 4.25, the Guadarrama Mountains are located in central Spain, north of Madrid. The range's southwest end is at 40°22′N, 4°18′W, from where it reaches predominantly northeast up until 41°4′N, 3°44′W.

Figure 4.26 shows the synoptic weather situation in Europe for the 1st of February 2012 at 0 UTC in the left column and 18 UTC in the right column by displaying the 500 hPa geopotential height in the top row and the 10 m wind in the bottom row. It can clearly be made out that the weather in Europe is influenced by a strong Siberian anticyclone, sending cold and dry air masses to Central Europe by northeastern winds, which fits the findings of Fernández-González et al. (2014). Spain was predominantly affected by northwestern winds, especially in the

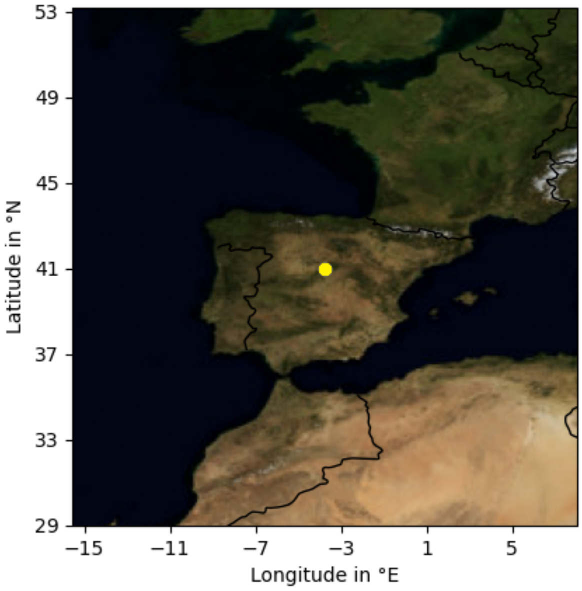

Figure 4.25: Location of the Guadarrama Mountains, Spain (marked with a yellow dot).

morning hours (Fernández-González et al. 2014), since the Iberian Peninsula was influenced by a large trough throughout that day, having a low pressure system pass through from the biscay eastwards into the Mediterranean Sea. Focusing on the research area of Fernández-González et al. (2014), the Guadarrama Mountains, figure 4.27 shows 3D distributions of the simulated liquid water content in the top left, the mean droplet diameter in the top right, the cloud temperature in the bottom left and the thickness of the accreted ice when traversing a grid cell in the bottom right panel, around the time the severe icing incident occured forcing the research flight to be cancelled. The plots show that the icing environments are locally confined to the actual mountains. Contrary to the Canada cases discussed previously, which show stratiform characteristics, this is a convective situation forced by the orography. The LWC shows spatial variance, both vertically and horizontally. The mean droplet diameter lies around 30 µm for the vast majority of environments. The top right plot also hints to a significant occurrence of higher mean droplet diameter values, compared to the previous cases investigated. The cloud temperature is sub-freezing in most instances. Some environments in lower altitudes, however have temperatures above 0 °C. The thickness of the accreted ice, which includes both rime and glaze ice, varies spatially, especially in the vertical dimension. As it is intuitively expected, colder environments enable greater values of accreted ice thickness. Overall, more and stronger icing environments are located to the northeast of the mountain range. Confirming the mentioned findings, figure 4.28 shows the horizontal distribution of the liquid water content in the left panel and the overall impingement efficiency in the right panel, in 2000 m of altitude above sea level. Here, the confinement to the orography is apparent, as well as the forced convective nature. The left plot shows that the highest LWC values are located in the centers of the convective cells, reducing gradually towards the edges. These two aspects confirm the high spatial variability of the LWC. The corresponding distribution of the overall impingement efficiency, calculated with the newly developed aircraft icing parameterization (E) shares structural similarities, which can be explained by the necessity of positive LWC to trigger the computation of the overall impingement efficiency. The actual value of the overall impingement efficiency, however, is mostly independend of the LWC. The plot shows areas of high overall impingement efficiency where LWC is high and where it is low. In general, this specific distribution is dominated by high impingement efficiency values. The edges of some convective cells, however, have low values which increase rapidly when approaching their respective centers. Other cells' edges, however, already have high overall impingement efficiency values, while again other regions introduce a sudden shift from low values to high values. To evaluate, if the described dominance of high overall impingement efficiency values

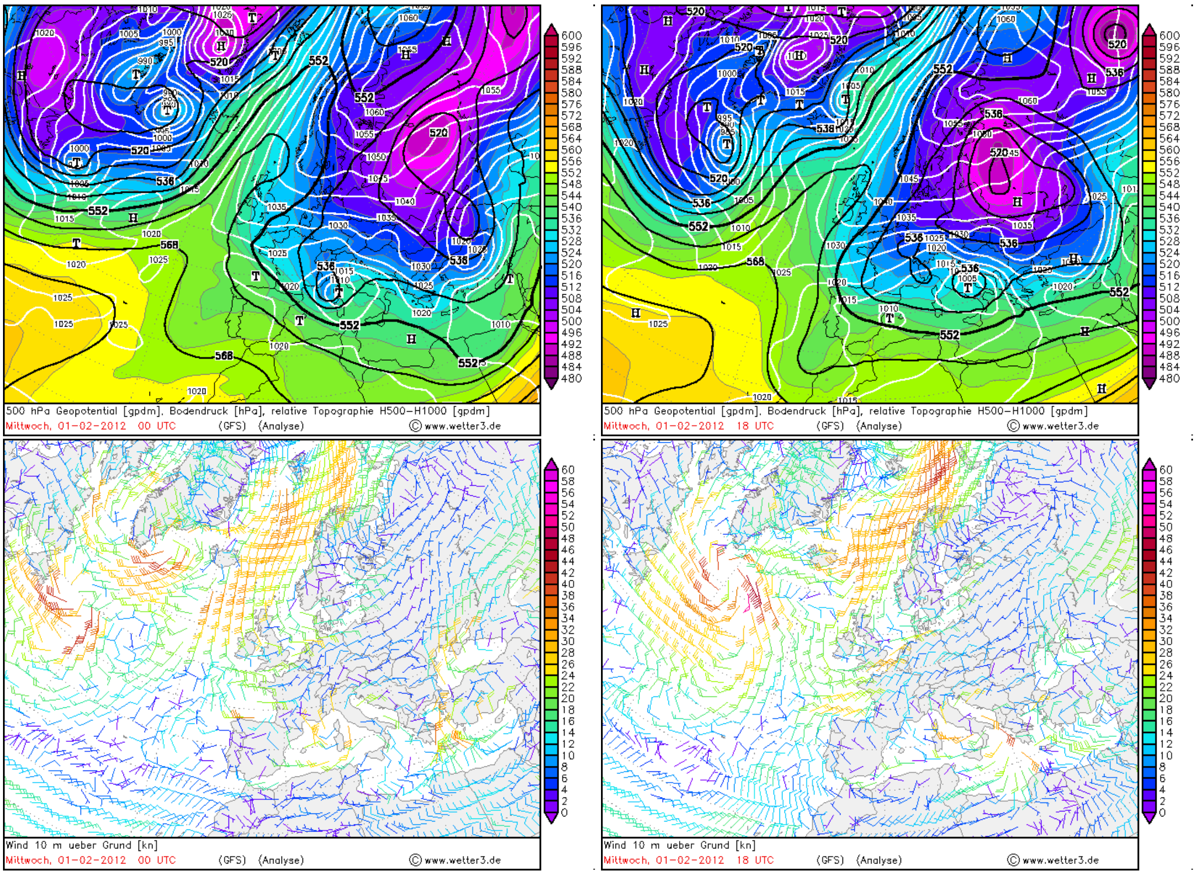
500 hPa Geopotential [gpdm], Bodendruck [hPa], relative Topographie H500−H1000 [gpdm]
Mittwoch, 01-02-2012 00 UTC (GFS) (Analyse) © www.wetter3.de
500 hPa Geopotential [gpdm], Bodendruck [hPa], relative Topographie H500−H1000 [gpdm]
Mittwoch, 01-02-2012 18 UTC (GFS) (Analyse) © www.wetter3.de
Wind 10 m ueber Grund [kn]
Mittwoch, 01-02-2012 00 UTC (GFS) (Analyse) © www.wetter3.de
Wind 10 m ueber Grund [kn]
Mittwoch, 01-02-2012 18 UTC (GFS) (Analyse) © www.wetter3.de

Figure 4.26: Synoptic weather situation for Europe on 1st of February 2012: (top) 500hPa Geopotential height and (bottom) 10 m wind speed at 00 UTC (left) and 18 UTC (right), [Source: (Behrendt and Mahlke 2003)]

persists beyond this particular instance, figure 4.29 presents the overall impingement efficiency's histogram in its left panel regarding the entire simulation domain and period. The histogram confirms what the previous horizontal distribution hints to, as high values of overall impingement efficiency occur more frequently than lower values. Compared to the previously investigated more stratiform Canada cases the primary maximum is shifted to higher values, extending the effective value range. Interestingly, the relative frequency of the lowest values, around the secondary maximum, is also increased compared to the stratiform cases, with a loss of relative frequencies of environments with mid-range overall impingement efficiency values. This ultimately amplifies the bimodal nature of the distribution. The histogram in the right panel of figure 4.29 also shows a frequency distribution of the overall impingement efficiency. This one, however, is computed by applying the empirical formulation introduced by Boudala et al. (2019) for the Canada scenarios, E_{emp}. This plot, for once, serves as a confirmation of the previous findings regarding the differences between the empirical formulation and the newly developed physical approach, indicating those differences being insensitive towards the weather situation itself. E_{emp} still tends to cap out at values around 0.7, while the more physical approach reaches E-values up to 0.9. Furthermore, figure 4.29 also shows a greater differentiation of higher impingement efficiency values when applying the physically based parameterization. This finds further support when looking into the standard deviations of these distribution, which evaluates to 0.287 for the physically based formulation and to 0.221 for the empirical one. In addition to this, the histogram for the empirical formulation (E_{emp}) also aids in attributing the previously identified differences between this convective and the former stratiform scenarios to either the nature of the scenario or the physical parameterization. Comparing this right histogram of figure 4.29 with the left histograms of figures 4.7 and 4.19, the same effects of the convective nature are indicated, if to a lesser extent. Both the peak of the distribution and the maximum value reached is slightly shifted towards higher overall impingement efficiency values, and also

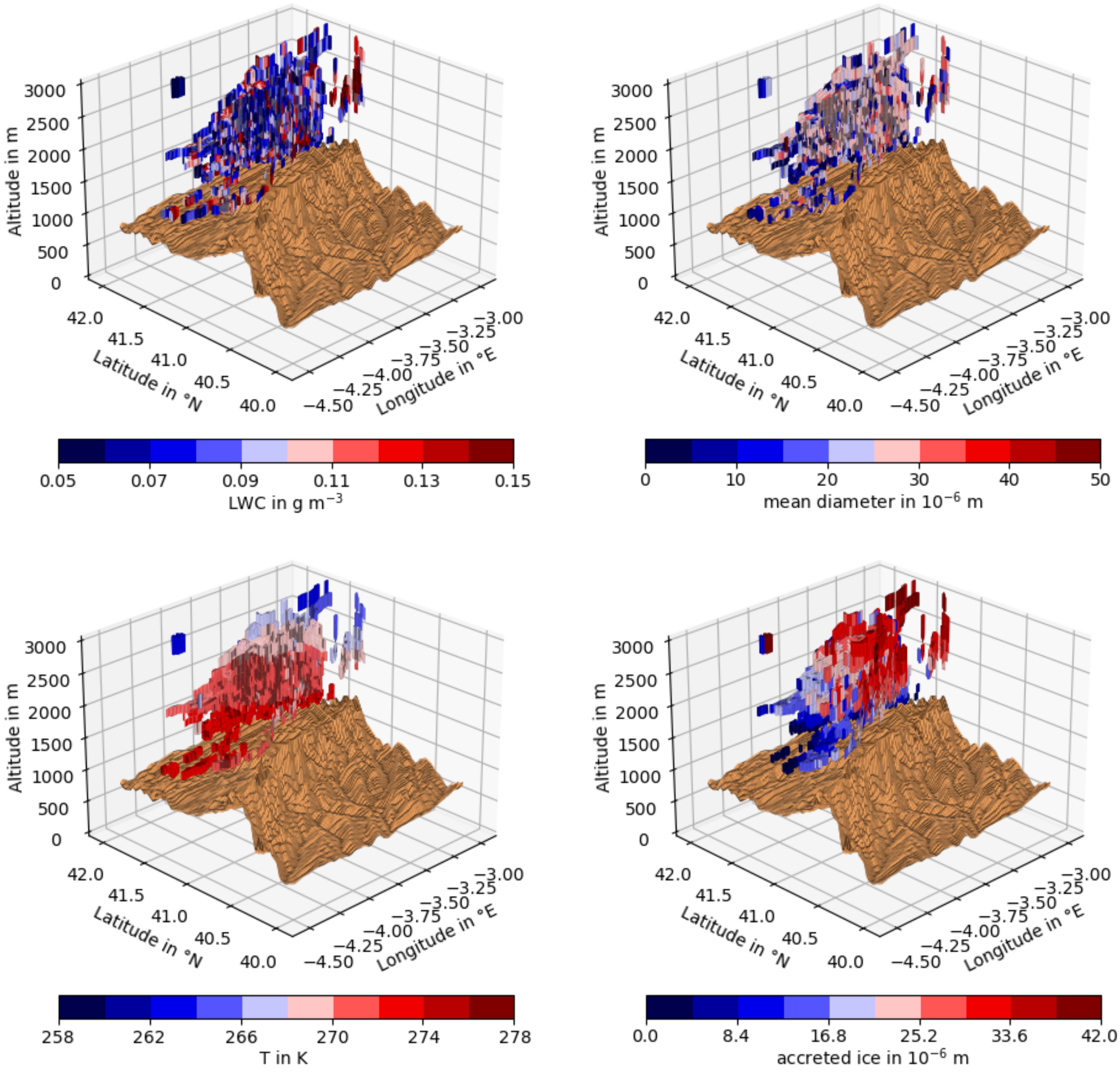

Figure 4.27: 3D distribution of simulated LWC (top left), mean droplet diameter (top right), cloud temperature (bottom left) and accreted ice (bottom right) at the Guadarrama Mountains on 1st of February 2012 at 13:00 UTC, matching the icing incident. Only environments with a LWC of at least 0.05 g m^{-3} are displayed.

the frequencies of the lowest overall impingement values increase for this empirical formulation compared to the stratiform cases, while the mid-range values decrease in frequency.

The overall impingement efficiency is a crucial quantity for aircraft icing, as it determines, combined with the LWC, how much water gets in contact with the aircraft. However, it is not an actual icing quantity itself. Figure 4.30 presents such icing quantities as a result of the newly developed physically based parameterization, namely the critical ice thickness in the top left, the rime ice thickness accreted traversing a grid cell in the top right, the accreted glaze ice thickness in the bottom left and the accreted water film thickness in the bottom right panel. The horizontal distributions of those quantities in 2000 m of altitude at 13:00 UTC are shown. The convective nature of this situation is represented in these plots as it was in the previously investigated quantities. The critical ice thickness, defining the transition between the initial dry icing and the subsequent wet icing phase, in general reaches its highest values at the edges of the convective structures. It is noted that values beyond 1×10^{-5} m exist, but are color coded as 1×10^{-5} m to allow greater differentiation of the lower values. The plot indicates in general that staying in the dry icing phase is more likely when traversing the edges of the convective cells, while transitioning into the wet icing phase is more expected when entering the central parts of those cells. However,

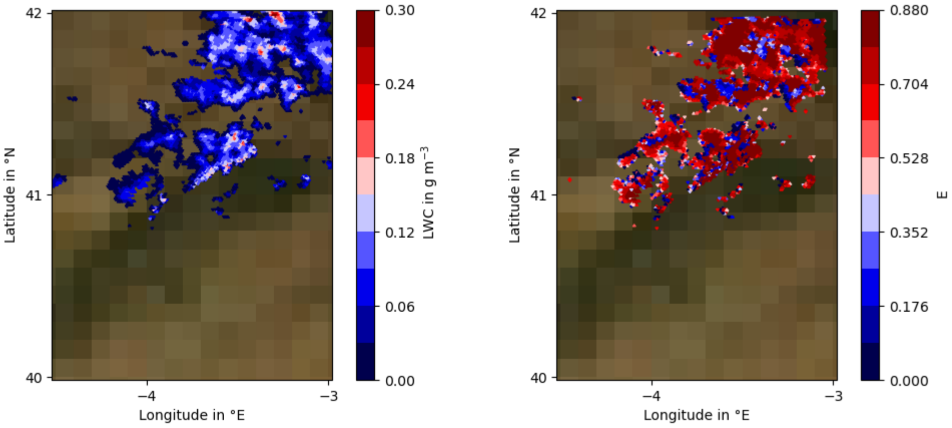

Figure 4.28: Horizontal distribution of LWC (left) and overall impingement efficiency (right) at Guadarrama Mountains on 1st of February 2012 13:00 UTC in an altitude of 2000 m above sea level, as simulated by the model.

there are also cases where parts of the edges already have low values of the critical ice thickness, hinting towards a sudden transition into the wet icing phase. The most pronounced instance of this is at the southern edge of the structure centered at around 41.25°N, 3.5°W. While the critical ice thickness acts as a good proxy for identifying dry and wet icing areas, it cannot provide the actual icing intensity on its own. The accreted rime ice thickness (top right) is more capable in this regard, as it shows how much ice is accreted during the dry icing phase, when traversing the grid cell. This quantity is capped by design by the corresponding critical ice thickness, as additional accretion leads to a transition into the wet icing phase, where glaze ice is accreted instead of rime ice. The top right plot shows clearly that the central parts of the convective cells reach the critical ice thickness. The accretion traversing the edges is for most instances significantly below that value, confirming those areas to solely experience dry icing. The glaze ice and water film accretions presented in the bottom panels visualize the areas in which an actual transition into the wet icing phase occurs. The overall structures in these two plots is identical as glaze ice and water film accretion occurs simultaneously, but to different extents. Depending on how much of the traversing time is spent in the wet icing phase, the quantitative differences differ. A short time spent favours overall glaze ice accretion, while a longer time spent favours water film accretion. In general the highest values of glaze ice and water film accretion are found in the centers of the convective cells, while their edges are mostly free of glaze ice and liquid water. The most pronounced exception, already identified above, however, shows that there can be areas where severe icing conditions can occur abruptly, which is in line with the experiences of the research aircraft of Fernández-González et al. (2014). Investigating the behaviour of these three accretion types beyond this particular

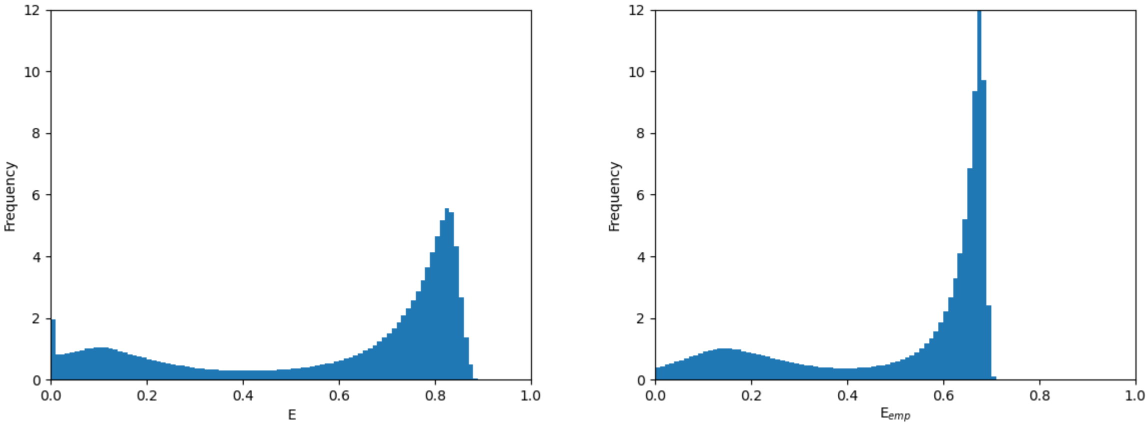

Figure 4.29: Histograms (relative frequency) of the overall impingement efficiency, as the result of the new parameterization (left) and calculated with an empirical formulation (right) for the entire simulation domain and period (1st February 2012).

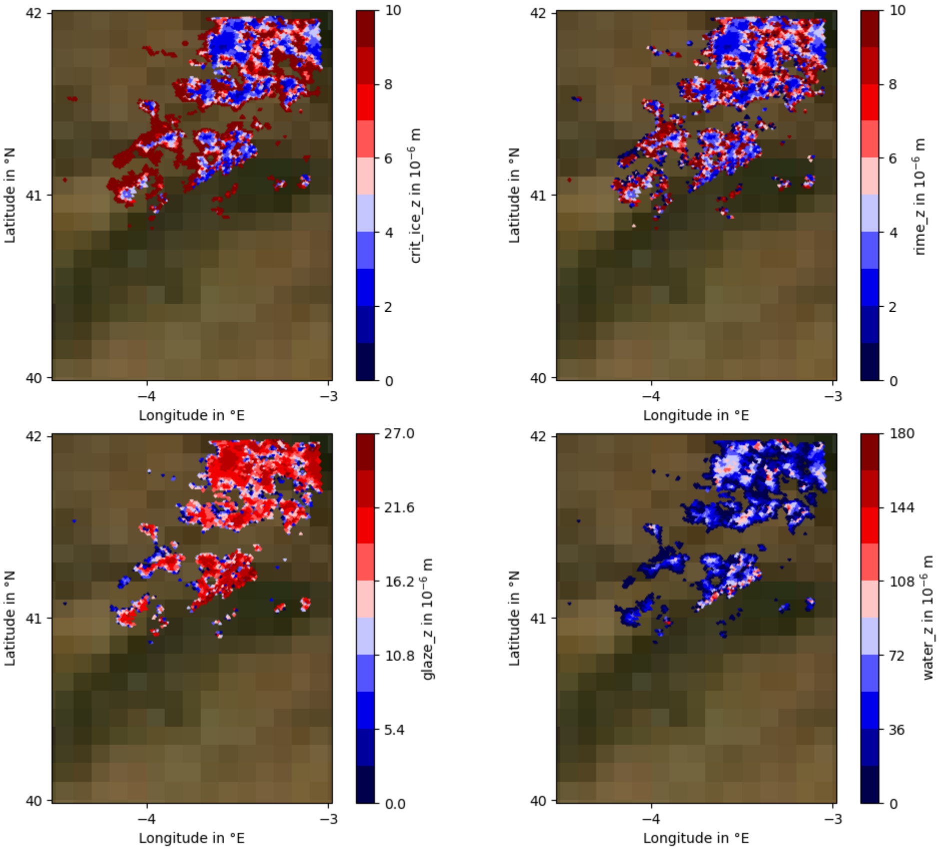

Figure 4.30: Horizontal distribution of the critical ice thickness (top-left), the accreted rime ice thickness (top-right), the accreted glaze ice thickness (bottom-left) and the accreted water film thickness (bottom-right) at Guadarrama Mountains on 1st of February 2012 13:00 UTC in an altitude of 2000 m above sea level, as simulated by the model.

horizontal distribution, figure 4.31 presents the overall relative frequency distribution for the rime fraction, so the fraction of the accreted material that is rime ice, in the left and the ratio between the accreted water film and glaze ice thickness, in the right histogram. The rime fraction's frequency distribution for this convective situation states clearly, by the large peak at 1.0, that a large part of the icing environments only cause dry icing to occur. This peak has a higher relative frequency value than the corresponding ones for the more stratiform cases (see figures 4.10 and 4.22). This is explained by the previous finding that most of the pure dry icing environments are at the edges of the clouds. The spatial confinement of convective cells compared to the more extended stratiform areas result in relatively more edge areas than central areas. The rest of the histogram behaves similarly to the previous ones, suggesting that, once the wet icing phase is initiated, the time spent in there results in large amounts of glaze ice and water film accretion, reducing the rime fraction rapidly. Interestingly however, the secondary maximum is shifted to a slightly higher value, indicating that rime fractions near 0.0 are far less common in this convective situation than in the previous stratiform scenarios. The right histogram for the ratio between liquid water film and glaze ice accretion also supports this statement. Overall, this plot indicates that there are relatively more cases in which the glaze ice thickness surpasses the water film thickness in this scenario than in the more stratiform ones. As the ratio between liquid water to glaze ice accretion rate increases the longer the wet icing phase persists, these high frequencies of ratios smaller than 1.0 hint to less time being spent in the wet icing phase. Consequently, the frequency of cases, where the water film accretion surpasses the glaze ice accretion is reduced compared to the stratiform scenarios. Returning to the absolute accretion of water in its different forms, figure 4.32 presents the horizontal distribution (at the same altitude and point in time as the previous instances) of the total water accretion rate, which considers the accretion of rime and glaze ice as well as of the water film. This conglomerate

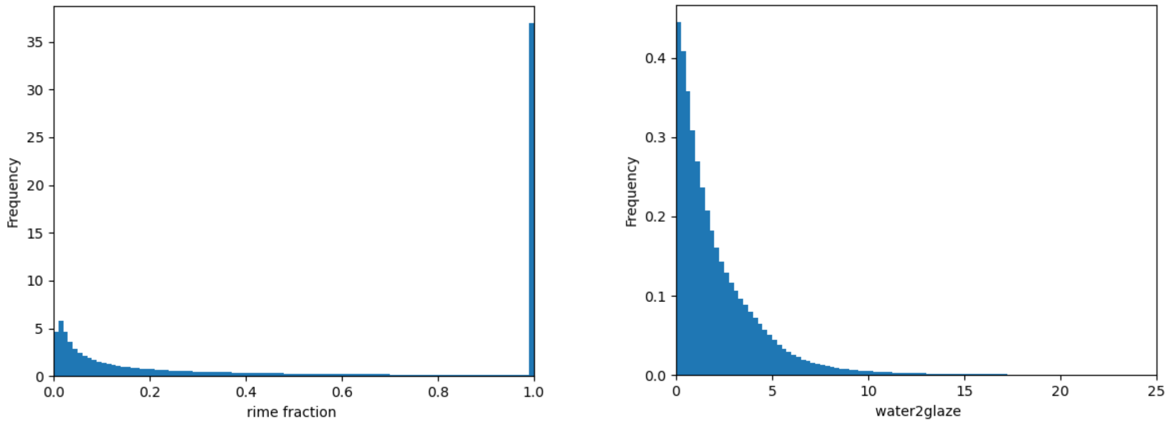

Figure 4.31: Histograms (relative frequency) of the fraction of rime accretion to the total accretion (left) and ratio between the simultaneously accreted liquid water and glaze ice (right) for the entire simulation domain and period of the 1st of February 2012.

of the three accretion types gives a simple estimate on the overall intensity of the icing environments and is more comparable to existing, less complex icing intensity algorithms and scales that do not consider the different icing phases. Unsurprisingly, the horizontal distribution is similar to the previous ones structurally. In most cases, the edges of the individual cells show reduced icing intensity, while this intensity increases towards the center of these cells. One exception to this is the southern edge of the cell centered around 41.25°N, 3.5°W abruptly introducing an icing environment with higher intensity. The distribution shows great spatial variance, indicating the necessity of accurately predicting such environments. Furthermore, the convective nature of this situation seems to generate higher total water accretion rates more frequently than the stratiform cases. The right panel of figure 4.32 supports this claim, as it shows the frequency distribution of the total water accretion rate for the entire simulation domain and period. Meeting expectations, the histogram indicates that lower accretion rates are more common than greater ones, as the relative frequency declines consistently the larger the total water accretion rate gets. However, between accretion rates of around 1.0 and 4.0 $\mathrm{cm\,h^{-1}}$, this decline is nearly linear. Comparing this to the corresponding histograms of the Canada cases which showed more stratiform characteristics (figures 4.12 and 4.24), this same interval looks structurally different, indicating more frequent occurences of lower accretion rates and less frequent higher accretion rates in the more stratiform environment. This remains true beyond this interval as well. This indicates that convective weather situation may be more capable of enabling more intense icing environments, already by applying this rudimentary metric.

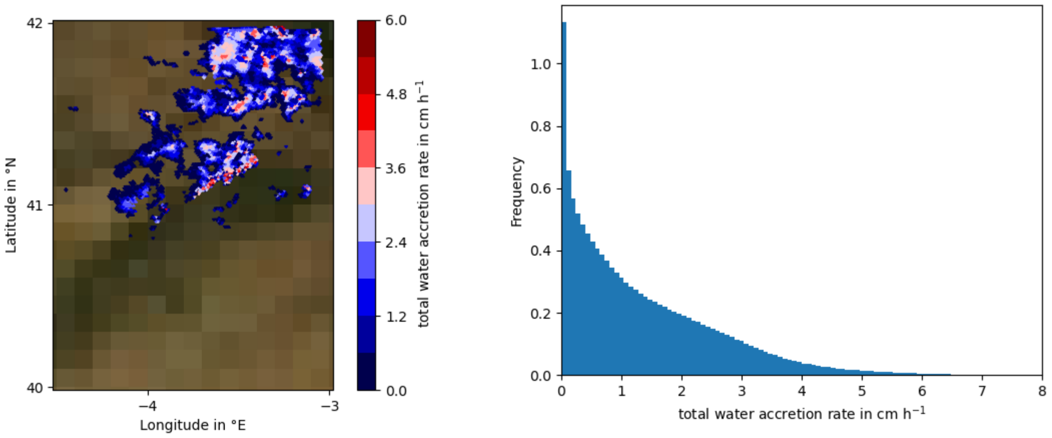

Figure 4.32: Horizontal distribution of the total water accretion rate - rime, glaze ice and liquid water (left) and its histogram (right). The former presents data at an altitude of 2000 m at 13:00 UTC on 1st of February 2012 and the latter incorporates data for the entire simulation domain and period.

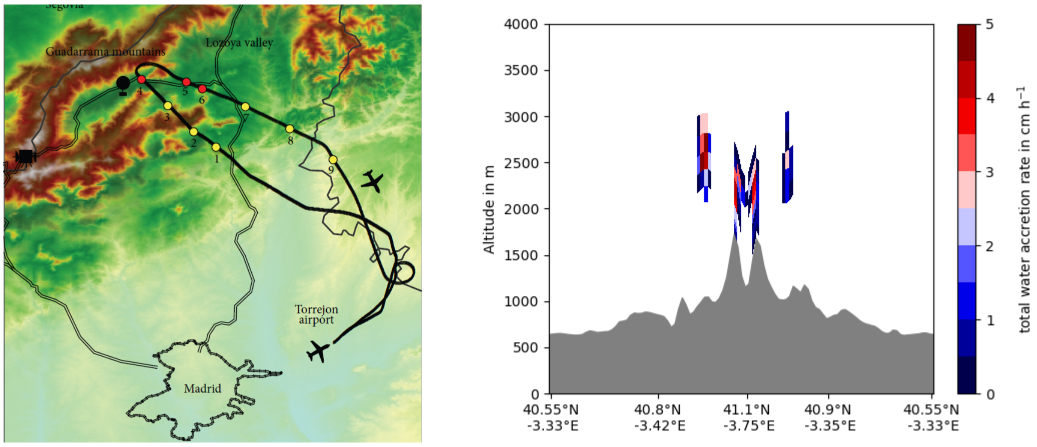

Figure 4.33: Flight path of the research flight conducted by Fernández-González et al. (2014) [Source: (Fernández-González et al. 2014) - modified] (left) and spatial development of the total water accretion rate's profile along this flight path (right) at 13:10 UTC on 1st February 2012.

The previous plots for the horizontal distribution show the spatial confinement of the icing environments well, but can only indicate the connection to the slopes of the mountains causing them. Additionally, they solely focus on one altitude. Further supporting these statements, figure 4.33 shows the spatial development of the total water accretion rate's profile in the right panel along the flight path of the research flight (shown in the left panel), which is provided by Fernández-González et al. (2014). The right plot unmistakenly presents the role the mountaineous orography has regarding the icing environments. One can identify four distinct aircraft icing regions, which are all found above the Guadarrama Mountains. All of them are clearly confined to the slopes of the mountaineous terrain. Outside of those regions, no icing environments are found. Additionally, the profile displays the large spatial inhomogeneities inside each of the icing environments. This applies to both the horizontal and vertical dimension and indicates that little differences in location decide between light and severe icing incidents in this orographically forced convective situation.

Overall, the new physically based aircraft icing parameterization is able to identify icing environments above the Guadarrama Mountains, also along the flight path of the research aircraft of Fernández-González et al. (2014) at its time of flight, contrary to the synoptic forecast (Fernández-González et al. 2014). Due to their orographically forced convective origin, they highlight the importance of a proper resolution of the underlying orography. Although the geographic location and point in time of the identified icing environments agree well with the results presented by Fernández-González et al. (2014), their altitude is underestimated in the present work. This may be a consequence of the basic model setup with a rather clean atmosphere assumed in this simulations, leading to larger droplets limiting their vertical reach. Additionally, the convective nature of this situation is reflected in the frequency distributions of the overall impingement efficiency and accretion rates, showing increased frequencies of higher values.

4.3 Reported icing incident: Baden-Wuerttemberg, Germany (BWF)

The final case, to which this newly developed physically based parameterization for aircraft icing is applied, stems from an informal, private icing report of a hobby pilot. The corresponding flight was conducted on the 7th of December 2019 in the afternoon hours in northern Baden-Wuerttemberg, Germany, as indicated in figure 4.34. To give an idea of the synoptic weather situation for this day, figure 4.35 displays the 500 hPa geopotential height in the top panels and the 10 m wind in the bottom panels at 0 UTC in the left panels and 18 UTC in the right panels. The weather situation over Germany for this day is defined by a trough in the geopotential height that passes through Germany during that day. The corresponding low pressure system is located in Scandinavia. The isobars over

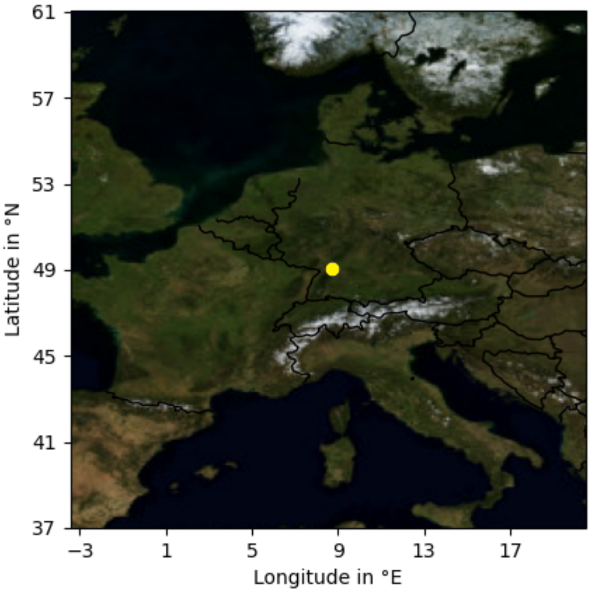

Figure 4.34: Location of the reported icing incident in Baden-Wuerttemberg, Germany (marked with a yellow dot).

Baden-Wuerttemberg suggest that approaching air masses come from a western direction. This situation remains throughout the day. The 10 m wind in Baden-Wuerttemberg comes mostly from a southwesterly direction, which is mostly due to the Rhine Valley with its southwest to northeast alignment generally channeling westerly winds into a southwesterly direction (Kalthoff and Vogel 1992; Fiedler 1983; Wippermann 1984). Throughout the day, the wind field stays invariant regarding the direction. However, the wind speed diminishes during the course of the day.

The reported icing incident occured at 14:56 UTC near Bretten, in the Northwest of Baden-Wuerttemberg (49.04°N 8.68°E). The reported flight level was FL70. With a surface pressure of about 990 hPa, this corresponds to an altitude of about 2000 m above ground level. Figure 4.36 shows the state of the lower atmosphere regarding the liquid water content in its top left 3D-plot. For this, it is noted that only LWC values above $0.1\,\mathrm{g\,m^{-3}}$ are plotted for better visibility, so the atmosphere is more cloudy than indicated. The elements shown suggest some extent of orographical influence, as they are located above inhomogeneities in the terrain. The top right 3D-plot in figure 4.36 shows the simulated mean droplet diameter in these LWC environments. Contrary to the previous cases, the droplet size seems to be between 30 to 40 µm for most of the instances shown, with the occasional environment with droplets of around 10 µm in diameter. The bottom left plot, displaying the three dimensional distribution of the cloud temperatures, indicates that the air is warmer than in the previous cases. A significant amount of LWC environments have temperatures greater than 0 °C, which can be confirmed by the official weather reports (provided by Deutscher Wetterdienst (n.d.)) for Baden-Wuerttemberg, which state the ground temperatures being significantly higher than 0 °C, indicating that significant altitude is required for finding subfreezing conditions. The bottom right plot highlights the effect of this generally warmer environment. It presents a result of the new aircraft icing parameterization giving the total amount of accreted ice, which includes rime and glaze ice accretion. Compared to the other plots in this figure, a significant portion seems to be missing as it experiences no icing due to the high temperatures. Comparable to the previous cases it shows, however, that the accreted ice thickness varies spatially, especially in the vertical dimension. These 3D-plots give a proper indication of the scope of potential icing environments throughout the simulation domain. For a more thorough analysis of the simulation results, however, it is lacking. So figure 4.37 displays the horizontal distribution of LWC in its top left and the mean droplet diameter in its top right panel. The bottom panels show values for the overall impingement efficiency. The bottom left one is the result of the empirical formulation introduced at the Canada cases above (E_{emp}) and the

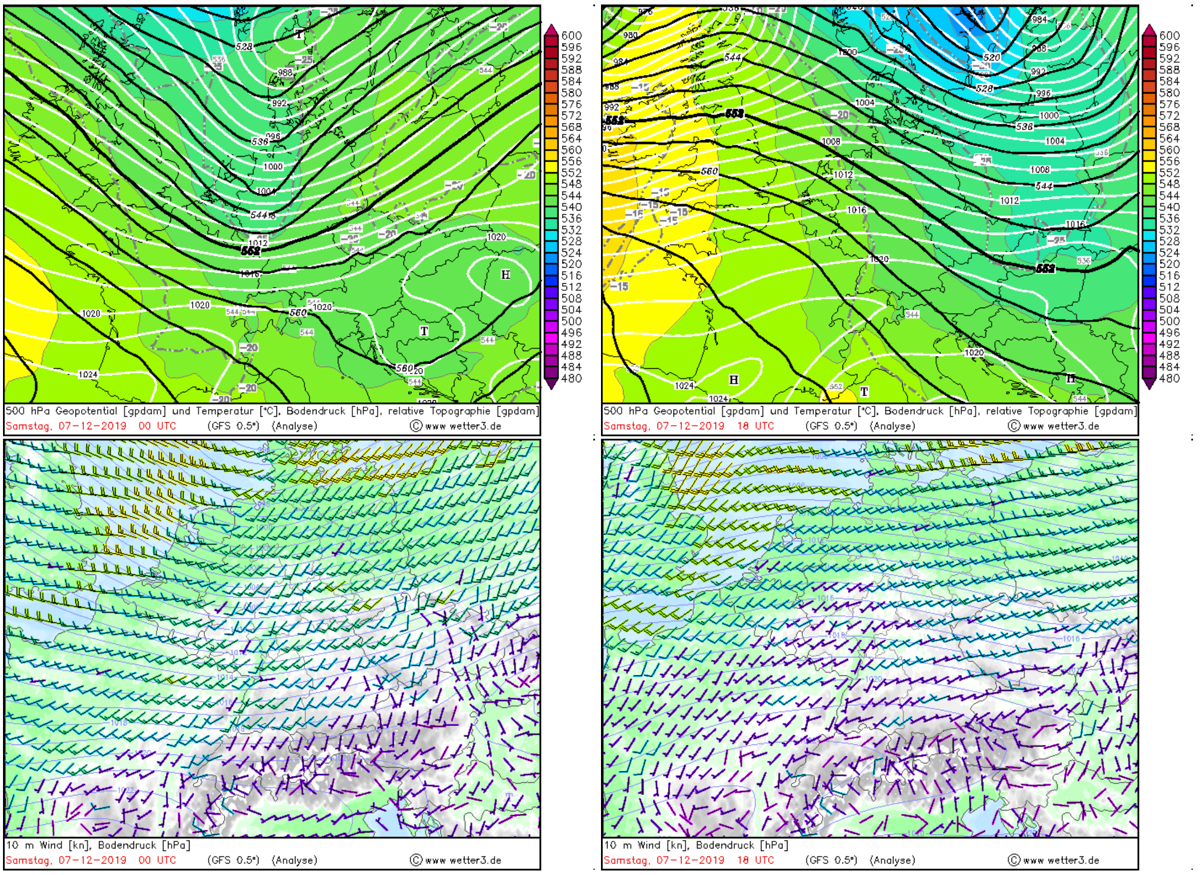
500 hPa Geopotential [gpdam] und Temperatur [°C], Bodendruck [hPa], relative Topographie [gpdam]
Samstag, 07-12-2019 00 UTC (GFS 0.5°) (Analyse) © www.wetter3.de
500 hPa Geopotential [gpdam] und Temperatur [°C], Bodendruck [hPa], relative Topographie [gpdam]
Samstag, 07-12-2019 18 UTC (GFS 0.5°) (Analyse) © www.wetter3.de
10 m Wind [kn], Bodendruck [hPa]
Samstag, 07-12-2019 00 UTC (GFS 0.5°) (Analyse) © www.wetter3.de
10 m Wind [kn], Bodendruck [hPa]
Samstag, 07-12-2019 18 UTC (GFS 0.5°) (Analyse) © www.wetter3.de

Figure 4.35: Synoptic weather situation for Germany on 7th of December 2019: (top) 500hPa Geopotential height and (bottom) 10 m wind speed at 00 UTC (left) and 18 UTC (right), [Source: (Behrendt and Mahlke 2003)]

bottom right one is computed by the newly developed, physically based parameterization (E). It shows the situation at an altitude of 2000 m at the time the icing incident is reported. The yellow dot marks the position of the icing incident. The horizontal distribution of the LWC supports the statement of a more convective situation present, when the icing incident was reported, since it shows high spatial inhomogeneities both in presence of liquid water and its amount. Convective cells can easily be identified throughout the simulation domain. The distribution of the mean droplet diameter also illustrates the convective nature of the weather situation. In some instances the spatial variance is more pronounced than in the LWC. As LWC and mean droplet size do not always correlate, it hints that more than the former is needed to accurately model icing situations. The yellow dot indicates that the reported icing incident occured at the edge of one of the convective cells, where the LWC is yet to be elevated, while the mean droplet size already is. Both versions of the overall impingement efficiency are also inhomogeneously distributed. However, while the lower values seem to match reasonably well between the two, the differences at the higher values are not negligible. Comparable to the previous cases, E_{emp} caps out at values of around 0.7, while the physically based approach evaluates to E-values up to 0.9. Since the instances of overall impingement efficiency values below 0.6 occur only rarely, for both formulations, most of the liquid water heading towards an aircraft also impinges onto its surface in this situation. Already using the empirical formulation, but even enhanced with the physical one, the internal structure of the overall impingement efficiency's distribution matches well the one for the mean droplet diameter. The icing incident occured in a region with elevated overall impingement efficiency values. Additionally, it is noted that the heavily alternating structures, especially for the mean droplet diameter and consequently both overall impingement efficiency formulations, for example at around 49°20′N 8°30′E, are due to atmospheric waves in this altitude.

The atmospheric state regarding aircraft icing at the location of the reported icing incident is indicated by figure

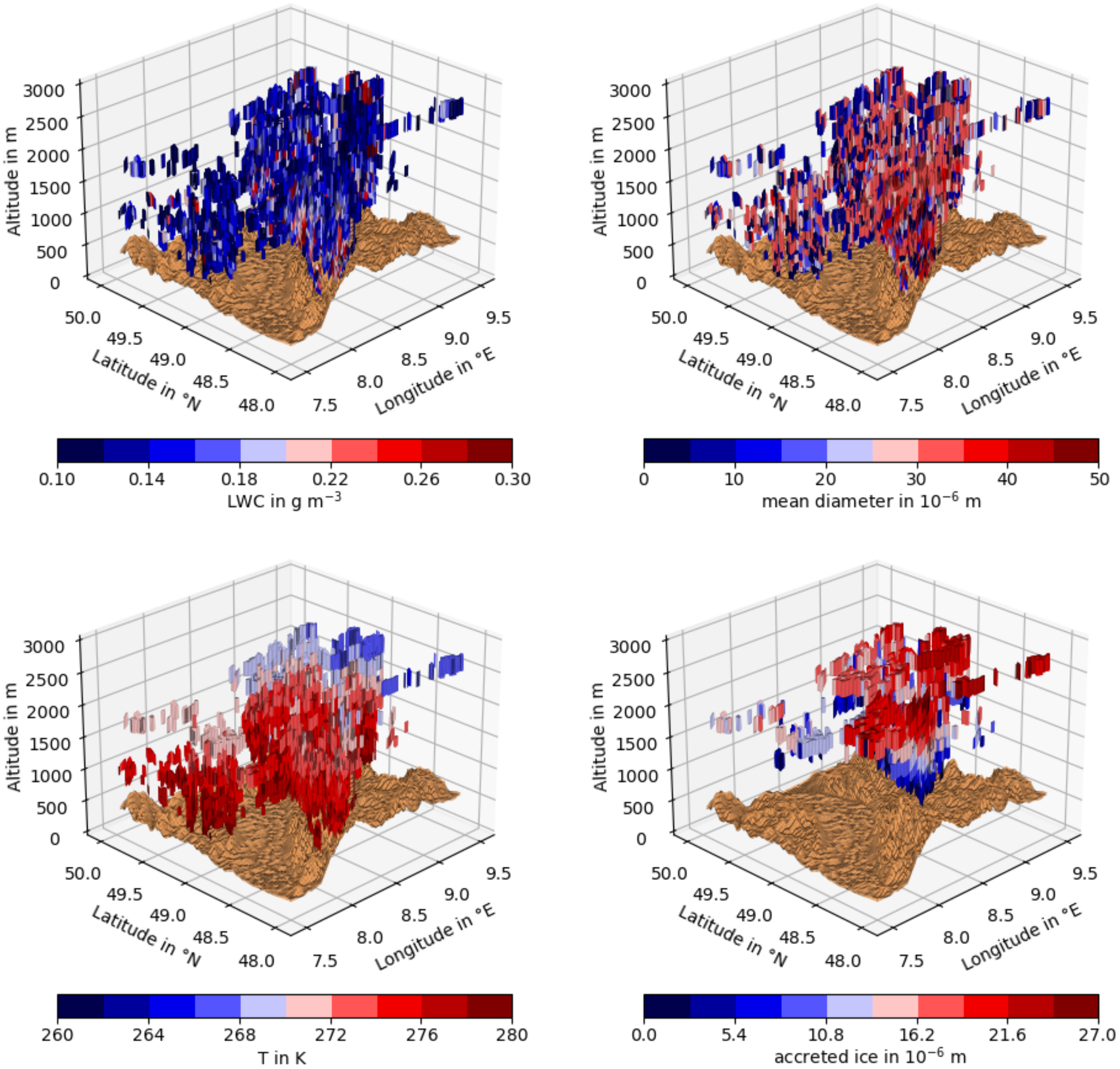

Figure 4.36: 3D distribution of simulated LWC (top left), mean droplet diameter (top right), cloud temperature (bottom left) and accreted ice (bottom right) in Baden-Wuerttemberg on 7th December 2019 at 15:00 UTC, matching the reported icing incident.Only environments with a LWC of at least 0.1 g m^{-3} are displayed.

4.38, as it shows the temporal development of the profiles for the liquid water content in its left and for the overall impingement efficiency, computed with the newly developed physically based parameterization, in its right plot. The high variability of the LWC profile in both time and altitude also supports the statement above of a more convectively influenced environment. The icing incident, marked with a yellow dot, coincides with the development of a cloud. The right plot shows high impingement efficiency values throughout the day, but also high vertical and temporal variance. In some instances the extent of this variance is such that small changes in time and altitude can cause a change from a low impinging environment to a high one and vice versa. At the point of the reported icing incident, the combination of LWC and overall impingement efficiency, suggests liquid water impinging onto the aircraft's surface in relevant amounts. To what extent this water freezes upon an aircraft is visualized in figure 4.39, as it displays the horizontal distribution of the accretion rates of ice (including both rime and glaze ice) and liquid water in the top panels in an altitude of 2000 m at the time the reported icing occured, and the temporal development of their vertical profiles at the location of the icing event in the bottom panels. The horizontal distribution of the total ice accretion rate looks significantly different than the former distributions investigated. The spatial variability is reduced, especially highlighted by the central parts of the

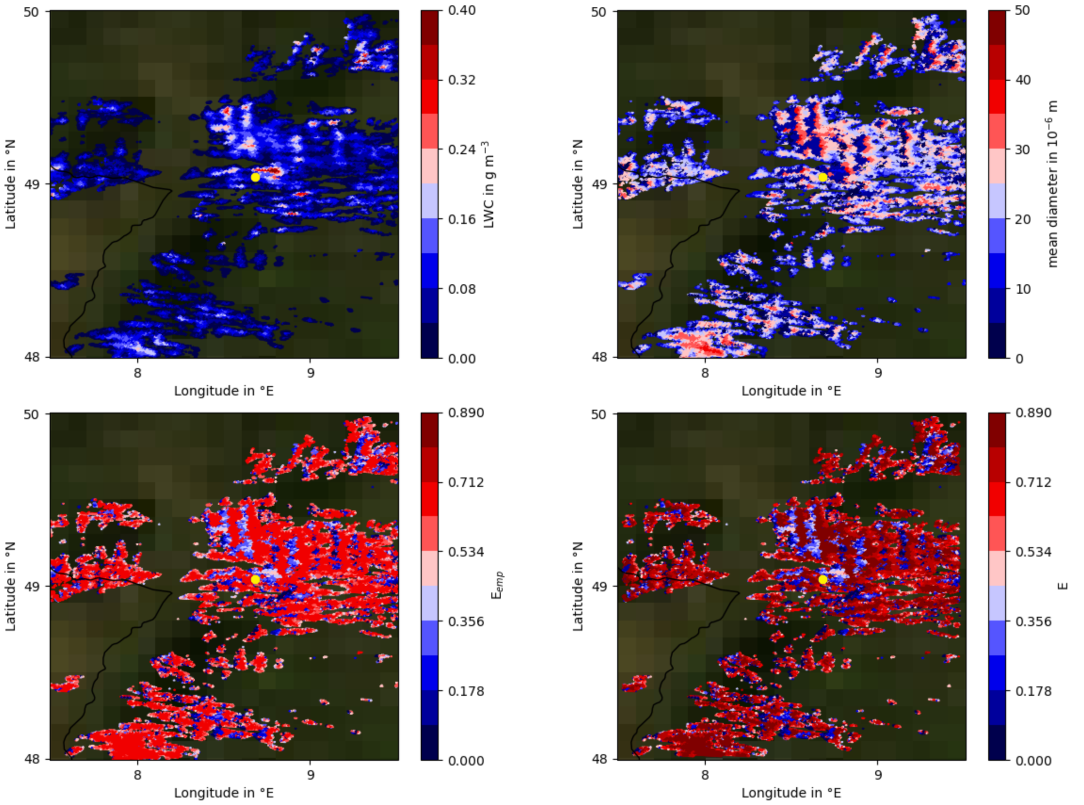

Figure 4.37: Horizontal distribution of the LWC (top left), the mean droplet diameter (top right), the overall impingement efficiency calculated empirically (bottom left) and with the newly developed physically based parameterization (bottom right) in an altitude of 2000 m at the time of the icing incident. Its position is marked with a yellow dot.

convective elements having more uniform values. The edges, however, continue to show variance. The uniform central values differ between the different complexes shown. Applying the insight gained from the previous cases that the total amount of accreted ice is quickly reached and depends on the temperature, these difference are most likely due to differences in temperature. The regions of uniform total ice accretion rate therefore also suggest that non negligible parts of the impinging water accrete as a liquid water film. This is confirmed by the corresponding plot of the horizontal distribution in the top right of figure 4.39. The variance that is lost for the ice accretion rate, is represented here. Especially those regions, where the uniform limit of the ice accretion rate is reached, show great spatial inhomogeneities in the liquid water accretion rate. Additionally, looking at the color scales

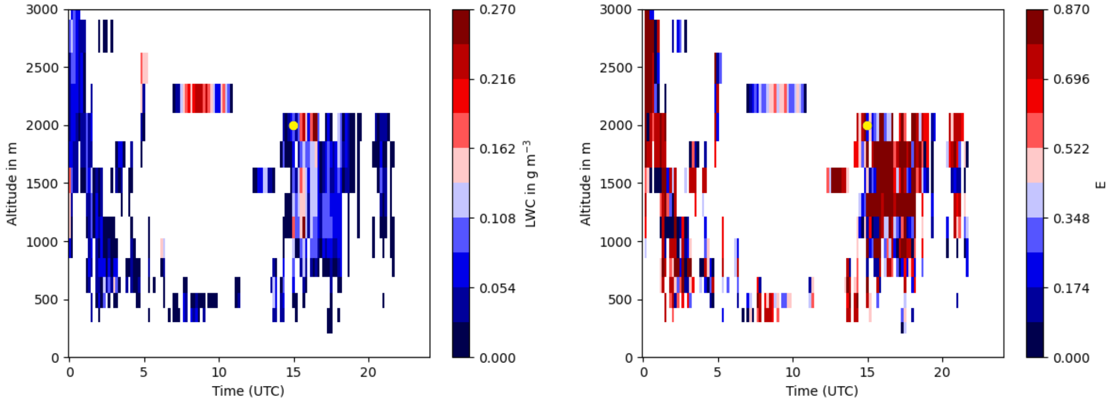

Figure 4.38: Temporal development of the vertical profiles of the LWC (left) and the overall impingement efficiency (right) at the location of the reported icing incident, the yellow dot marks its time and altitude.

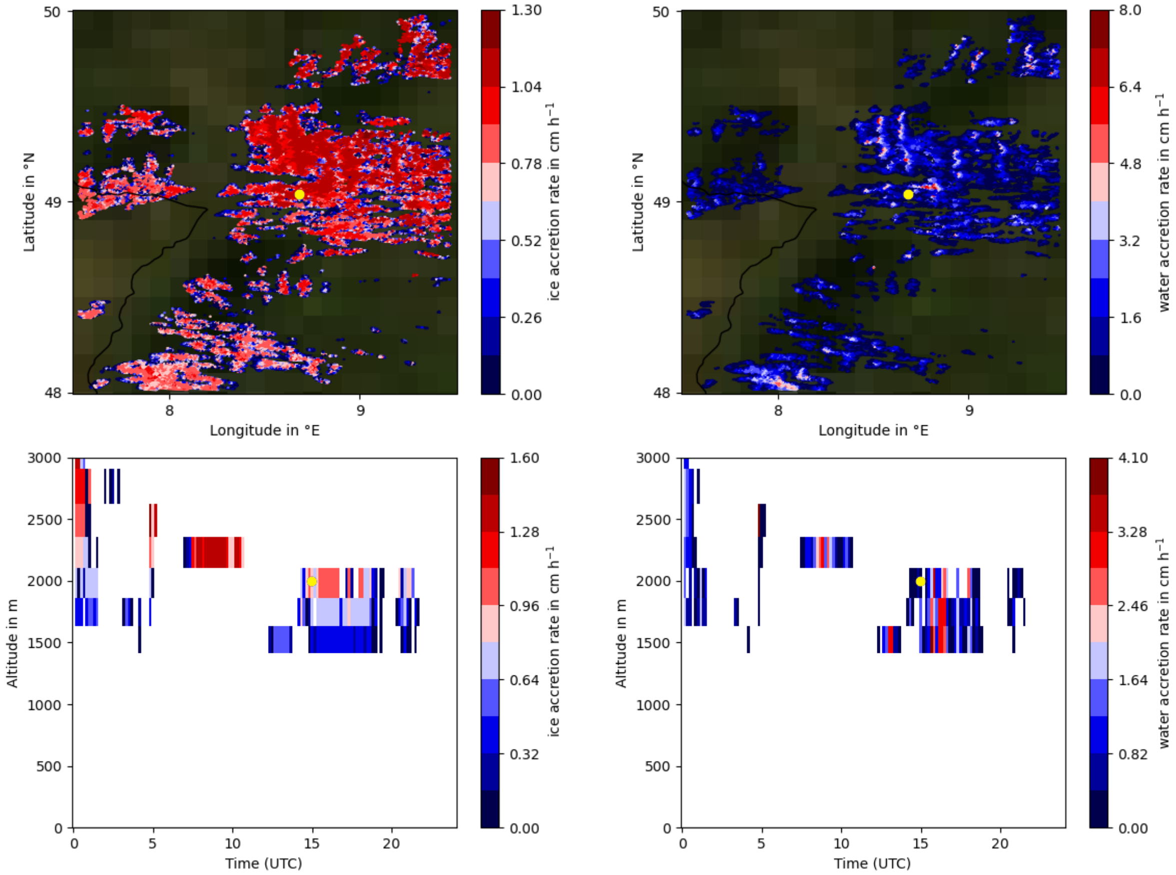
Latitude in °N
Longitude in °E
ice accretion rate in cm h^{-1}
water accretion rate in cm h^{-1}
Altitude in m
Time (UTC)

Figure 4.39: Horizontal distribution (top) and temporal development of the vertical profiles (bottom) of the mean accretion rates of ice (left) and liquid water (right) as the result of the newly developed physically based parameterization in an altitude of 2000 m and at the location of the reported icing incident, repectively. The icing incident's position and time and altitude, respectively, is marked with a yellow dot.

of these two plots, the water accretion rate tends to surpass the ice accretion rate significantly, especially in the aforementioned regions. This also agrees well with the findings in the previous cases. Inspecting the location of the icing incident reported, it is inside one of these uniform regions, indicating a near maximum rate of ice accretion that the environment enables. Due to it being towards the edge of a convective cell, the residual liquid water film still accretes at a lower rate. The temporal development of the respective profiles at this position, in the bottom two panels, show similar characteristics. The temporal variance is reduced for the ice accretion rate. However, its vertical variability persists to some degree, which again supports its connection to the ambient air temperature. The missing temporal variability is delivered again by the residual accretion of liquid water. Comparing these profiles to the previous one, it stands out that there are no values for both the ice and liquid water accretion rate in the lower parts of the atmosphere, while LWC or impingement efficiency show non-zero values. This is due to the temperature that needs to be below 0 °C for icing to occur. So the lower 1500 m are too warm. The yellow dot, indicating the time and altitude of the reported icing incident, shows again that this icing is currently only connected with a minor amount of liquid water accretion rate. The ice accretion rate, however, seems to be close to the temperature defined maximum value. In addition, it is noted that although occuring seldomly, there are regions and points in time, respectively, where only values for the ice accretion rate are displayed. Since here no liquid water film is accreted, icing occuring here stays in the dry icing phase.

Expanding the scope from the individual icing incident to the entire simulation domain and period, figure 4.40 shows the relative frequency distribution of the overall impingement efficiency. The left panel represents the result of the empirical formulation (E_{emp}) and the right panel the result of the newly developed physically based parameterization (E). The histograms confirm the findings of the previously shown horizontal distributions:

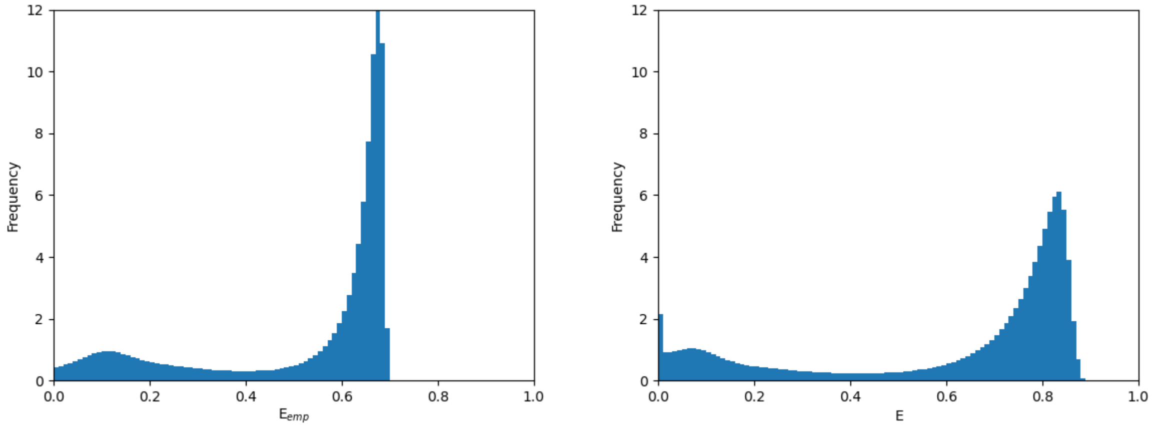

Figure 4.40: Histograms (relative frequency) of the overall impingement efficiency as a result of the introduced empirical formulation (left) and of the newly developed physically based parameterization (right) for the entire simulation domain and period of the 7th of December 2019.

For once, the maximum value for E_{emp} is around 0.7, while the physically based parameterization reaches E-values up to 0.9, therefore enabling a greater differentiation of high impingement efficiency environments. As a consequence, the relative frequency of values between 0.5 and 0.7 is higher for the empirical formulation, further supporting the greater differentiation introduced by the physical parameterization. Additionally, the secondary maximum occuring at low overall impingement efficiency values is shifted to lower values for the physically based parameterization compared to the empirical formulation. This agrees with the findings of the previously investigated cases. As this case is also predominantly convectively influenced, the same differences to the more stratiform Canada cases are found as for the Spain case: The primary maximum is shifted to higher values, especially the peak moves to values above 0.8, and the secondary maximum is shifted towards lower values, reducing the frequency of mid-range values in the process. This increases both the range and the variance of the distributions, with a standard deviation of 0.217 for the empirical formulation and 0.284 for the physically based parameterization. These effects can therefore be attributed to the convective nature of the scenarios. The histograms in figure 4.41 focus on the separation feature of the newly developed aircraft icing parameterization. The left panel shows the frequency distribution of the fraction of the impinging water that accretes as rime ice in the dry icing phase and the right panel displays the ratio between the accreted water film and glaze ice thickness, which are accreted simultaneously during the wet icing phase once the critical ice thickness is reached. The frequency of the rime fraction diminishes with higher values, except for values of 1.0 that indicate that the critical ice thickness is not reached and therefore only rime ice is accreted. The highest frequency outside of this case being at the

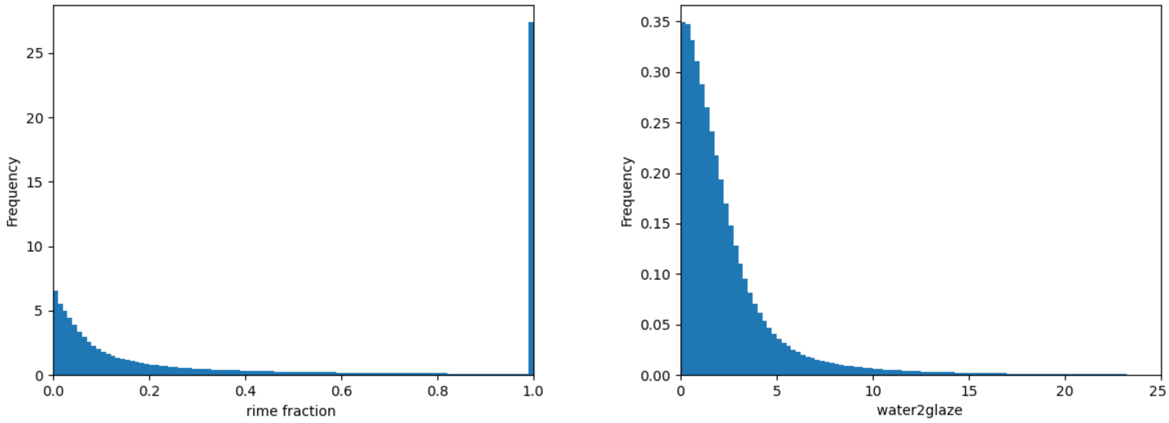

Figure 4.41: Histograms (relative frequency) of the fraction of rime accretion to the total accretion (left) and ratio between the simultaneously accreted liquid water and glaze ice (right) for the entire simulation domain and period of the 7th of December 2019.

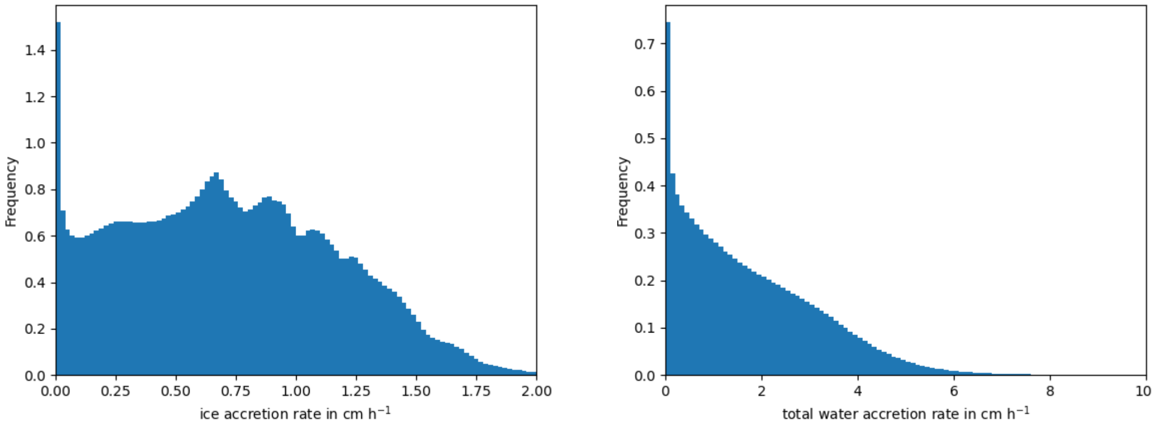

Figure 4.42: Histograms (relative frequency) of the mean total ice accretion rate, including rime and glaze ice (left) and the total water accretion rate, including rime and glaze ice and the liquid water film (right) for the entire simulation domain and period of the 7th of December 2019.

lowest rime fraction values conclude that in most cases the critical ice thickness is surpassed rapidly, leading to an accretion of most of the impinging water in the form of glaze ice and liquid water. This distribution is similar to the previously discussed scenarios, supporting the conclusion that the wet icing phase once triggered tends to dominate the icing process. Additionally, the peak at 1.0 exceeding even the frequency of the lowest rime fraction values significantly reminds of the corresponding distribution in the Spain scenario (see figure 4.31). As both of these scenarios are convectively influenced, this seems to be a feature caused by that influence. The ratio between the accreted liquid water film and the glaze ice shows that in most cases most of the impinging water stays initially liquid. This agrees well with the findings of the histogram of the rime fraction, as low rime fractions are achieved by having longer wet icing phases. The longer these are, the more of the impinging water remains liquid. Since the early parts of the wet icing phase is heavily glaze ice favoured, some time is required for the liquid water to break even, hence, the high frequencies of low values for the ratio between water film and glaze ice thickness. Influences of the convective situation are more subtle as they manifest in an overall higher frequency of ratios below 1.0 and a more rapid decline of the frequencies beyond that. Interestingly, the frequencies of the lowest ratios between water film and glaze ice thickness are considerably smaller than in the Spain case.

Since the horizontal distribution of the ice accretion rate in the top left panel of figure 4.39 showed an interesting change compared to the other distributions, the left panel of figure 4.42 displays the corresponding frequency distribution in its entirety. The right panel of this figure shows the resulting histogram, when next to the rates of rime and glaze ice also those of the liquid water film is considered. The histogram of the ice accretion rate presents peaks at 0.0, around 0.7, 0.9, 1.1 and around $1.25\,\mathrm{cm\,h^{-1}}$. Overall the relative frequency value up to an accretion rate of $1.4\,\mathrm{cm\,h^{-1}}$ (70 % of the range of values) differ relatively little. This agrees well with the findings in the horizontal distribution. The connection between ice and water accretion analysed in the Canada cases (figures 4.11 and 4.23) shows a feature of the icing algorithm to be that the ice accretion limit imposed by the ambient air temperature is rapidly reached once the wet icing phase is initiated, also giving a temperature dependent upper limit of the mean ice accretion rate. This is represented in this left frequency distribution. The peaks represent favored temperature regimes where icing conditions are met. Higher values occur less often, as the corresponding temperature tends to be too low for liquid water to be present. The lower values correspond to warmer environments. However, those are also fed by those instances in colder environments that do not reach their maximum ice accretion yet. The histogram for the total water accretion rate resembles those of the other scenarios, as the frequency of higher accretion rates diminishes. Contrary to the ice accretion rate, the total water accretion rate mostly depends on the LWC and the overall impingement efficiency. This frequency distribution seems to structurally lie in between the Canada cases and the Spain case, as it shows a very linear decline in frequency starting at around $0.5\,\mathrm{cm\,h^{-1}}$, while the Canada cases' corresponding distributions are more convex, favouring low accretion rates, and the Spain case's is more concave, favouring high accretion rates. Since the weather situation in the Spain case is more convectively influenced than this scenario, it is fitting that the more concave structure in the decline representing this influence is distorted.

In summary, the application of the newly developed aircraft icing parameterization identifies a multitude of icing environments in the simulation domain. One of those matches well with the reported icing incident in time, position and altitude. While clouds below 1500 m of altitude are simulated at the position of the icing incident, icing conditions only occur above this altitude due to the high temperatures below. The findings regarding the differences between the empirical formulation and the more physical based approach of the new parameterization for the overall impingement efficiency match the corresponding findings of the previous cases investigated, highlighting the intrinsic nature of these differences. Additionally, the more convective nature of this situation is similarly reflected in the icing quantities as for the SPN case.

5 Sensitivity to the explicit consideration of the droplet spectrum

The previous chapter introduced the possibilities the newly developed physically based parameterization for aircraft icing offers to forecast and investigate icing conditions by applying it to different scenarios. This and the following chapters extend its possibilities further by investigating sensitivities of icing conditions towards different aspects. One of these aspects is the explicit consideration and resolution of the droplet spectrum. In the following, the question will be discussed whether the explicit resolution of the cloud droplet spectrum in the newly developed parameterization is beneficial for the detection of icing environments and for the quantification of its intensity.

5.1 Expectations

The droplet size is a crucial quantity for the computation of the overall impingement efficiency and also has a role in the determination of the initial rime ice density on the surface of the impinged object. The latter's implementation, however, is an empirical estimate that uses the mean droplet size and has only a minor effect on the overall freezing process. The overall impingement efficiency, on the other hand, defines the flux of the actual freezing material onto the object significantly, therefore heavily influencing the freezing process. As chapter 2.3 describes, the inertia of the incoming droplets determines to which extent they impinge onto the airflow disturbing object, and that this inertia is strongly dependent on the droplets diameter. Additionally, since SLDs are of particular interest regarding aircraft icing, the consideration of the actual droplet spectrum introduces their influence as part of the spectrum into the icing process. Solely relying on the mean droplet size instead only achieves their consideration once the mean droplet size itself fits the SLD criteria. Since the parameterization considers the droplet spectrum up to five times the mean droplet mass and the impingement efficiency influencing inertia depends heavily on the considered droplet mass, it is expected that the actual resolution of the droplet spectrum leads to increased values of the overall impingement efficiency. The reduced individual impingement efficiency values of the lower mass parts of the spectrum may not fully counteract the greater values of the higher mass parts as their mass fraction, which is used as the weight, is smaller. How the effect on the overall impingement efficiency influences the different icing phases and their relation cannot be stated beforehand, however, the total water accretion as the sum of all contributions is expected to be influenced similarly to the overall impingement efficiency.

5.2 Results

With the expectations set and formulated, the following part looks into the result of the corresponding sensitivity study conducted, by comparing and analysing the simulations that do not consider the droplet spectrum (labelled BULK) and the reference simulations that do (labelled REF). While the REF simulations compute the overall impingement efficiency according to the description in chapter 3.3, the BULK simulations do not use equation 3.33, but instead $E_{\text{total}} = E\left(\overline{m}\right)$, so only the overall impingement efficiency of the mean sized droplets is used.

Figure 5.1 shows the differences in overall impingement efficiency between the BULK simulations and the REF simulations for the previously discussed scenarios: CAN24 and CAN26 with its profile's temporal developments around Cold Lake in the top left and top right panel, respectively, and its horizontal distribution for SPN and BWF

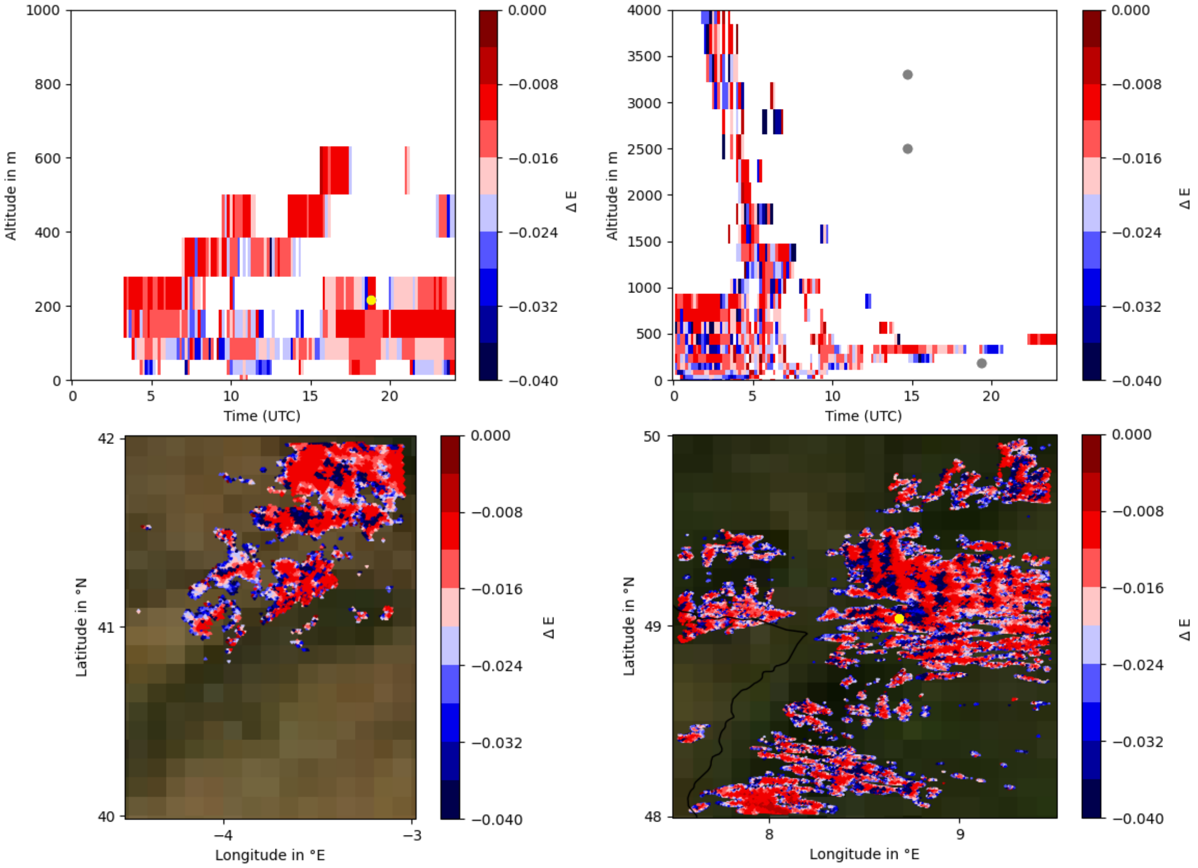

Figure 5.1: Differences in overall impingement efficiency between the BULK simulation and the REF simulation as the temporal development of its vertical profile in the CAN24 case (top left) and in the CAN26 case (top right) and as its horizontal distribution in the SPN case (bottom left) and in the BWF case (bottom right). The position of the icing reports and incidents are marked with a yellow and gray dot.

in the bottom left and bottom right panel, respectively. Indiscriminate to time, altitude and horizontal position, the overall impingement efficiency evaluates to lower values in the BULK simulations in virtually all cases. The range of this reduction of up to around 0.04 is displayed to be similar across all the presented scenarios, indicating an independency to whether a more convective or stratiform weather situation is presented. The amplitude of the changes, however, shows temporal and vertical variability in the upper panels and also horizontal variability in the bottom panels. Comparing these profiles to the CAN24 and CAN26 profiles of the overall impingement efficiency in figures 4.6 and 4.18, repectively, finds that the instances with high overall impingement efficiencies experience the weakest reduction in the BULK simulations and vice versa. The bottom plots support this finding, as the lowest reductions are found in the centers of the convective cells, which have the highest values of overall impingement efficiency (see the corresponding plots in figures 4.28 and 4.37), while the strongest reductions are found towards the edges of those cells, where the impingement efficiency is generally lower. Hence, the sign of the explicit consideration of the cloud droplet spectrum's effect is introduced to be consistent, while its amplitude tends to favour low impingement efficiency environments. However, the effect is in either case weak. Extending these specific situations to the entirety of their respective simulations, figures 5.2 and 5.3 show the relative frequency distributions of the overall impingement efficiency for the respective REF simulations in their left panels and for the BULK simulations in their right. The more stratiform CAN24 and CAN26 cases are presented in the top and bottom panels of figure 5.2, respectively, while the more convectively influenced SPN and BWF cases are shown in the top and bottom panels of figure 5.3, respectively. Comparing the BULK histograms with the REF histograms in figure 5.2 supports the findings stated above. In both the CAN24 and CAN26 cases the overall impact of the negligence of the actual droplet spectrum is weak. The strongest effect is found at the lower end

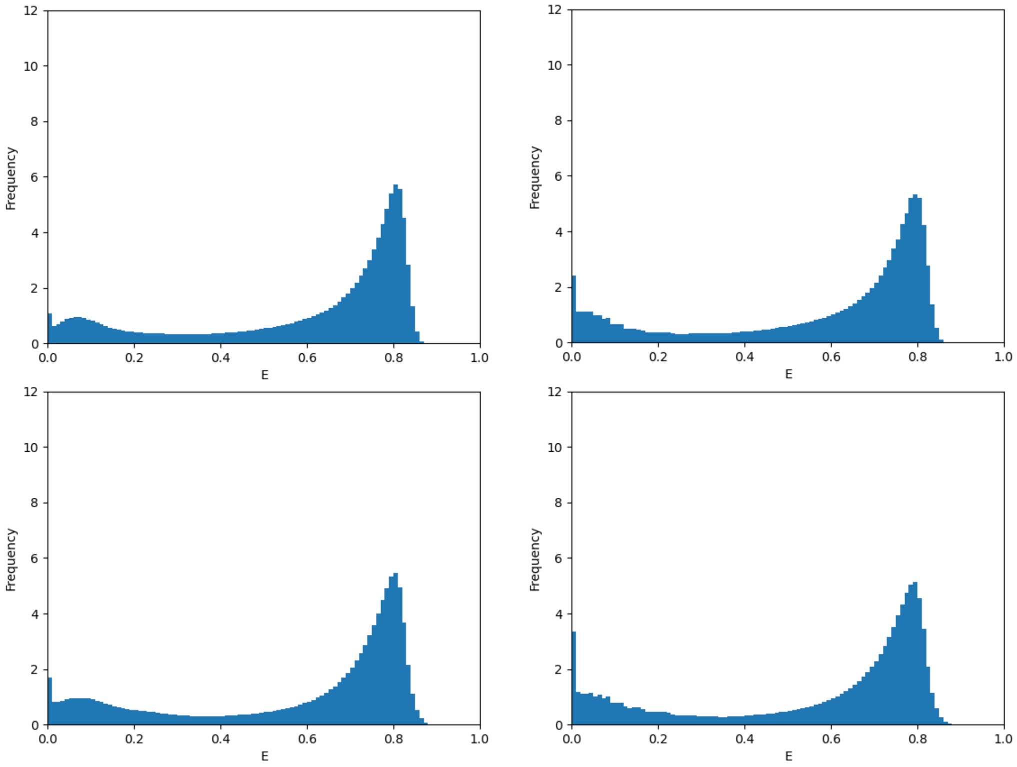

Figure 5.2: Relative frequency distributions of the overall impingement efficiency for the REF simulations (left) and the BULK simulations (right) in the CAN24 case (top) and the CAN26 case (bottom).

of the distributions, where the secondary maximum is shifted towards lower values in the BULK simulations, resulting in a significant increase in frequency for overall impingement efficiency values below 0.05. The primary maximum on the other end of the distributions, however, seems only minorly affected, which confirms the higher sensitivity in low impinging environments than in higher ones. The mean values of the BULK distributions, 0.582 for the CAN24 case and 0.566 for the CAN26 case, confirm the overall slight reduction of the overall impingement efficiency due to the negligence of the actual droplet spectrum, as the REF distributions evaluate to mean values of 0.602 and 0.586 for the CAN24 and CAN26 case, respectively. The corresponding histograms for the more convectively influenced cases in figure 5.3 show that the effects do not depend on whether the situation is stratiform or convective, as the structure of the impact on the distributions of the overall impingement efficiency is similar, as is the effect on their mean values. The SPN case experiences a mean reduction from 0.584 in the REF simulation to 0.565 in the BULK simulation, while the BWF's mean overall impingement efficiency value diminishes from 0.611 to 0.593, respectively.

Concluding, by neglecting the cloud droplet spectrum, the overall impingement efficiency is consistently underestimated. The scale of this underestimation, while small in general, depends on the actual value of the overall impingement efficiency itself with higher values experiencing lower underestimations. The mean underestimation is comparable between the more stratiformly influenced situations and the more convectively influenced ones.

To further investigate the effects of cloud droplet spectrum negligence, figure 5.4 displays the effects on the total water accretion rate. The panels are organized the same way as the ones in figure 5.1. Comparable to the effect on the overall impingement efficiency, the total water accretion rate is also reduced in all shown instances. This meets expectations, as the reduced impingement efficiency leads to a reduced amount of liquid water impinging, so less water is available to accrete. The overall small changes agree with the amplitude on the effect on the overall impingement efficiency also. However, it seems that the smallest changes occur where the actual total water accretion rate is smallest as well, which is opposite from the findings regarding the overall impingement efficiency.

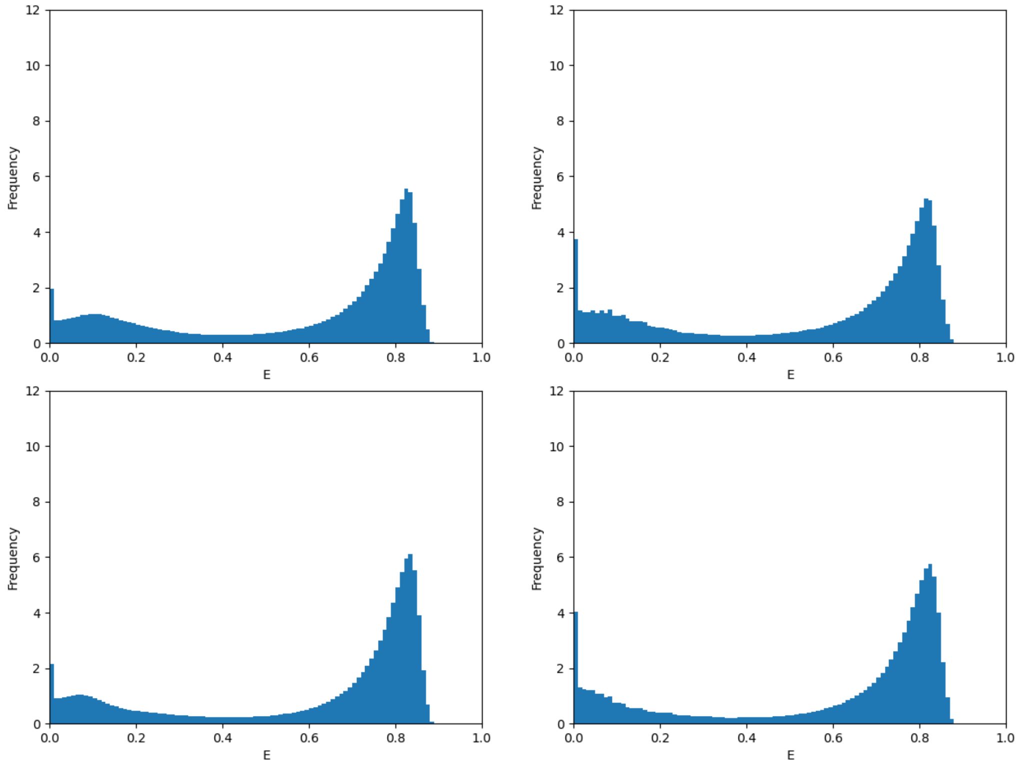

Figure 5.3: Relative frequency distributions of the overall impingement efficiency for the REF simulations (left) and the BULK simulations (right) in the SPN case (top) and the BWF case (bottom).

The best explanation for this is that in the shown cases, a high impingement efficiency is reached in regions with high LWC, so although the induced changes for the impingement efficiency are small, the underestimated impinging liquid water amount still surpasses the corresponding amount in low impingement region with low LWC. The plots for the more convective situations in the bottom panels indicate a greater amplitude of underestimation by the negligence of the droplet spectrum, than those of the more stratiform scenarios in the top panels. This agrees well with the fact that maximum LWC values are also higher in those scenarios. Again expanding this investigation onto the entire simulation domains, figure 5.5 displays the relative frequency of changes in total water accretion rate caused by the negligence of the cloud droplet spectrum. The top left panel shows the CAN24 case, the CAN26 case is presented in the top right panel, while the more convectively influenced cases are displayed in the bottom panels, SPN on the left and BWF on the right. The shown histograms support what the previous plots indicated. Firstly, the BULK simulations underestimate the total water accretion rate in all instances and secondly, the effect's amplitude is small with most instances experiencing not more than a $0.05\,\mathrm{cm\,h^{-1}}$ reduction and no instances with an underestimation of more than $0.4\,\mathrm{cm\,h^{-1}}$. The fact that the highest frequency of changes are on the lower end of the reduction range, combined with the previously found knowledge that less actual water accretion rates are more common than high ones (see figures 4.12, 4.24, 4.32 and 4.42), agrees with the above indication that instances with low total water accretion rates are underestimated to a lesser extent. The convective situations that are represented in the bottom panels, cover a larger range of underestimations than the more stratiform situations in the top panels. The mean underestimation due to negligence of the cloud droplet spectrum evaluates to $0.039\,\mathrm{cm\,h^{-1}}$ for the CAN24 case, $0.036\,\mathrm{cm\,h^{-1}}$ for the CAN26 case, $0.045\,\mathrm{cm\,h^{-1}}$ for the SPN case and $0.048\,\mathrm{cm\,h^{-1}}$ for the BWF case. So the more convectively influenced situations experience a higher mean effect than the more stratiform ones. One of the features this newly developed aircraft icing parameterization offers, is the separation of the accretion process into the different occuring phases of freezing. So, with the effects on the total water accretion analysed, figure 5.6 introduces a detailed look into the effects on ice accretion by displaying the differences in total ice

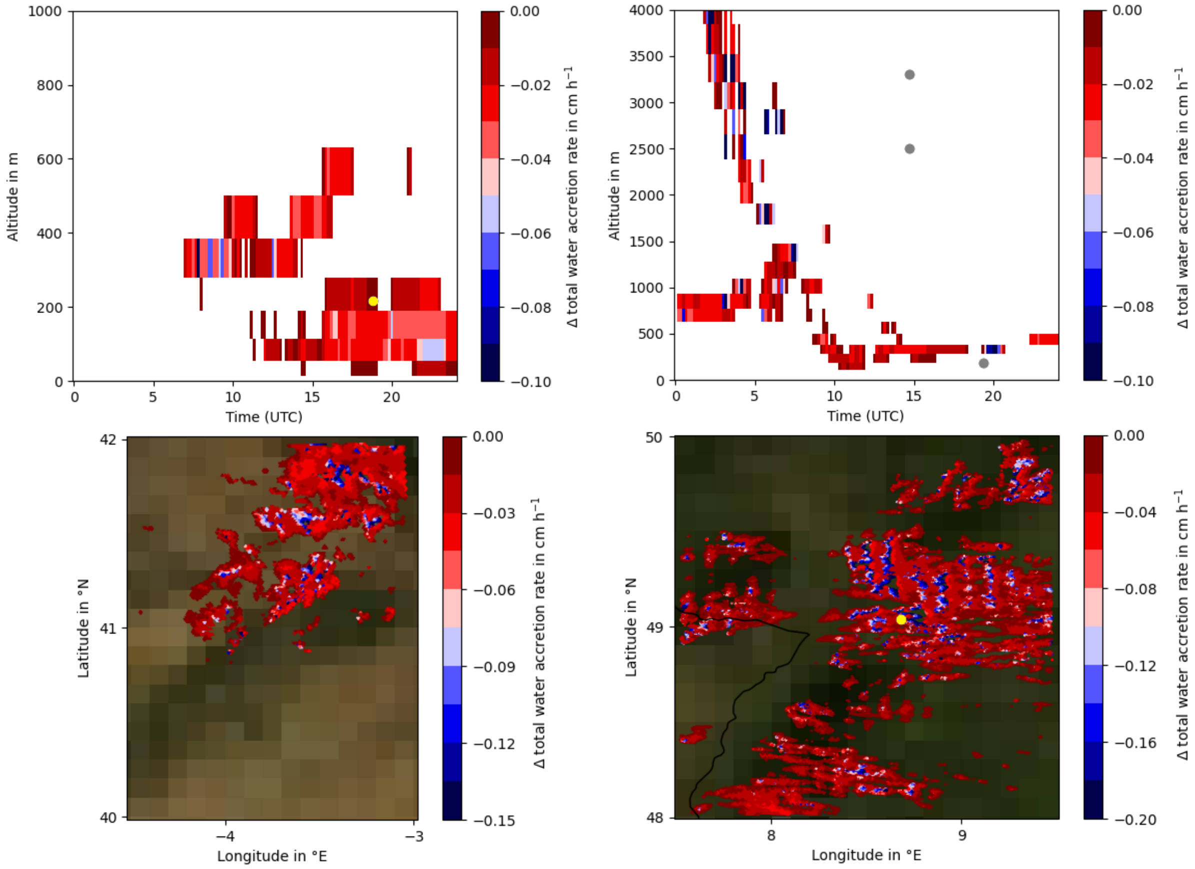

Figure 5.4: Differences in total water accretion rate - including rime and glaze ice and liquid water accretion - between the BULK simulation and the REF simulation as the temporal development of its vertical profile in the CAN24 case (top left) and in the CAN26 case (top right) and as its horizontal distribution in the SPN case (bottom left) and in the BWF case (bottom right). The position of the icing reports and incidents are marked with a yellow and gray dot.

thickness (as the sum of the rime and glaze ice thickness) introduced by the BULK simulations. The panel organization remains the same as in figure 5.1. The plots indicate an underestimation of the total ice thickness, if the cloud droplet spectrum is neglected, in all presented instances, comparable to the previously investigated quantities. Also similar to the previous investigations is the minor amplitude of the introduced changes. The typical actual values of the total ice thickness are in the order of 1×10^{-6} to 1×10^{-5} m. In most instances, and especially in lower altitudes and the centers of convective cells, the plots indicate effects with a small amplitude of around 1×10^{-8} m. Interestingly, these tend to also be those environments that experience the largest actual ice thicknesses. So comparable to the effects on the overall impingement efficiency, the BULK simulation cause the lowest impact on the total ice thickness, where that thickness is largest. In addition, the bottom panels that represent more convectively influenced situations, present a high spatial variability of the underestimation's extent, especially at the edges of the convective cells, which is not matched by the variability of the previous quantities, visualizing the complexity of the connections between those and other quantities. Ultimately, even the largest underestimations are still about an order of magnitude smaller than the actual values themselves. Extending the view to the entire simulation, figure 5.7 shows the relative frequency distribution of the change in total ice thickness induced by neglecting the cloud droplet spectrum for a more stratiformly influenced case (CAN24) in its left and a more convectively influenced case (BWF) in its right panel. Both histograms support the statement that the effect of neglecting the cloud droplet spectrum is an underestimation of the total ice thickness accreted in all instances as well as that the induced changes are very small for most instances. The frequency drops rapidly heading towards larger changes. This is especially true for the more stratiformly influenced CAN24 case. The more convectively

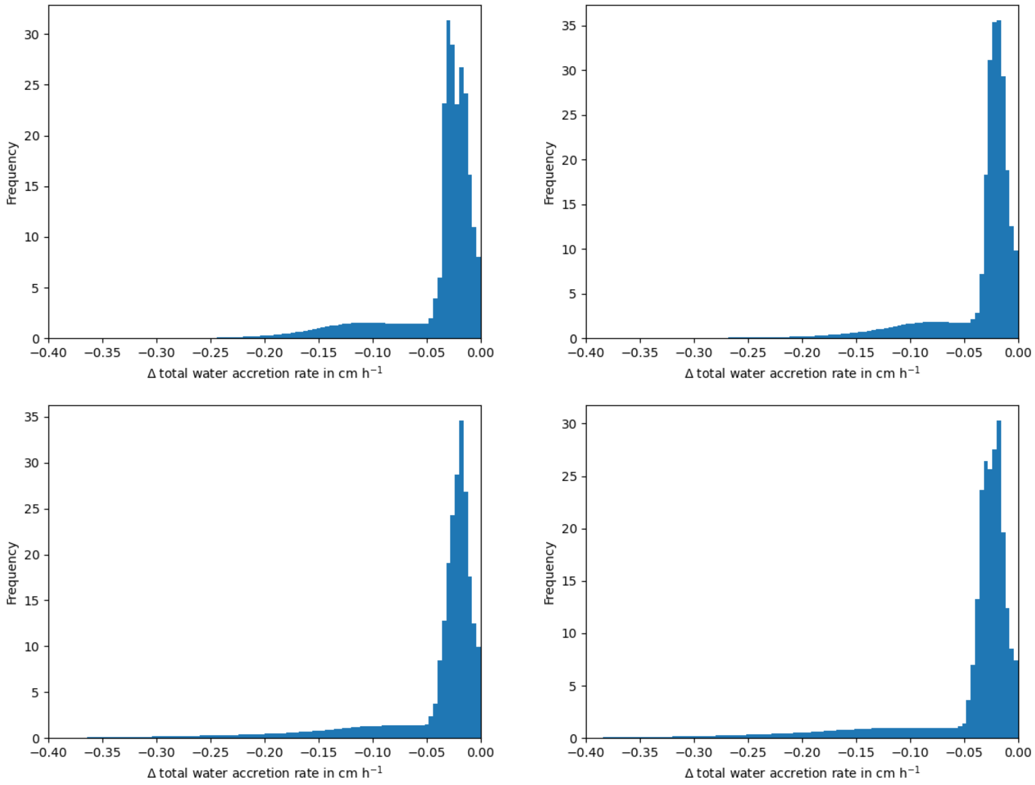

Figure 5.5: Relative frequency distribution of the differences in total water accretion rate between the BULK simulation and the REF simulation for the CAN24 case (top left), the CAN26 case (top right), the SPN case (bottom left) and the BWF case (bottom right)

influenced BWF case also shows the described drop in frequency, but to a lesser extent. Up to changes of about -3×10^{-7} m the frequency is significantly higher than in the stratiform case. This is explained by the higher occurences of edges in a more convective scenario with lower ice thickness values and the fact that lower ice thickness values experience a stronger effect of the neglected cloud droplet spectrum. Hence, the findings of the specific situations are also represented and supported by the findings of the entire simulation.

One finding regarding the effect the BULK simulations exert on the total water accretion rate is that the strongest underestimations coincide with higher actual values of the total water accretion rate. On the other hand, one effect of the BULK simulations on the total ice thickness is that the weakest underestimations coincide with higher values of the total ice thickness. High values of the total water accretion rate and of the total ice thickness coincide themselves, for example in the center of convective cells. So in these regions, the effect on the total water accretion rate is strong, while the effect on the total ice thickness is weak. Hence, this should have an effect on the relation between ice and water accretion. To investigate this further, figure 5.8 displays the effect of neglecting the cloud droplet spectrum on the rime fraction. The top panels show the relative frequency distributions of the rime fraction for the more stratiform CAN24 case, while the bottom panels show the corresponding distributions for the more convectively influenced BWF case. The left panels represent the REF simulations and the right panels the BULK simulations. Although both the total ice thickness and the total water accretion rate are consistently underestimated when neglecting the droplet spectrum, the rime fraction tends to be overestimated. The mean value for the rime fraction in the stratiform CAN24 case increases due to the negligence of the actual droplet spectrum from 0.217 to 0.235, while the more convectively influenced BWF case shows a corresponding increase from 0.407 to 0.419. The overall qualitative structure of the distributions, however, does not change much. The effect manifests mostly by an increase in frequency of the 1.0 values, so the purely rime ice accreting environments. This states that neglecting the cloud droplet spectrum leads to an overestimation of regions where the wet icing phase is not triggered. With the property of liquid water, which is only accreted during the wet icing phase, to flow along the aircraft's surface

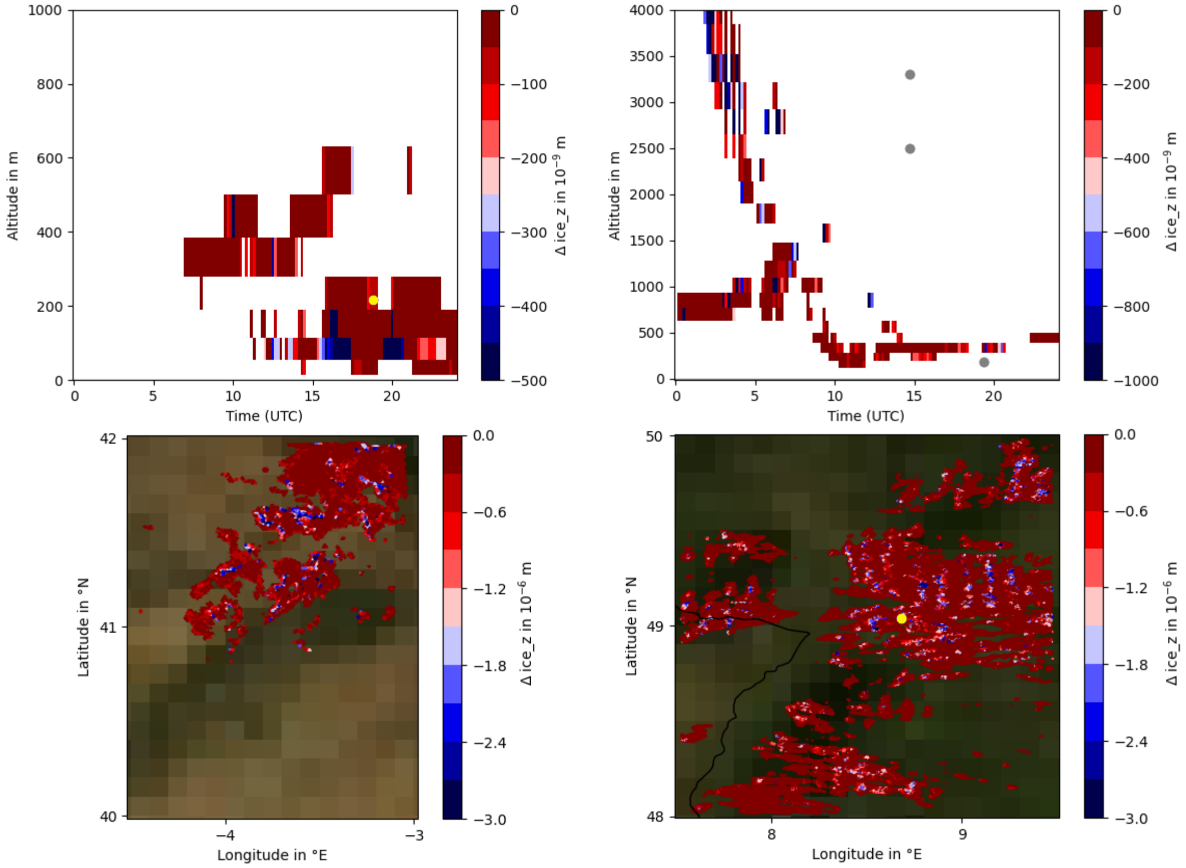

Figure 5.6: Differences in accreted ice thickness - including rime and glaze ice - between the BULK simulation and the REF simulation as the temporal development of its vertical profile in the CAN24 case (top left) and in the CAN26 case (top right) and as its horizontal distribution in the SPN case (bottom left) and in the BWF case (bottom right). The position of the icing reports and incidents are marked with a yellow and gray dot.

to freeze upon potentially unprotected elements, this may lead to potentially severe underestimations of the icing hazard, in these instances. Comparable to the previously investigated quantities, the effects on the rime fraction caused by neglecting the actual droplet spectrum does not depend significantly on whether the situation is more stratiformly or convectively influenced.

In conclusion, the droplet spectrum plays a role in the computation of the overall impingement efficiency of the newly developed aircraft icing parameterization, as the individual impingement efficiency values for the resolved droplet sizes along the spectrum are computed and weighted with its mass fraction in the spectrum. Neglecting the consideration of the droplet spectrum results in only the impingement efficiency of the mean droplet mass being used. The effects this has on the results of the newly developed aircraft icing parameterization are a consistent underestimation of the overall impingement efficiency, of the total water accretion rate respecting rime ice, glaze ice and liquid water and of the accreted total ice thickness. The scale of the effects depend on the actual values, where environments of originally higher values are less affected regarding the overall impingement efficiency and the total ice accretion, but more affected regarding the total water accretion rate. Hence, neglecting the droplet spectrum overestimates the rime fraction, including an overestimation of the frequency of purely dry icing environments. However, the induced effects are overall small, so that neglecting the actual cloud droplet spectrum may be acceptable with regards to its reduced computational costs.

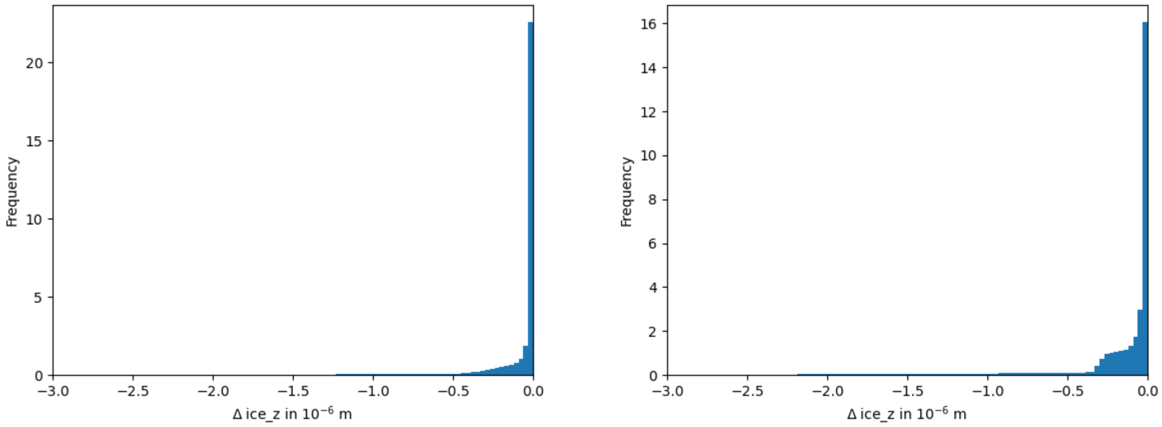

Figure 5.7: Relative frequency distribution of the differences in total ice thickness between the BULK simulation and the REF simulation for the stratiform CAN24 case (left), and the convective BWF case (right).

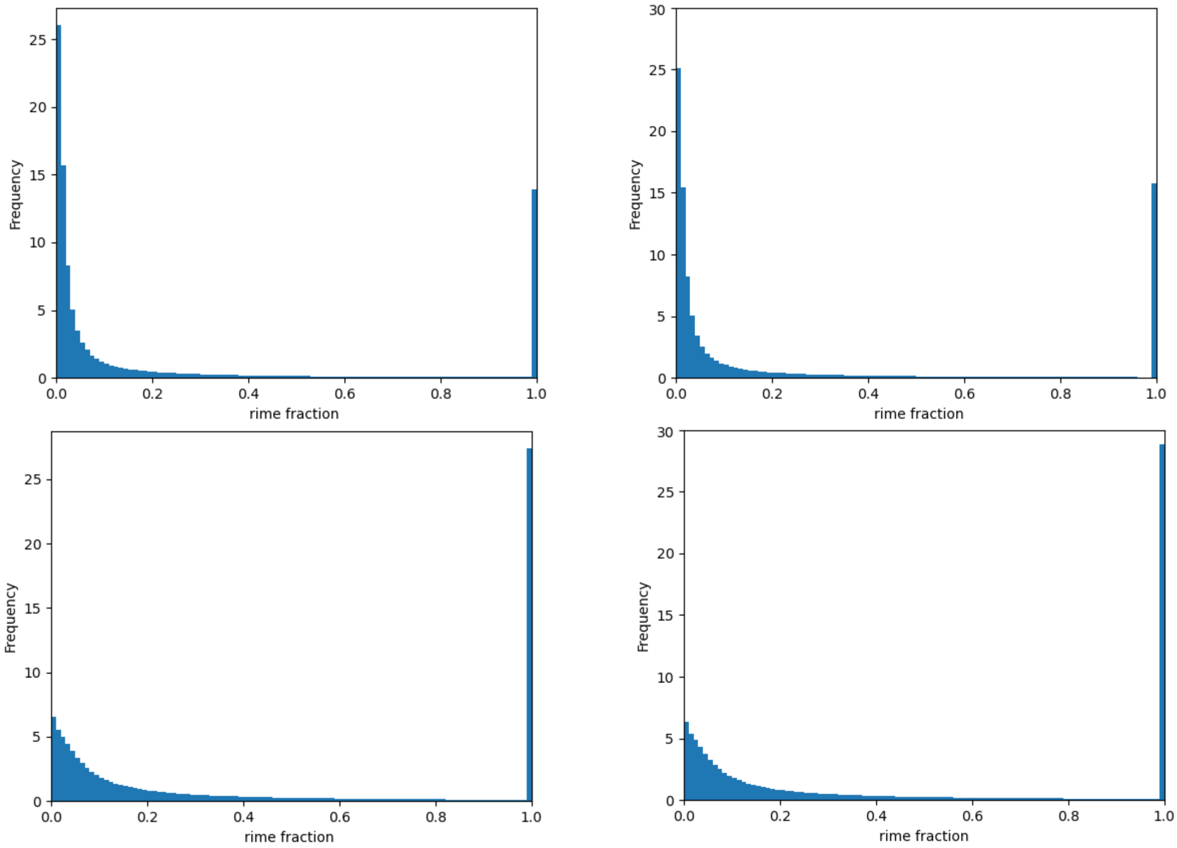

Figure 5.8: Relative frequency distribution of the rime fraction for the CAN24 case (top) and the BWF case (bottom) in the REF simulation (left) and the BULK simulation (right).

6 Sensitivity to aerosol load

Aerosols and aerosol load may interact with the formation of cloud droplets, depending on their ability to act as cloud condensation nuclei (CCN). Since cloud droplets form the source of water for aircraft icing, this chapter investigates the effects a change in aerosol load, acting as CCN, exerts onto the presence and intensity of aircraft icing environments. Hence, it also looks into the importance of a proper representation of the development of such aerosol concentrations. This sensitivity analysis is conducted in two stages: Firstly, the sensitivity is investigated when the aerosol load is solely influencing the new aircraft icing parameterization, which is represented in an induced change in cloud droplet number density used in the parameterization. Secondly, a change in the CCN aerosol load is applied to the entire simulation and therefore to the cloud droplet nucleation process itself.

6.1 Modification of cloud droplet numbers

The following section discusses the sensitivity of the results of the new aircraft icing parameterization to the cloud droplet number density. The liquid water content remains unchanged in this process, only the droplet number density is altered for the new aircraft icing parameterization, which effectively alters the droplet sizes of the environment. Only applying the changes to the parameterization itself gives an idea on how sensitive the parameterization is to only this change without any potential compensating forces. The found sensitivities are also mostly independent of the actual cloud droplet nucleation parameterization used, which make them applicable for simplified parameterizations that are for example less dependend on the aerosol load.

6.1.1 Expectations

Since larger droplets are more likely to impinge onto the surface of an airflow disturbing object than smaller ones that are easier diverted around the object, the droplet size is a crucial parameter for aircraft icing. Altering the cloud droplet number density while keeping the LWC unchanged, distributes the LWC onto more or less droplets, resulting in smaller or larger median diameters of the droplets respectively. Depending on the scale of the alteration, this is expected to lead to significant changes in the overall impingement efficiency. Combined with an unchanged LWC the resulting total accretion of water, hence, changes accordingly. As stated by the results in the previous chapter, where a reduced overall impingement efficiency lead to an increase in rime fraction, this same connection can be expected to be found in this sensitivity analysis as well. However, the droplet size is not only relevant for the overall impingement efficiency, but also for the initial rime ice density forming directly at the surface of the object, which may in turn alter the rime ice accretion and the rime fraction.

6.1.2 Results

For this investigation of the influence of the aerosol load solely on the newly developed aircraft icing parameterization, two sensitivity simulations are conducted for each of the analysed cases. These sensitivity simulations alter the cloud droplet number density (as a proxy for the aerosol load) used by the aircraft icing parameterization by applying a factor of 0.1 and 10.0 and are labelled NC01 and NC10, respectively. To give a visual expression of the effects introduced by these sensitivity simulations, figure 6.1 displays the differences in overall impingement efficiency between them and the REF simulation for the BWF case. The left panels are temporal developments of its profile and the right panels its horizontal distribution at the time, the reported icing

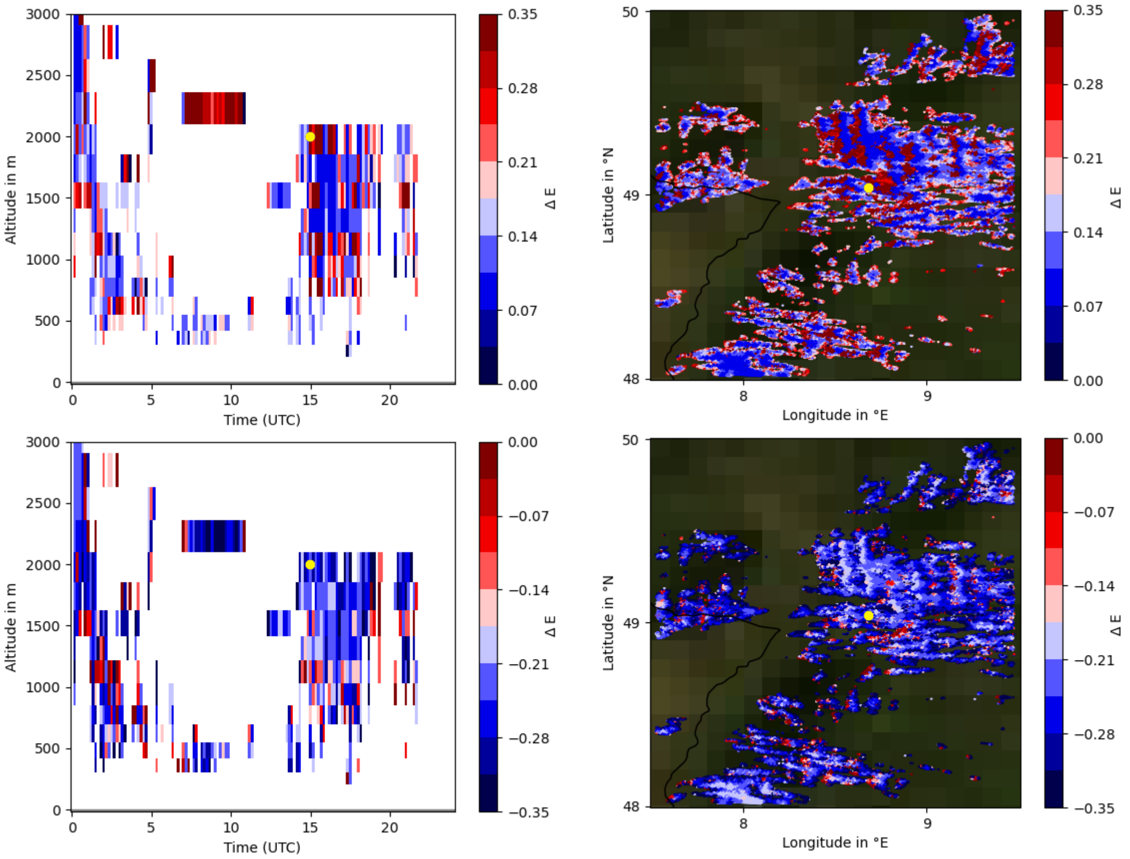

Figure 6.1: Differences in overall impingement efficiency between the NC01 (top), NC10 (bottom) simulation and the REF simulation as the temporal development of its vertical profile (left) and as its horizontal distribution (right) for the BWF case, the profile is taken at the location of the reported icing incident and horizontal distribution at its time in an altitude of 2000 m. The position of the icing incident is marked with a yellow dot.

incident occured. The top panels represent the effects of the NC01 and the bottom panels of the NC10 simulation. The top panels indicate that a decrease in cloud droplet number density leads to an increase in overall impingement efficiency, which meets expectations as the consequently larger droplets have higher inertia and are therefore more likely to impinge. The amplitude of the effect seems to depend on the actual impingement efficiency value with higher values experiencing minor increases and lower values experiencing larger increases. This is best portrait in the horizontal distribution where the centers of the convective cells are less affected than their edges. The bottom panels introduce the opposite effect: An increase in cloud droplet number density leading to a reduction in overall impingement efficiency. Interestingly, the amplitude of this effect is similarly distributed to the one above, indicating the same dependency of the effect's amplitude on the actual overall impingement efficiency. The effects of the altered cloud droplet number density exceed those of the previously discussed explicit consideration of the cloud droplet spectrum, because of the former affecting the mean droplet size, which remained unchanged in the latter. Although the plots displayed in figure 6.1 give a good indication on how the sensitivity to the cloud droplet number density manifests itself, the fixed horizontal position for the profiles and the fixed time and altitude for the maps pose limits to its generalization, which are further enhanced by the fact that only the BWF case is shown. To support and confirm the findings, figure 6.2 collects the relative frequency distributions of the overall impingement efficiency for the NC01, REF and NC10 simulations (from left to right) in the CAN24, CAN26, SPN and BWF case (from top to bottom). The histograms incorporate data from the entire respective simulation domain and period. Looking at the three columns representing the NC01, REF and NC10 simulations, respectively, it is imminent how strongly the cloud droplet number density can affect the overall impingement efficiency distribution. The NC01 simulations present a distribution that resembles in a way the one for the empirical formulation introduced in

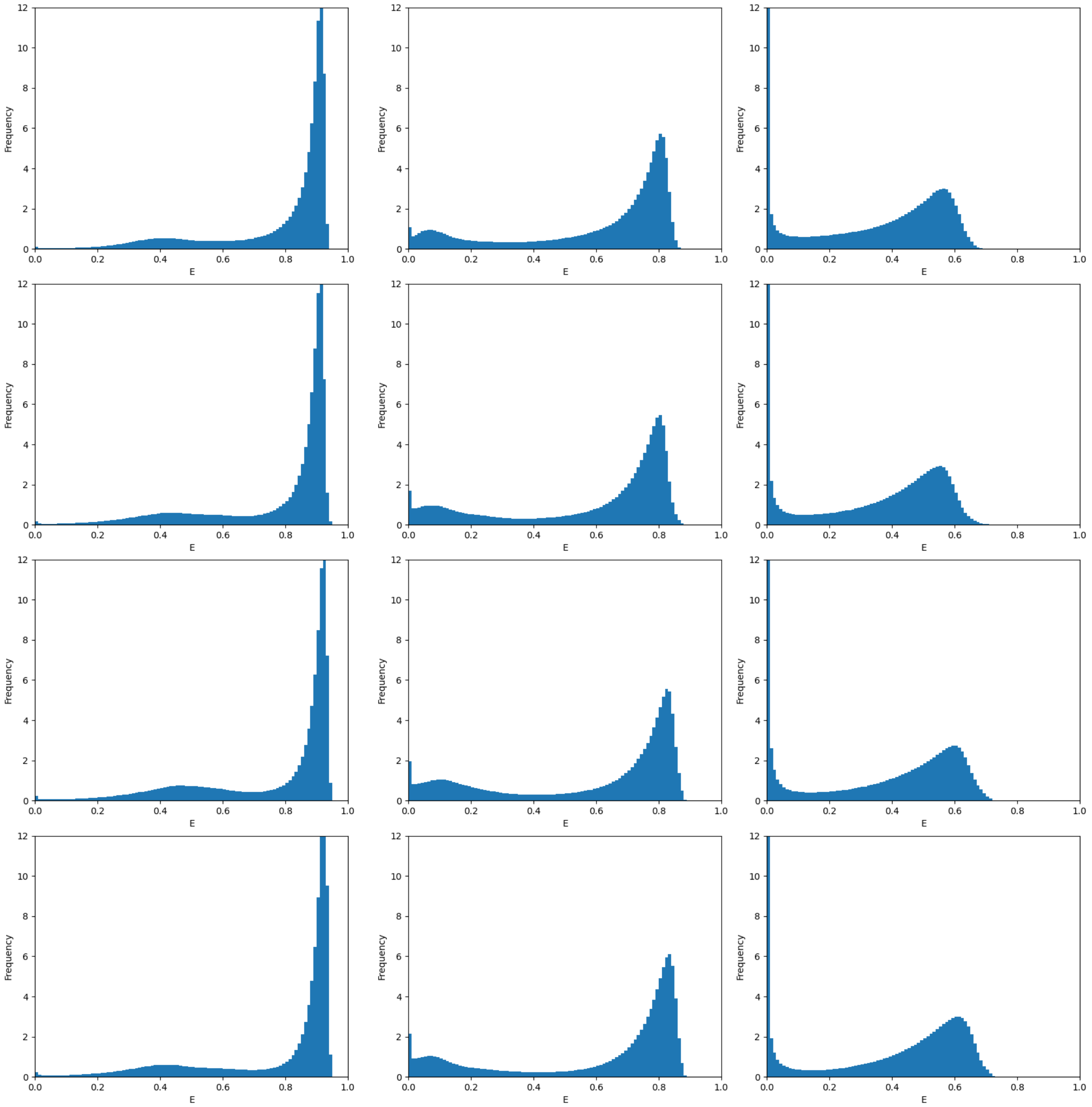

Figure 6.2: Relative frequency distributions of the overall impingement efficiency in the NC01 (left), REF (center) and NC10 (right) simulations for the CAN24 (1st row), CAN26 (2nd row), SPN (3rd row) and BWF case (4th row).

chapter 4.1 but shifted to larger values. The main difference of this empirical formulation to the newly developed physically based one, is the lack of differentiation, especially at higher values. Since the NC01 simulation generates higher impingement efficiency values, the limit of 1.0 results in a reduction of the differentiation, so the similarity to a shifted form of the empirical formulation is sensible. Additionally, compared to the relative distributions of the REF simulations in the central column, the distance between the primary and secondary maximum shortens in the NC01 simulation, reducing the variability. Interestingly, a difference between the more stratiformly and the more convectively influenced cases is still represented as a more pronounced secondary maximum at lower overall impingement efficiency values for the convective cases. The frequency distributions of the NC10 simulations show a mirrored effect, confirming the aforementioned findings. The primary maximum at high overall impingement efficiency values is significantly shifted towards lower values, as is the secondary maximum at the lower end of the value range. The latter, however, encounters the natural lower limit of the overall impingement efficiency value range of $E = 0$, resulting in a heavily increased peak at around that limit. This also results in the loss of that corresponding characteristic of more convectively influenced situations, namely the more pronounced secondary maximum at lower impingement values. However, the two more convectively influenced cases still stand out in the NC10 simulations, since their characteristic concerning the primary maximum, its shift to larger values, still remains. Interestingly, the range of this distribution is similar to the one of the empirical formulation in chapter 4.1. As it is still significantly different in other aspects shows that the empirical formulation actually misses physical features beyond its range. Regarding the mean value of the overall impingement efficiency, the effects of the alteration of the cloud droplet number density are well within expectations. The NC01 simulations increase it from 0.602, 0.586, 0.584 and 0.611 to 0.788, 0.776, 0.771 and 0.784 for the CAN24, CAN26, SPN and BWF case, respectively, while the NC10 simulations result in decreased mean values of 0.350, 0.337, 0.350 and 0.382. Concluding the effect on the overall impingement efficiency, it is found that environments with higher overall impingement efficiency values are less affected by the change in cloud droplet number density than those with low values. However, in all instances the effect shows relevant amplitudes. Meeting expectations, a reduction in cloud droplet number density leads to an increase in overall impingement efficiency, while an increase in cloud droplet number density leads to a reduction. Additionally, as the impingement efficiency can only have values between 0 and 1, there are limits to the effects that can be induced, which are met by changing the cloud droplet number density to the given extents.

The following part covers the analysis of how the actual icing quantities are affected by the NC01 and NC10 simulations compared to the REF simulation. Since one of the features of the newly developed aircraft icing parameterization is the separation of the freezing phases during icing and the computation of rime ice, glaze ice and water film accretion as well as their rates, these are the quantities investigated. Starting with the mean rime ice accretion rate during the dry icing phase, figure 6.3 plots the relative frequency distributions of this quantity for the sensitivity and the reference simulations. The panel organisation remains as it is in the previous figure. The NC01 simulations result in reduced frequencies of rime accretion rates below $1.0\,\mathrm{cm\,h^{-1}}$ compared to the corresponding REF simulations, as well as an increase in frequencies of higher rime accretion rates and an extension of the value range. This is in line with the findings regarding the overall impingement efficiency, since its increase results in a higher impinging flux of liquid water and therefore an increased accretion is sensible. The same reasoning applies to the NC10 simulations that show increased frequencies for lower rime accretion rates as well as decreased frequencies for higher values and a reduction in the overall value range. One can clearly see that the vast majority of instances in the different cases experience next to no rime accretion in the NC10 simulations and the frequencies of environments with increasing rime accretion rates diminish rapidly. On the other hand, for the NC01 simulations the diminishing of the relative frequencies occurs to a considerable lesser extent, especially for the first few rime accretion rate values. This is qualitatively shared among all of the shown cases. However, the more convectively influenced situations of the SPN and BWF cases extend the reduced diminishing of the frequencies to higher rime accretion values, retaining their characteristica comparable to the REF simulations. For the mean values of the shown distributions, the NC01 simulations yield increased values of $1.926\,\mathrm{cm\,h^{-1}}$, $1.635\,\mathrm{cm\,h^{-1}}$, $1.925\,\mathrm{cm\,h^{-1}}$ and $2.355\,\mathrm{cm\,h^{-1}}$ for the CAN24, CAN26, SPN and BWF cases, respectively, compared to the REF simulations' values of $1.513\,\mathrm{cm\,h^{-1}}$, $1.257\,\mathrm{cm\,h^{-1}}$, $1.477\,\mathrm{cm\,h^{-1}}$ and $1.881\,\mathrm{cm\,h^{-1}}$. The NC10 simulations' mean values for the rime accretion rate are strongly reduced throughout, evaluating to $0.944\,\mathrm{cm\,h^{-1}}$, $0.778\,\mathrm{cm\,h^{-1}}$, $0.973\,\mathrm{cm\,h^{-1}}$ and $1.258\,\mathrm{cm\,h^{-1}}$.

Concluding, the rime accretion rate is quite sensitive to an alteration of the cloud droplet number density. The changes are in line with the expectations and the findings regarding the overall impingement efficiency and they are reflected in both the changes in frequencies of low and high rime accretion rates as well as in the mean value. However, the characteristica separating the more convectively influenced cases from the more stratiform ones remain.

Rime ice accretion halts, if the aircraft leaves the icing conditions or the critical ice thickness is accreted and the wet icing phase is initiated. Ice accretes in glaze form during this phase. To understand how the NC01 and NC10 simulations alter the glaze accretion rate compared to the REF simulations, figure 6.4 displays its relative frequency

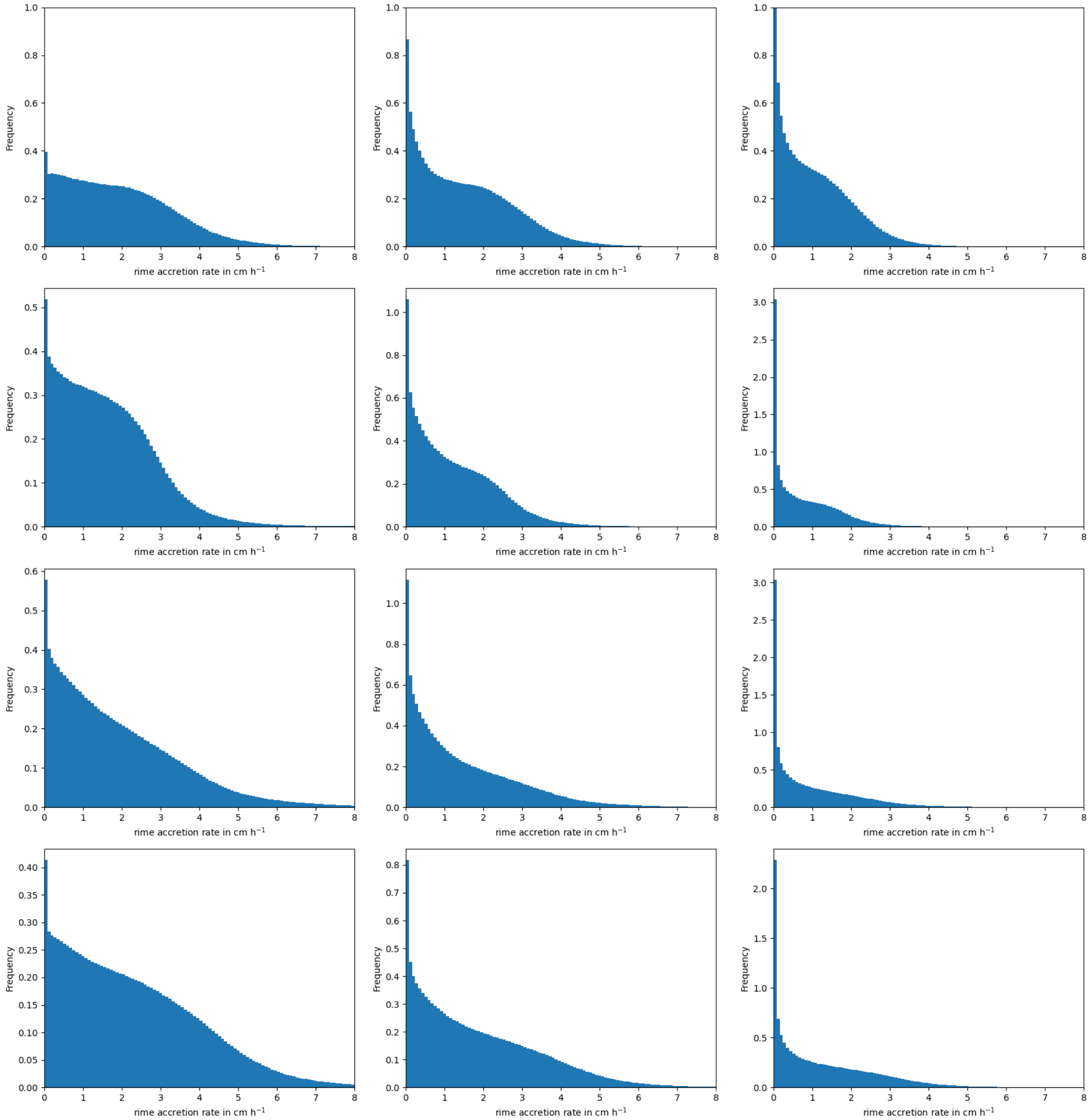

Figure 6.3: Relative frequency distributions of the mean rime accretion rate in the NC01 (left), REF (center) and NC10 (right) simulations for the CAN24 (1st row), CAN26 (2nd row), SPN (3rd row) and BWF case (4th row).

distributions for the different sensitivities and cases. The panels are organised the same way as in the previous figures. For both sensitivity simulations, NC01 and NC10, the impact on the glaze accretion rate is weak. Contrary to the previously analysed rime accretion rate, this ice accretion during the wet icing phase shows no obvious sensitivity, neither in a shift nor a structural change in the shown distributions. Upon closer inspection, however, there are some consistent effects found for the alteration of the cloud droplet number density. While the frequencies of the lowest glaze accretion values increase slightly with increasing cloud droplet number density, the highest frequencies of the upper ends of the shown distributions are found in the NC01 simulation. Still these effects are of small scale, which is also represented in the means of these glaze accretion rate distributions. Their values from the REF simulation, $0.294\,\mathrm{cm\,h^{-1}}$, $0.462\,\mathrm{cm\,h^{-1}}$, $0.686\,\mathrm{cm\,h^{-1}}$ and $0.758\,\mathrm{cm\,h^{-1}}$ for the CAN24, the CAN26, the SPN and the BWF case, respectively, increase slightly, but consistently, to $0.300\,\mathrm{cm\,h^{-1}}$, $0.479\,\mathrm{cm\,h^{-1}}$, $0.714\,\mathrm{cm\,h^{-1}}$ and $0.783\,\mathrm{cm\,h^{-1}}$ in the NC01 simulations, and decrease with a similar scale and consistency to $0.282\,\mathrm{cm\,h^{-1}}$, $0.438\,\mathrm{cm\,h^{-1}}$, $0.652\,\mathrm{cm\,h^{-1}}$ and $0.720\,\mathrm{cm\,h^{-1}}$ in the NC10 simulations, respectively. Since these effects are small

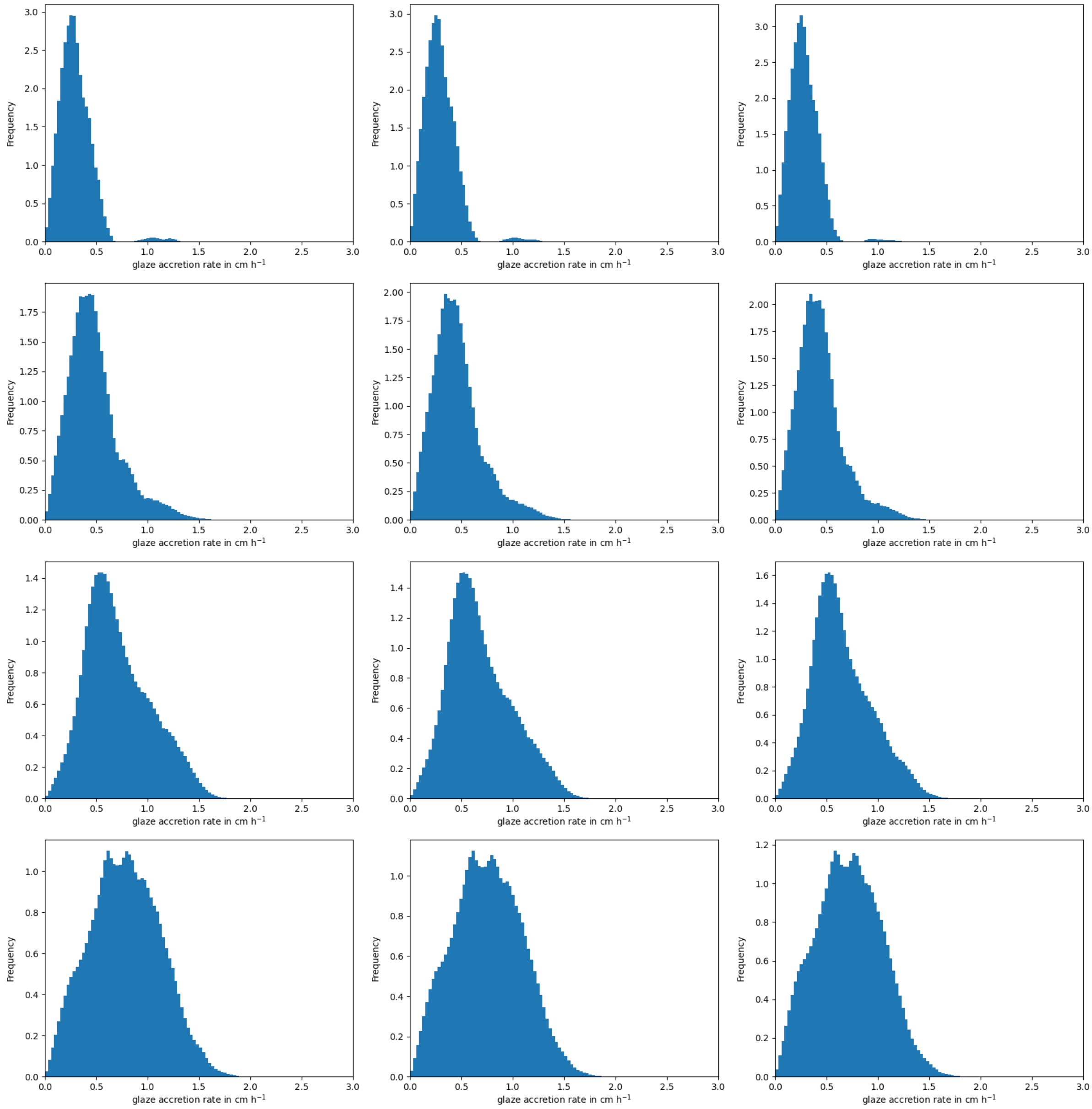

Figure 6.4: Relative frequency distributions of the mean glaze accretion rate in the NC01 (left), REF (center) and NC10 (right) simulations for the CAN24 (1st row), CAN26 (2nd row), SPN (3rd row) and BWF case (4th row).

in scale, the differences between the different cases remain. This is especially true for the characteristics a more convective situation has over a stratiform one, which in the case of the glaze accretion rate is a reduced incline and decline to and from the maximum of the corresponding distribution, resulting in more frequent occurences of higher glaze accretion rates. A likely explanation for the reduced sensitivity of the glaze accretion rate to the cloud droplet number density is for once, the reduced value of the quantity compared to the other accretion types, so effects on the general accretion rate are only represented to a reduced scale, especially since glaze ice accretes concurrently with liquid water, other than rime ice, which accretes independently. Additionally, as stated in chapter 4, actual ice accretion seems to be limited depending on the ambient air temperature, so increased effects on the rime accretion rate likely result in decreased effects for the glaze accretion rate.

Concluding, the glaze accretion rate is only minorly impacted by the changes in cloud droplet number density. The sign of the effect is in line with the effect exerted on the overall impingement efficiency, and consequently the impinging water flux.

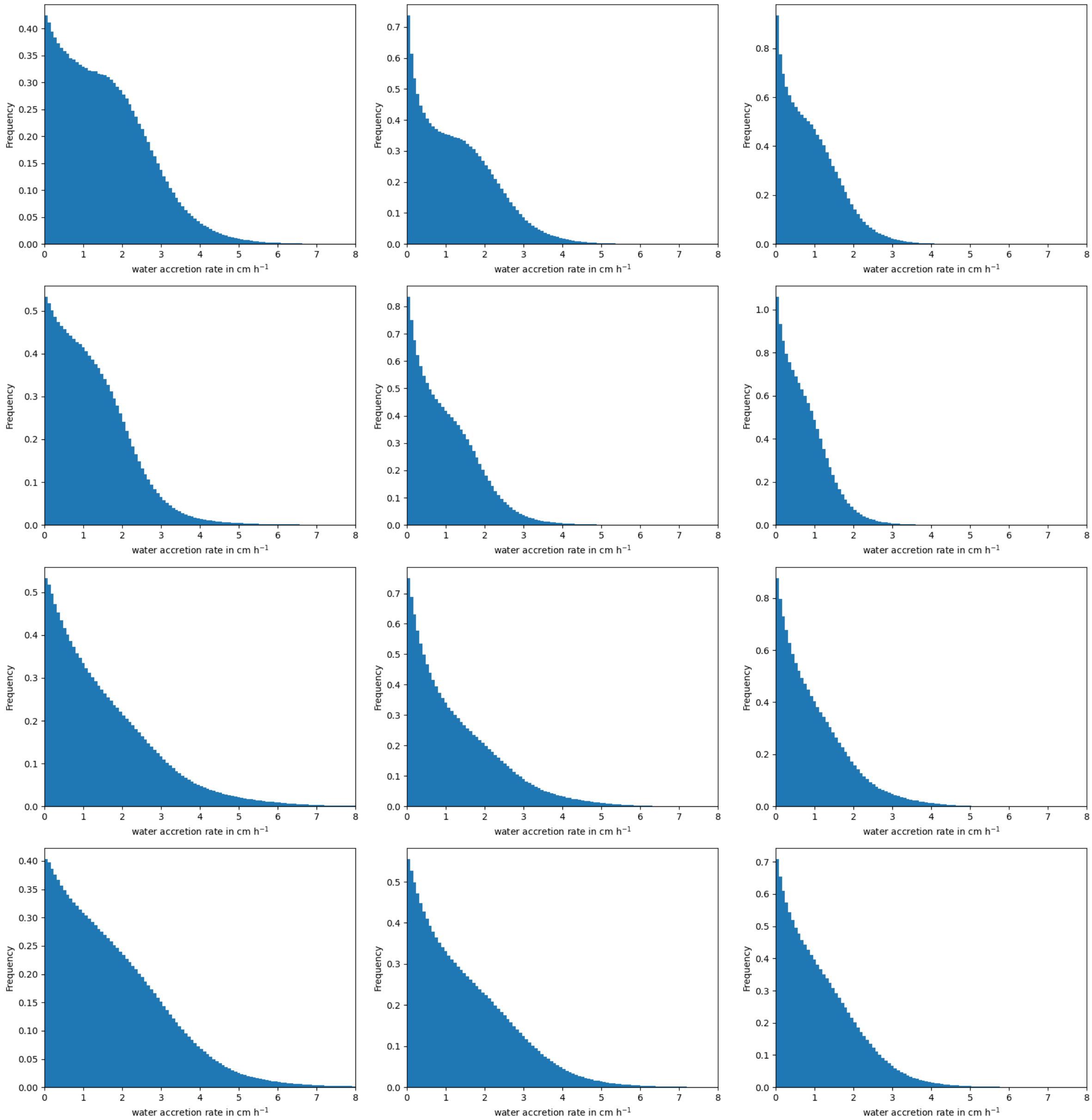

Figure 6.5: Relative frequency distributions of the mean water accretion rate in the NC01 (left), REF (center) and NC10 (right) simulations for the CAN24 (1st row), CAN26 (2nd row), SPN (3rd row) and BWF case (4th row).

The final part of the accretion process is the accretion of a liquid water film, whose sensitivity to a change in cloud droplet number density is presented in figure 6.5. The panels are arranged as in the previous figures. Since the liquid water accretion becomes increasingly more dominant the more impinging water is accreted, the effects of the NC01 and NC10 simulations are significantly greater than for the glaze accretion rate. Throughout all the displayed cases, a reduction of the cloud droplet number density results in decreasing frequencies of low water accretion rates and increasing frequencies of greater ones. Consequently an increase in cloud droplet number density yields higher frequencies of lower water accretion rates and a reduction of environments with high water accretion rate. Additionally the value range of this quantity is affected, with the NC01 simulations having greater maximum water accretion values than the REF simulations, which themselves have greater maximum values than the NC10 simulations. Also the characteristics of the convectively influenced cases, namely SPN and BWF represented in the bottom two rows, remain, as they still show increased frequencies of the highest water accretion rates on the expanse of the frequencies of lower water accretion rates compared to the more stratiform cases in the sensitivity

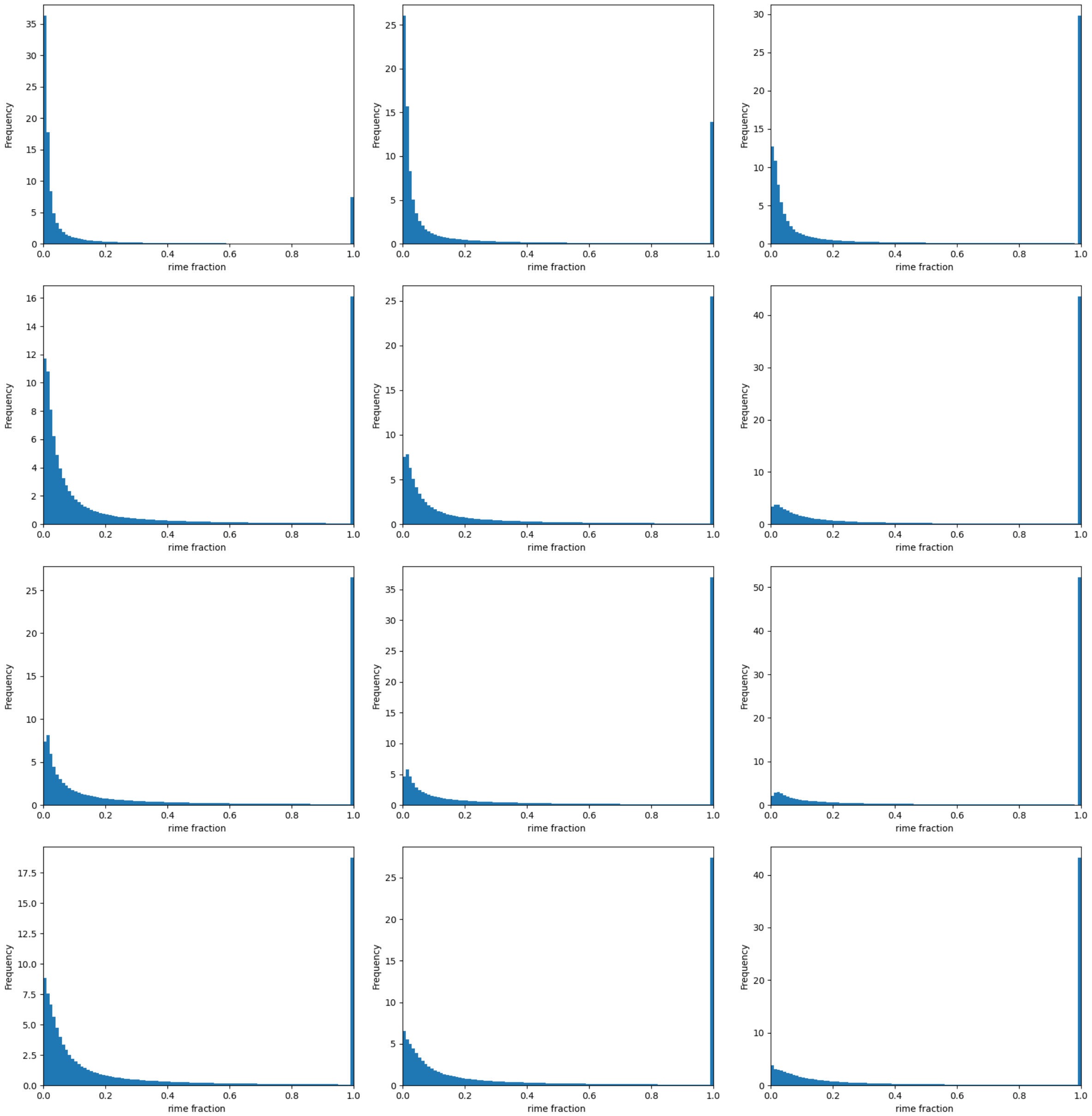

Figure 6.6: Relative frequency distributions of the rime fraction of the accreted material in the NC01 (left), REF (center) and NC10 (right) simulations for the CAN24 (1st row), CAN26 (2nd row), SPN (3rd row) and BWF case (4th row).

simulations. Overall the effects are similar to those experienced by the rime accretion rate. This is sensible, as the accretion rates are the expression of the impinging water flux, which does not change when transitioning from the dry to the wet icing phase. While the quantitive impact is reduced, compared to the rime accretion rate, since parts of the impinging water are accreted as glaze ice, the ever increasing part of the liquid water accretion during the wet icing phase results in this qualitative similarity to the rime accretion rates. Unsurprisingly, the mean values of this quantity reflect the effects on the distribution the alteration of the cloud droplet number density exerts accordingly. The mean values for the REF simulations, $1.277\,\mathrm{cm\,h^{-1}}$ for the CAN24 case, $1.011\,\mathrm{cm\,h^{-1}}$ for the CAN26 case, $1.285\,\mathrm{cm\,h^{-1}}$ for the SPN and $1.500\,\mathrm{cm\,h^{-1}}$ for the BWF case, increase to $1.567\,\mathrm{cm\,h^{-1}}$, $1.252\,\mathrm{cm\,h^{-1}}$, $1.550\,\mathrm{cm\,h^{-1}}$ and $1.786\,\mathrm{cm\,h^{-1}}$ in the NC01 simulations and decrease to $0.908\,\mathrm{cm\,h^{-1}}$, $0.731\,\mathrm{cm\,h^{-1}}$, $1.004\,\mathrm{cm\,h^{-1}}$ and $1.156\,\mathrm{cm\,h^{-1}}$ in the NC10 simulations, respectively.

As the previous analyses show, the variation in cloud droplet number density influences the different parts of the icing process to differing extents. This can have a resulting effect on the composition of the accreted material,

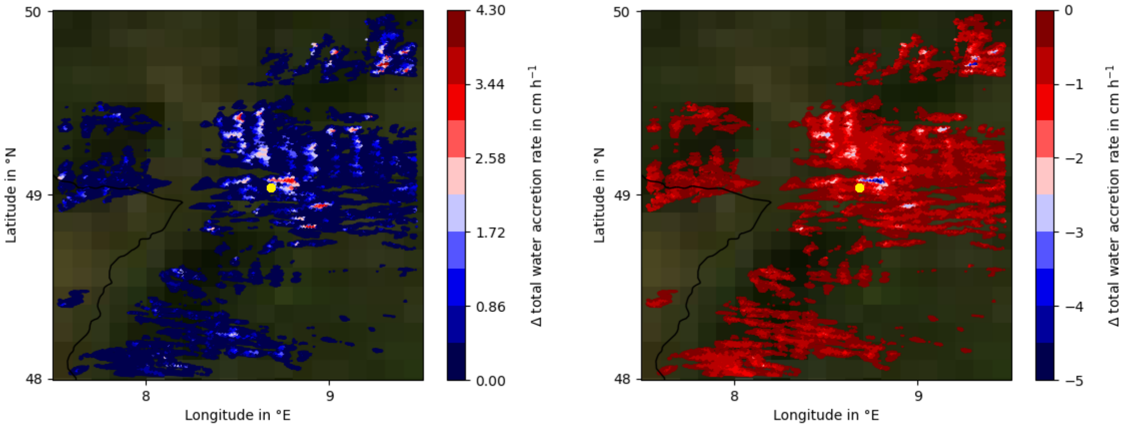

Figure 6.7: Horizontal distribution of the difference in total water accretion rate for the BWF case between the NC01 (left), NC10 (right) and the REF simulation at the time of the reported icing incident in an altitude of 2000 m. The location of the icing incident is marked with a yellow dot.

which is of importance as it may alter the intensity of an icing environment. This is due to the fact that accreted liquid water may freeze upon potentially unprotected parts of the aircraft as it flows further downstream. Hence, figure 6.6 highlights the sensitivity of the rime fraction, as part of the accreted material that is rime ice, to the cloud droplet number density, with the same panel organisation as the previous figures. For all simulated cases the frequency of purely dry icing environments, having a rime fraction of 1.0, increases with increasing cloud droplet number density. Consequently, environments with low rime fraction values, so where a majority of the time is spent in the wet icing phase, increases with decreasing cloud droplet number density. Although not to the same extent as the pure dry icing environments, icing environments with high rime fraction values below 1.0 are also more common when the cloud droplet number density increases. However, the distributions for the respective NC01, REF and NC10 simulation are structurally similar with the isolated peak at 1.0, showing high sensitivity to the cloud droplet number density, and a second maximum structure around 0.0 which rapidly reduces in frequency for higher rime fractions. The highest sensitivity is shown at the lowest values here. The sensitivity of the isolated peak representing purely dry icing conditions is of particular interest, as in those environments the impinging water freezes in its entirety, voiding the dangers of runback icing caused by liquid water flowing downstream the aircraft's body. Hence, an overestimation of the cloud droplet number density (at constant LWC) may result in the forecasting of wet icing environments as dry ones. And due to its isolation in the frequency distribution it is likely that the falsely forecasted dry icing environment actually has a low rime fraction, indicating that a significant amount of the accreted mass is liquid water.

Meeting expectations, the mean values of the rime fraction distributions reflect these findings. With the reduction of the droplet number density by a factor of 10 in the NC01 simulations, the mean rime fractions are reduced from the REF's 0.217, 0.377, 0.500 and 0.407 for the CAN24, CAN26, SPN and BWF case, respectively, to 0.134, 0.269, 0.395 and 0.313. The NC10s' increasing of the droplet number density, on the other hand, yields an increase of the mean rime fraction values to 0.379, 0.548, 0.632 and 0.554. Concluding, while the NC01 simulations underestimate the rime fraction, the NC10 simulations overestimate it. This indicates that the latter are likely to underestimate the hazards liquid water imposes by overestimating the frequencies of environments with low or no liquid water accretion.

With all these sensitivities investigated, figure 6.7 concludes this part by visualizing the differing outcomes of these sensitivity simulations combining the prior elements to the simple total water accretion rate. The plots show the horizontal distribution of the impact exerted on this quantity by the NC01 and NC10 simulations compared to the REF simulation in the BWF case at the time of the reported icing incident in an altitude of 2000 m. The NC01 simulation, whose impact is shown in the left plot, results in overall higher values of the total water accretion rate throughout the simulation area. This is due to the larger cloud droplets more efficiently impinging, increasing the influx of impinging water, which accretes in one form or another. As these different forms are combined in this visualization, the total water accretion rate experiences an increase. Most predominant are these increases in the centers of the convective cells. The right plot highlights the effect of the NC10 simulation and shows a clear reduction of the total water accretion rate. The smaller droplets are more easily diverted around the aircraft and impinge thereby less efficiently, ultimately reducing the influx of impinging water. Applying the same logic as before, the reduction of the total water accretion rates is sensible. Interestingly, the different icing environments seem to not be affected to the same extent as another. Environments with higher REF-values of the total water accretion rate, e.g. the centers of the convective cells, are affected more than those with lower REF-values, e.g. the edges of the convective cells. For enhancing effects, like the NC01 simulation, this ultimately results in an increase in horizontal heterogeneity, while the weakening effects of the NC10 simulation, homogenize the horizontal distribution of this quantity. Hence, already with this simple metric the sensitivity of the icing environments to the cloud droplet number density, as a proxy for the aerosol load, manifests itself in both intensity and variability of the icing environments.

6.2 Modification of CCN numbers

The previous section gives an idea on the maximum effect of the aerosol load, using the cloud droplet number density as proxy, on the intensity of icing environments. The following section, however, intends to discuss the sensitivity of the results of the newly developed aircraft icing parameterization to the actual aerosol load acting as CCN instead. While the previous section applied alterations only on the cloud droplet number density passed into the parameterization, the idea for this section is to apply the alterations to the aerosol load acting as CCN to also affect other processes, most importantly the cloud droplet nucleation parameterization, which affects in turn the liquid water content and the cloud droplet number density and therefore also the cloud droplet size.

6.2.1 Expectations

As in this part of the study the sensitivity factors are not applied only to the aircraft icing parameterization, but to the droplet nucleation parameterization, it is expected that the effects on the cloud droplet size are reduced. This reduction may be by potentially not all of the additional aerosols being activated as CCN or by a differing total amount of LWC being nucleated or by icing environments that are less influenced by droplet nucleation. The qualitative effects of altered droplet size on the overall impingement efficiency remains, but a differing amplitude with potentially altered LWC or other atmospheric quantities as a side effect of the altered nucleation parameterization may lead to more complex effects on different parts of the aircraft icing parameterization.

6.2.2 Results

The overall impingement efficiency is the main driver of this new aircraft icing parameterization, as it determines the extent of the water flux that gets in contact with the aircraft. Figure 6.8 visualizes how an altered aerosol load for the droplet nucleation parameterization used affects the icing situation of the reported icing incident in the BWF case. The left panels present the temporal development of the vertical profile of the induced changes onto the overall impingement efficiency at the location of the icing incident, while the right panels show their horizontal distribution at the time of the incident in an altitude of 2000 m. The top panels display the effects of the ACI01 simulation, which reduces the aerosol load by a factor of 10, while the bottom panels illustrate those of the ACI10 simulation, which increases the aerosol load by a factor of 10. Contrary to the effects the sole alteration of the cloud droplet number density induce, all sensitivity simulations affect the overall impingement efficiency both negatively and positively, depending on the actual environment, which is most likely due to small changes in position of the

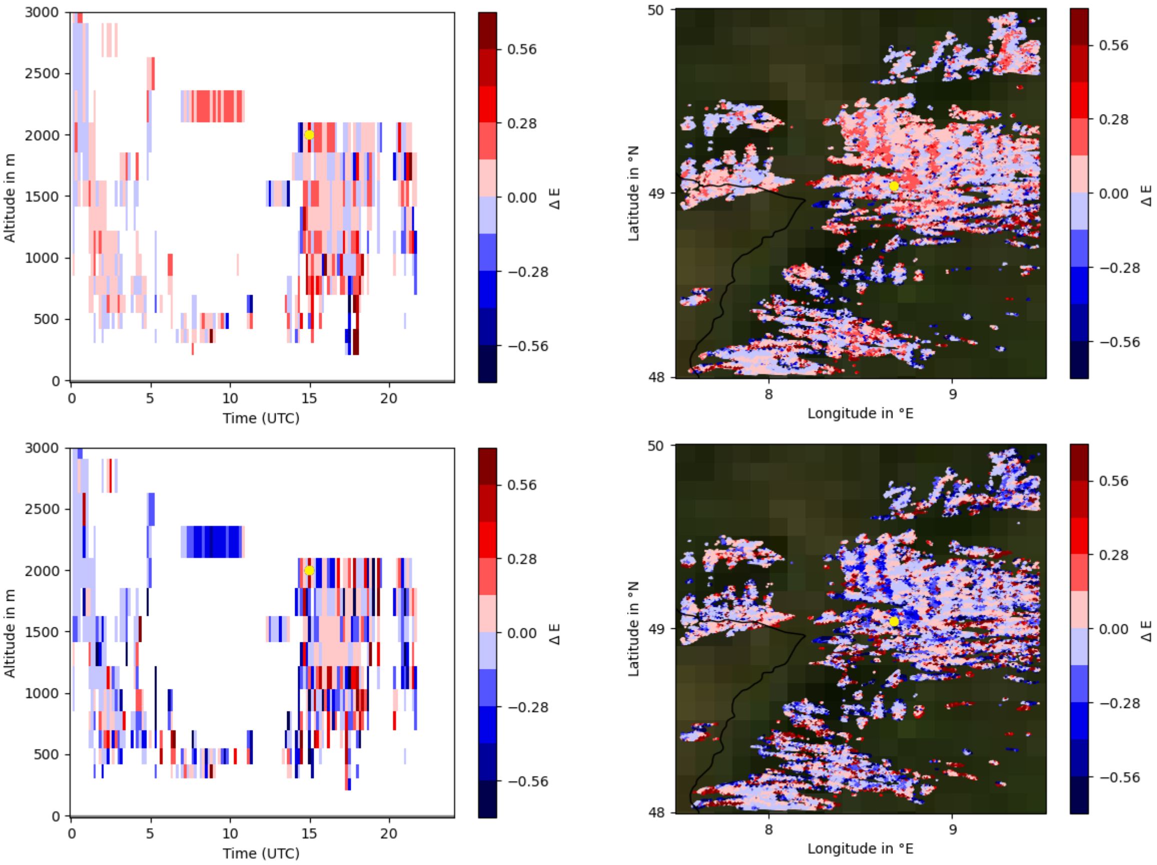

Figure 6.8: Differences in overall impingement efficiency between the ACI01 (top), ACI10 (bottom) simulation and the REF simulation as the temporal development of its vertical profile (left) and as its horizontal distribution (right) for the BWF case, the profile is taken at the location of the reported icing incident and the horizontal distribution at its time in an altitude of 2000 m. The position of the icing incident is marked with a yellow dot.

icing environments indicating a feedback of the altered droplet nucleation on the atmospheric state. Overall, the plots suggest, however, a general reduction of the impingement efficiency with higher aerosol load. The smallest effects are found, where high impingement efficiency values are simulated in the REF simulation, like the centers of convective cells. In addition, the effects have a high temporal, vertical and horizontal variability, as small changes in time and space can lead to severly different experienced changes in overall impingement efficiency. The illustrated large changes, towards both ends of the spectrum, are mostly due to new grid points having LWC values and other grid points losing them. This introduces another way of sensitivity: Not only does the aerosol load impact the amplitude of the overall impingement efficiency, but also the identification of the position of a potential icing environment itself, making an accurate aerosol representation valuable.

To get an idea on how the cloud droplet number density is affected by the alteration of the CCN number density, figure 6.9 provides its frequency distribution of the ACI01 simulation in its left, the REF simulation in its central and the ACI10 simulation in its right panel for the CAN24 case. One can see that although the cloud droplet number densities increase with increasing CCN number densities, the overall effect is reduced compared to the factor applied to the CCN number density itself. Additionally, the distributions also change structurally, so the effect induced by the change in CCN number density varies. This indicates a more complex effect on the droplets' sizes and therefore also on the overall impingement efficiency supporting the above findings. Further investigating the effects on the overall impingement efficiency, figure 6.10 provides an overview of the relative frequency distribution of this quantity in the ACI01, REF and ACI10 simulations from left to right for the CAN24, CAN26, SPN and BWF case from top to bottom. While the previously investigated sensitivity in cloud droplet number

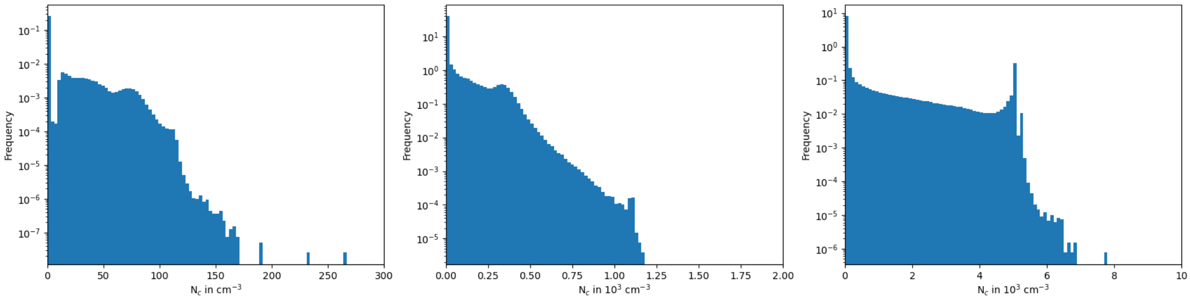

Figure 6.9: Relative frequency distributions of the cloud droplet number density in the ACI01 (left), REF (center) and ACI10 (right) simulations for the CAN24 case.

density manifests in an alteration of the entire distribution of overall impingement efficiency, the effect exerted by an alteration of the CCN number density seems to heavily prioritize the secondary maximum structure. In all of the shown cases a reduction of the CCN number density results in a shift of the secondary structure to higher overall impingement efficiency values. Consequently, when increasing the CCN number density, the secondary maximum shifts towards lower impingement efficiency values, ultimately gathering around $E = 0.0$, due to the impingement efficiency's inability to have negative values. This heavily resembles the way this structure is affected by altering cloud droplet number densities, as previously investigated. The primary maximum at high impingement efficiency values, however, remains largely unaffected in all displayed cases. While this structure also showed reduced sensitivity, compared to the secondary maximum, for the alteration of the cloud droplet number densities, this present highlighted inertness suggests that in the corresponding environments the CCN number density is not a significant factor for the droplets' size. This especially highlights that the humidity in these environments is not the limiting factor for the processes growing the droplets to the sizes required to reach these overall impingement efficiencies. The corresponding environments for the secondary maximum, however, seem to limit the droplets size by the available humidity or the droplets have just nucleated here. Hence, an alteration of the CCN number density results in altered droplet sizes, comparable to the alteration of the cloud droplet number density in the previous sensitivity investigation. As the described effects are shown in all presented cases, the different characteristica of these cases largely remain. This is especially true for the two more convectively influenced cases, SPN and BWF in the bottom two rows, whose primary maximum remains shifted to slightly higher values compared to the more stratiform cases, and they remain to have a more pronounced secondary structure.

As only parts of the distributions are affected by the alteration of the CCN, the mean values of the overall impingement efficiency change to a lesser extent than for the previously investigated alteration of the cloud droplet number density, yet the sign of the changes remains consistent. The mean overall impingement efficiency values of the REF simulations 0.602, 0.586, 0.584 and 0.611 for the CAN24, the CAN26, the SPN and the BWF case, respectively, increase in the ACI01 simulations to 0.632, 0.621, 0.628 and 0.648 and decrease in the ACI10 simulations to 0.568, 0.553, 0.547 and 0.586, respectively. Summarizing, the effects of the ACI simulations on the overall impingement efficiency depend heavily on the actual environment itself: Environments with already high overall impingement efficiency values are largely unaffected, which is mainly due to the fact that those environments are not limited in humidity for the droplets to grow to the respective sizes. Low impingement environments, however, are either more limited in the available humidity or are in the early stages of droplet growth, so that an alteration of the CCN number density has a direct stark impact on the droplet size and therefore the overall impingement efficiency.

Initiating the investigation of the effects on actual icing quantities, figure 6.11, using the same panel organisation as above, illustrates how the rime accretion rate is affected. Throughout all the presented cases, a reduction of the CCN number density leads to a reduced frequency of environments with lower rime accretion rates, while an increase results higher frequencies of these environments. This is most clearly highlighted by the frequency of the

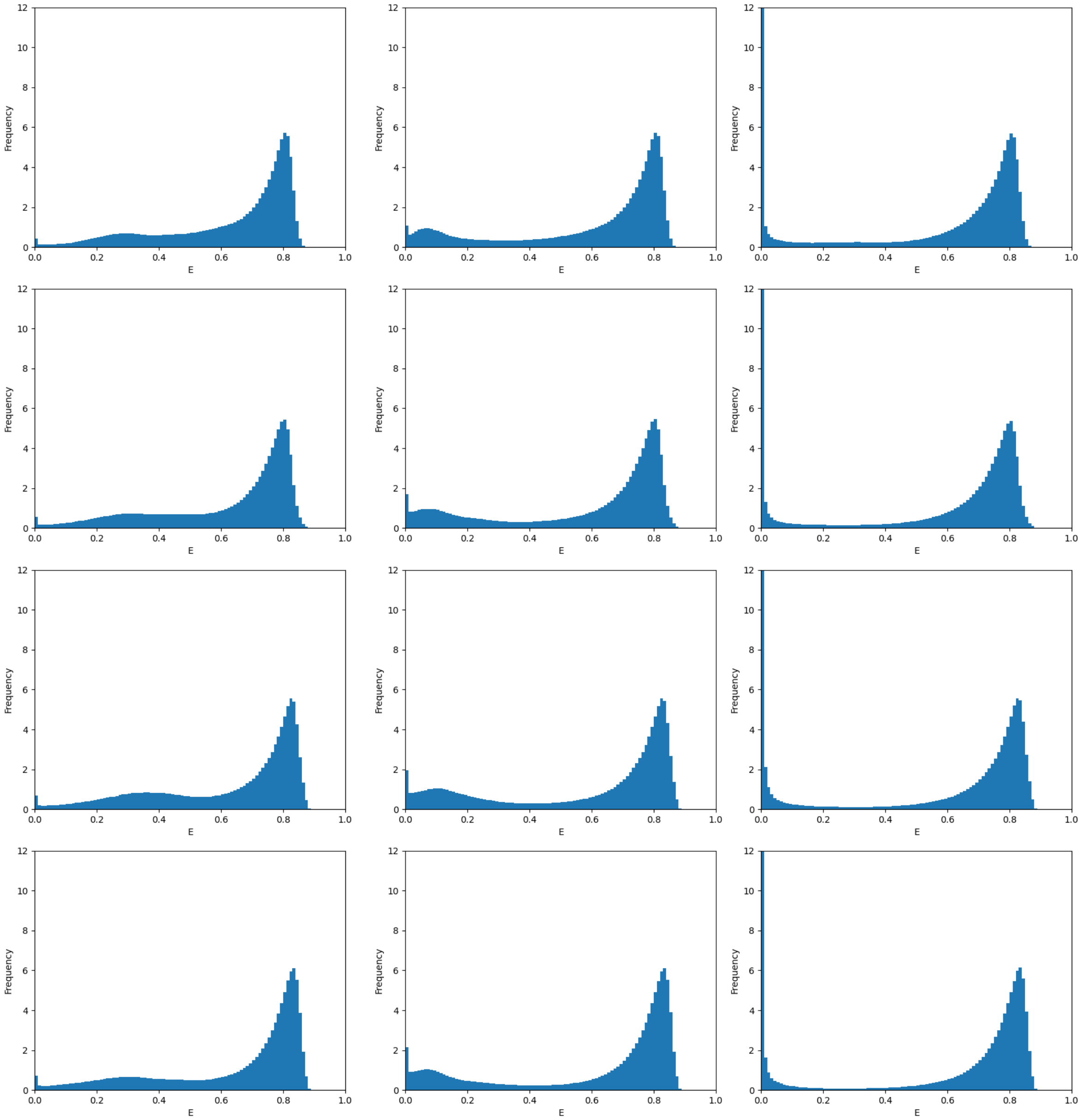

Figure 6.10: Relative frequency distributions of the overall impingement efficiency in the ACI01 (left), REF (center) and ACI10 (right) simulations for the CAN24 (1st row), CAN26 (2nd row), SPN (3rd row) and BWF case (4th row).

lowest rime accretion rate near $0.0\,\mathrm{cm\,h^{-1}}$. This is qualitatively in line with the findings for the direct alteration of the cloud droplet number density previously investigated and with the effect on the overall impingement efficiency, where the secondary maximum structure of low impinging environments shows significant sensitivity to the CCN number density. It is sensible to assume that these low impinging environments cause these low rime accretion rates. That the highest rime accretion rates are linked to environments with high overall impingement efficiency is also apparent. Contrary to the effect induced by an alteration of the cloud droplet number density, the alteration of the CCN number density only minorly affects the frequencies of environments with high rime accretion rates. As stated above, high impinging environments also stay largely unaffected by the alteration of the CCN number. Hence, it is safe to assume that these unaffected environments are also represented here. Since all presented cases are affected similarly by the changing CCN number densities, the characteristic differences between the more stratiform CAN24 and CAN26 cases, whose distributions form plateau-like structures up to about $2.0\,\mathrm{cm\,h^{-1}}$ followed by a stark diminishing of frequencies beyond that point, and the more convectively influenced cases SPN

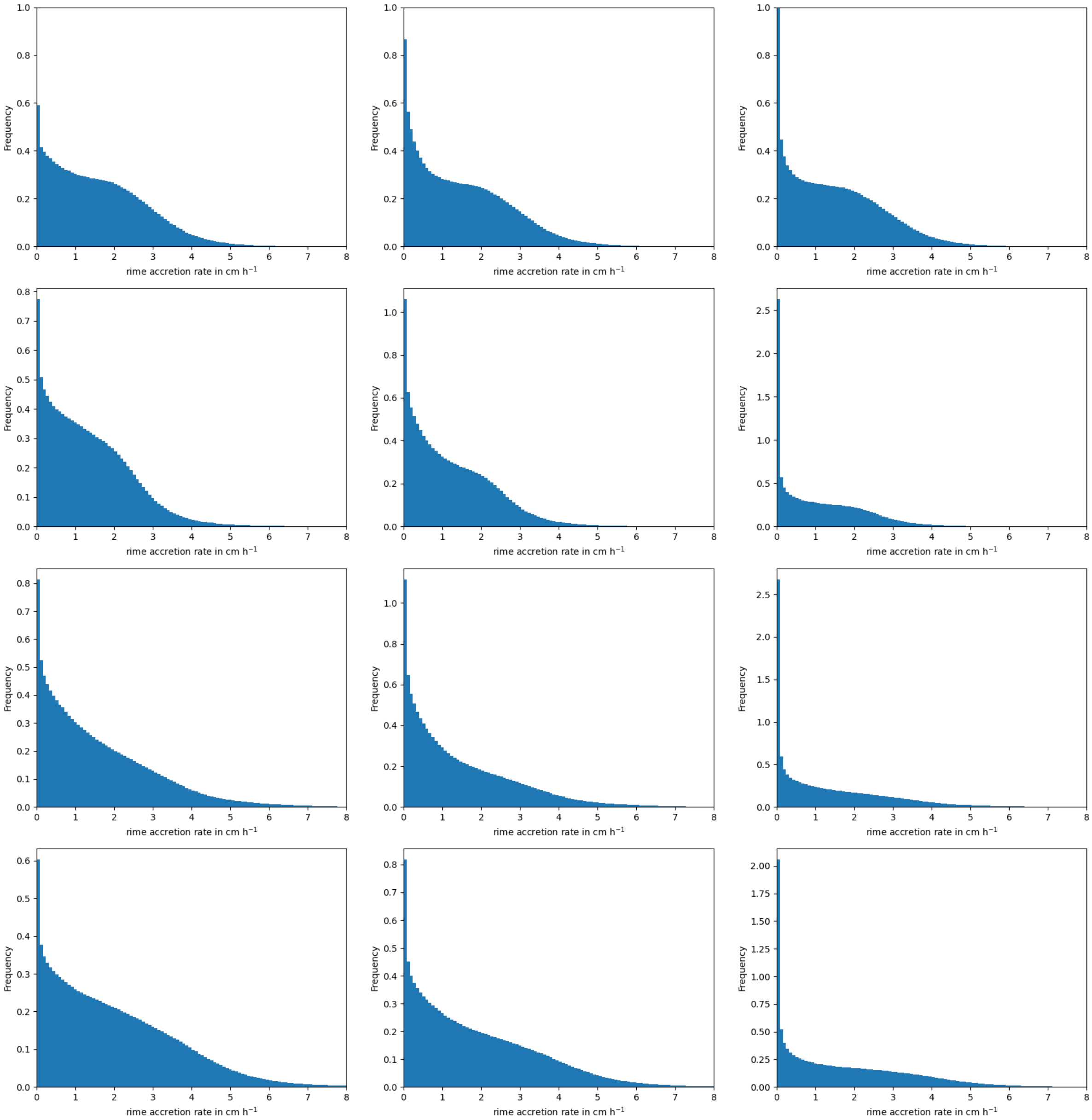

Figure 6.11: Relative frequency distributions of the mean rime accretion rate in the ACI01 (left), REF (center) and ACI10 (right) simulations for the CAN24 (1st row), CAN26 (2nd row), SPN (3rd row) and BWF case (4th row).

and BWF that show a more steady diminishing of frequencies, resulting in higher frequencies of environments with high rime accretion rates, remain. Due to the reduced effect on the high rime accretion rates' frequencies, this latter characteristic is additionally slightly enhanced. Although only parts of environments seem to be affected by the changing of the CCN number density, the qualitative effect matches the previously investigated cloud droplet number density sensitivity, if to a lesser extent. This is also represented in the mean values of these distributions, which are increased from the REFs' $1.513\,\mathrm{cm\,h^{-1}}$, $1.257\,\mathrm{cm\,h^{-1}}$, $1.477\,\mathrm{cm\,h^{-1}}$ and $1.881\,\mathrm{cm\,h^{-1}}$ for the CAN24, CAN26, SPN and BWF case, respectively, to $1.613\,\mathrm{cm\,h^{-1}}$, $1.365\,\mathrm{cm\,h^{-1}}$, $1.621\,\mathrm{cm\,h^{-1}}$ and $2.040\,\mathrm{cm\,h^{-1}}$ in the ACI01 simulations, and decreased to $1.364\,\mathrm{cm\,h^{-1}}$, $1.123\,\mathrm{cm\,h^{-1}}$, $1.351\,\mathrm{cm\,h^{-1}}$ and $1.708\,\mathrm{cm\,h^{-1}}$, respectively.

The second accretion type for impinging water is glaze ice, so figure 6.12 presents the relative frequency distribution of the mean glaze accretion rate, again using the same panel organisation as above. Since a direct alteration of the cloud droplet number density in the scope of the previously conducted sensitivity investigation yields only weak effects on the glaze accretion rate at the higher ends of the respective distribution, it is sensible that

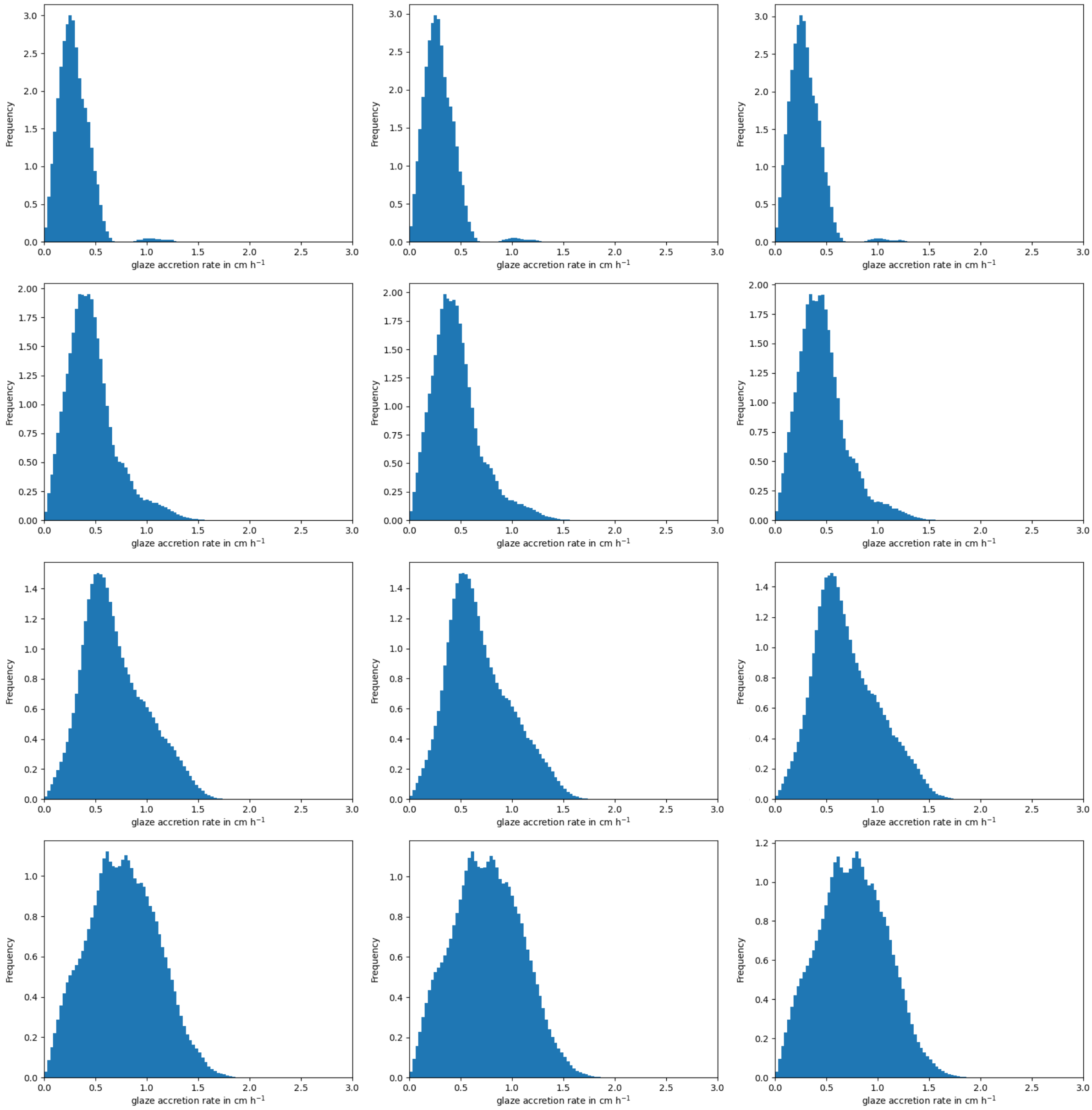

Figure 6.12: Relative frequency distributions of the mean glaze accretion rate in the ACI01 (left), REF (center) and ACI10 (right) simulations for the CAN24 (1st row), CAN26 (2nd row), SPN (3rd row) and BWF case (4th row).

also the ACI01 and ACI10 simulations presented here result in no considerable difference to the REF simulation in this regard. Additionally, as the analysis of the overall impingement efficiency highlighted that high impinging environments remain largely unaffected by the alteration of the CCN number density, also these weak effects on the higher ends of the distributions are reduced. One can clearly see that although there are some minor differences at places in the shown distributions between the corresponding ACI01, REF and ACI10 simulations, like the increased frequency of the second peak in the ACI10 simulation of the BWF case (bottom right), no general overall tendency can be stated. It is likely that these changes are rather due to slight shifts in the position of the respective environments, because of alterations in the feedback to the atmospheric state, as hinted at in figure 6.8, than to intrinsic changes in the icing environment itself. This void of tendency is also reflected in the mean values of these distributions, which are negligible in scale as well. The REFs' mean values for the glaze accretion rate evaluates to $0.294\,\mathrm{cm\,h^{-1}}$, $0.462\,\mathrm{cm\,h^{-1}}$, $0.686\,\mathrm{cm\,h^{-1}}$ and $0.758\,\mathrm{cm\,h^{-1}}$ for the CAN24, CAN26, SPN and BWF case, respectively. These values change only minorly to $0.295\,\mathrm{cm\,h^{-1}}$, $0.466\,\mathrm{cm\,h^{-1}}$, $0.691\,\mathrm{cm\,h^{-1}}$

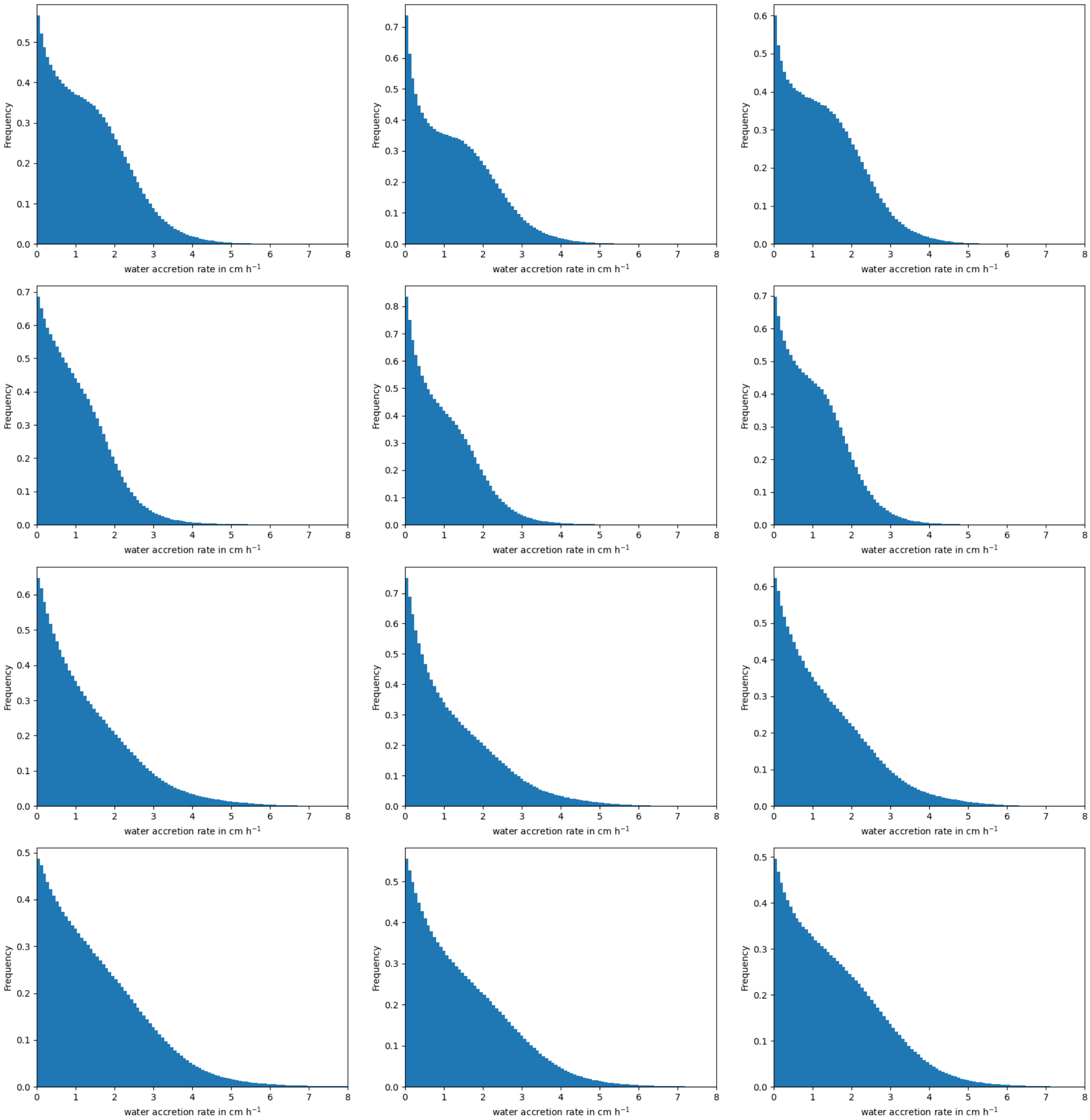

Figure 6.13: Relative frequency distributions of the mean water accretion rate in the ACI01 (left), REF (center) and ACI10 (right) simulations for the CAN24 (1st row), CAN26 (2nd row), SPN (3rd row) and BWF case (4th row).

and $0.768\,\mathrm{cm\,h^{-1}}$ in the ACI01 simulations and to $0.295\,\mathrm{cm\,h^{-1}}$, $0.465\,\mathrm{cm\,h^{-1}}$, $0.698\,\mathrm{cm\,h^{-1}}$ and $0.756\,\mathrm{cm\,h^{-1}}$ in the ACI10 simulations.

The remainder of the impinging water flux is accreted as a liquid water film. The effects the water accretion rate experiences due to alterations in the CCN number density for the introduced cases is shown in figure 6.13. The panel organisation matches those of the previous figures. While the similarly reduced sensitivity of the glaze accretion rate to the cloud droplet number density previously investigated yields a significant higher sensitivity of the concurrent water accretion rate, as this is the dominant accretion type in most cases, this connection does not seem to apply for the sensitivity to the CCN number density shown here. Although the presented distributions show differences between the ACI01, REF and ACI10 simulations for the respective cases, their scales are heavily reduced compared to the cloud droplet number density investigation, where these sensitivities were comparable to that of the respective rime accretion rate. Especially the distributions for the convective cases, SPN and BWF in the bottom rows, show only slight alterations without a clear tendency. The CAN24 and CAN26 cases show stronger

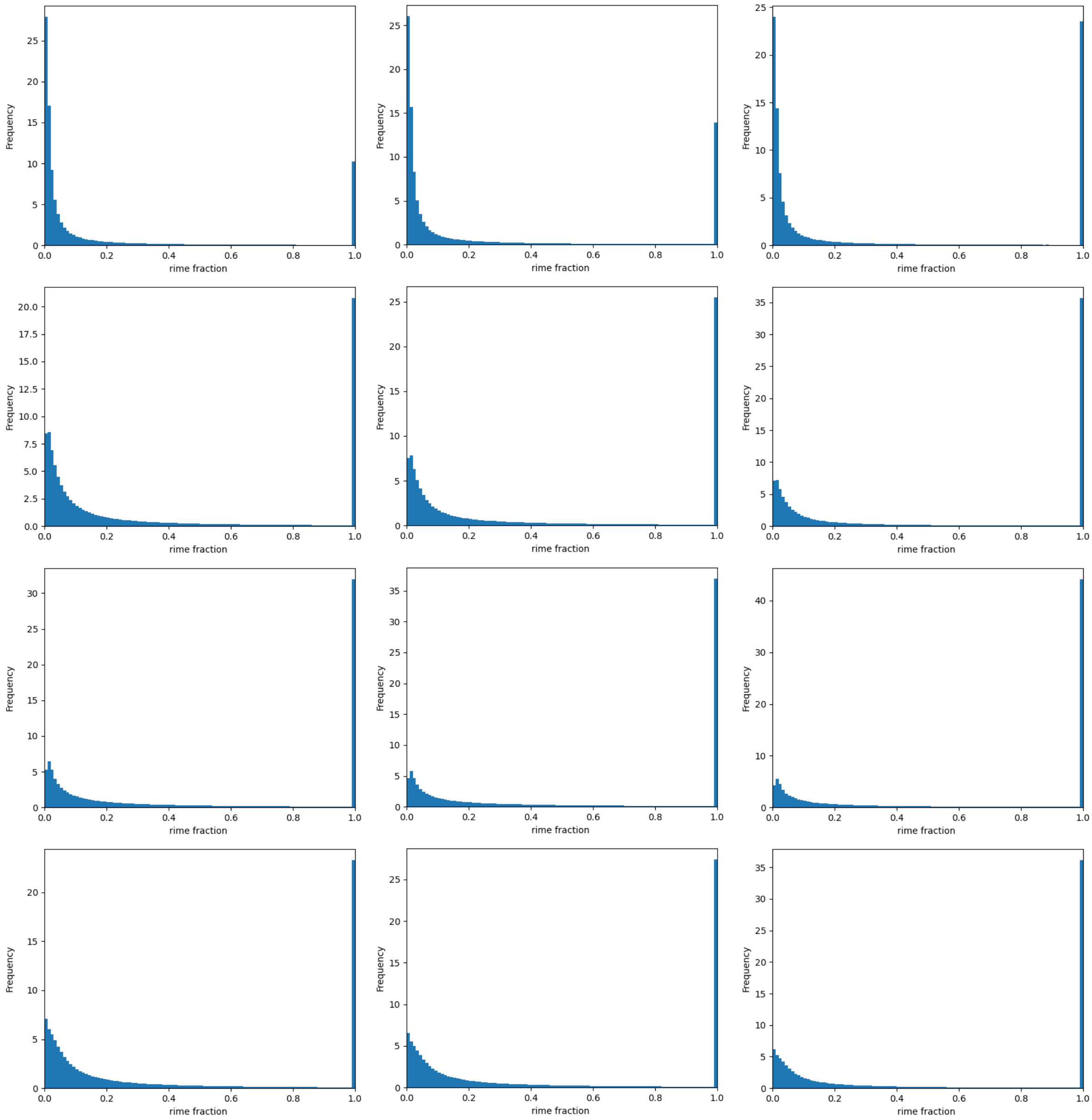

Figure 6.14: Relative frequency distributions of the rime fraction of the accreted material in the ACI01 (left), REF (center) and ACI10 (right) simulations for the CAN24 (1st row), CAN26 (2nd row), SPN (3rd row) and BWF case (4th row).

reductions in frequency for the lowest water accretion rates in both the ACI01 and ACI10 simulations, but no significant changes beyond that. While the direct alteration of cloud droplet number density affected the effective value range, the CCN number density alteration has no such effect. This heavily reduced scale of the effect as well as the fact that no clear tendency can be made out is also represented in the mean values of these water accretion rate distributions. The REF simulations yield values of $1.277\,\mathrm{cm\,h^{-1}}$, $1.011\,\mathrm{cm\,h^{-1}}$, $1.285\,\mathrm{cm\,h^{-1}}$ and $1.500\,\mathrm{cm\,h^{-1}}$ for the CAN24, CAN26, SPN and BWF case, respectively. These are slightly altered to $1.315\,\mathrm{cm\,h^{-1}}$, $1.052\,\mathrm{cm\,h^{-1}}$, $1.334\,\mathrm{cm\,h^{-1}}$ and $1.569\,\mathrm{cm\,h^{-1}}$ in the ACI01 simulations and to $1.298\,\mathrm{cm\,h^{-1}}$, $1.062\,\mathrm{cm\,h^{-1}}$, $1.354\,\mathrm{cm\,h^{-1}}$ and $1.575\,\mathrm{cm\,h^{-1}}$, so no general statement about the sign of the effect can be made. Comparable to the glaze accretion rate, the induced effects seem to originate more in a relocation of the icing environment, by effects onto the atmospheric state, than in an actual change of the environment.

As both accretion types of the wet icing phase, the glaze ice and liquid water accretion, are mostly unaffected by changes in the CCN number density, it is reasonable to conclude that icing environments with considerable wet icing phases have high overall impingement efficiencies, as those are also mostly unaffected. This is furthermore sensible considering the fact that enough water needs to impinge to accrete the critical ice thickness to transition into the wet icing phase.

A main feature of this newly developed aircraft icing parameterization is the differentiation between the dry and wet icing phases. This offers additional quantities to be considered in quantifying the intensity of an icing situation. One such quantity is the fraction of the rime ice thickness to the complete accreted material, the rime fraction, quantifying how strongly the icing event is influenced by the dry icing phase. Figure 6.14 illustrates the impact the ACI01 and ACI10 simulations have on this rime fraction quantity, keeping the same panel organisation as above. Comparable to the effects induced by the direct alteration of the cloud droplet number density previously investigated, and although the wet icing phase seems to be mostly unaffected, a reduction of the CCN number density leads to a reduction in pure dry icing environments, with a rime fraction of 1.0, an increase in CCN number density, on the other hand, results in more dry icing environments detected. The compensating effect is mostly an alteration of the frequencies of the lowest rime fraction, while the overall structure of the distribution stays the same between the ACI01, REF and ACI10 simulations of the respective cases: Increased frequencies of rime fraction around 0.0 rapidly diminishing towards higher rime fractions, with an isolated peak of increased frequency at 1.0 indicating pure dry icing environments. Since the effects on the other quantities are dampened compared to the previously investigated sensitivity to the cloud droplet number density, also the impact on the rime fraction is of reduced scale, although it matches qualitatively. This is also reflected in the mean values of the rime fraction, as the REFs' mean rime fraction values of 0.217, 0.377, 0.500 and 0.407 for the CAN24, the CAN26, the SPN and the BWF case, respectively, are consistently reduced in the ACI01 simulations to 0.173, 0.328, 0.453 and 0.365 and increase in the ACI10 simulations to 0.298, 0.453, 0.548 and 0.470. This allows the general statement that increased CCN number density leads to increased rime fraction. Additionally, again comparable to the sensitivity to the cloud droplet number density, the alteration of the isolated peak at 1.0 can lead to an icing environment with considerable liquid water accretion to be forecast as pure dry, hence, underestimating the potential hazard caused by runback icing, when the CCN number density is overestimated.

Visualizing how the discussed changes already affect a simplified metric of icing intensity, the horizontal distribution of the total water accretion rate, which is comparable to the result of existing ice accretion algorithms, which do not differentiate between the different icing phases, is shown for the BWF case in the panels of figure 6.15. As with the prior horizontal distributions for this case, the altitude is 2000 m and the point in time is chosen to match the reported icing incident. The left panel represents the effect the ACI01 simulation has compared to the REF simulation, while the right panel is dedicated to the changes induced by the ACI10 simulation. As

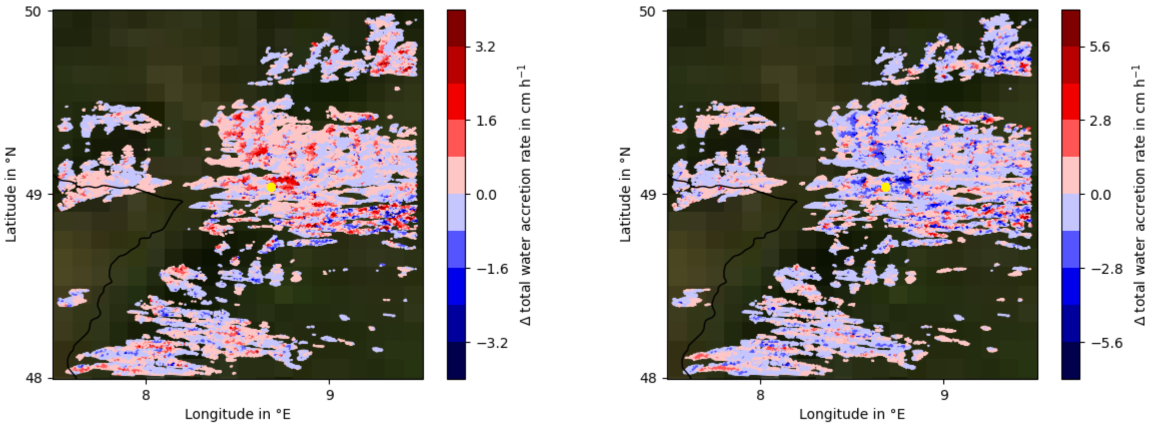

Figure 6.15: Horizontal distribution of the differences in total water accretion rate introduced by the ACI01 (left), ACI10 (right) compared to the REF simulation at the time of the reported icing incident in an altitude of 2000 m. The location of the icing incident is marked with a yellow dot.

already indicated by the horizontal distribution of the overall impingement efficiency in figure 6.8, there are positive and negative changes introduced by both cases. This is due to the fact that, contrary to the previous sensitivities, only altering quantities for the parameterization itself, this sensitivity investigation altered the CCN number density and therefore the cloud droplet nucleation parameterization, which in turn affects the atmospheric state. This and the alteration of the droplets' size, which affects their transport and sedimentation behaviour, cause positional shifts of icing environments, vertically and horizontally. Hence, to accurately predict the location of these icing environments a proper representation of the aerosol load is beneficial. Nevertheless, one can clearly see that the reduction of the CCN number density in the ACI01 simulation leads to increased total water accretion rates, especially in the centers of the convective cells, while the ACI10's increase in CCN number density yields an overall reduction of the total water accretion rate, also especially in the centers of the convective cells. This sensitivity highlights the importance of a proper representation of the aerosol load to accurately predict the intensity of icing environments, even with this simplified metric. It can additionally be stated that due to the already high total water accretion rates in the centers of the convective cells, a reduction in CCN number density leads to a more heterogen distribution of the total water accretion rate, while an increase tends to homogenize it.

7 Sensitivity to the relative airspeed

Aircrafts experience different relative airspeeds during their flights. For most icing prediction schemes and ice accretion algorithms a relative airspeed of $89.4\,\mathrm{m\,s^{-1}}$ is used, which is considered a representative value for commercial flights in cruising altitude. Icing related incidents, however, occur most often in lower altitudes during take-off and landing, where the relative airspeed is considerably lower. The representative value in those phases is $60\,\mathrm{m\,s^{-1}}$. Extending the application of an icing prediction scheme to lighter aircrafts like gliders, an even lower relative airspeed of $30\,\mathrm{m\,s^{-1}}$ is more appropriate. The present newly developed physically based parameterization for aircraft icing introduces the possibility to alter the relative airspeed used for the computation of the icing related quantities. The following part investigates how sensitive the icing intensity is to the relative airspeed.

7.1 Expectations

Next to the LWC and the overall impingement efficiency, the relative airspeed determines the impinging water flux onto the object. It also influences further auxiliary quantities that are used in the aircraft icing parameterization, like the initial rime density at the object's surface or the kinetic energy of the impinging droplets or the overall impingement efficiency itself. Additionally, the time of stay in a grid cell is highly depending on the relative airspeed. Due to its great influence on the impinging water flux, expectations are that the accretion rates are highly sensitive to the relative airspeed. Since the time of stay is inversely affected by the relative airspeed (see chapter 3.3), the total accreted thickness for traversing a grid cell, however, should be unaffected, when no other influences are in effect. Because of its many points of potential impact, expectations are that this is not the case and the relative airspeed also affects the total accretion, as well as potentially its composition.

7.2 Results

Figure 7.1 illustrates the impact an alteration in relative airspeed has on the overall impingement efficiency, as it shows its differences between the V60 (V30) simulation and the REF simulation, which will be referred to as V89 indicating the used relative airspeed of $89.4\,\mathrm{m\,s^{-1}}$, in the top (bottom) panels as the temporal development of its vertical profile on the left panels and its horizontal distribution on the right ones for the BWF case. In all shown instances, the overall impingement efficiency is reduced. This effect is stronger in the V30 simulation, with changes of up to 0.2, than in the V60 one, whose effects do not extend beyond 0.08. The left panels show a great temporal and vertical variability in the changes induced, which is especially pronounced for the V30 simulation. In general, high actual impingement efficiency values are less strongly reduced than lower ones. The right panels present this behaviour as well in the horizontal dimensions. The centers of the convective cells generally experience less change in overall impingement efficiency than their respective edge regions. A clear example of this spatial variability of the effect is around 49.3°N, 8.6°E, where in between two areas that experiences reductions of about 0.1 there is a stripe of abruptly higher reductions of about 0.2, in the V30 simulation. These plots hint towards a significant reduction of the overall impingement efficiency at smaller relative airspeeds with an increase in both spatial and temporal variability.

Further investigating the sensitivity of the overall impingement efficiency on the relative airspeed, figure 7.2 shows the overall impingement efficiency's relative frequency distributions for the V89 simulations (or REF simulations) in its left column, the V60 simulations in its central column and the V30 simulations in its right column, for all cases

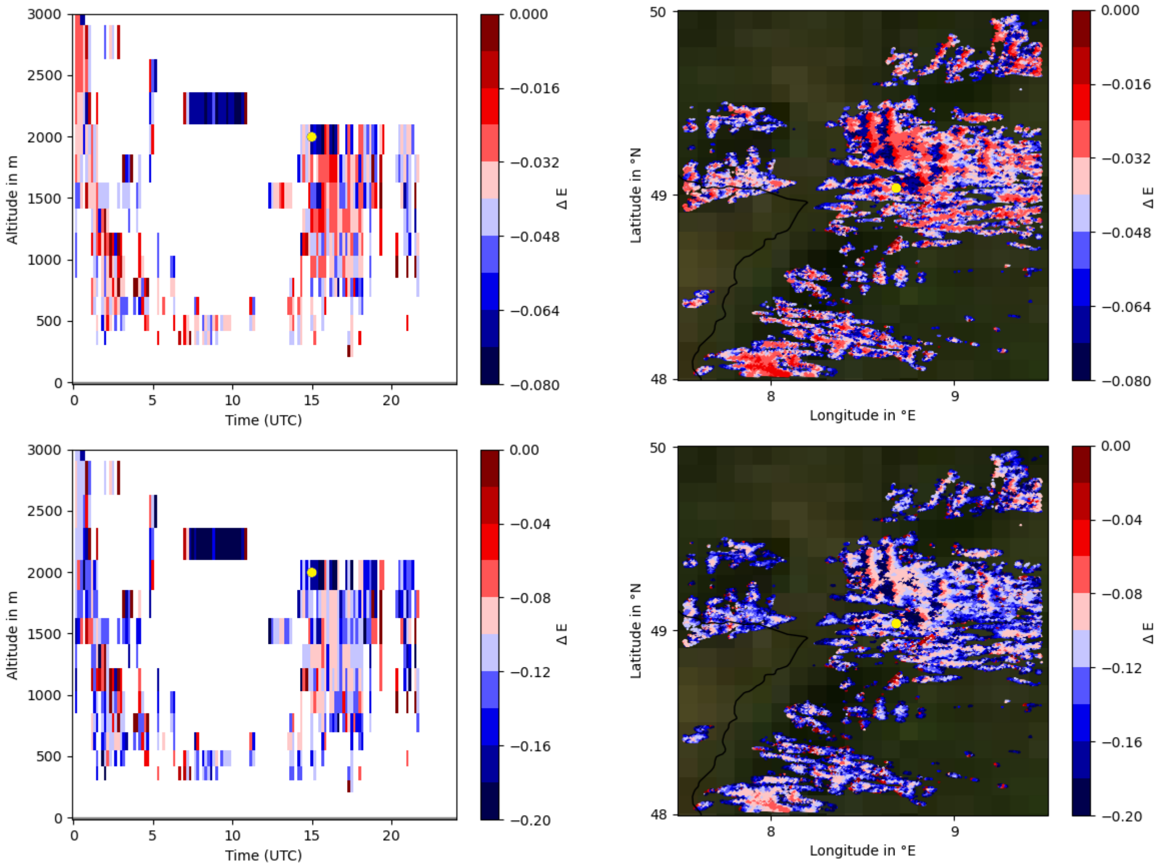

Figure 7.1: Differences in overall impingement efficiency between the V60 (top), V30 (bottom) simulation and the REF simulation as the temporal development of its vertical profile (left) and as its horizontal distribution (right) for the BWF case, the profile is taken at the location of the reported icing incident and horizontal distribution at its time in an altitude of 2000 m. The position of the icing incident is marked with a yellow dot.

investigated in the present work: the top row represents the CAN24 case, the second the CAN26 case, while the third and the bottom row present the more convectively influenced cases SPN and BWF. Although the individual frequency distributions for the different cases are different from one another, like the two more convective cases showing increased frequencies on the lower and upper end of the distributions, the effects of a change in relative airspeed are consistent throughout them all. Additionally, this supports and confirms the previously mentioned findings. With decreasing relative airspeed the primary maximum in the distributions is less pronounced and moves towards smaller values. The secondary structure is also shifted towards smaller values, however, especially for the V30 simulations a limit to the reduction of low impingement efficiency values is imposed by design, as this quantity cannot be negative. The characteristics of the more convectively influenced cases regarding this frequency distribution remain. To confirm the statements above, the shift of the overall impingement efficiency is indicated by the shift of its mean value and the change in the variability or spread by the standard deviation of the shown frequency distributions. The CAN24 case experiences a mean reduction in overall impingement efficiency from 0.602 in the V89 simulation over 0.559 in the V60 simulation to 0.473 of the V30 simulation. The standard deviation, however, increases slightly from 0.256 to 0.260 in the V60 simulation and decreases to 0.255 in the V30 simulation, which is due to the aforementioned limit ultimately limiting the overall spread. The CAN26 case shows similar values, while the more convectively influenced cases are more oriented towards higher variability, which is most clearly made out by the increased separation between the primary and secondary maxima. Nevertheless, these cases also show the previously described reduction of the mean, from 0.584 and 0.611 over 0.542 and 0.572 to 0.460 and 0.495 in the SPN and BWF case, respectively, and only slight changes in the standard deviation,

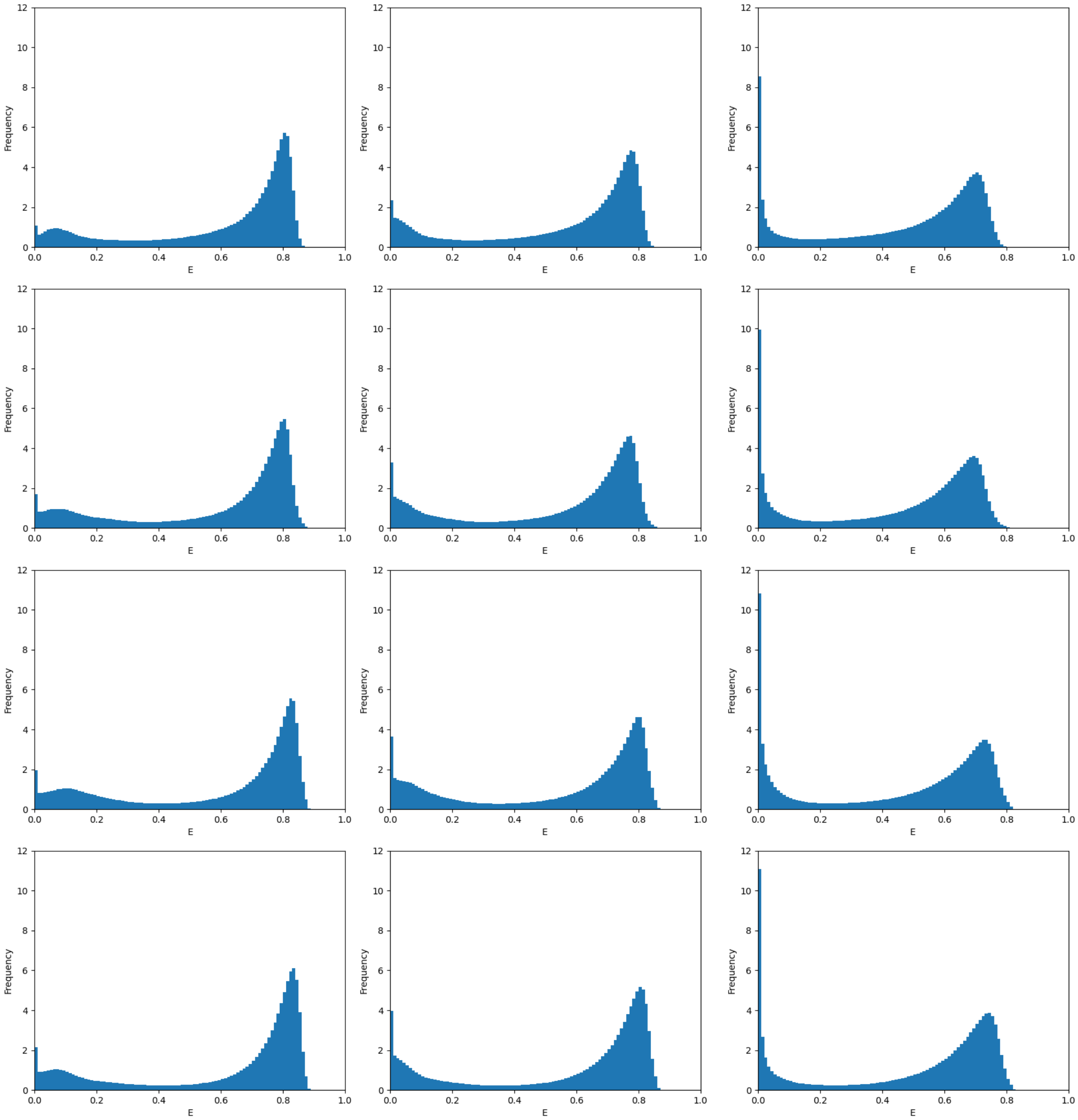

Figure 7.2: Relative frequency distributions of the overall impingement efficiency in the V89 (left), V60 (center), V30 (right) simulations for the CAN24 (1st row), CAN26 (2nd row), SPN (3rd row) and BWF case (4th row).

from 0.287 and 0.284 over 0.292 and 0.289 to 0.285 and 0.282, respectively, with decreasing relative airspeed. The different forms of accretion during the icing process require a flux of impinging supercooled water, which depends both on the relative airspeed and the overall impingement efficiency, which, as shown above, is sensitive to this quantity itself. Figure 7.3 illustrates how this sensitivity translates into the dry icing phase. For this, it displays the relative frequency distributions of the mean rime accretion rate experienced while traversing the icing environment, following the same panel organisation as above. The plots show clearly that with decreasing relative airspeed the distributions get narrower reducing their range of values. This may lead to the conclusion that less relative airspeed greatly reduces rime icing. However, it is to be noted that by having less relative airspeed, the time of stay in the icing environment lengthens proportionally. Hence, the differences in the actual accreted rime ice thickness after traversing are reduced. However, these greatly reduced rime accretion rates potentially allow the pilot to properly react. Another aspect these plots highlight is that the more convectively influenced cases SPN and BWF have higher frequencies of higher rime accretion rates, which persists throughout all the relative airspeed

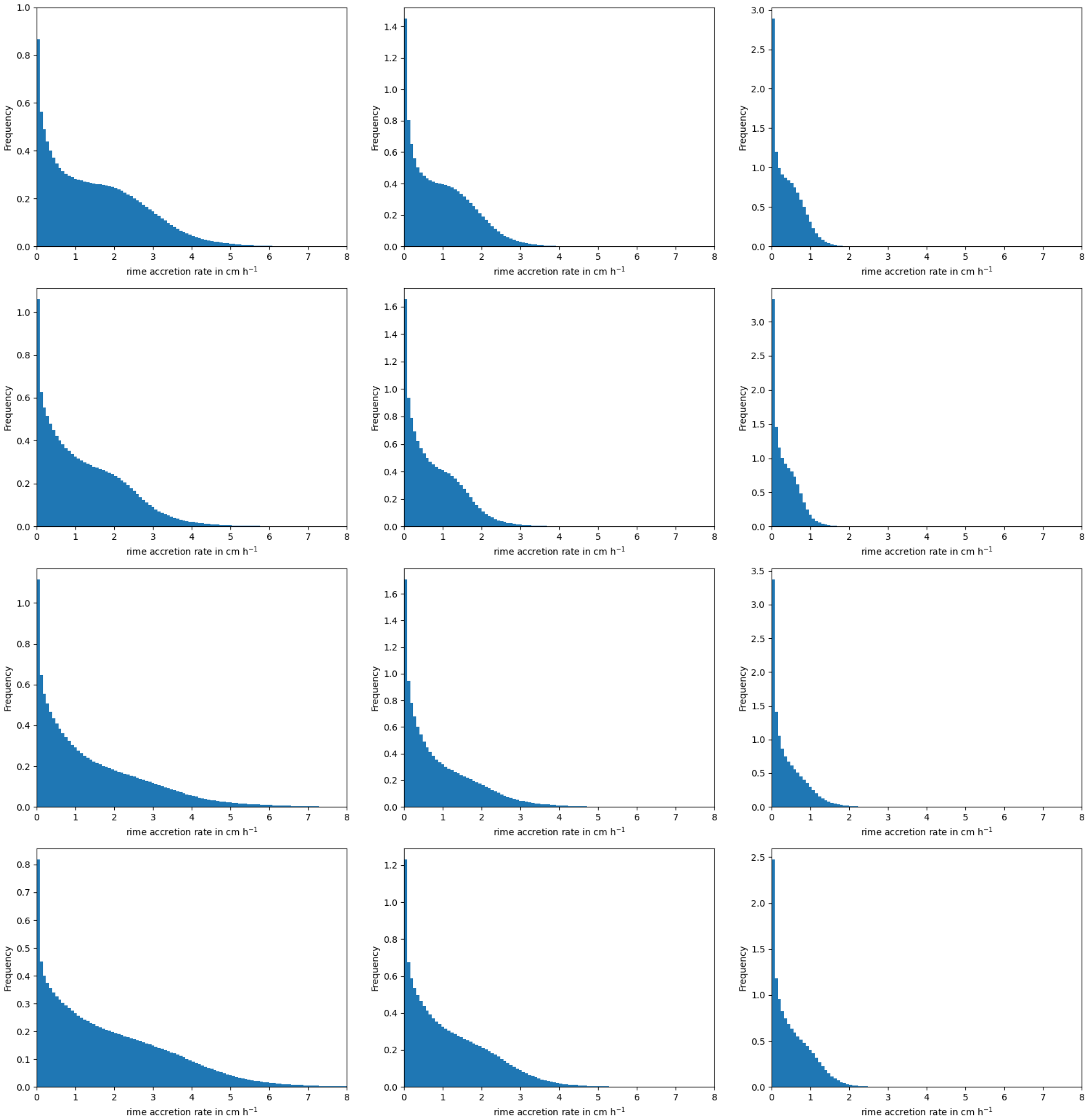

Figure 7.3: Relative frequency distributions of the mean rime accretion rate in the V89 (left), V60 (center), V30 (right) simulations for the CAN24 (1st row), CAN26 (2nd row), SPN (3rd row) and BWF case (4th row).

simulations shown. The stratiform cases CAN24 and CAN26 lean more toward the lower values developing plateau-like structures in their histograms, which also persist. Further investigating the relative airspeed's impact, the shifts in the mean value of the histograms indicate that it goes beyond the relative airspeed's direct effect on the impinging water flux. Scaling up the mean values of the V60 and V30 simulations by the quotient of the V89's relative airspeed and theirs and hence negating this direct effect, they still differ from the V89's mean value significantly: The CAN24 case experiences a mean rime accretion rate of $1.513\,\mathrm{cm\,h^{-1}}$, $0.952\,\mathrm{cm\,h^{-1}}$ and $0.414\,\mathrm{cm\,h^{-1}}$ for the V89, V60 and V30 simulations, respectively. For CAN26 these values are $1.257\,\mathrm{cm\,h^{-1}}$, $0.789\,\mathrm{cm\,h^{-1}}$ and $0.343\,\mathrm{cm\,h^{-1}}$, SPN experiences $1.477\,\mathrm{cm\,h^{-1}}$, $0.932\,\mathrm{cm\,h^{-1}}$ and $0.415\,\mathrm{cm\,h^{-1}}$ and BWF returns the highest values of $1.881\,\mathrm{cm\,h^{-1}}$, $1.194\,\mathrm{cm\,h^{-1}}$ and $0.532\,\mathrm{cm\,h^{-1}}$, respectively. The adjusted difference is caused by the sensitivity of the impingement efficiency, which also determines the impinging water flux, and of auxiliary aspects like the initial rime ice density that depends on the relative airspeed or the kinetic energy of the impinging droplets. However, the impingement efficiency is the main contributor to this adjusted difference. The fact that the

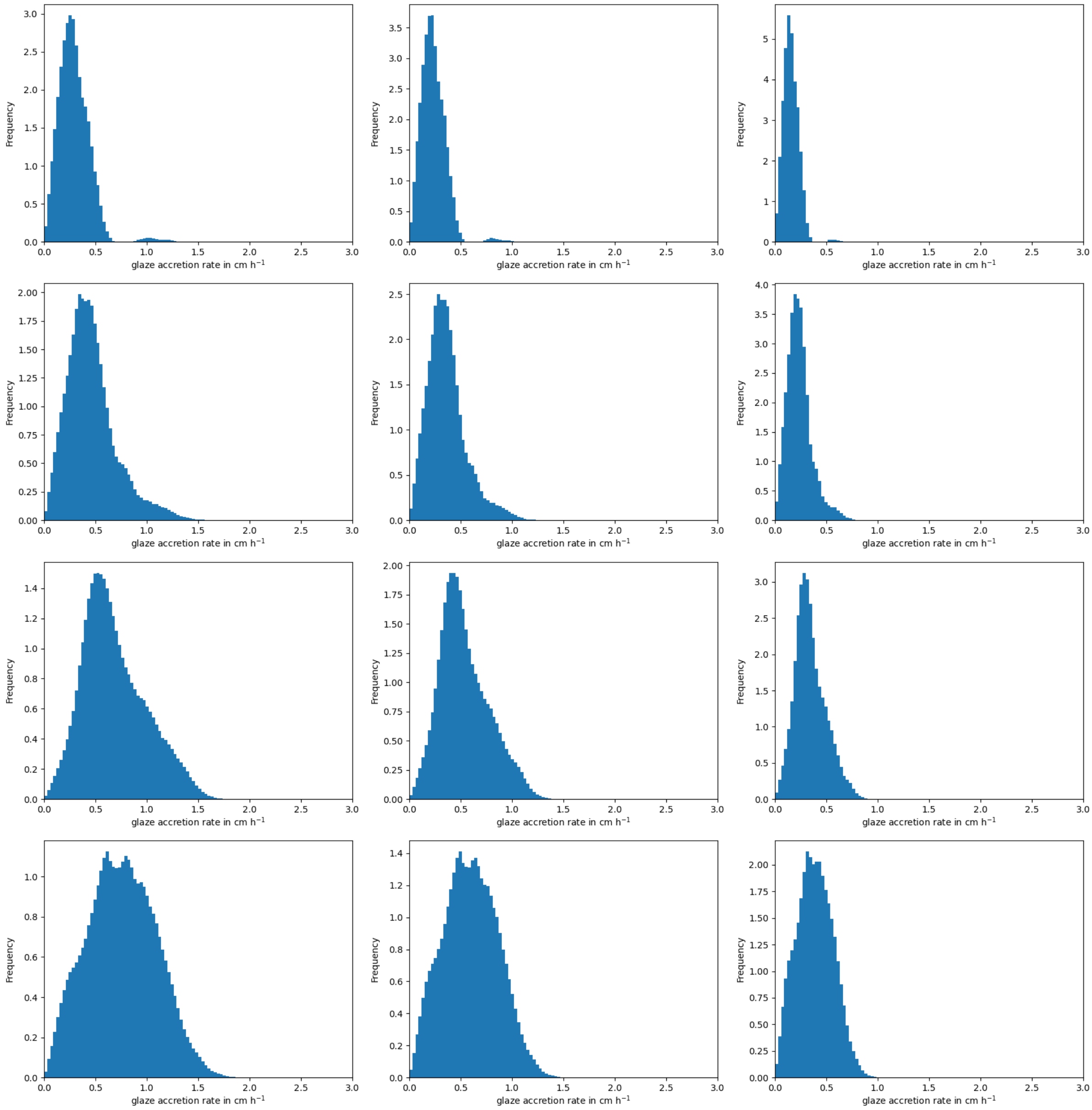

Figure 7.4: Relative frequency distributions of the mean glaze accretion rate in the V89 (left), V60 (center), V30 (right) simulations for the CAN24 (1st row), CAN26 (2nd row), SPN (3rd row) and BWF case (4th row).

distributions get narrower with decreasing relative airspeed, is reflected in the standard deviations of the histograms. With the relative frequency distributions of the glaze accretion rate, figure 7.4 highlights the extent of the sensitivity on one part of the wet icing phase. The panel organisation matches the previous ones. Similar to the rime accretion rate the main impact a reduction of the relative airspeed exerts on the distributions is a compressing effect, due to the directly reduced flux of impinging water. Since the time of stay in the icing environment is lengthened by the reduced relative airspeed, this counteracts this effect to some degree. Interestingly, while for the rime accretion rate above an adjustment (by scaling with the relative airspeed) could not counteract the shown effect entirely, applying the same adjustment to the glaze accretion rate (hence, transforming it into a measure of the accreted glaze thickness) yields an overcompensation. This means that the V30 and V60 simulations introduce a weaker reduction in glaze accretion rate than the lengthened time of stay suggests. This is based upon the mean values of the shown distributions, which in the CAN24 case are $0.294\,\mathrm{cm\,h^{-1}}$, $0.234\,\mathrm{cm\,h^{-1}}$ and $0.156\,\mathrm{cm\,h^{-1}}$ for the V89, V60 and V30 simulations, respectively. The CAN26 case yields $0.462\,\mathrm{cm\,h^{-1}}$, $0.364\,\mathrm{cm\,h^{-1}}$ and $0.236\,\mathrm{cm\,h^{-1}}$, the

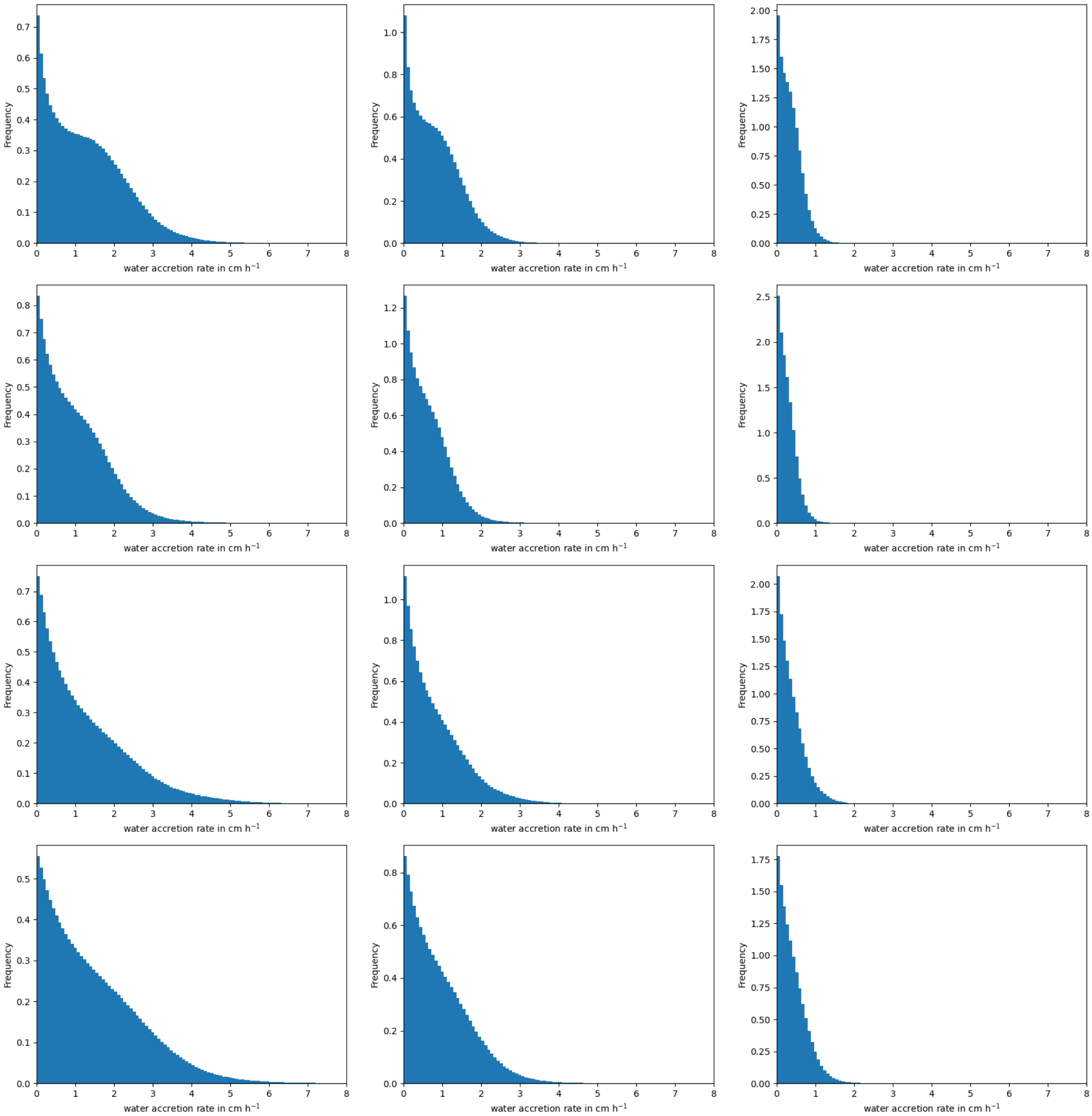

Figure 7.5: Relative frequency distributions of the mean water accretion rate in the V89 (left), V60 (center), V30 (right) simulations for the CAN24 (1st row), CAN26 (2nd row), SPN (3rd row) and BWF case (4th row).

SPN case experiences mean glaze accretion rate values of $0.686\,\mathrm{cm\,h^{-1}}$, $0.537\,\mathrm{cm\,h^{-1}}$ and $0.345\,\mathrm{cm\,h^{-1}}$, and the BWF case $0.758\,\mathrm{cm\,h^{-1}}$, $0.598\,\mathrm{cm\,h^{-1}}$ and $0.390\,\mathrm{cm\,h^{-1}}$, respectively. It is noted that the overall structure of the distributions remains mostly unchanged between the different relative airspeeds applied, which in turn means that the differences between the more stratiform and the more convective cases, increased frequency of higher glaze accretion rates, also remains.

The second type of accretion occuring in the wet icing phase next to glaze ice, is the liquid water film. Figure 7.5 displays its relative frequency distributions for the different relative airspeed simulations and cases. The organisation of the panels remains the same as in the previous figures. As expected, the distributions highlight the same compressing effect of reducing the relative airspeed. Again the differences between the cases, and therefore the effects of a more convective influence against a more stratiform one, which for the water accretion rate is an increase in relative frequency of higher values, persists throughout the varying relative airspeed simulations. Looking at the way the mean values of the distributions change with varying relative airspeed, gives insight on whether the secondary effects dampen or enhance the primary one and thereby if the dampening role is a feature of the wet icing phase in general or only of the glaze accretion rate. The CAN24 case experiences a mean liquid water accretion rate of $1.277\,\mathrm{cm\,h^{-1}}$ in the V89 simulation, which is reduced to $0.812\,\mathrm{cm\,h^{-1}}$ and $0.356\,\mathrm{cm\,h^{-1}}$ in the V60 and V30 simulations, respectively. Adjusting those values with the corresponding relative airspeeds, negating this primary effect, yields that the simulations with reduced relative airspeeds still experience a reduction in the adjusted values, hence the secondary effects of the relative airspeeds on the overall impingement efficiency and auxiliary parameters enhance the primary effect, comparable to the findings for the rime accretion rate. This is supported by the other cases as well, as the mean values for the CAN26 case are $1.011\,\mathrm{cm\,h^{-1}}$, $0.638\,\mathrm{cm\,h^{-1}}$ and $0.274\,\mathrm{cm\,h^{-1}}$. For the SPN case these evaluate to $1.285\,\mathrm{cm\,h^{-1}}$, $0.831\,\mathrm{cm\,h^{-1}}$ and $0.377\,\mathrm{cm\,h^{-1}}$ and the BWF case experiences mean values of $1.500\,\mathrm{cm\,h^{-1}}$, $0.951\,\mathrm{cm\,h^{-1}}$ and $0.419\,\mathrm{cm\,h^{-1}}$, respectively.

Concluding, the sensitivity of the different accretion types on the relative airspeed is high for the respective accretion rates, since the relative airspeed directly influences the impinging water flux. The sensitivity towards the accreted amount is expected to be lower, because of the increased length of time the aircraft is exposed to the icing environment when experiencing lower relative airspeeds. However, even with considering this aspect, the accretion still reacts sensitive, as other parameters that depend on the relative airspeed, like the overall impingement efficiency, contribute to the accretion rates and amounts. For the rime and water accretion rates, these secondary effects enhance the overall reduction experienced by the reduced relative airspeed, while the glaze accretion rate's reduction is dampened.

As the accretion types react with differing sensitivity to the alteration of the relative airspeed, figure 7.6 highlights the respective sensitivity of their relationship to one another by presenting the relative frequency distributions of the rime fraction, in essence the part of the impinging water that accretes as rime ice. Also this figure shares the same panel organisation as the previous ones. Contrary to the previous analyses of the individual accretion types, there is no compressing effect for the rime fraction. This supports the idea that this compressing effect is a feature of the accretion rates, not the actual accreted amount, since the rime fraction is determined based on the latter. However, the rime fraction still experiences effects due to the varying relative airspeeds. Comparable to the other sensitivities investigated, the reducing effect on the overall impingement efficiency translates to an increasing effect on the rime fraction when reducing the relative airspeed. For once, this manifests in the frequency reduction of rime fractions near 0.0 for decreasing relative airspeeds, which is consistent in all cases. Additionally, the frequency of icing environments that remain entirely in the dry icing phase, or have a rime fraction of 1.0, increases significantly in all cases as well. Hence, underestimating an aircraft's relative airspeed may underestimate icing hazards by underestimating the role of runback icing. The mean values of the shown distributions confirm this steady increase of the rime fraction: In the CAN24 case, the mean rime fraction increases from 0.217 in the V89 simulation, over 0.280 in the V60 simulation to 0.398 in the V30 simulation. The CAN26 case experiences mean rime fractions of 0.377, 0.458 and 0.600 for these simulations, respectively, while the simulations for the SPN case yield 0.500, 0.576 and 0.696. Although the BWF case does not reach these high values for these simulations, its mean rime fractions of 0.407, 0.486 and 0.626 show the same sensitivity to the relative airspeed. Hence, not only does the relative airspeed impact the accretion rates and total accreted amounts of the different accretion types, but also their composition.

Due to the aircraft's stay in an icing environment also being affected by the relative airspeed, which is not the case for the other sensitivity parameters investigated, there is a discrepancy between the effects on the accretion rates and on the total accreted amount, as already previously stated. Visualizing these differing effects, figure 7.7 shows the horizontal distributions of both the total water accretion rate in its left panels and the total amount of accreted water in its right panels, as a result of the V89, V60 and V30 simulations in the top, central and bottom panels, respectively, for the BWF case. The altitude chosen is 2000 m and they match the point in time of the reported icing event. While the total water accretion rate experiences great reductions for reduced relative airspeeds, the effect on the total amount of accreted water is reduced. Hence, a large part of the reductions of the total water accretion

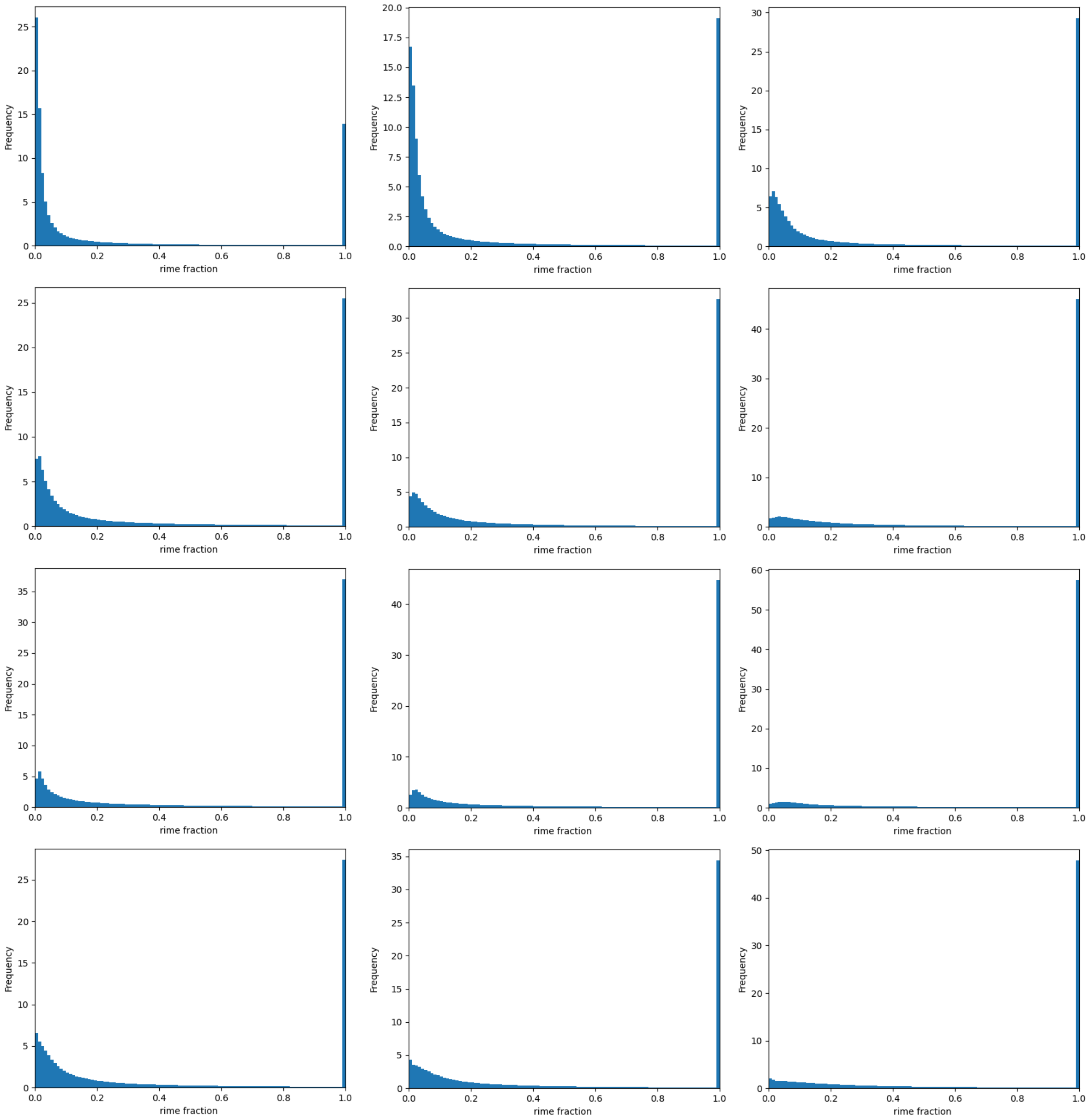

Figure 7.6: Relative frequency distributions of the rime fractions in the V89 (left), V60 (center), V30 (right) simulations for the CAN24 (1st row), CAN26 (2nd row), SPN (3rd row) and BWF case (4th row).

rate is due to the directly decreased flux of impinging water by slower traversing the icing environment. Since the time it takes for this traversing to complete increases proportional to the reduction of the impinging water flux, the total amount of accreted water is unaffected by this primary effect on the total water accretion rate. However, as the previous analyses demonstrate, the varying relative airspeed's influence is not restricted to its direct impact on the impinging water flux. These horizontal distributions of the total accreted water show that although the direct effect on the impinging water flux is compensated, there are still differences in total accretion amounts, which can be made out in the center of the convective cells the easiest, where the original value is highest. Nevertheless, the scope of these secondary effects is greatly reduced beyond those regions.

Concluding, the main effect of varying the relative airspeed is the direct alteration of the impinging water flux, which causes great changes in accretion rates. The lower the relative airspeed, the lower are the accretion rates. The overall impingement efficiency, also a contributor to the impinging water flux as well as other icing related quantities, is additionally sensitive to the relative airspeed, also experiencing an overall reduction. The accretion

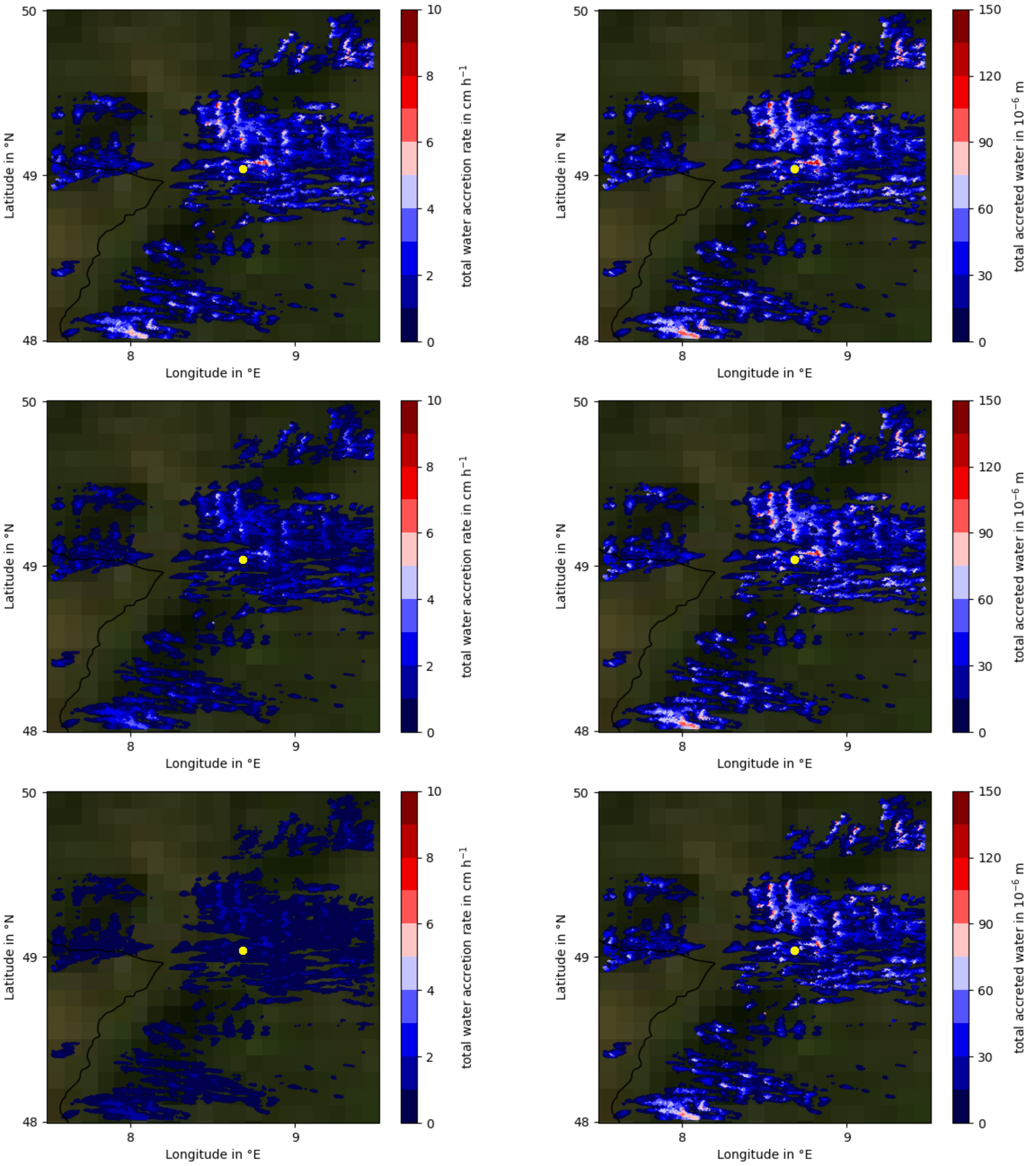
50
49
48
Latitude in °N
8
9
Longitude in °E
10
8
6
4
2
0
total water accretion rate in cm h^{-1}
150
120
90
60
30
0
total accreted water in 10^{-6} m

Figure 7.7: Horizontal distribution of the total water accretion rate (left) and the total accreted water (right) for the BWF case as a result of the V89 (top), V60 (center) and V30 (bottom) simulation at the time of the reported icing incident in an altitude of 2000 m. The location of the icing incident is marked with a yellow dot.

rates, which are already greatly affected by the relative airspeed's impact on the impinging water flux, experience additional effects mainly due to the impact on the overall impingement efficiency. For the rime and liquid water accretion rates, this results in an enhancement of the primary effect, while the glaze accretion rate experiences a dampening. And whilst the total amount of accreted water is only slightly affected by the varying relative airspeeds, as relevant amplitudes are restricted to already high accreting environments, the contributions of the different accretion types to it shift towards higher rime fractions for lower relative airspeeds. This also manifests in significantly increased frequencies of purely dry icing environments. So, a differentiation of the relative airspeeds considered is beneficial for the forecast or analysis of icing environments.

8 Application in a future improved icing prediction scheme

The previous chapters introduced some applications of the newly developed physically based aircraft icing parameterization and its features and resulting quantities. Since the parameterization is implemented into a version of an operationally used weather model, however, it additionally offers a new possibility for creating an online icing prediction scheme, contrary to current icing prediction schemes that produce their results in the post-processing stage. This online design allows for the usage of more model variables than those that are output and the computation of a larger set of icing related quantities. In the present case, this is accomplished by using microphysical quantities or relative airspeed information to compute not only the overall impingement efficiency, but also the thickness of the accreted material, which also differentiates between rime ice, glaze ice and liquid water, as well as their respective accretion rates. Those accretion rates are a common quantity for investigating icing conditions, as they are used to determine the intensity level of the icing environment investigated, but are not used for forecasting. A further potential of the accretion rates and thicknesses is the potential calculation of the additional weight the ice puts on the aircraft, which could be used in a future icing prediction scheme. In addition, the differentiation of the accreted materials enables the forecast or computation of the composition of the accreted material, which in regards to the role of runback icing, caused by liquid water accretion, may be crucial to appropriately quantify the icing experience. Also auxiliary quantities, like the critical ice thickness, which defines the point at which the dry icing phase shifts into a wet icing phase, are accessible for the generation of an icing prediction scheme.

Furthermore, this newly developed aircraft icing parameterization offers a configuration setup, enabling the possibility to compute its result taylored to specific scenarios. One of the more obvious is the already previously applied possibility to specify the relative airspeed, which can taylor a potential icing prediction scheme to aircrafts in cruise, during landing or take-off, or for different classes of aircrafts, e.g. commercial aircrafts, light aircrafts or gliders. Other possibilities are to specify the effects of heating elements, no longer assuming the aircraft's surface temperature equals the one of the ambient air, or adjusting the size of the reference cylinder.

Icing prediction schemes assign intensity categories to icing environments, which is done by applying icing intensity scales to numerical values returned by icing intensity algorithms. For the present new aircraft icing parameterization such an icing intensity scale would need to be developed to design an icing prediction scheme. There are already scales in use that map an ice accretion rate to several intensity categories, as for example Boudala et al. (2019) mentions. Although these use a simplified metric, they can form a basis for an icing intensity scale for this present aircraft icing parameterization, which can be extended and adjusted by the inclusion of the features mentioned above.

With the application and implementation of the icing intensity scale, the next step would be testing and tuning of this new icing prediction scheme. As it is already implemented in ICON-ART, which is an operationally used model, the icing prediction scheme could be run in a pre-operational global setup. The scheme's results are then compared with icing reports in PIREPs. The global setup allows a better coverage of the consideration of these observations. The comparisons highlight required adjustments, which can be based in numerals or setup configuration. Next to the validation and tuning of the results, the pre-operative setup also highlights potential performance issues that may be needed to be addressed. Contrary to current icing prediction schemes, which are applied in the post-processing stage and do not affect the model's performance directly, this new online aircraft icing parameterization does, so optimization efforts are required and need to be evaluated against the potential benefits the new prediction scheme offers compared to existing ones. One of such points of performance improvement would probably originate from the present work as well, since the computational expensive explicit consideration of the cloud droplet spectrum offers only little benefits for a potential icing prediction scheme. Another possibility for performance improvement is the tabularization of the overall impingement efficiency values. However, for performance optimizations, a representative local setup is more appropriate once the general validation and tuning is concluded. Once the performance of the setup is fit for the actual operational use and the benefits of the new icing prediction scheme, based on the aircraft icing parameterization, newly developed in the scope of the present work, are positively evaluated, it could then enter a full operational setup.

9 Conclusions

The present work investigates the modelling of aircraft icing conditions and intensities with respect to microphysical quantities. In its scope, a new aircraft icing parameterization is developed and implemented in the numerical weather forecast model ICON-ART to enable simulating case studies of aircraft icing and answering questions regarding the sensitivities of aircraft icing environments, some of which stem from the possibilities of the new aircraft icing parameterization itself.

The main research question, the present work answers, is the role of some microphysical quantities for aircraft icing. However, current icing prediction schemes, like ADWICE or CIP, do not directly depend on such quantities (Kalinka et al. 2017; Bernstein et al. 2005). There are some analytical tools that allow for some minor degree of dependency on the droplet's size (Boudala et al. 2019; Finstad et al. 1988), which is, however, not sufficient for the present scope. Consequently, the first part of the present work is the development of a new aircraft icing parameterization that allows for microphysical investigations. While current prediction schemes, methods and algorithms are based in heuristics, this new parameterization takes a physical based approach: The two main physical processes required for the modelling of aircraft icing are the impingement efficiency that describes what proportion of the ambient LWC impinges onto the aircraft (Gent et al. 2000) and the actual freezing process of the impinged water. The former is achieved by computing droplet trajectories around the object, for which a cylinder is used as a commonly used proxy (Boudala et al. 2019; Hauf and Schröder 2006; McComber and Touzot 1981), by employing strategies of a binary search. These trajectories depend heavily on the droplet size, due to their inertia (Gent et al. 2000), hence an explicit consideration of the droplet spectrum is employed. The latter part of the parameterization implements the freezing model by Zhang et al. (2016), which computes the accreted thickness of water in form of rime ice, glaze ice and residual liquid water. This separation of the accretion phases is a unique aspect of this new aircraft icing parameterization and allows for the quantification of the runback icing phenomenon, which is of special interest for the hazards aircraft icing poses.
With the new aircraft icing parameterization developed and implemented in the numerical weather model ICON-ART to enable online calculations, instead of the post-processing approaches of current icing prediction schemes (Kalinka et al. 2017; Bernstein et al. 2005), first steps of its validation are taken. For this, two case studies (Boudala et al. 2019; Fernández-González et al. 2014) are simulated as well as one inofficial private report of icing by a hobby pilot. The investigation areas are around Cold Lake in Alberta, Canada on the 24th and 26th of October 2016, above the Guadarrama Mountains in Spain on the 1st of February 2012 and in northwest Baden-Wuerttemberg in Germany on the 7th of December 2019. These different cases are labelled CAN24, CAN26, SPN and BWF, respectively. The simulations show that the new aircraft icing parameterization produces comparable values in accretion rates as the case studies. However, the exact position of the icing reports in the case studies is not always hit. This meets expectations, as the model setup is chosen to be basic and the locations are not consistently well documented in the first place. Overall, the new aircraft icing parameterization shows high temporal and spatial inhomogeneities of the icing environments in the simulated cases that current methods undercut. This is especially apparent, when comparing the distribution of an empirically determined impingement efficiency (Finstad et al. 1988) that is in use in the Canada case study, to the impingement efficiency computed by the new aircraft icing parameterization. The empirical formulation caps out consistently at values of around 0.7 and evaluates a vast majority of the environments to around that value, while the physical formulation of the new aircraft

icing parameterization covers a larger span of values, reaching up to 0.9, with a greater differentiation of these higher values. Additionally, the separation of the different accretion phases, allows for a more detailed analysis, especially regarding the composition of the accreted material. This simple validation process also highlights a feature of the new aircraft icing parameterization that describes a maximum value of the accreted ice thickness (including both rime and glaze ice accretion), which depends on the ambient temperature. While it is intuitively understandable that the maximum ice thickness decreases with increasing temperature, it further highlights that the maximum value is rapidly reached: Hence, once the accreted liquid water film is around the same thickness as the accreted ice, further impinging water is nearly exclusively accreted to the liquid water film. Another interesting result of these simulations is the possible identification of distribution features for more stratiformly and more convectively influenced scenarios. So for example, the frequency distribution of the impingement efficiency show elevated frequencies of low-level impingement efficiency values as well as, to a lesser degree, of high values for more convective situations, effectively increasing its variance. Additionally, the highest accretion rates are found in the centers of convective cells. Further validating the new aircraft icing parameterization, the frequencies of total water accretions rates match the reports provided in the case studies. Overall, the features of this newly developed physically based parameterization for aircraft icing enhance the possibilities to quantify the intensity of aircraft icing environments.

With the functionality of the new aircraft icing parameterization presented and validated, the present work then focuses on the answering of further research questions. The first one looks into the role of the microphysical quantity of the cloud droplet spectrum and whether its explicit consideration is beneficial for the detection and quantification of icing environments and intensities. For this two simulations are preformed that differ in the way the droplet spectrum is represented. One explicitly considers the droplet spectrum by numerically integrating over it, while the other only uses the mean droplet mass of the spectrum, to compute the impingement efficiency, which is a crucial aspect of the new aircraft icing parameterization and considered sensitive to the droplet size. The sensitivity investigation shows that, while the negligence of the actual droplet spectrum results in consistently underestimated values for the impingement efficiency, the effects are small (the mean differences are about 0.02), especially compared to the additional computational effort that is required to explicitly consider the droplet spectrum. This also applies to the actual total water accretion rates, which only seldomly experiences underestimations of more than $0.05\,\mathrm{cm\,h^{-1}}$, and the total accreted ice thickness, which, however, highlights a clear difference between more stratiformly and more convectively influenced environments by increased frequencies of higher underestimations. The separation of the different accretion phases of the new aircraft icing parameterization allows for the investigation of the effect on the composition of the accreted material, which is represented by the rime fraction. This fraction of the accreted rime ice, contrary to the other quantities, experiences a consistent overestimation when neglecting the cloud droplet spectrum. While the values are overall small, there are instances, where environments that accrete liquid water (and therefore may be affected by runback icing) are simulated to only accrete rime ice, when the actual droplet spectrum is not considered. Due to the overall small effects found, however, the consideration of the actual droplet spectrum is not beneficial enough to outweigh the additional computational costs.

The next research question investigates the role of the aerosol load, which in of itself is not a microphysical quantity, but affects the microphysics by providing cloud condensation nuclei. This sensitivity investigation is conducted in two parts. The first part aims to give an idea of the maximum impact, also mostly independent of the actual nucleation parameterization used, an altered aerosol load can have, by directly altering the cloud droplet number density, which is the main quantity the cloud condensation nuclei impact. Hence, sensitivity simulations are conducted that alter the cloud droplet number density the new aircraft icing parameterization receives as input. The alterations are achieved by the multiplication of the actual value with the factors 0.1 and 10.0, respectively. Meeting expectations, applying the factor 0.1 leads to increased impingement efficiency values, as the corresponding frequency distribution shifts to larger values. Interestingly, the higher the actual impingement efficiency value is, the lower is the experienced effect. The mean value of these distributions increases from 0.602, 0.586, 0.584 and 0.611 to 0.788, 0.776, 0.771 and 0.784 for the CAN24, CAN26, SPN and BWF case, respectively. The factor 10.0 leads to a significant reduction of the impingement efficiency, to mean values of 0.350, 0.337, 0.350 and 0.382, respectively. The accretion rates of the different accretion phases are also affected. The amplitude of the effect is considerably lower for the glaze accretion rate than for the rime and liquid water accretion rates, which is due to the generally lower values of the glaze accretion rate. In line with the effect on the impingement efficiency, the accretion rates experience a consistent increasing effect induced by the reduction of the cloud droplet number density and a consistent decreasing effect by its increase. The rime fraction, however, is again inversely affected. A reduction of the cloud droplet number density leads to a reduction in rime fraction, while an increase has the opposite effect. This also manifests in significantly different frequencies of pure dry icing environments identified, with increased cloud droplet number densities leading to more of such environments. Due to the potential hazards of runback icing, which can only occur in wet icing environments, this can be crucial for aviation.

The second part of investigating the sensitivity on the aerosol load is the modification of the CCN number density for the droplet nucleation parameterization using the same factors as before. Due to the effects this exerts onto the atmospheric state, slight shifts in position of the identified icing environments are found. Regarding the frequency distribution of the overall impingement efficiency of these environments, the sign of the changes matches those caused by direct alteration of the cloud droplet number density, as expected. The scale of the changes, however, is comparable only for the low impingement environments, while the large impingement environments stay mostly unchanged. This highlights that the latter are less influenced by the actual droplet nucleation than the former. This leads to an overall reduced effect, manifesting in an increase of the mean values to 0.632, 0.621, 0.628 and 0.648 when reducing the CCN number density by a factor of 10, and a reduction to 0.568, 0.553, 0.547 and 0.586 for the CAN24, CAN26, SPN and BWF case, when increasing it by a factor of 10, respectively. The effects on the rime accretion are comparable. The overall effect is reduced compared to direct alteration of the cloud droplet number density, as environments with the highest rime accretion rates, which are mostly linked to high impingement environments, stay largely unaffected. Interestingly, the effects on the remaining accretion types, glaze ice and liquid water both have no significant scale. While this meets expectations for the glaze ice accretion, regarding its already low sensitivity to the cloud droplet number density, the heavily reduced sensitivity of the liquid water accretion suggests that this occurs mostly in high impingement environments. The composition of the accreted material, represented by the rime fraction, however, is sensitive to the alteration of the CCN number density. Although reduced in scale compared to the direct alteration of cloud droplet number density, it shares its sign, overall decreasing the rime fraction for increased CCN number density and increasing it for decreased CCN number density. This also manifests in corresponding changes in frequencies of purely dry icing environments. The effects are overall large enough to encourage the usage of a proper prognostic representation of the development of the aerosol load (as it is done in ICON-ART) to accurately forecast the position and intensity of aircraft icing environments.

The final sensitivity investigated stems from the development of the new aircraft icing parameterization itself, as it introduces further influencing quantities. The relative airspeed differs between different types of aircrafts as well as in different phases of an aircraft's flight. The most often used relative airspeed of $89.4\,\mathrm{m\,s^{-1}}$ is a representative value for commercial aircrafts in cruise, while a value of $60.0\,\mathrm{m\,s^{-1}}$ is more appropriate for landing and take-off, as well as for smaller aircrafts. The smallest aircrafts, e.g. gliders, may experience relative airspeeds down to about $30.0\,\mathrm{m\,s^{-1}}$. Investigating the effects of these different airspeeds on the impingement efficiency shows that a reduction in relative airspeed causes an overall reduction in impingement efficiency of moderate amplitude. Its mean value reduces to 0.559, 0.542, 0.542 and 0.572 for the CAN24, CAN26, SPN and BWF case, respectively, when reducing the relative airspeed to $60.0\,\mathrm{m\,s^{-1}}$ and further to 0.473, 0.456, 0.460 and 0.495, respectively, at a relative airspeed of $30.0\,\mathrm{m\,s^{-1}}$, while the REF simulations employ a relative airspeed of $89.4\,\mathrm{m\,s^{-1}}$. The accretion rates, however, experience large changes, which meets expectations, since the relative airspeed directly influences the incoming water flux. Interestingly, the amplitude of the effect is not solely explained by this direct influence. Secondary influences enhance the reduction for the accretion rate of rime ice and liquid water, and dampen it for the glaze ice accretion rate. This is highlighted in the effects on the rime fraction, as this quantity is not influenced by the change in incoming water flux directly. The secondary effects lead to an increase in rime fraction overall and to higher frequencies of purely dry icing environments for lower relative airspeeds. Hence, a differentiation of the relative airspeed offers a benefit for different flight phases and aircraft types.

While the newly developed physically based parameterization for aircraft icing is used for simulating past icing events and investigating sensitivities relevant for aircraft icing in the scope of this present work, its design and implementation in an operationally used weather forecast model offer further application possibilities. One of these is the development of a new online aircraft icing prediction scheme based on this new parameterization. This requires the design of an appropriate icing intensity scale that uses the resulting quantities of the new parameterization to map the numerical values to the different icing intensities. This needs then to be used in a pre-operational global setup to validate and tune the configuration and results with icing reports by pilot reports. Additionally, it is required to optimize the performance of the setup to reduce the computational cost. One of these optimizations can already stem from this present work, as the computationally expensive explicit consideration of the cloud droplet spectrum may be neglected.

The scientific future of this present work and the new aircraft icing parameterization also includes a more extensive validation effort, especially for the validation of the accretion's composition. Since the different accretion phases depend on the time of stay in a grid cell or environment, the role of the horizontal resolution in the simulation for the composition of the accreted material is a possible investigation point in the future. Additionally, while this present work investigates the sensitivity to the aerosol load as CCN, so a more source-based approach on water droplets, the sensitivity to INPs in a more sink-based approach on water droplets may yield further insight on the role of aerosols. Further specialized sensitivities to be investigated, as the new parameterization offers the corresponding configuration options, are heating elements, the flight angle or the size of the object. The parameterization's modular design also allows for different shapes to be flown around, once the appropriate wind field is represented.

Bibliography

Bangert, M et al. (2012). “Saharan dust event impacts on cloud formation and radiation over Western Europe”. In: *Atmospheric Chemistry and Physics* 12.9, pp. 4045–4063.

Barahona, D et al. (2010). “Comprehensively accounting for the effect of giant CCN in cloud activation parameterizations”. In: *Atmospheric Chemistry and Physics* 10.5, pp. 2467–2473.

Barahona, Donifan and Athanasios Nenes (2007). “Parameterization of cloud droplet formation in large-scale models: Including effects of entrainment”. In: *Journal of Geophysical Research: Atmospheres* 112.D16.

Behrendt, R and H Mahlke (2003). *Archiv-Version des Animationstools*. accessed 10.08.2022. URL: `https://www.wetter3.de/archiv_gfs_dt.html`.

Bernstein, Ben C et al. (1997). “The relationship between aircraft icing and synoptic-scale weather conditions”. In: *Weather and forecasting* 12.4, pp. 742–762.

Bernstein, Ben C et al. (2005). “Current icing potential: Algorithm description and comparison with aircraft observations”. In: *Journal of Applied Meteorology and Climatology* 44.7, pp. 969–986.

Boudala, Faisal et al. (2019). “Aircraft icing study using integrated observations and model data”. In: *Weather and Forecasting* 34.3, pp. 485–506.

Cao, Yihua et al. (2016). “Numerical simulation of three-dimensional ice accretion on an aircraft wing”. In: *International Journal of Heat and Mass Transfer* 92, pp. 34–54.

Cao, Yihua et al. (2018). “Aircraft icing: An ongoing threat to aviation safety”. In: *Aerospace science and technology* 75, pp. 353–385.

Cober, Stewart G and George A Isaac (2012). “Characterization of aircraft icing environments with supercooled large drops for application to commercial aircraft certification”. In: *Journal of Applied Meteorology and Climatology* 51.2, pp. 265–284.

Cober, Stewart G et al. (1995). “Aircraft icing measurements in east coast winter storms”. In: *Journal of Applied Meteorology and Climatology* 34.1, pp. 88–100.

Cober, Stewart G et al. (1996). “An example of supercooled drizzle drops formed through a collision-coalescence process”. In: *Journal of Applied Meteorology* 35.12, pp. 2250–2260.

Cober, Stewart G et al. (2001). “Characterizations of aircraft icing environments that include supercooled large drops”. In: *Journal of Applied Meteorology* 40.11, pp. 1984–2002.

Dai, Hao et al. (2021). “A new ice accretion model for aircraft icing based on phase-field method”. In: *Applied Sciences* 11.12, p. 5693.

Deiler, Christoph (2013a). *DLR@Uni Projekt - Supercooled Large Droplet Icing (SuLaDI) - Konzept zur Detektion von aerodynamischer Vereisung mittels Methoden der Systemidentifizierung*. Tech. rep. URL: `https://elib.dlr.de/88222/`.

– (2013b). *DLR@Uni Projekt - Supercooled Large Droplet Icing (SuLaDi) - Qualitative Parameterstudie zu Flugleistungen eines eiskontaminierten Flugzeuges*. Tech. rep. URL: `https://elib.dlr.de/80913/`.

Denbigh, Kenneth George and Kenneth George Denbigh (1981). *The principles of chemical equilibrium: with applications in chemistry and chemical engineering*. Cambridge University Press.

Deutscher Wetterdienst (n.d.). *Wetter und Klima - Deutscher Wetterdienst - Leistungen - Klimadaten Deutschland - Monats- und Tageswerte (Archiv)*. accessed 10.08.2022. URL: `https://www.dwd.de/DE/leistungen/klimadatendeutschland/klarchivtagmonat.html?nn=16102#buehneTop`.

Environment and Climate Change Canada (2022a). *Hourly Data Report for October 24, 2016 - Climate - Environment and Climate Change Canada*. accessed 10.08.2022. URL: `https://climate.weather.gc.ca/climate_data/hourly_data_e.html?StationID=2832&Month=10&Day=24&Year=2016`.

– (2022b). *Hourly Data Report for October 26, 2016 - Climate - Environment and Climate Change Canada*. accessed 10.08.2022. URL: `https://climate.weather.gc.ca/climate_data/hourly_data_e.html?StationID=2832&Month=10&Day=26&Year=2016`.

Fernández-González, Sergio et al. (2014). “Weather features associated with aircraft icing conditions: A case study”. In: *The Scientific World Journal* 2014.

Fiedler, F (1983). “Einige Charakteristika der Strömung im Oberrheingraben”. In: *Wissenschaftliche Berichte des Instituts für Meteorologie und Klimaforschung der Universität Karlsruhe* 4, pp. 113–123.

Finstad, Karen J et al. (1988). “A computational investigation of water droplet trajectories”. In: *Journal of atmospheric and oceanic technology* 5.1, pp. 160–170.

Forbes, Gregory S et al. (1993). “Examination of conditions in the proximity of pilot reports of aircraft icing during STORM-FEST”. In: *International Conference on Aviation Weather Systems, 5 th, Vienna, VA*, pp. 282–286.

Fountoukis, Christos and Athanasios Nenes (2005). “Continued development of a cloud droplet formation parameterization for global climate models”. In: *Journal of Geophysical Research: Atmospheres* 110.D11.

Gassmann, Almut (2011). “Inspection of hexagonal and triangular C-grid discretizations of the shallow water equations”. In: *Journal of Computational Physics* 230.7, pp. 2706–2721.

Gassmann, Almut and Hans-Joachim Herzog (2008). “Towards a consistent numerical compressible non-hydrostatic model using generalized Hamiltonian tools”. In: *Quarterly Journal of the Royal Meteorological Society* 134.635, pp. 1597–1613.

Gent, Roger W et al. (2000). “Aircraft icing”. In: *Philosophical Transactions of the Royal Society of London. Series A: Mathematical, Physical and Engineering Sciences* 358.1776, pp. 2873–2911.

Geresdi, I et al. (2005). “Sensitivity of freezing drizzle formation in stably stratified clouds to ice processes”. In: *Meteorology and Atmospheric Physics* 88.1, pp. 91–105.

Hauf, T and F Schröder (2006). “Aircraft icing research flights in embedded convection”. In: *Meteorology and Atmospheric Physics* 91.1, pp. 247–265.

Hill, Geoffrey E (1980). “Seeding-opportunity recognition in winter orographic clouds”. In: *Journal of Applied Meteorology and Climatology* 19.12, pp. 1371–1381.

Jung, Sung Ki et al. (2011). “An efficient CFD-based method for aircraft icing simulation using a reduced order model”. In: *Journal of Mechanical Science and Technology* 25.3, pp. 703–711.

Kalinka, Frank et al. (2017). “The In-flight icing warning system ADWICE for European airspace-Current structure, recent improvements and verification results”. In: *Meteorologische Zeitschrift 26 (2017), Nr. 4* 26.4, pp. 441–455.

Kalthoff, N and B Vogel (1992). “Counter-current and channelling effect under stable stratification in the area of Karlsruhe”. In: *Theoretical and applied climatology* 45.2, pp. 113–126.

Köhler, Felix and Ulrich Görsdorf (2014). “Towards 3D prediction of supercooled liquid water for aircraft icing: Modifications of the microphysics in COSMO-EU”. In: *Meteorol. Z* 23, pp. 253–262.

Korolev, Alexei V et al. (2003). “Microphysical characterization of mixed-phase clouds”. In: *Quarterly Journal of the Royal Meteorological Society: A journal of the atmospheric sciences, applied meteorology and physical oceanography* 129.587, pp. 39–65.

Kringlebotn Nygaard, Bjørn Egil et al. (2011). “Prediction of in-cloud icing conditions at ground level using the WRF model”. In: *Journal of Applied Meteorology and Climatology* 50.12, pp. 2445–2459.

Lee, Thomas F et al. (1997). “Stratus and fog products using GOES-8–9 3.9-μ m data”. In: *Weather and Forecasting* 12.3, pp. 664–677.

Leifeld, Christoph (2004). *Weiterentwicklung des nowcastingsystems ADWICE zur Erkennung vereisungsgefährdeter Lufträume*. Selbstverlag des Deutschen Wetterdienstes.

Lohmann, Ulrike et al. (2016). *An Introduction to Clouds: From the Microscale to Climate*. Cambridge: Cambridge University Press. DOI: `10.1017/CBO9781139087513`.

Lundgren, K et al. (2013). "Direct radiative effects of sea salt for the Mediterranean region under conditions of low to moderate wind speeds". In: *Journal of Geophysical Research: Atmospheres* 118.4, pp. 1906–1923.

Majewski, Detlev et al. (2002). "The operational global icosahedral–hexagonal gridpoint model GME: description and high-resolution tests". In: *Monthly Weather Review* 130.2, pp. 319–338.

McComber, Pierre and Gilbert Touzot (1981). "Calculation of the impingement of cloud droplets in a cylinder by the finite-element method". In: *Journal of Atmospheric Sciences* 38.5, pp. 1027–1036.

McDonough, Frank and BC Bernstein (1999). "Combining satellite, radar and surface observations with model data to create a better aircraft icing diagnosis". In: *Proceedings, 8th Conference on Aviation, Range and Aerospace Meteorology*, pp. 467–471.

Mecikalski, John R et al. (2007). "Aviation applications for satellite-based observations of cloud properties, convection initiation, in-flight icing, turbulence, and volcanic ash". In: *Bulletin of the American Meteorological Society* 88.10, pp. 1589–1607.

Messinger, Bernard L (1953). "Equilibrium temperature of an unheated icing surface as a function of air speed". In: *Journal of the aeronautical sciences* 20.1, pp. 29–42.

Milbrandt, Jason A et al. (2016). "The pan-Canadian high resolution (2.5 km) deterministic prediction system". In: *Weather and Forecasting* 31.6, pp. 1791–1816.

Myers, Tim G (2001). "Extension to the Messinger model for aircraft icing". In: *AIAA journal* 39.2, pp. 211–218.

Nenes, Athanasios and John H Seinfeld (2003). "Parameterization of cloud droplet formation in global climate models". In: *Journal of Geophysical Research: Atmospheres* 108.D14.

Papadakis, Michael et al. (1991). "Experimental water droplet impingement data on modern aircraft surfaces". In: *29th Aerospace Sciences Meeting*, p. 445.

Papadakis, Michael et al. (2004). "Water impingement experiments on a NACA 23012 airfoil with simulated glaze ice shapes". In: *42nd AIAA aerospace sciences meeting and exhibit*, p. 565.

Phillips, Vaughan TJ et al. (2013). "Improvements to an empirical parameterization of heterogeneous ice nucleation and its comparison with observations". In: *Journal of the Atmospheric Sciences* 70.2, pp. 378–409.

Politovich, Marcia K and Ben C Bernstein (1995). "Production and depletion of supercooled liquid water in a Colorado winter storm". In: *Journal of Applied Meteorology and Climatology* 34.12, pp. 2631–2648.

Pruppacher, Hans R and James D Klett (2012). *Microphysics of Clouds and Precipitation: Reprinted 1980*. Springer Science & Business Media.

Raschendorfer, Matthias (2001). "The new turbulence parameterization of LM". In: *COSMO newsletter* 1, pp. 89–97.

Rauber, Robert M et al. (2000). "The relative importance of warm rain and melting processes in freezing precipitation events". In: *Journal of Applied Meteorology* 39.7, pp. 1185–1195.

Rieger, Daniel et al. (2015). "ICON–ART 1.0–a new online-coupled model system from the global to regional scale". In: *Geoscientific Model Development* 8.6, pp. 1659–1676.

Sand, Wayne R et al. (1984). "Icing conditions encountered by a research aircraft". In: *Journal of Applied Meteorology and Climatology* 23.10, pp. 1427–1440.

Schultz, Paul and Marcia K Politovich (1992). "Toward the improvement of aircraft-icing forecasts for the continental United States". In: *Weather and Forecasting* 7.3, pp. 491–500.

Seifert, Axel and Klaus Dieter Beheng (2006). "A two-moment cloud microphysics parameterization for mixed-phase clouds. Part 1: Model description". In: *Meteorology and atmospheric physics* 92.1, pp. 45–66.

Seinfeld, John H and Spyros N Pandis (2016). *Atmospheric Chemistry and Physics: From Air Pollution to Climate Change*. 3rd Edition. Hoboken, New Jersey: John Wiley & Sons, p. 1120.

Skamarock, William C et al. (2012). “A multiscale nonhydrostatic atmospheric model using centroidal Voronoi tesselations and C-grid staggering”. In: *Monthly Weather Review* 140.9, pp. 3090–3105.

Squires, P and Charles A Knight (1982). *Hailstorms of the Central High Plains*. Colorado Associated University Press.

Stevens, Bjorn et al. (2013). “Atmospheric component of the MPI-M Earth system model: ECHAM6”. In: *Journal of Advances in Modeling Earth Systems* 5.2, pp. 146–172.

Tafferner, A et al. (2003). “ADWICE: Advanced diagnosis and warning system for aircraft icing environments”. In: *Weather and forecasting* 18.2, pp. 184–203.

Thompson, Gregory et al. (1997). “Intercomparison of in-flight icing algorithms. Part I: WISP94 real-time icing prediction and evaluation program”. In: *Weather and Forecasting* 12.4, pp. 878–889.

Thompson, Gregory et al. (2017). “A numerical weather model’s ability to predict characteristics of aircraft icing environments”. In: *Weather and Forecasting* 32.1, pp. 207–221.

Tiedtke, MICHAEL (1989). “A comprehensive mass flux scheme for cumulus parameterization in large-scale models”. In: *Monthly weather review* 117.8, pp. 1779–1800.

Tomita, Hirofumi and Masaki Satoh (2004). “A new dynamical framework of nonhydrostatic global model using the icosahedral grid”. In: *Fluid Dynamics Research* 34.6, p. 357.

Tomita, Hirofumi et al. (2001). “Shallow water model on a modified icosahedral geodesic grid by using spring dynamics”. In: *Journal of Computational Physics* 174.2, pp. 579–613.

Ullrich, Paul A and Christiane Jablonowski (2012). “MCore: A non-hydrostatic atmospheric dynamical core utilizing high-order finite-volume methods”. In: *Journal of Computational Physics* 231.15, pp. 5078–5108.

Villedieu, Philippe et al. (2019). “MUSIC-Haic: 3D multidisciplinary tools for the simulation of in-flight icing due to high altitude ice crystals”. In: *SAE International journal of advances and current practices in mobility*.

Vogel, Bernhard et al. (2009). “The comprehensive model system COSMO-ART–Radiative impact of aerosol on the state of the atmosphere on the regional scale”. In: *Atmospheric Chemistry and Physics* 9.22, pp. 8661–8680.

Wippermann, F (1984). “Air flow over and in broad valleys: Channeling and counter-current”. In: *Beiträge zur Physik der Atmosphäre* 57.1, pp. 92–105.

Xu, Mei et al. (2019). “On the value of time-lag-ensemble averaging to improve numerical model predictions of aircraft icing conditions”. In: *Weather and Forecasting* 34.3, pp. 507–519.

Zängl, Günther et al. (2015). “The ICON (ICOsahedral Non-hydrostatic) modelling framework of DWD and MPI-M: Description of the non-hydrostatic dynamical core”. In: *Quarterly Journal of the Royal Meteorological Society* 141.687, pp. 563–579.

Zhang, Xuan et al. (2016). “Model for aircraft icing with consideration of property-variable rime ice”. In: *International Journal of Heat and Mass Transfer* 97, pp. 185–190.

List of Figures

2.1 Ice accretion on the leading edge of a lightweight aircraft's airfoil. Minor incidents of runback icing are also indicated (Photo taken during private flight by a hobby pilot). 6
2.2 Koehler curves for the dependency of the supersaturation on the droplet diameter for NaCl solution droplets with dry diameters 0.05,0.1 and 0.5 µm at 293 K. Dry NaCl particles are assumed to be spherical (Seinfeld and Pandis 2016). 10
2.3 Illustration of the local impingement efficiency (top) and the overall impingement efficiency (bottom) (Source: (Gent et al. 2000)). 12
2.4 Representation of the icing model by Zhang et al. (2016), illustrating the thicknesses of the different accreted substances z_r, z_g and z_w as well as the critical ice thickness z_c. It also highlights the development of the rime ice density, reaching the value of glaze ice once z_c is reached (Source: (Zhang et al. 2016)). 16
2.5 ADWICE's PIP output. Horizontal distribution of the icing scenarios identified (left) and of the associated icing intensity levels (right) (Source: (Kalinka et al. 2017)). 20
2.6 ADWICE's PIA scenario identification. Temperature and dewpoint profiles highlighting the scenarios „General“ (blue), „Freezing“ (red), „Stratiform“ (yellow) and „Convective“ (green) (Source: (Kalinka et al. 2017) - modified). 21
2.7 ADWICE's membership functions for the supersaturation over ice (top left), its vertical extent (top center), convective clouds' vertical extent (top right) and the two LWC alternatives, as the model result (bottom left) and computed via a parcel method (bottom right) (Source: (Kalinka et al. 2017)). . 22

3.1 Schematic of the computation of the overall impingement efficiency for a cylinder. The colorful lines on the left side of the circle, as a projection of the cylinder, represent the different droplet trajectories of which only the top and bottom most manage to avoid the cylinder. 30
3.2 Representative path (red) an aircraft takes traversing a triangular grid cell. This information is used to compute its traversing time to determine the different phases of aircraft icing. 34
3.3 Sensitivity of the overall impingement efficiency (black) and the critical ice thickness (blue), as computed by the newly developed aircraft icing parameterization, on the droplet diameter (top left), the ambient wind speed (top right), the cylinder radius (center left), the LWC (center right) and the ambient air temperature (bottom). 35

4.1 Location of Cold Lake Regional Airport in Alberta, Canada (marked with a yellow dot). 39
4.2 Synoptic weather situation for North America on 24th of October 2016: (top) 500hPa Geopotential height and (bottom) 10 m wind speed at 00 UTC (left) and 18 UTC (right), [Source: (Behrendt and Mahlke 2003)] 41
4.3 3D distribution of simulated LWC (top left), mean droplet diameter (top right), cloud temperature (bottom left) and accreted ice (bottom right) around Cold Lake on 24th October 2016 at 18:50 UTC, matching the icing report. Only environments with a LWC of at least $0.1\,\mathrm{g\,m^{-3}}$ are displayed. 42
4.4 Time series of vertical profiles for temperature (left) and specific humidity (right) at Cold Lake on 24th October 2016 as simulated by the model, the icing report (18:49 UTC at 217 m of altitude) is marked as a yellow dot. 43

4.5 Time series of vertical profiles for LWC (left) and cloud droplet number density (right) at Cold Lake on 24th October 2016 as simulated by the model, the icing report (18:49 UTC at 217 m of altitude) is marked as a yellow dot. 43
4.6 Time series of vertical profiles for overall impingement efficiency, calculated with an empirical formulation (left) and as the result of the new parameterization (right) at Cold Lake on 24th October 2016, the icing report (18:49 UTC at 217 m of altitude) is marked as a yellow dot. 44
4.7 Histograms (relative frequency) of the overall impingement efficiency, calculated with an empirical formulation (left) and as the result of the new parameterization (right) for the entire simulation domain and period (24th October 2016). 44
4.8 Time series of vertical profiles for the critical ice thickness (left) and the critical time (right) at Cold Lake on 24th October 2016, the icing report (18:49 UTC at 217 m of altitude) is marked as a yellow dot. 45
4.9 Time series of vertical profiles for the accreted thickness (left) and the accretion rate (right) for rime (top), glaze (center) and liquid water (bottom) accretion at Cold Lake on 24th October 2016, the icing report (18:49 UTC at 217 m of altitude) is marked as a yellow or gray dot. 46
4.10 Histograms (relative frequency) of the fraction of rime accretion to the total accretion (left) and ratio between the simultaneously accreted liquid water and glaze ice (right) for the entire simulation domain and period of the 24th of October. 47
4.11 Relation between ice and liquid water accretion and temperature, the abscissa shows the accreted ice thickness, the ordinate gives the thickness of the liquid water film and the temperature of the grid cell is color coded. Data for the entire simulation domain and period is used. 47
4.12 Time series of vertical profile for the total water accretion rate - rime, glaze ice and liquid water (left) and its histogram (right). The reported icing event is marked with a yellow dot in the former and the latter incorporates data for the entire simulation domain and period. 48
4.13 Synoptic weather situation for North America on 26th of October 2016: (top) 500hPa Geopotential height and (bottom) 10 m wind speed at 00 UTC (left) and 18 UTC (right), [Source: (Behrendt and Mahlke 2003)] 49
4.14 3D distribution of simulated LWC (top left), mean droplet diameter (top right), cloud temperature (bottom left) and accreted ice (bottom right) around Cold Lake on 26th October 2016 at 14:40 UTC, matching the first icing report. Only environments with a LWC of at least 0.05 $\text{g}\,\text{m}^{-3}$ are displayed. . . 50
4.15 Time series of vertical profiles for temperature (left) and specific humidity (right) at Cold Lake on 26th October 2016 as simulated by the model, the icing reports (14:42 UTC at 2500 m to 3300 m of altitude and 19:22 UTC at 186 m of altitude) are marked as yellow dots. 51
4.16 Time series of vertical profiles for LWC (left) and cloud droplet number density (right) at Cold Lake on 26th October 2016 as simulated by the model, the icing reports (14:42 UTC at 2500 m to 3300 m of altitude and 19:22 UTC at 186 m of altitude) are marked as gray dots. 51
4.17 Time series of vertical profiles for LWC at potential locations for the first (left) and the second (right) icing report on 26th October 2016 as simulated by the model. the icing reports (14:42 UTC at 2500 m to 3300 m of altitude and 19:22 UTC at 186 m of altitude) are marked as gray and yellow dots. 52
4.18 Time series of vertical profiles for overall impingement efficiency, calculated with an empirical formulation (left) and as the result of the new parameterization (right) at Cold Lake on 26th October 2016, the icing reports (14:42 UTC at 2500 m to 3300 m of altitude and 19:22 UTC at 186 m of altitude) are marked as gray dots. 52
4.19 Histograms (relative frequency) of the overall impingement efficiency, calculated with an empirical formulation (left) and as the result of the new parameterization (right) for the entire simulation domain and period (26th October 2016). 53

4.20 Time series of vertical profiles for the critical ice thickness (left) and the critical time (right) at Cold Lake on 26th October 2016, the icing reports (14:42 UTC at 2500 m to 3300 m of altitude and 19:22 UTC at 186 m of altitude) are marked as gray dots. 53

4.21 Time series of vertical profiles for the accreted thickness (left) and the accretion rate (right) for rime (top), glaze (center) and liquid water (bottom) accretion at Cold Lake on 26th October 2016, the icing reports (14:42 UTC at 2500 m to 3300 m of altitude and 19:22 UTC at 186 m of altitude) are marked as gray dots. 54

4.22 Histograms (relative frequency) of the fraction of rime accretion to the total accretion (left) and ratio between the simultaneously accreted liquid water and glaze ice (right) for the entire simulation domain and period of the 26th of October. 55

4.23 Relation between ice and liquid water accretion and temperature, the abscissa shows the accreted ice thickness, the ordinate gives the thickness of the liquid water film and the temperature of the grid cell is color coded. Data for the entire simulation domain and period is used. 55

4.24 Time series of vertical profile for the total water accretion rate - rime, glaze ice and liquid water (left) and its histogram (right). The reported icing events are marked with a gray dot in the former and the latter incorporates data for the entire simulation domain and period. 56

4.25 Location of the Guadarrama Mountains, Spain (marked with a yellow dot). 57

4.26 Synoptic weather situation for Europe on 1st of February 2012: (top) 500hPa Geopotential height and (bottom) 10 m wind speed at 00 UTC (left) and 18 UTC (right), [Source: (Behrendt and Mahlke 2003)] 58

4.27 3D distribution of simulated LWC (top left), mean droplet diameter (top right), cloud temperature (bottom left) and accreted ice (bottom right) at the Guadarrama Mountains on 1st of February 2012 at 13:00 UTC, matching the icing incident. Only environments with a LWC of at least $0.05\,\mathrm{g\,m^{-3}}$ are displayed. 59

4.28 Horizontal distribution of LWC (left) and overall impingement efficiency (right) at Guadarrama Mountains on 1st of February 2012 13:00 UTC in an altitude of 2000 m above sea level, as simulated by the model. 60

4.29 Histograms (relative frequency) of the overall impingement efficiency, as the result of the new parameterization (left) and calculated with an empirical formulation (right) for the entire simulation domain and period (1st February 2012). 60

4.30 Horizontal distribution of the critical ice thickness (top-left), the accreted rime ice thickness (top-right), the accreted glaze ice thickness (bottom-left) and the accreted water film thickness (bottom-right) at Guadarrama Mountains on 1st of February 2012 13:00 UTC in an altitude of 2000 m above sea level, as simulated by the model. 61

4.31 Histograms (relative frequency) of the fraction of rime accretion to the total accretion (left) and ratio between the simultaneously accreted liquid water and glaze ice (right) for the entire simulation domain and period of the 1st of February 2012. 62

4.32 Horizontal distribution of the total water accretion rate - rime, glaze ice and liquid water (left) and its histogram (right). The former presents data at an altitude of 2000 m at 13:00 UTC on 1st of February 2012 and the latter incorporates data for the entire simulation domain and period. 62

4.33 Flight path of the research flight conducted by Fernández-González et al. (2014) [Source: (Fernández-González et al. 2014) - modified] (left) and spatial development of the total water accretion rate's profile along this flight path (right) at 13:10 UTC on 1st February 2012. 63

4.34 Location of the reported icing incident in Baden-Wuerttemberg, Germany (marked with a yellow dot). 64

4.35 Synoptic weather situation for Germany on 7th of December 2019: (top) 500hPa Geopotential height and (bottom) 10 m wind speed at 00 UTC (left) and 18 UTC (right), [Source: (Behrendt and Mahlke 2003)] 65

4.36 3D distribution of simulated LWC (top left), mean droplet diameter (top right), cloud temperature (bottom left) and accreted ice (bottom right) in Baden-Wuerttemberg on 7th December 2019 at 15:00 UTC, matching the reported icing incident.Only environments with a LWC of at least $0.1\,\mathrm{g\,m^{-3}}$ are displayed. 66

4.37 Horizontal distribution of the LWC (top left), the mean droplet diameter (top right), the overall impingement efficiency calculated empirically (bottom left) and with the newly developed physically based parameterization (bottom right) in an altitude of 2000 m at the time of the icing incident. Its position is marked with a yellow dot. 67

4.38 Temporal development of the vertical profiles of the LWC (left) and the overall impingement efficiency (right) at the location of the reported icing incident, the yellow dot marks its time and altitude. 67

4.39 Horizontal distribution (top) and temporal development of the vertical profiles (bottom) of the mean accretion rates of ice (left) and liquid water (right) as the result of the newly developed physically based parameterization in an altitude of 2000 m and at the location of the reported icing incident, repectively. The icing incident's position and time and altitude, respectively, is marked with a yellow dot. 68

4.40 Histograms (relative frequency) of the overall impingement efficiency as a result of the introduced empirical formulation (left) and of the newly developed physically based parameterization (right) for the entire simulation domain and period of the 7th of December 2019. 69

4.41 Histograms (relative frequency) of the fraction of rime accretion to the total accretion (left) and ratio between the simultaneously accreted liquid water and glaze ice (right) for the entire simulation domain and period of the 7th of December 2019. 69

4.42 Histograms (relative frequency) of the mean total ice accretion rate, including rime and glaze ice (left) and the total water accretion rate, including rime and glaze ice and the liquid water film (right) for the entire simulation domain and period of the 7th of December 2019. 70

5.1 Differences in overall impingement efficiency between the BULK simulation and the REF simulation as the temporal development of its vertical profile in the CAN24 case (top left) and in the CAN26 case (top right) and as its horizontal distribution in the SPN case (bottom left) and in the BWF case (bottom right). The position of the icing reports and incidents are marked with a yellow and gray dot. 74

5.2 Relative frequency distributions of the overall impingement efficiency for the REF simulations (left) and the BULK simulations (right) in the CAN24 case (top) and the CAN26 case (bottom). 75

5.3 Relative frequency distributions of the overall impingement efficiency for the REF simulations (left) and the BULK simulations (right) in the SPN case (top) and the BWF case (bottom). 76

5.4 Differences in total water accretion rate - including rime and glaze ice and liquid water accretion - between the BULK simulation and the REF simulation as the temporal development of its vertical profile in the CAN24 case (top left) and in the CAN26 case (top right) and as its horizontal distribution in the SPN case (bottom left) and in the BWF case (bottom right). The position of the icing reports and incidents are marked with a yellow and gray dot. 77

5.5 Relative frequency distribution of the differences in total water accretion rate between the BULK simulation and the REF simulation for the CAN24 case (top left), the CAN26 case (top right), the SPN case (bottom left) and the BWF case (bottom right) 78

5.6 Differences in accreted ice thickness - including rime and glaze ice - between the BULK simulation and the REF simulation as the temporal development of its vertical profile in the CAN24 case (top left) and in the CAN26 case (top right) and as its horizontal distribution in the SPN case (bottom left) and in the BWF case (bottom right). The position of the icing reports and incidents are marked with a yellow and gray dot. 79

5.7 Relative frequency distribution of the differences in total ice thickness between the BULK simulation and the REF simulation for the stratiform CAN24 case (left), and the convective BWF case (right). . . 80

5.8 Relative frequency distribution of the rime fraction for the CAN24 case (top) and the BWF case (bottom) in the REF simulation (left) and the BULK simulation (right). 80

6.1 Differences in overall impingement efficiency between the NC01 (top), NC10 (bottom) simulation and the REF simulation as the temporal development of its vertical profile (left) and as its horizontal distribution (right) for the BWF case, the profile is taken at the location of the reported icing incident and horizontal distribution at its time in an altitude of 2000 m. The position of the icing incident is marked with a yellow dot. 82

6.2 Relative frequency distributions of the overall impingement efficiency in the NC01 (left), REF (center) and NC10 (right) simulations for the CAN24 (1st row), CAN26 (2nd row), SPN (3rd row) and BWF case (4th row). 83

6.3 Relative frequency distributions of the mean rime accretion rate in the NC01 (left), REF (center) and NC10 (right) simulations for the CAN24 (1st row), CAN26 (2nd row), SPN (3rd row) and BWF case (4th row). 85

6.4 Relative frequency distributions of the mean glaze accretion rate in the NC01 (left), REF (center) and NC10 (right) simulations for the CAN24 (1st row), CAN26 (2nd row), SPN (3rd row) and BWF case (4th row). 86

6.5 Relative frequency distributions of the mean water accretion rate in the NC01 (left), REF (center) and NC10 (right) simulations for the CAN24 (1st row), CAN26 (2nd row), SPN (3rd row) and BWF case (4th row). 87

6.6 Relative frequency distributions of the rime fraction of the accreted material in the NC01 (left), REF (center) and NC10 (right) simulations for the CAN24 (1st row), CAN26 (2nd row), SPN (3rd row) and BWF case (4th row). 88

6.7 Horizontal distribution of the difference in total water accretion rate for the BWF case between the NC01 (left), NC10 (right) and the REF simulation at the time of the reported icing incident in an altitude of 2000 m. The location of the icing incident is marked with a yellow dot. 89

6.8 Differences in overall impingement efficiency between the ACI01 (top), ACI10 (bottom) simulation and the REF simulation as the temporal development of its vertical profile (left) and as its horizontal distribution (right) for the BWF case, the profile is taken at the location of the reported icing incident and the horizontal distribution at its time in an altitude of 2000 m. The position of the icing incident is marked with a yellow dot. 91

6.9 Relative frequency distributions of the cloud droplet number density in the ACI01 (left), REF (center) and ACI10 (right) simulations for the CAN24 case. 92

6.10 Relative frequency distributions of the overall impingement efficiency in the ACI01 (left), REF (center) and ACI10 (right) simulations for the CAN24 (1st row), CAN26 (2nd row), SPN (3rd row) and BWF case (4th row). 93

6.11 Relative frequency distributions of the mean rime accretion rate in the ACI01 (left), REF (center) and ACI10 (right) simulations for the CAN24 (1st row), CAN26 (2nd row), SPN (3rd row) and BWF case (4th row). 94

6.12 Relative frequency distributions of the mean glaze accretion rate in the ACI01 (left), REF (center) and ACI10 (right) simulations for the CAN24 (1st row), CAN26 (2nd row), SPN (3rd row) and BWF case (4th row). 95
6.13 Relative frequency distributions of the mean water accretion rate in the ACI01 (left), REF (center) and ACI10 (right) simulations for the CAN24 (1st row), CAN26 (2nd row), SPN (3rd row) and BWF case (4th row). 96
6.14 Relative frequency distributions of the rime fraction of the accreted material in the ACI01 (left), REF (center) and ACI10 (right) simulations for the CAN24 (1st row), CAN26 (2nd row), SPN (3rd row) and BWF case (4th row). 97
6.15 Horizontal distribution of the differences in total water accretion rate introduced by the ACI01 (left), ACI10 (right) compared to the REF simulation at the time of the reported icing incident in an altitude of 2000 m. The location of the icing incident is marked with a yellow dot. 98

7.1 Differences in overall impingement efficiency between the V60 (top), V30 (bottom) simulation and the REF simulation as the temporal development of its vertical profile (left) and as its horizontal distribution (right) for the BWF case, the profile is taken at the location of the reported icing incident and horizontal distribution at its time in an altitude of 2000 m. The position of the icing incident is marked with a yellow dot. 102
7.2 Relative frequency distributions of the overall impingement efficiency in the V89 (left), V60 (center), V30 (right) simulations for the CAN24 (1st row), CAN26 (2nd row), SPN (3rd row) and BWF case (4th row). 103
7.3 Relative frequency distributions of the mean rime accretion rate in the V89 (left), V60 (center), V30 (right) simulations for the CAN24 (1st row), CAN26 (2nd row), SPN (3rd row) and BWF case (4th row). 104
7.4 Relative frequency distributions of the mean glaze accretion rate in the V89 (left), V60 (center), V30 (right) simulations for the CAN24 (1st row), CAN26 (2nd row), SPN (3rd row) and BWF case (4th row). 105
7.5 Relative frequency distributions of the mean water accretion rate in the V89 (left), V60 (center), V30 (right) simulations for the CAN24 (1st row), CAN26 (2nd row), SPN (3rd row) and BWF case (4th row). 106
7.6 Relative frequency distributions of the rime fractions in the V89 (left), V60 (center), V30 (right) simulations for the CAN24 (1st row), CAN26 (2nd row), SPN (3rd row) and BWF case (4th row). . . 108
7.7 Horizontal distribution of the total water accretion rate (left) and the total accreted water (right) for the BWF case as a result of the V89 (top), V60 (center) and V30 (bottom) simulation at the time of the reported icing incident in an altitude of 2000 m. The location of the icing incident is marked with a yellow dot. 109

List of Tables

3.1 Overview of the simulations conducted in the present work. The bold font highlights the change in setup compared to the REF simulation. 36

Acknowledgements

This work was performed on the HoreKa supercomputer funded by the Ministry of Science, Research and the Arts Baden-Württemberg and by the Federal Ministry of Education and Research.
Furthermore resources of the Deutsches Klimarechenzentrum (DKRZ) granted by its Scientific Steering Committee (WLA) under project ID bb1070 have been used.

Danksagung

Zuerst gilt mein Dank Prof. Dr. Christoph Kottmeier für die Übernahme der Referentenrolle für diese Arbeit. Ebenso danke ich Ihnen für die erkenntnisreichen Gespräche, die kritischen Fragen, die Hinweise und Ratschläge und nicht zuletzt für das Korrekturlesen der Dissertation.
Zudem danke ich Prof. Dr. Corinna Hoose dafür, dass Sie die Rolle der Korreferentin übernommen haben. Die Gespräche mit Ihnen waren nicht weniger erkenntnisreich. Vielen Dank, dass ich von Ihrem Wissen und Ihrer Erfahrung im Thema der Mikrophysik profitieren konnte. Wenngleich das Ergebnis Ihres Korrekturlesens die letzten Wochen dieses Unterfangens spannend gemacht haben, seien Sie sich definitiv meines Dankes hierfür gewiss und in dem Zusammenhang auch für das stets kritische Auge für die Ergebnisse.
Ohne Ihrer beider Einfluss und Interesse wäre diese Arbeit nicht in dieser Form entstanden.
Für die Durchführung der Promotion hätte ich mir kein passenderes und besseres Umfeld wünschen können als die Arbeitsgruppe „Spurenstoffmodellierung und Klimaprozesse“ des IMK-TRO, in welcher ich schon weit vor meinem Promotionsvorhaben beschäftigt war, da meine Zeit hier sogar vor meiner Bachelorarbeit anfing. Da ein solcher allgemeiner Dank der Situation nicht gerecht wird, werde ich hier mit Freuden einige gesondert erwähnen, denen mein Dank gilt: Zuerst danke ich dem (nun ehemaligen) Gruppenleiter, Dr. Bernhard Vogel, für das Angebot dieses Themas und deiner tatkräftigen Unterstützung, insbesondere auch nach dem Antritt deines Ruhestands. Das kritische Auge, das du auf die Zwischenergebnisse geworfen hast, hat den weiteren Verlauf der Arbeit maßgeblich geprägt. Danke, dass du mich gebremst hast, wenn ich mich zu früh zu sehr in Kleinigkeiten verstrickte, und meinen Blick wieder auf das Wesentliche gelenkt hast. Ich konnte über die Jahre viel von dir lernen, insbesondere über das wissenschaftliche Schreiben und Vortragen. Auch vielen Dank für das Entschlacken meiner Folien. Jenseits der Wissenschaft danke ich dir auch für das entgegengebrachte Vertrauen für die Übernahme der Rolle eines Gatekeepers für ICON-ART und dafür, dass du dafür Sorge getragen hast, dass meine Promotion nicht zu sehr darunter litt. Ich hoffe, ich habe dieses Vertrauen nicht enttäuscht. Ebenso möchte ich Dr. Heike Vogel danken. Die Gespräche mit dir, seien sie in deinem Büro, zwischen Tür und Angel oder am Mittagstisch, waren mir stets eine Freude und manches Mal auch eine sehr willkommene Ablenkung, wenngleich so manches hätte „gruselig“ sein können. Vielen Dank, dass ich von deinen Erfahrungen habe profitieren dürfen, seien sie wissenschaftlich, technisch oder auch bürokratisch, und dafür, dass du stets ein offenes Ohr für Fragen hattest. Des Weiteren danke ich auch dem jetzigen Gruppenleiter, Dr. Gholamali Hoshyaripour, für deine Fragen, Anmerkungen und Anregungen sowie insbesondere dein Verständnis und Entgegenkommen in den letzten Monaten dieses Unterfangens. Obwohl es nur ein kurzes Überschneiden unserer Doktorandenzeit war, möchte ich auch Dr. Simon Gruber danken für die Hilfe bei den bürokratischen Prozessen, die für den Anfang dieses Unterfangens notwendig waren. Ebenso danke ich den zwei Personen, mit denen ich für den Großteil meiner Promotion ein Büro teilte, Dr. Lukas Muser und Julia Bruckert. Eure herzliche und offene Art hat ein Büroklima geschaffen, in welchem ich gerne arbeitete. Mein weiterer Dank gilt Dr. Anika Rohde für deine Hilfsbereitschaft und nicht zuletzt für all die Protokolle der Treffen. Vielen Dank auch an Lisa Muth und Sascha Bierbauer unter anderem für die Gespräche über Gott und die Welt beim Mittagessen und generell für die Freundschaft, die meinen Arbeitsalltag stets bereichert hat. Und natürlich danke ich euch allen für die produktiven Kommentare und Diskussionen in den Gruppentreffen und Probevorträgen, die entscheidend zum Verlauf meiner Promotion beigetragen haben, und nicht zuletzt für die Geduld und vermutlich auch die Nerven, die ihr teilweise aufbringen musstet bis ich mit meinen Berichten durch war. Ebenso danke ich Gabi Klinck für die Unterstützung in IT-Angelegenheiten.

Zudem gilt mein großer Dank der ICON(-ART)-Community am IMK, am SCC, beim DWD, am DKRZ und MPI-M und beim C2SM, und in diesem Zusammenhang auch Dr. Daniel Rieger und Dr. Jennifer Buchmüller, die mich in das Gatekeeper-Dasein einführten und vorstellten, sowie meinen Mit-Gatekeepern am IMK-ASF, Khompat Satitkovitchai und Dr. Stefan Versick (und zuvor Dr. Michael Weimer), ohne deren Unterstützung die Gatekeeper-Aufgaben wohl schnell Überhand genommen hätten.
Ebenso danke ich allen ehemaligen und aktuellen Mitarbeitern am IMK für die angenehme Arbeitsatmosphäre.
Eine gute Work-Life-Balance sollte wohl auch für die Promotion wichtig sein, zumindest war sie es bei dieser. Deswegen möchte ich hiermit noch meiner Familie und Freunden danken: Zunächst möchte ich erklären, dass ohne den Rückhalt durch meine Familie, diese Arbeit wohl nicht zustande gekommen wäre. Jörg, Michaela, Jens und Inga, vielen Dank, dass ich mich stets habe auf euch verlassen können, dass ihr Verständnis gezeigt habt, mir ermöglicht habt diesen Weg zu gehen und einfach für alles andere auch. Auch danke ich meiner Mutter, Sabine, die mir so viel, in leider viel zu kurzer Zeit, auf den Weg gegeben hat, dass es mich bis hierhin geführt hat und vermutlich noch weiter führen wird. Und zu guter Letzt bedanke ich mich bei meinen Freunden, die es irgendwie geschafft haben, es mit mir auszuhalten, insbesondere in den letzten Monaten. Auch wenn ich hier nicht alle nennen kann, so möchte ich doch zumindest einige nennen: Alexander, Christoph, Nadine und Robin, die Tatsache, dass wir mit DnD angefangen haben, hat die Pandemiezeit deutlich erträglicher gemacht und mir erlaubt nach dem ein oder anderen stressigen Tag buchstäblich in eine andere Welt zu flüchten - Danke für all die schönen Stunden. Zudem danke ich euch sowie Steffen, Corinna, Sven, Marco, Lena und Maren für all die moralische Unterstützung und den Rückhalt.